Abstract of "Interferometry in Topological Quantum Liquids" by Zezhu Wei, Ph.D., Brown University, May 2024.

Topological phases of matter have recently attracted intense interest. Among topological phases, topological quantum liquids, such as fractional quantum Hall liquids and gapped quantum spin liquids, possess exotic excitations with fractional statistics, known as anyons. They are of great interest to quantum information science. The most direct method to probe anyonic statistics involves electronic interferometers, which have proven successful in fractional quantum Hall liquids very recently. This thesis gives a comprehensive description of the interferometery technique and explains how electronic interferometers can be adapted to thermal interferometry that can probe the non-Abelian anyonic statistics of charge-neutral excitations in Kitaev spin liquids. We compare the Fabry–Pérot geometry and the Mach–Zehnder geometry and identify unique signatures of Ising statistics in Kitaev spin liquids. Furthermore, the idea of thermal interferometry can be generalized to probe almost any Abelian or non-Abelian anyonic statistics in topological liquids. In general, the absence of interference current in a Mach–Zehnder device is a smoking-gun evidence of non-trivial anyonic statistics. This thesis also addresses the problem of electronic quantum Hall interferometers with multiple edge channels, explaining how a closed inner edge channel affects the measured I–V curve at a finite source-drain bias voltage. When the inner mode is completely reflected and the outer mode is partially transmitted, we find striking features at low temperatures related to the resonance of excitations of the closed inner channel. However, these features disappear rapidly with increasing temperature. Another feature brought by the closed inner channel is the exponential decay in the I–V curve at a high bias, which is due to the fluctuations of the quasiparticle number on the inner channel.

Interferometry in Topological Quantum Liquids

by

Zezhu Wei

B. Sc., City University of Hong Kong, 2019

A dissertation submitted in partial fulfillment of the
requirements for the Degree of Doctor of Philosophy
in the Department of Physics at Brown University

Providence, Rhode Island
May 2024

This dissertation by Zezhu Wei is accepted in its present form by
the Department of Physics as satisfying the dissertation requirement
for the degree of Doctor of Philosophy.

Date ________________ ________________________________

Dmitri Feldman, Advisor

Recommended to the Graduate Council

Date ________________ ________________________________

Jia (Leo) Li, Reader

Date ________________ ________________________________

Brad Marston, Reader

Approved by the Graduate Council

Date ________________ ________________________________

Thomas A. Lewis
Dean of the Graduate School

Vita

Zezhu Wei

Education

2019–2024 PhD in Physics. Brown University.
Advisor: Dmitri Feldman

2015–2019 Bsc in Applied Physics with First Class Honours. City University of Hong Kong.

Publications

1. Z. Wei, D. E. Feldman, and B. I. Halperin, Quantum Hall interferometry at finite bias with multiple edge channels, in preparation.

2. T. Werkmeister, J. R. Ehrets, Y. Ronen, M. E. Wesson, D. Najafabadi, K. Watanabe, T. Taniguchi, Z. Wei, D. E. Feldman, B. I. Halperin, A. Yacoby, and P. Kim, Strongly coupled edge states in a graphene quantum Hall interferometer, arXiv:2312.03150.

3. N. Batra, Z. Wei, S. Vishveshwara, and D. E. Feldman, Anyonic Mach-Zehnder interferometer on a single edge of a two-dimensional electron gas, Phys. Rev. B **108**, L241302 (2023).

4. Z. Wei, N. Batra, V. F. Mitrović, and D. E. Feldman, Thermal interferometry of anyons, Phys. Rev. B **107**, 104406 (2023).

5. Z. Wei, V. F. Mitrović, and D. E. Feldman, Thermal interferometry of anyons in spin liquids, Phys. Rev. Lett. **127**, 167204 (2021).

6. X.-M. Zhang, Z. Wei, R. Asad, X.-C. Yang, and X. Wang, When does reinforcement learning stand out in quantum control? a comparative study on state preparation, npj Quantum Inf. **5**, 85 (2019).

Honors and Awards

2023 Physics Dissertation Fellowship. Department of Physics, Brown University.

2019 Best Poster Award (Postgraduate Category). Celebration of Physics - Department of Physics Annual Symposium 2019, City University of Hong Kong.

2019 Distinguished Final Year Project Award. Department of Physics, City University of Hong Kong.

2018–2019 CityU Scholarship. City University of Hong Kong.

2017–2019 Academic Award. Department of Physics, City University of Hong Kong.

Teaching and Mentoring

Fall 2021 PHYS 2430 Quantum Many Body Theory, Teaching Assistant

Fall 2021 PHYS 2320 Quantum Theory of Fields II, Grader

Fall 2021 PHYS 2030 Classical Theoretical Physics I, Grader

Spring 2020 PHYS 0500 Advanced Classical Mechanics, Teaching Assistant

Fall 2019 PHYS 0030 Basic Physics A, Teaching Assistant

Preface

In modern condensed matter physics, topology is an important concept in studying the exotic properties of matter. The introduction of topology starts with Kosterlitz and Thouless' discovery of topological phase transitions in 1973 [1]. Since von Klitzing discovered the integer quantum Hall effect (IQHE) in 1980 [2], the phrase "topological phase of matter" was coined to describe a phase of matter whose properties are precisely quantized in a wide range of parameters. Topological quantum liquids are a subset of topological phases. Strong quantum fluctuations in topological quantum liquids prevent them from forming a crystal-like phase [3]. This thesis focuses on two primary examples of topological quantum liquids: fractional quantum Hall (FQH) states and gapped quantum spin liquids (QSL). They exhibit "topological orders", and have fractional excitations known as anyons. These anyons have different exchange statistics from fermions or bosons and can be used to build a topological quantum computer.

As implied in the title, the interferometry technique is the main theme of this thesis. Electronic interferometers are proven to be powerful tools for probing the fractional statistics of anyons in the $\nu = 1/3$ FQH state. This thesis aims to extend the theory of interferometers in two directions: one is electronic interferometers for quantum Hall (QH) states with multiple channels, and another is thermal interferometers for topological liquids with an arbitrary topological order. The latter goal originates from the problem of adapting the interferometry technique to gapped QSLs. QSLs are known to have no charge excitations; hence, there is no electric current to measure. However, thermal transport is universal in all topological liquids, and we will show that thermal interferometers are capable of probing neutral excitations in spin liquids.

Chapter 1 of this thesis is an introduction to fundamental concepts in topological liquids, anyons, and electronic quantum Hall interferometers. We introduce the thermal interferometers for spin liquids in Chapter 2, where we focus on the Kitaev spin liquid. We compare the Fabry–Pérot geometry and the Mach–Zehnder geometry and identify unique signatures of Ising statistics in Kitaev spin liquids. The idea of thermal interferometry is generalized to probe almost any Abelian or non-Abelian anyonic statistics in topological liquids. In general, the absence of interference current in a Mach–Zehnder device is a smoking-gun evidence of non-trivial anyonic statistics. Chapter 3 addresses the problem of electronic quantum Hall interferometers with multiple edge channels, explaining how a closed inner edge channel affects the measured I–V curve at a finite source-drain bias voltage. When the inner mode is completely reflected and the outer mode is partially transmitted, we find striking features at low temperatures related to the resonance of excitations of the closed inner channel. However, these features disappear rapidly with increasing temperature. Another feature brought by the closed inner channel is the exponential decay in the I–V curve at a high bias, which is due to the fluctuations of the quasiparticle number on the inner channel.

Acknowledgements

At the end of my five-year PhD program, I would like to express my deepest gratitude to my advisor, Prof. Dima Feldman. His philosophy of physics, including the enthusiasm for bridging the gap between theories and experiments, the emphasis on correctness, and the cautious attitude towards numerical results, has greatly shaped my view of physics. As a brilliant physicist, he knows things far more than I could imagine. Throughout these years, I have learned so much from the discussions with him. Of course, the things I learned are not limited to the pure theory of condensed matter physics, and they also include things like estimation methods of experimental scales, asymptotic approximations of integrals, and even projective geometry in mathematics. What fascinates me even more is his extensive understanding of subjects other than natural science. I always enjoy chatting with him about history and literature in different nations, as well as the linguistics of languages from throughout the world. He is an exceptional teacher who can explain things in a clear and lucid style. I would like to credit the presentation abilities that I may have acquired during my PhD for his demonstration. For a number of times, his patience and guidance saved me from struggling with the research problems and making stupid mistakes. I also benefited from the care he put into proofreading my manuscripts and presentation slides. I consider myself really fortunate to have the opportunity to study under him. Without his support, I could not have reached this far on the lonely road of physics research. I cannot thank him enough for everything he has taught me.

I am indebted to Prof. Brad Marston and Prof. Jia (Leo) Li for serving on my defense committee and carefully reading my thesis. Moreover, I really enjoyed the three courses taught by Prof. Brad Marston that I have attended: Classical Theoretical Physics I, Quantum Many-Body Theory, and Advanced Statistical Mechanics. I am also grateful to have Prof. Marston write recommendation letters for me. I want to thank Prof. Andrey Gromov and Prof. Vesna Mitrović for serving on my preliminary exam committee. I still remember the recognition I received from Prof. Gromov's Solid State Physics course. I benefited from the collaboration with Prof. Mitrović, who provides helpful support for the findings discussed in Chapter 2 of this thesis. Many thanks to all the professors and instructors at Brown who taught me courses. I want to express my gratitude to the Department of Physics and the Graduate School for providing the travel fund and selecting me as a Physics Dissertation Fellow.

I would like to express my deep appreciation to Prof. Bert Halperin at Harvard for collaborating with me and writing recommendation letters for me. He used his remarkable physics intuition to point out the missing parts in the naive physical model I had. Chapter 3 of this thesis would not be polished to its current form without his wisdom. I also have the pleasure of collaborating with Thomas Werkmeister, James Ehrets and, Prof. Philip Kim at Harvard. They kindly presented their experimental findings and spent time discussing them with me. Big thanks to my groupmate Nav Batra, who is always willing to discuss physics problems and share his views on physics with me. He was also a nice roommate when we went to the APS March Meeting together, and I thank him for tolerating my bad jokes. I am glad to collaborate with him on two of my papers. He helped me with preparing the slides and proofreading some of my manuscripts. Also, I should not forget to thank him for bringing the delicious cake to my thesis defense.

Tracing back my own path of physics, I must acknowledge my high school physics teacher, Yuli Ding, and my undergraduate advisor, Prof. Xin (Sunny) Wang, for teaching me physics and guiding me to the academic world.

I'm extremely grateful to have Yuanqi Li, Tianyu He, Xianlong Liu, Naiyuan Zhang, Lecheng Ren, Lingfeng Li, and Jiang-Xiazi Lin as my roommates and "quasi-roommates" in Providence. The fun time we spent together brought me so much joy and was extremely precious during the COVID-19 pandemic. Moreover, serious physics-related discussions with them always taught me new perspectives on physics. The moments with them will be treasured for a lifetime. Thanks should also go to Junjie Zheng for teaching me field theories and listening to all of my nonsense. I would like to thank Rishabh Bhardwaj for organizing and participating in the conformal field theory discussion group. I want to acknowledge all the fellow students and friends I have met during my years at Brown, including Xuli Yan, Calvin Bales, Qiaochu Wang, Shiyu Zhou, Boyuan Xu, Silverio Johnson, Eric Barrett, Erin Morissette, Alex Jacoby, Chen Ding, Zifei Liu, Pranay Sampat, Zhaoji Fang, Yang Huangpu, Li Feng, Zhenghao Rao, and many others. It is a pleasant experience to befriend them at Brown.

I dedicate this thesis to my parents, Guguo Wei and Qingdi Shu. My endeavor in physics would not have been possible without their support and encouragement. Throughout my life, whenever I confront challenges and feel depressed, their words provide me strength to overcome the obstacles. This thesis is also dedicated to my grandfather, Youchun Shu, who passed away during my PhD. The unconditional love he gave me is remembered forever.

Contents

⋆ Chapter 2 and Appendices B to I are published as Z. Wei, N. Batra, V. F. Mitrović, and D. E. Feldman, Thermal interferometry of anyons, Phys. Rev. B **107**, 104406 (2023). Chapter 3 and Appendices J to P are parts of an on-going project in collaboration with D. E. Feldman and B. I. Halperin. Appendix A is published as a part of Z. Wei, V. F. Mitrović, and D. E. Feldman, Thermal interferometry of anyons in spin liquids, Phys. Rev. Lett. **127**, 167204 (2021).

List of Tables

List of Figures

Chapter 1

Introduction

1.1 Fractional quantum Hall effect

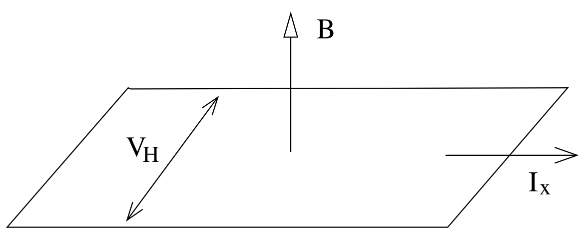

Figure 1.1: The basic setup for the Hall effect. Source: D. Tong, "Lectures on the quantum Hall effect", arXiv:1606.06687 [hep-th].

The classical Hall effect, shown in Fig. 1.1, is a well-known phenomenon in classical electrodynamics. When a voltage V_H is applied to a conductor under a magnetic field B, it will generate a steady transverse current I_x. It occurs when the electrostatic force balances the Lorentz force on charge carriers (electrons or holes). To reach the quantum limit, one needs to restrict the motion of electrons to a two-dimensional (2D) plane, which can be realized in semiconductor devices. These electrons form the so-called two-dimensional electron gas (2DEG). In 1980, von Klitzing found that when applying a perpendicular magnetic field to the 2DEG, its transverse resistance R_{xy} is quantized at integer values [2],

$$R_{xy} = \frac{V_y}{I_x} = \frac{1}{\nu}\frac{h}{e^2} \tag{1.1}$$

where $\nu = 1, 2, 3, \ldots$ is known as the filling factor. This is known as the integer quantum Hall effect (IQHE). These integer quantum Hall (IQH) states manifest themselves as plateaux in the plot of transverse resistance R_{xy} versus magnetic field B. Later in 1982, the quantization of R_{xy} at fractional filling factors, which is known as the fractional quantum Hall effect (FQHE), was observed in experiments [5, 6]. The first observed fractional filling factors are $1/3$ and $2/3$, but more filling

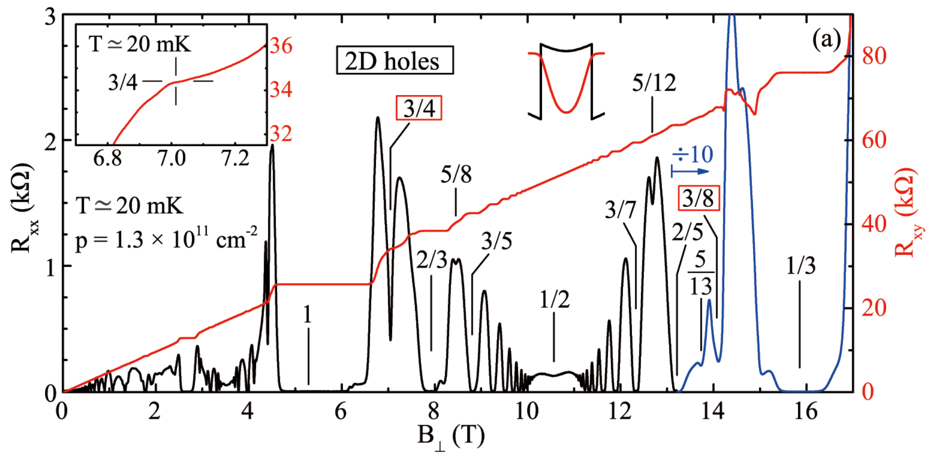

Figure 1.2: Fractional quantum Hall traces in 2D hole systems. The longitudinal resistance R_{xx} (black and blue) and transverse resistance R_{xy} (red) are traced against the perpendicular magnetic field $B_\perp$. The fractional quantum Hall states are marked with their filling factors. Source: C. Wang et al., "Even-denominator fractional quantum Hall state at filling factor $\nu = 3/4$", Phys. Rev. Lett. **129**, 156801 (2022)

factors have been observed subsequently, including, but not limited to, 1/5, 2/5, 3/7, 4/3, and 5/2. Fig. 1.1 shows the FQHE in 2D hole systems, and a number of fractional filling factors are visible, including an exotic $\nu = 3/4$ filling [7].

1.1.1 Landau levels and integer quantum Hall effect

To understand the quantum Hall effect, one has to solve the problem of free electrons under a magnetic field B in quantum mechanics first. It turns out that the eigen energy of electrons is quantized at the so-called Landau levels,

$$E_n = \hbar\omega_B\left(n + \frac{1}{2}\right), \tag{1.2}$$

where $\omega_B = eB/m$ is the cyclotron frequency and the Landau level index $n = 0, 1, 2, \ldots$ is an integer. If we adopt a symmetric gauge for the magnetic field, the vector potential is set to $\mathbf{A} = (-yB/2, xB/2)$, and the wave function of the state in the lowest Landau level ($n = 0$) takes a simple form [4],

$$\psi_{0,m}(z, \bar{z}) = \frac{1}{\sqrt{2\pi 2^m m!}} \frac{z^m}{l_B^{m+1}} e^{-|z|^2/4l_B^2} \tag{1.3}$$

where $z = x - iy$ and $\bar{z} = x + iy$ are complex coordinates, m is the angular momentum quantum number, and l_B is the magnetic length defined by

$$l_B = \sqrt{\frac{\hbar}{eB}}. \tag{1.4}$$

To find the degeneracy $\mathcal{N}$ of each Landau level, we notice that the probability density $|\psi_{0,m}|^2$ is maximized on a ring of radius $\sqrt{2m}l_B$, then

$$\mathcal{N} = \frac{A}{2\pi l_B^2} = \frac{AB}{\Phi_0}, \tag{1.5}$$

where A is the area of the sample and Φ_0 is the magnetic flux quanta defined by

$$\Phi_0 = \frac{2\pi\hbar}{e} = B \times 2\pi l_B^2. \tag{1.6}$$

In fact, the IQHE is the result of ν fully-filled Landau levels of non-interacting electrons. The density of electrons of ν fully-filled Landau levels is

$$n = \frac{B}{\Phi_0}\nu, \tag{1.7}$$

which is consistent with the experimental fact that the center of a plateau occurs at the magnetic field

$$B = \frac{n}{\nu}\frac{h}{e} = \frac{n}{\nu}\Phi_0. \tag{1.8}$$

Using the so-called "Laughlin's charge pumping" argument, one can show that the resistivity R_{xy} is indeed quantized at integer values in a Corbino geometry [8]. Actually, the transport properties of the QHE could be better understood in terms of the edge states [9]. Every real-world material has its boundary, and the boundary of a two-dimensional material is its edge. The confining potential on the edge leads to edge excitations without an energy gap, while the bulk state has an energy gap $\hbar\omega_B$ set by the Landau levels. Furthermore, the disorder potentials inside the material will create localized states in the bulk, but the edge states will remain extended. It is known that only the extended states carry the electric current, and the energy of a localized state lies either above or below the extended states in a given Landau level. Therefore, this explains the robustness of plateaux in the Hall resistance plot versus the magnetic field.

To summarize, the IQH state is a quantum liquid state with a gapped bulk and gapless edge states. The bulk is also called incompressible due to the analogy of hydrodynamics. However, the same picture cannot explain the FQH states, since one expects no energy gap for partially filled Landau levels. The crucial ingredient missing in the argument is the Coulomb interaction between electrons, and the FQHE is a problem of strongly corrected electrons rather than non-interacting electrons. In 1983, Laughlin constructed a many-body wave function that can explain the FQHE at filling factor $\nu = 1/3$ [10]. This ground-breaking result leads to theoretical studies of QH states at various filling factors, and opens the door to a new world of topological order. Like IQH states, FQH states are also incompressible quantum liquids and host gapless edge excitations. The most striking feature of FQH states is that they have quasiparticle excitations with fractional charge and fractional statistics.

The next two subsections are devoted to the FQHE, including aspects of their bulk physics and edge modes. This arrangement is a reflection of the bulk-edge correspondence, which is a widely accepted idea for topologically non-trivial systems. It asserts that there is a one-to-one correspondence between the bulk physics and the edge physics. In the context of QH physics, the bulk is described by Chern–Simons theories in $2+1$ dimensions, and the edge is described by conformal field theories in $1+1$ dimensions.

1.1.2 Physics in the bulk

Laughlin wave function

At filling factor $\nu = 1/m$, where m is an odd integer, the many-body bulk state is described by the Laughlin wave function [8],

$$\Psi(z_i) \sim \prod_{i<j}(z_i - z_j)^m \exp\left(-\sum_{i=1}^{n}\frac{|z_i|^2}{4l_B^2}\right), \tag{1.9}$$

where z_i is the complex coordinate of the i-th electron, and n is the total number of electrons. This state is an incompressible quantum fluid with a gapped spectrum. Excitations in FQH states are called quasiparticles or quasiholes. The wave function for the FQH state with a localized quasihole sitting at a complex coordinate η is given by

$$\Psi_{\mathrm{qh}}(z_i) \sim \prod_{i=1}^{n}(z_i - \eta)\prod_{k<l}(z_k - z_l)^m \exp\left(-\sum_{i=1}^{n}\frac{|z_i|^2}{4l_B^2}\right). \tag{1.10}$$

One can show that a quasihole carries a fractional charge of $e/3$ [10] and obeys a fractional statistics with an exchange phase of $\alpha = \pi/m$ [11, 12]. In contrast, a quasiparticle carries a fractional charge of $-e/3$ but has the same exchange phase of π/m. The exchange phase of the combined object with n quasiholes is $n^2\pi/m$. Excitations with fractional statistics are called anyons and will be discussed in detail in Section 1.3.

Hierarchical states

The Laughlin wave function is only for FQH states at filling factor $\nu = 1/m$, and it was pointed out later that quasiparticles and quasiholes can form a QH condensate on top of the $\nu = 1/m$ state and give birth to a daughter state [12, 13]. One can successively build FQH states in this way, and these states are called hierarchical states. For the daughter states of $\nu = 1/m$, the additional filling factor due to the quasiparticles is

$$\nu_{\mathrm{quasi}} = \pm\frac{1}{2pm^2 \pm m}, \tag{1.11}$$

where p is a positive integer, and the total filling factor is

$$\nu = \frac{2p}{2pm \pm 1}, \tag{1.12}$$

where -1 is for quasiparticles and $+1$ is for quasiholes. When $m = 3, p = 1$, the daughter state due to quasiparticles is $\nu = 2/5$, and the daughter state due to quasiholes is $\nu = 2/7$. If we continue to condense quasiparticles of the $\nu = 2/5$ state and keep doing these, we can get a series of hierarchical states with $\nu = 3/7, 4/9, 5/11, \ldots$ As will be seen in the subsequent sections, these hierarchical states can be thought of as composite electrons with integer fillings, and they have multiple edge channels.

Composite fermion

The composite fermion picture introduced by Jain [14, 15] provides an alternative and more intuitive way to understand the FQH states. In this picture, the FQH states of electrons can be viewed as the IQH states of composite fermions, which are electrons attached with an infinitely thin magnetic flux tube. We attach $2s$ units of magnetic flux quanta Φ_0 to electrons and let these composite fermions form an IQH state under magnetic field B^* with filling factor $\nu^* = p$, where s and p are integers. From the theory of IQHE, $|B^*| = n\Phi_0/p$, where n is the density of electrons. Next, we smear out the flux attached to the electrons to a uniform magnetic field, and the total magnetic field for electrons is

$$B = B^* + 2sn\Phi_0 = n\Phi_0(2s \pm \frac{1}{p}). \tag{1.13}$$

We can immediately find the filling factors for electrons

$$\nu = \frac{n\Phi_0}{B} = \frac{p}{2sp \pm 1}. \tag{1.14}$$

A sequence of these states is known as the Jain sequence. When $s = 1$ and $B^* > 0$, $\nu = 1/3, 2/5, 3/7, 4/9$ for $p = 1, 2, 3, 4$. These are exactly the hierarchical states we have seen in the previous section—daughter states of the $\nu = 1/3$ Laughlin state. The composite fermion also tells us what happens when the Landau level is hall-filled. When $s = 1, p \to \infty$, the filling factor $\nu \to 1/2$, but the effective magnetic field for composite fermions $B^* \to 0$ simultaneously. In the absence of a magnetic field, the state is a Fermi liquid of composite fermions without an energy gap, and this explains why no FQH plateau at $\nu = 1/2$ is observed in experiments.

Non-Abelian states

Despite the absence of a $\nu = 1/2$ plateau, a FQH plateau at $\nu = 5/2$ is visible in experiments, suggesting that the $\nu = 5/2$ state is an incompressible fluid. Since $5/2 = 2 + 1/2$, the state should have a fully-filled lowest Landau level with both spins and a half-filled second Landau level. One candidate for the half-filled incompressible state is the non-Abelian Moore–Read Pfaffian state, where the composite fermions pair up and form a $p_x + ip_y$ superconducting state. The Moore–Read wave function for an even number of electrons at filling factor $\nu = 1/m$, where m is an even integer, is given by [16]

$$\Psi(z_i) = \mathrm{Pf}\left(\frac{1}{z_i - z_j}\right) \prod_{i<j} (z_i - z_j)^m \exp\left(-\sum_{i=1}^{n} \frac{|z_i|^2}{4l_B^2}\right), \tag{1.15}$$

where Pf denotes the Pfaffian of a skew-symmetric matrix. The wave function of two quasihole excitations at coordinates η_1 and η_2 is

$$\Psi_{\mathrm{qh}}(z_i) = \mathrm{Pf}\left(\frac{(z_i - \eta_1)(z_j - \eta_2) + (z_j - \eta_1)(z_i - \eta_2)}{z_i - z_j}\right) \prod_{i<j} (z_i - z_j)^m \exp\left(-\sum_{i=1}^{n} \frac{|z_i|^2}{4l_B^2}\right). \tag{1.16}$$

Each quasihole excitation has an electric charge of $e/2m$. It is shown that the $2n$-quasiholes states are degenerate, and the degeneracy is 2^{n-1} [17]. This is quite an exotic property since it suggests that the Hilbert space dimension of a single quasihole is $\sqrt{2}$. In fact, quasiholes of the Moore–Read Pfaffian state are non-Abelian anyons that follow the Ising statistics, while excitations of hierarchical states are Abelian anyons. Since the Moore–Read Pfaffian state is a $p_x + ip_y$ superconductor of composite fermions, it also has Majorana fermion excitations. The Ising topological order in this non-Abelian state manifests in the presence of both anyonic excitations. These non-Abelian anyons are also seen as candidates for topological qubits, which can be used to build a topological quantum computer [18].

Effective theory: Chern–Simons theory

Effective theories are powerful tools to study low-energy excitations in the topological phases of matter. The effective theory for the bulk of a $\nu = 1/m$ (m odd) FQH liquid is a Chern–Simons theory in $2+1$ dimension with a Lagrangian density [3]

$$\mathcal{L} = -\frac{1}{4\pi\nu} a_\mu \partial_\nu a_\lambda \epsilon^{\mu\nu\lambda} + \frac{e}{2\pi} A_\mu \partial_\nu a_\lambda \epsilon^{\mu\nu\lambda}, \tag{1.17}$$

where μ, ν, λ take the values of $0, 1, 2$, $\epsilon^{\mu\nu\lambda}$ is the Levi-Civita tensor, A_μ is the vector potential for the magnetic field, and a_μ is an emergence gauge field such that the electron number current J^μ is given by

$$J^\mu = \frac{1}{2\pi} \partial_\nu a_\lambda \epsilon^{\mu\nu\lambda}. \tag{1.18}$$

If we use j^μ for the quasiparticle number current and assume the quasiparticle carries l units of a_μ charge, then the effective theory has an additional term

$$\mathcal{L} = ... + l a_\mu j^\mu. \tag{1.19}$$

We can find that the quasiparticle carries a fractional electric charge of $-l\nu e$. Furthermore, the statistical phase of exchanging two quasiparticles is $l^2\nu\pi$. Both properties match those of the combined object of l fundamental quasiparticles that carry electric charge $-\nu e$. Indeed, the Chern–Simons theory in Eq. (1.17) and the Laughlin wave function describe the same FQH state.

According to the hierarchical picture, quasiparticles can form their own condensate. We use a matrix K to construct the corresponding Chern–Simons theory for hierarchical states [3]. The Lagrangian density is

$$\mathcal{L} = -\frac{1}{4\pi} K_{IJ} a_{I\mu} \partial_\nu a_{J\lambda} \epsilon^{\mu\nu\lambda} + \frac{e}{2\pi} q_I A_\mu \partial_\nu a_{I\lambda} \epsilon^{\mu\nu\lambda} \tag{1.20}$$

where $a_{I\mu}$ is the gauge field for the I-th condensate, and q is a charge vector that tells how the gauge fields couple to the magnetic field. The filling factor of the state is found to be $\nu = q^T K^{-1} q$. If we denote the quasiparticle current of a hierarchical state as j^μ, and add the following term to the Lagrangian density

$$\mathcal{L} = \cdots + l_I a_{I\mu} j^\mu, \tag{1.21}$$

where l_I are integers, the charge and statistical phase of the quasiparticle labeled by l are

$$Q_l = -el^T K^{-1} q, \quad \theta_l = \pi l^T K^{-1} l. \tag{1.22}$$

The matrix K and charge vector q, together with the Wen–Zee shift S and spin vector s [19], are topological quantum numbers that characterize the topological orders of Abelian QH states. The Wen–Zee shift S and spin vector s are associated with QH states on a curved space. If we ignore S and s, two states (K_1, q_1) and (K_2, q_2) are equivalent if there exists a $W \in \mathsf{SL}(n, \mathbb{Z})$ that

$$q_2 = W q_1, \qquad K_2 = W K_1 W^T. \tag{1.23}$$

For example, the $\nu = 2/5$ state described by $K_1 = \begin{pmatrix} 3 & -1 \\ -1 & 2 \end{pmatrix}, q_1 = \begin{pmatrix} 1 \\ 0 \end{pmatrix}$ is equivalent to $K_2 = \begin{pmatrix} 3 & 2 \\ 2 & 3 \end{pmatrix}, q_2 = \begin{pmatrix} 1 \\ 1 \end{pmatrix}$. The transformation matrix is $W = \begin{pmatrix} 1 & 0 \\ 1 & 1 \end{pmatrix}$.

As one would expect, the effective theory for non-Abelian QH states is the non-Abelian Chern–Simons theory. In a general Chern–Simons theory, the gauge field a_μ is a Lie-algebra-valued field. If the corresponding Lie group G is a non-Abelian group, then the theory is known as a non-Abelian Chern–Simons theory. A Chern–Simons theory also contains a quantized coupling constant k, which is called the level. Therefore, the Abelian Chern–Simons theory in Eq. (1.17) is a U(1) Chern–Simons theory at level $k = 1/\nu$. The Chern–Simons theory for the $\nu = 1/2$ Moore–Read Pfaffian state has two gauge fields: one is U(1) at level 2, and another is SU(2) at level 2. More details of the non-Abelian Chern–Simons theory can be found in Ref. [20].

1.1.3 Physics on the edge

Effective theories for FQH edges are conformal field theories in $1+1$ dimension. For Abelian states, their edge excitations are chiral Luttinger liquids. At filling factor $\nu = 1/m$, the Lagrangian of a right-moving edge is

$$L = -\frac{\hbar}{4\pi\nu} \int dx \, [(\partial_x \phi)(\partial_t + v\partial_x)\phi] \tag{1.24}$$

where ϕ is a Bose field, and v is the velocity of the edge mode. The edge Hamiltonian is given by

$$H = \frac{\hbar v}{4\pi\nu} \int dx \, (\partial_x \phi)^2. \tag{1.25}$$

The equal-time commutation relation is

$$[\phi(x), \phi(y)] = i\pi\nu \, \mathrm{sgn}(x-y). \tag{1.26}$$

The charge density of the FQH edge is

$$\rho = \frac{e}{2\pi} \partial_x \phi. \tag{1.27}$$

The operator that annihilates quasiparticles with charge $-\nu e$ (or create quasiholes with charge νe) is given by a vertex operator,

$$\Psi(x) = \frac{F}{\sqrt{2\pi a}} e^{ik_F x} e^{-i\phi(x)}, \tag{1.28}$$

where F is a unitary Klein factor and a is a cutoff length [21, 22]. One can verify the charge of the quasiparticle operator by computing the commutator of the charge density and the quasiparticle operator,

$$[\rho(x), \psi(y)] = \nu e \delta(x-y)\psi(y). \tag{1.29}$$

As a side note, one can always scale the field ϕ without changing the edge physics, and a convenient choice is $\tilde{\phi} = \phi/\sqrt{\nu}$, in which the correlation function is $[\tilde{\phi}(x), \tilde{\phi}(y)] = i\pi \,\mathrm{sgn}(x-y)$ and the quasiparticle annihilation operator is $\Psi(x) = \frac{F}{\sqrt{2\pi a}} e^{ik_F x} e^{-i\sqrt{\nu}\tilde{\phi}(x)}$.

For Abelian hierarchical FQH states characterized by the K-matrix and charge vector q, its Lagrangian is

$$L = -\frac{\hbar}{4\pi}\int dx\, (K_{IJ}\partial_t\phi_I\partial_x\phi_J + V_{IJ}\partial_x\phi_I\partial_x\phi_J), \tag{1.30}$$

where V is a positive-definite matrix. The edge Hamiltonian is

$$H = \frac{\hbar}{4\pi}\int dx\, V_{IJ}\partial_x\phi_I\partial_x\phi_J, \tag{1.31}$$

with commutation relations given by

$$[\phi_I(x), \phi_J(y)] = i\pi(K^{-1})_{IJ}\,\mathrm{sgn}(x-y). \tag{1.32}$$

The charge density is given by

$$\rho = \frac{e}{2\pi} q_I \partial_x\phi_I, \tag{1.33}$$

and a quasiparticle operator of the form

$$\Psi_l \propto e^{-il_I\phi_I} \tag{1.34}$$

annihilates quasiparticles of charge $Q_l = -el^T K^{-1} q$. One can simultaneously diagonalize K and V by the transformation $\phi_I \to U_{IJ}\tilde{\phi}_I$, such that

$$\tilde{K}_{IJ} = (U^T K U)_{IJ} = s_I\delta_{IJ}, \quad \tilde{V}_{IJ} = (U^T V U)_{IJ} = v_I\delta_{IJ}, \tag{1.35}$$

where $s_I = \pm 1$ represents the parity of the eigenvalues of K and $v_I > 0$. The Hamiltonian and commutation relations can be expressed as

$$H = \sum_I \frac{\hbar v_I}{4\pi}\int dx\, (\partial_x\tilde{\phi}_I)^2, \tag{1.36}$$

$$[\tilde{\phi}_I(x), \tilde{\phi}_J(y)] = i\pi s_I\delta_{IJ}\,\mathrm{sgn}(x-y). \tag{1.37}$$

We can see that v_I is the velocity of the I-th eigenmode, and s_I determines its chirality, with $+1$ for right-moving and -1 for left-moving.

The edge theory of the non-Abelian Pfaffian state at filling factor $\nu = 1/2$ consists of a chiral boson charge mode and a co-propagating Majorana neutral mode [23, 24]

$$L = -\frac{\hbar}{2\pi}\int dx\, (\partial_x\phi)(\partial_t + v_c\partial_x)\phi + \frac{i\hbar}{4\pi}\int dx\, \psi(\partial_t + v_n\partial_x)\psi, \tag{1.38}$$

where v_c and v_n are velocities of the charge mode and the neutral mode respectively. The corresponding Hamiltonian is

$$H = \frac{\hbar v_c}{2\pi} \int dx \, (\partial_x \phi)^2 - \frac{i\hbar v_n}{4\pi} \int dx \, \psi \partial_x \psi, \tag{1.39}$$

where the boson operator satisfies the usual commutation relation in Eq. (1.26), and the Majorana fermion operator ψ satisfies the anticommutation relation

$$\{\psi(x), \psi(y)\} = 2\pi\delta(x - y). \tag{1.40}$$

The electron operator is given by $\Phi_{el} = \psi e^{i\sqrt{2}\phi}$. The operator for quasiparticles with charge $e/4$ is $\Phi_{1/4} = \sigma e^{i\phi/2\sqrt{2}}$, where σ is the (non-local) Ising spin field in the free Majorana fermion theory. Details of the free Majorana fermion theory and its connection with the Ising model can be found in Chapter 12 of Ref. [25].

1.2 Quantum spin liquid

Unlike the FQHE, another kind of topological phase, the spin liquid, is yet less understood in experiments. QSLs are highly correlated spin systems, and our understanding of quantum spin liquids started with the theoretical proposals made by Anderson in 1973 [26]. Some spin liquids with gapped bulk excitations have non-trivial topological orders, including the Kalmeyer–Laughlin liquid [27] and the Kitaev magnet [28]. Since the proposal of the Kitaev magnet, there have been many experimental attempts to find any material that can realize this topological phase. Some [29] claimed that $RuCl_3$ has a Kitaev spin liquid phase, but some other experiments cast doubts on this claim [30]. In this section, I will give a brief introduction to the Kitaev magnet model, and discuss its topological order and edge theory.

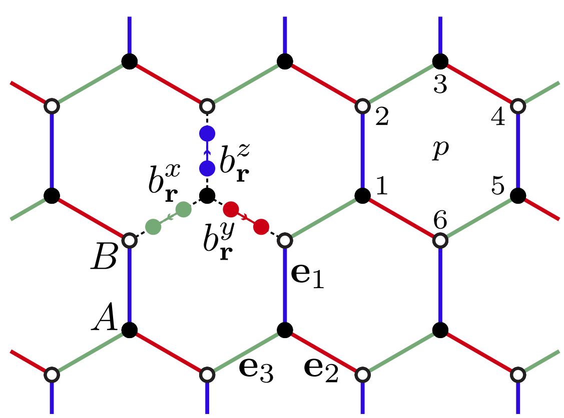

Figure 1.3: The Kitaev magnet defined on a honeycomb lattice. Source: D. Aasen et al., "Electrical probes of the non-Abelian spin liquid in Kitaev materials", Phys. Rev. X **10**, 031014 (2020).

The Kitaev magnet is a model of spins on a honeycomb lattice model, with the Hamiltonian defined by

$$H = -J_x \sum_{x \text{ links}} \sigma_j^x \sigma_j^x - J_y \sum_{y \text{ links}} \sigma_j^y \sigma_j^y - J_z \sum_{z \text{ links}} \sigma_j^z \sigma_j^z \tag{1.41}$$

where $\sigma^x, \sigma^y, \sigma^z$ are spin (Pauli) operators, J_x, J_y, J_x are coupling parameters, and x, y, z-links refer to links of three different orientations, marked with green, red, and blue in Fig. 1.3. Kitaev showed that it can be exactly solved by a spin-fermion transformation:

$$\sigma^\alpha = i b^\alpha c, \tag{1.42}$$

where b^α and c are emergent fermions and $\alpha = x, y, z$. The Hamiltonian is transformed into

$$H = \frac{i}{4} \sum_{j,k} 2 J_\alpha \hat{u}_{jk} c_j c_k, \tag{1.43}$$

where $\hat{u}_{jk} = i b_j^\alpha b_k^\alpha$ and it commutes with the Hamiltonian.

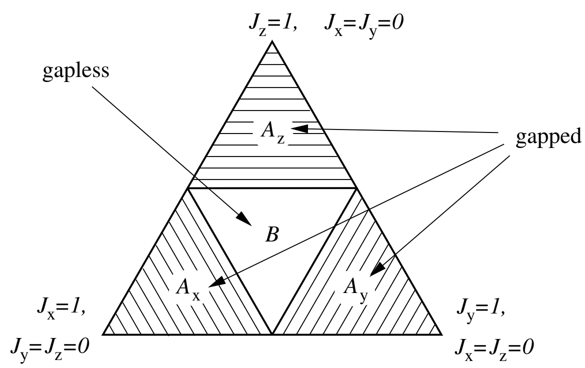

Figure 1.4: Phase diagram of the Kitaev magnet. Source: A. Kitaev, "Anyons in an exactly solved model and beyond", Ann. Phys. (N. Y.) **321**, 2–111 (2006).

There are two distinct phases in the Kitaev magnet model depending on the parameters (J_x, J_y, J_z), and the phase diagram is shown in Fig. 1.4. Phase B is gapless, but one can open a gap by applying an external magnetic field and adding a perturbation H' to the original Hamiltonian,

$$H' = -\mathbf{H} \cdot \sigma, \tag{1.44}$$

where $\mathbf{H}$ is the magnetic field. Two types of excitations would emerge in the gapped phase B: one is emergent Majorana fermion ψ, and another is $\mathbb{Z}_2$-vortex σ, as known as the Ising anyon. The statistics of the σ excitations is the same as the $e/2m$ quasiparticles in the Moore–Read Pfaffian state discussed in the previous section.

Similar to the case of FQHE, the edge of the gapped bulk hosts chiral gapless excitations. Since the gapped bulk has excitations with the Ising statistics, by the bulk-edge correspondence, its edge theory also contains the free Majorana fermion theory like the Moore–Read Pfaffian state. The edge Hamiltonian is

$$H = -\frac{i\hbar v}{4\pi} \int \mathrm{d}x \, \psi \partial_x \psi, \tag{1.45}$$

where v is the edge velocity. The only difference is that there is no charge mode in the Hamiltonian, as one would expect from the fact that the Kitaev magnet is a spin model.

1.3 Anyons

In the previous two sections, we showed that topological liquids with topological orders have exotic excitations with fractional statistics. This seems to be incompatible with our basic notions of particle statistics in quantum mechanics, namely the classification of fermions and bosons. As explained in standard quantum mechanics textbooks, exchanging two particles would induce a phase factor $e^{i\alpha}$ to their wave function

$$\psi(\mathbf{r}_1, \mathbf{r}_2) \to e^{i\alpha}\psi(\mathbf{r}_2, \mathbf{r}_1). \tag{1.46}$$

Therefore, when one particle goes in a full circle around the other, it acquires a phase $e^{i\theta} = e^{2i\alpha}$ in its wave function. Usually, we think the two-particle system returns to its original state after one cycle, and hence $2\alpha = 2n\pi$. However, it was pointed out that particles in two (spatial) dimensions do not necessarily follow this rule [32]. Wilczek coined the name "anyons" for particles that do not follow the boson or fermion statistics [33]. The exchange of anyons is a unitary operator on the state, and is also called braiding because it is described by representations of the braid group [20, 28]. We usually use a braiding diagram shown in Fig. 1.5 to illustrate the braiding process. If braiding acts on the state of anyons as a single phase factor, then the anyon is an Abelian anyon; otherwise, it is a non-Abelian anyon. Equivalently, we call an anyon non-Abelian if there are degenerate states for n anyons at fixed positions.

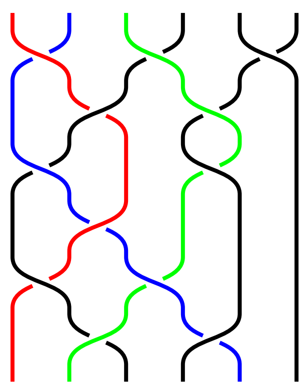

Figure 1.5: A typical braiding diagram of anyons.

Anyons are closely related to the topological order. Characterizing a topological order is equivalent to characterizing the anyonic excitations it contains. To achieve this, we use the algebraic theory of anyons [28, 34]. Let the letters $a, b, c, \ldots$ denote different types of anyons. They form a finite set M. This letter is also known as the superselection sector, the topological charge, or simply the label. Two anyons with topological charge a and b can have a total topological charge c in multiple ways, forming a Hilbert space V_{ab}^c. This process, known as fusion, is governed by fusion rules written as

$$a \times b = \sum_c N_{ab}^c c, \tag{1.47}$$

where $N_{ab}^c = \dim V_{ab}^c$ is the fusion multiplicity that counts the number of ways of fusing a and b

into c. Equivalently, anyons with topological charge c can also be split into a and b in N_{ab}^{c} ways, and the Hilbert space is the split space V_c^{ab}. The set M contains a trivial topological charge, also known as a vacuum sector, denoted by $\mathbf{1}$. Each anyon a has its own unique antiparticle $\bar{a}$, such that $N_{ab}^{\mathbf{1}} = \delta_{b\bar{a}}$. A quantum dimension d_a can be defined for anyons with topological charge a, such that the Hilbert space dimension of fusing n anyons $\sim (d_a)^n$ when n is large. When two anyons a and b fuse, the probability that they fuse into anyon c is

$$p_{ab}^{c} = N_{ab}^{c} \frac{d_c}{d_a d_b}. \tag{1.48}$$

Another important piece of information in the fusion theory is the F-matrix, denoted as F_{abc}^{d}, which appears when we fuse three anyons of topological charge a, b, c into d. Specifically, the matrix F_{abc}^{d} is a transformation from $\bigoplus_e V_e^{ab} \otimes V_d^{ec}$ to $\bigoplus_f V_d^{af} V_f^{bc}$.

The braiding of two anyons a, b that fuse into c is represented using the R-matrix R_c^{ab} defined as the transformation between two split spaces V_c^{ab} and V_c^{ba} in the counterclockwise direction. The topological spin θ_a is a complex number associated with anyon a and is defined by

$$\theta_a = d_a^{-1} \sum_c d_c \operatorname{Tr} R_c^{aa}. \tag{1.49}$$

The absolute value of the topological spin is always unity, and $\theta_a = \theta_{\bar{a}}$. When a and b fuse to c, the statistical phase $\exp\left(i\phi_{ab}^{c}\right)$ of a circling around b can be calculated from the topological spins,

$$R_c^{ba} R_c^{ab} = \frac{\theta_c}{\theta_a \theta_b} \operatorname{id}_{V_c^{ab}} = \exp(i\phi_{ab}^{c}) \operatorname{id}_{V_c^{ab}}. \tag{1.50}$$

It is also worth mentioning the topological S matrix defined by

$$s_{ab} = \frac{1}{D} \sum_c N_{a\bar{b}}^{c} \frac{\theta_c}{\theta_a \theta_b} d_c, \tag{1.51}$$

where $D = \sqrt{\sum_a d_a^2}$ is known as the global dimension.

As examples, the data for anyons in the semion order and Ising order are shown in Table 1.1 and 1.2.

Table 1.1: Basic data in the algebraic theory of semions.

Algebraic property	Value
Topological charge	$\mathbf{1}$, s (semion)
Fusion rule	$s \times s = \mathbf{1}$
Quantum dimension	$d_{\mathbf{1}} = d_s = 1$
F-matrix	$F_s^{sss} = -1$, other F-matrices $= 1$
R-matrix	$R_{\mathbf{1}}^{ss} = i$
Topological spin	$\theta_{\mathbf{1}} = 1$, $\theta_s = i$

1.4 Electronic interferometry

Electronic interferometers, especially their applications in FQH systems, are studied extensively in the past 20 years, both in theories [18, 35–56] and experiments [57–78]. They are analogies to their

Table 1.2: Basic data in the algebraic theory of Ising anyons.

Algebraic property	Value
Topological charge	$\mathbf{1}$, σ (Ising anyon), ψ (Majorana fermion)
Fusion rule	$\sigma \times \sigma = \mathbf{1} + \psi$, $\sigma \times \psi = \sigma$, $\psi \times \psi = \mathbf{1}$
Quantum dimension	$d_{\mathbf{1}} = d_\psi = 1$, $d_\sigma = \sqrt{2}$
F-matrix	$F_\sigma^{\sigma\sigma\sigma} = \begin{pmatrix} 1/\sqrt{2} & 1/\sqrt{2} \\ 1/\sqrt{2} & -1/\sqrt{2} \end{pmatrix}$, $F_\psi^{\sigma\psi\sigma} = -1$, $F_\sigma^{\psi\sigma\psi} = -1$, other F-matrices $= 1$
R-matrix	$R_{\mathbf{1}}^{\sigma\sigma} = e^{-\pi i/8}$, $R_\psi^{\sigma\sigma} = e^{3\pi i/8}$, $R_\sigma^{\sigma\psi} = R_\sigma^{\psi\sigma} = e^{-\pi i/2}$, $R_{\mathbf{1}}^{\psi\psi} = -1$
Topological spin	$\theta_{\mathbf{1}} = 1$, $\theta_\psi = -1$, $\theta_\sigma = e^{i\pi/8}$

optical counterparts. But instead of photons, it is quasiparticles that travel in loops inside the device. When quasiparticles travel, they would braid with other localized quasiparticles inside the loop and hence introduce an additional braiding phase to the interference current. By measuring the current, one can identify the fractional statistics of the quasiparticles and further understand the topological order of the QH liquid.

1.4.1 Fabry–Pérot geometry

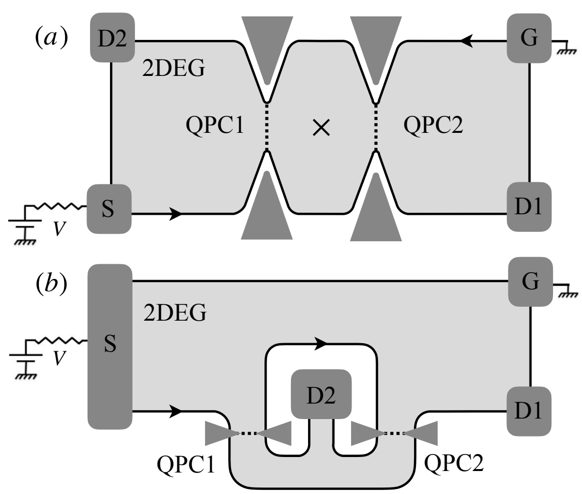

Figure 1.6: Schematics of a Fabry–Pérot interferometer (a) and a Mach–Zehnder interferometer (b).

Two basic geometries for electronic interferometers are the Fabry–Pérot type and the Mach–Zehnder type. We first discuss the Fabry–Pérot interferometer shown in Fig. 1.6(a). The QPC1 and QPC2 in the figure refer to the quantum point contacts. A quantum point contact is a constriction in the QH liquid created by either applying a gate voltage or etching the edges. Two edges are brought close by a quantum point contact, allowing quasiparticles to tunnel between the edges. The Fabry–Pérot interferometer has two counter-propagating edges, and quasiparticles can tunnel across either of the QPCs. The tunneling amplitudes at two QPCs are denoted as Γ_1 and Γ_2. When we apply a bias voltage on the edge, to the lowest order of $\Gamma_{1,2}$, the quasiparticles would follow one of the two paths: one is S-QPC1-D2, and another is S-QPC2-D2. The interference loop is the difference between the two paths, and the quasiparticle going around this loop would acquire a phase. The cross inside the interference loop denotes localized quasiparticles. For Abelian FQH states, this phase is the combination of the Aharonov–Bohm (AB) phase and a total statistical phase,

$$\theta = 2\pi \frac{e^*}{e}\frac{BA_I}{\Phi_0} + N_L\theta_a, \tag{1.52}$$

where e^* is the quasiparticle charge, A_I is the area of the interference loop, θ_a is the phase of a single quasiparticle, and N_L is the number of localized quasiparticles. The tunneling electric current of the interferometer is

$$I_T = e^*(|\Gamma_1|^2 + |\Gamma_2|^2)r_0(V,T) + 2e^*|\Gamma_1\Gamma_2|r_1(V,T)\cos\theta, \tag{1.53}$$

where V is the bias voltage and T is the temperature. It is worth mentioning that if the voltage bias is not applied symmetrically on two edges, the phase θ has an additional contribution from the charge accumulated on the edges, which is equal to $2ea\tilde{V}/\hbar v$, where a is the distance between the QPCs and $\tilde{V}$ is an average of the voltages on two edges [39].

Eq. (1.52) and Eq. (1.53) are actually results of a highly idealized case, where the bulk is in an incompressible QH state and the bulk-edge coupling is absent. The situation for experiments might be much more complicated. If the bulk state is a compressible state and the interfering edge is coupled to the compressible bulk, then the interference pattern would fall into a Coulomb-dominated (CD) regime, different from the ideal Aharonov–Bohm (AB) regime [49, 55]. However, we will focus on the ideal AB regime in this thesis.

For QH liquids at $\nu = 1/m$, the oscillatory coefficient $r_1(V,T)$ in Eq. (1.53) can be computed in the weak backscattering limit, namely, assuming small $\Gamma_{1,2}$. If we set the edge velocity $v = 1$, r_1 will be expressed as [35]

$$r_1(V,T) \sim 4(\pi T)^{2g-1} B\left(g - i\frac{\omega_J}{2\pi T}, g + i\frac{\omega_J}{2\pi T}\right) H_g(\omega_J, a, T)\sinh\left(\frac{\omega_J}{2T}\right), \tag{1.54}$$

where $g = \nu$, $\omega_J = e^*V/\hbar$, a is the distance between two QPCs, $B(x,y)$ is the Beta function, and $H_g(\omega, x, T)$ is defined by

$$H_g(\omega, x, T) = 2\pi \frac{\Gamma(2g)}{\Gamma(g)} \frac{e^{-2g\pi T|x|}}{\sinh\frac{\omega}{2T}} \,\mathrm{Im}\left\{ \frac{e^{i\omega|x|}\; F(g, g - i\frac{\omega}{2\pi T}; 1 - i\frac{\omega}{2\pi T}; e^{-4\pi T|x|})}{\Gamma(g + i\frac{\omega}{2\pi T})\,\Gamma(1 - i\frac{\omega}{2\pi T})} \right\}, \tag{1.55}$$

where $\Gamma(x)$ is the Gamma function, and F is the hypergeometric function. When $m = 1$, the bulk state is an IQH state and the tunneling particles are free fermions; therefore, the tunneling current can be solved exactly for any $\Gamma_{1,2}$, and the result is

$$r_1(V,T) \sim \frac{4\pi^2 T}{\sinh(2\pi T a)}\sin(\omega_J a). \tag{1.56}$$

Recent experiments have successfully observed the fractional statistics in the $\nu = 1/3$ FQH state using electronic Fabry–Pérot interferometers [70]. Novel device designs that screen the Coulomb interactions made this breakthrough possible. The experimental conductance plot is shown in Fig. 1.7,

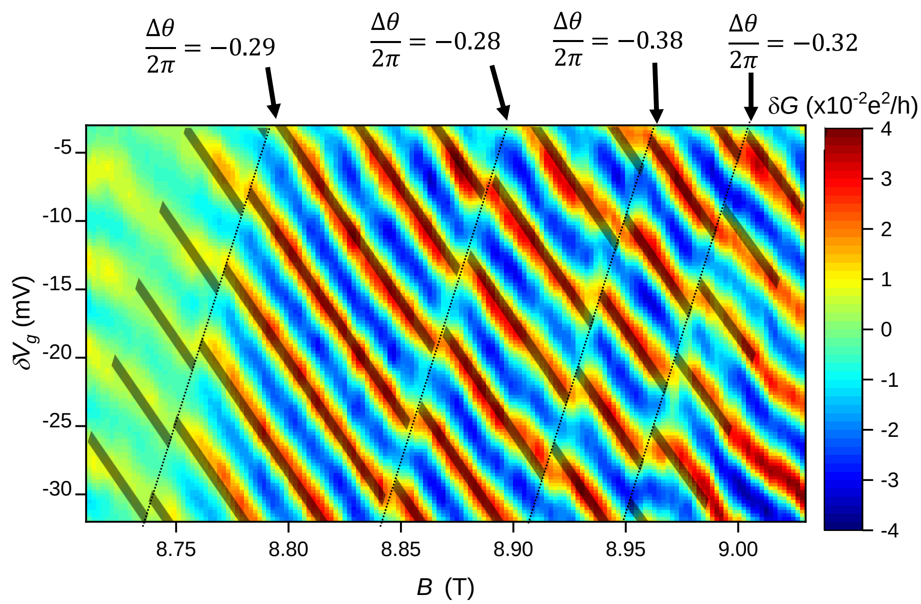

Figure 1.7: Conductance oscillations versus magnetic field and side gate voltage in the Fabry–Pérot interferometer. Source: J. Nakamura et al., "Direct observation of anyonic braiding statistics at the $\nu = 1/3$ fractional quantum Hall state", Nat. Phys. **16**, 931 (2020)

where the side gate voltage V_g on the vertical axis is used to change the interference area A_I. Values of the discrete phase jumps in this figure are close to the theoretically predicted value $\Delta\theta = 2\pi/3$, which is twice the value of the exchange phase of quasiparticles in a $\nu = 1/3$ FQH state.

For the non-Abelian Moore–Read Pfaffian state at $\nu = 5/2$, it was shown that there is no interference pattern when the number of localized $e/4$ quasiparticles in the bulk is odd [36, 37]. This is the even-odd effect. To explain this effect, we notice that the total topological charge of localized quasiparticles is σ when the number of localized quasiparticles is odd. The tunneling $e/4$ quasiparticle also carries a topological charge σ, and it will fuse with the total localized charge σ, with a result of $\mathbf{1}$ or ψ in equal probabilities. The two fusion channels lead to two statistical phases that differ by π. They cancel each other, and hence no interference current would appear.

1.4.2 Mach–Zehnder geometry

The Mach–Zehnder geometry, shown in Fig. 1.6(b), also has two QPCs, and resembles the Fabry–Pérot geometry. There are two major differences. First, the two edges in a Mach–Zehnder interferometer are co-propagating; therefore, the interference current depends on the difference of distances between QPCs along two edges, not the sum. Second, the drain denoted by D2 is topologically inside the interference loop; therefore, the interference phase depends on the topological charge of the drain, which determines the state of a Mach–Zehnder interferometer. The topological charge of the drain changes after each tunneling event; therefore, the state of the interferometer will change during the measurement, and all measured quantities should be averaged over all possible states.

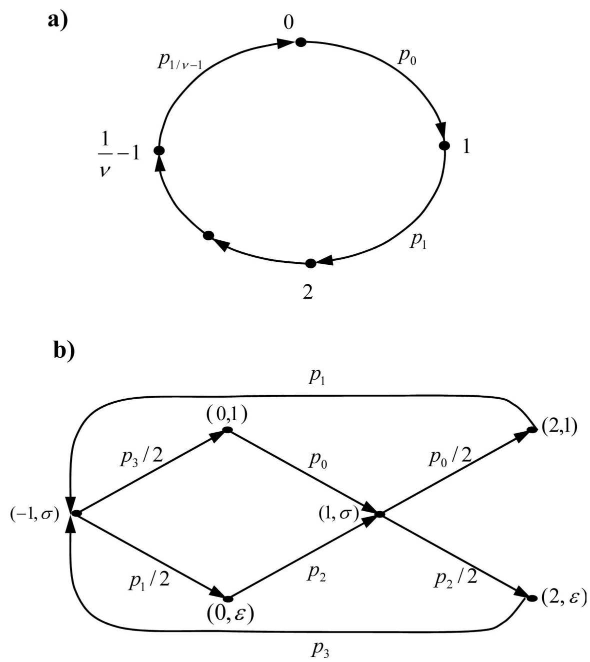

Figure 1.8: Transitions between states of a Mach–Zehnder interferometer in a Laughlin $\nu = 1/m$ FQH liquid (a) and a Pfaffian $\nu = 5/2$ FQH liquid (b) at zero temperature. Source: D. E. Feldman et al., "Shot noise in an anyonic Mach-Zehnder interferometer", Phys. Rev. B **76**, 085333 (2007).

Fig. 1.8(a) shows transitions in a $\nu = 1/m$ FQH liquid, and the label denotes the number of quasiparticles in the drain mod $1/\nu$. The transition rate connecting state n and state $n+1$ is given by

$$p_k = (|\Gamma_1|^2 + |\Gamma_2|^2) r_0(V,T) + 2|\Gamma_1\Gamma_2| r_1(V,T) \cos\left(2\pi \frac{e^*}{e} \frac{BA_I}{\Phi_0} + \theta_k\right), \tag{1.57}$$

where $\theta_k = 2\pi\nu k$ is the statistical phase accumulated by the quasiparticle when it encircles n quasiparticles, and r_0 and r_1 are coefficients defined in Eq. (1.53). At zero temperature, the average current is

$$I = \frac{e}{\sum_{k=0}^{1/\nu-1} t_k}, \tag{1.58}$$

where $t_k = 1/p_k$ is the average time for one transition [39].

Transitions in a Pfaffian $\nu = 5/2$ FQH state are shown in Fig. 1.8(b), and the states are labeled by both the number of quasiparticles mod 4 and the topological charge. The transition rates are still given by Eq. (1.52), but the statistical phase now takes four difference values, $\theta_k = \pi k/2$, $k = 0, 1, 2, 3$ [40]. Since the Pfaffian state is a non-Abelian state with Ising order, by its fusion rules, a state of interferometer with topological charge σ has equal probabilities to transit into two different states, and we need to multiply the transition rate p_k by the probability $1/2$.

If we consider the shot noise in the Mach–Zehnder interferometer defined by

$$S(\omega) = \frac{1}{2} \int_{-\infty}^{\infty} dt\, e^{i\omega t} \langle \hat{I}(0)\hat{I}(t) + \hat{I}(t)\hat{I}(0) \rangle, \tag{1.59}$$

the non-Abelian states would show unique features. At zero temperature, the Fano factor, which is defined as the ratio between shot noise and current in the unit of electron charge e, is smaller than 1 for Laughlin states and can be greater than 1 for the Pfaffian state [40]. Also, in the high-frequency limit, the shot noise shows no inference effect for an arbitrary fractional statistics, while the interference would appear for fermions [40].

Chapter 2

Thermal interferometry in topological quantum liquids

2.1 Introduction

A key feature of topological order is the existence of anyons obeying fractional statistics [55]. The statistics of Abelian anyons manifests itself in braiding phases, accumulated by particles traveling around each other. To define the statistics of non-Abelian anyons one also needs to know how different particles fuse into composite anyons. Fractional statistics has been discussed for decades in the context of the fractional quantum Hall effect (QHE), and multiple probes of anyons in the quantum Hall effect have been proposed [55]. Several of them have recently been implemented [55].

The bulk-edge correspondence hypothesis connects the statistics of anyons in the bulk of a 2D system with the structure of a 1D gapless edge theory [3]. The latter determines the quantized thermal conductance at the temperatures much below the bulk energy gap [79–81]. Thus, the experimentally measured thermal conductance [82–84] gives an evidence of fractional statistics. In particular, fractional quantization of thermal conductance has brought experimental evidence of non-Abelian statistics in the QHE at $\nu = 5/2$ in GaAs [83]. Thermal conductance yields however a rather indirect evidence of statistics. A more direct approach involves anyon collision experiments [85]. Arguably, the most direct approach is anyonic interferometry [35–40, 49, 62, 69, 70].

The idea of anyonic interferometry naturally follows from the definition of the braiding phase. The schematics of the setup is illustrated in Fig. 2.1. Two QHE edges are brought close to each other at two constrictions. Charge tunnels between the edges at the constrictions and hence two paths emerge, which connect source S1 and drain D2 via one of the two constrictions. The electric current in D2 depends on the phase difference of the two trajectories. The phase difference includes a sample-dependent contribution from the constrictions, the Aharonov–Bohm phase, proportional to the device area, and the statistical phase, which depends on the number of anyons localized in the device. Only the sum of the three phases is observed, but they can be disentangled by changing the magnetic field. Indeed, the non-universal phase shows a weak field dependence, the Aharonov–Bohm phase changes continuously, and the statistical phase jumps every time a new anyon enters the device. This has been observed [70] at $\nu = 1/3$, and interesting interferometry data exist at other filling factors [55].

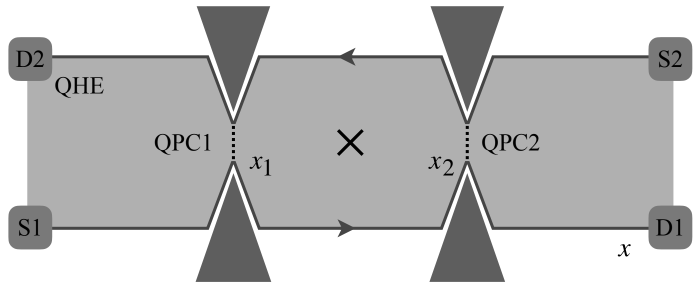

Figure 2.1: Schematics of an electronic interferometer. Constrictions bring the QHE edges closer. This facilitates the tunneling of charge from one edge to the other. Interference between the two paths that connect source S1 to drain D2 gives information about a localized anyon indicated with a $\times$ symbol.

Quantum Hall anyons carry charge. What about neutral systems such as Kitaev magnets [28]? The Aharonov–Bohm technique is no longer applicable in the absence of an electric current. We propose to employ thermal currents instead. In contrast to an electric, spin, or any other current, an energy current can flow in any system. This idea was introduced for one particular anyon type, Ising anyons in Kitaev magnets, in the Letter [86] and in a rather different form in Ref. [87]. In this chapter we systematically address signatures of various possible Abelian and non-Abelian fractional statistics in thermal interferometry experiments. The idea applies to both charged and neutral anyons, but has to be implemented in somewhat different ways in those two cases. Indeed, the magnetic field may not be a useful knob in chargeless systems, and hence a different knob is needed. As we show, useful information comes instead from the comparison of different interferometer topologies.

A possibility [29] that α-$RuCl_3$ hosts a neutral Kitaev liquid with non-Abelian Ising statistics has attracted much interest recently. The existing experimental results are controversial [30], and one of our motivations consists in the development of a probe of anyonic statistics, suitable to a Kitaev spin liquid.

Thermal interferometry of fermions has been previously investigated for heterostructures based on topological superconductors [88]. We demonstrate that heat transport changes dramatically for anyons in comparison with fermions and bosons.

We introduce two interferometer topologies: Fabry–Pérot and Mach–Zehnder in Sec. 2.2. We also briefly review Ising topological liquids [28] in that section, since the Ising topological order is particularly important for us. An interferometer is made of two constrictions. As a starting point it is hence essential to analyze a single constriction. We do that in Sec. 2.3.1 in the simplest problem of tunneling between two separate topological liquids. In that case, only bosons can tunnel through a point contact. We consider a single tunneling contact in an Ising liquid in Sec. 2.4.1 and address a general statistics in Sec.2.5.2. In the low-energy limit, the heat current through a constriction exhibits scaling as a function of the temperature at a fixed ratio of the temperatures on the two sides of the device. It is easy to identify the scaling exponent for an arbitrary anyon statistics. The exponent is different for different anyon types and hence can be used as a probe of topological order. In the most interesting case of a Kitaev spin liquid, we go beyond scaling analysis and derive a general expression for the heat current as a function of the two temperatures.

A single-constriction probe of statistics is indirect. The bulk of this chapter focuses on double-constriction geometries, which allow probes of anyon braiding. Sec. 2.3.2 considers the Fabry–Pérot and Mach–Zehnder interferometers made of two separate topological liquids so that only bosons can tunnel through the vacuum between the two liquids. After that warming-up exercise, Sec. 2.4 contains a detailed study of the two interferometer geometries for Ising anyons in Kitaev liquids. We discover that the heat current depends on the topological charge localized inside a Fabry–Pérot interferometer. This can be used to probe statistics provided that we can control the trapped topological charge. If such control is unavailable, a dramatically different behavior of the heat current in a Mach–Zehnder interferometer can be combined with Fabry–Pérot data to identify fractional statistics.

Sec. 2.5 investigates interferometry for an arbitrary topological order. The case of Abelian statistics is straightforward in both interferometer geometries. For non-Abelian statistics we have to separately consider the tunneling of anyons which are identical and different from their antiparticles. Sec. 2.6 addresses another signature of topological order: telegraph noise of heat current in Fabry–Pérot devices with a hole. We discuss experimental realizations and summarize in Sec. 2.7.

Several Appendixes contain technical details. Appendix B addresses a toy model of fermion tunneling in interferometers for Kitaev spin liquids. Appendix C contains detailed calculations for an interferometer made of two separate Kitaev magnets. Appendix D deals with correlation functions of Ising anyon operators in Kitaev systems. Appendix E goes through the tedious calculations of the heat current in a Fabry–Pérot interferometer made of a single piece of a Kitaev material. Appendix F discusses subtleties of Mach–Zehnder interferometry. Appendix G considers an exotic topological order that defies naive expectations of how interference of anyons works in a Fabry–Pérot device. Appendix H contains detailed calculations of telegraph noise. Appendix I addresses the dependence of the heat current on the interferometer size for systems with a single edge mode.

2.2 Models

In this section we introduce the three basic models we consider below: a single constriction between two edges of a topological liquid, a Fabry–Pérot interferometer, and a Mach–Zehnder interferometer.

We focus on systems with a bulk energy gap and gapless edge states [20, 55]. The fractional quantum Hall effect gives rise to many such systems. Another relevant situation involves some spin liquids, a Kalmeyer–Laughlin liquid [27] being the simplest example. Non-Abelian statistics in Kitaev magnets has recently attracted much interest, and we will pay particular attention to

Kitaev magnets [28]. Their edge theory contains a single chiral Majorana mode. The low-energy Hamiltonian of one right(left)-moving edge is [20, 28]

$$H = \mp \frac{iv}{4\pi} \int dx\, \psi \partial_x \psi, \tag{2.1}$$

where v is the edge velocity. The Majorana fermion ψ satisfies the anticommutation relation,

$$\{\psi(x), \psi(y)\} = 2\pi\delta(x - y). \tag{2.2}$$

Kitaev magnets contain three types of anyons: trivial bosons $\mathbf{1}$, Majorana fermions ψ, and Ising anyons σ. These quasiparticles obey the following fusion rules:

$$\psi \times \psi = \mathbf{1}; \quad \psi \times \sigma = \sigma; \quad \sigma \times \sigma = \mathbf{1} + \psi, \tag{2.3}$$

where the final equality represents two possible fusion outcomes. The topological spin θ_x of these quasiparticles is given by $\theta_{\mathbf{1}} = 1$, $\theta_\psi = -1$, and $\theta_\sigma = e^{i\pi/8}$. The topological spin determines the phase ϕ^c_{ab} accumulated when a quasiparticle of type a encircles a quasiparticle of type b in counterclockwise sense under the assumption that they fuse to a quasiparticle of type c: $\exp\left(i\phi^c_{ab}\right) = \theta_c/(\theta_a\theta_b)$. Another important piece of information is the quantum dimension of anyons. It is 1 for $\mathbf{1}$ and ψ, and $\sqrt{2}$ for σ. More details and a discussion of other topological orders can be found in Refs. [55, 89].

2.2.1 Single point contact

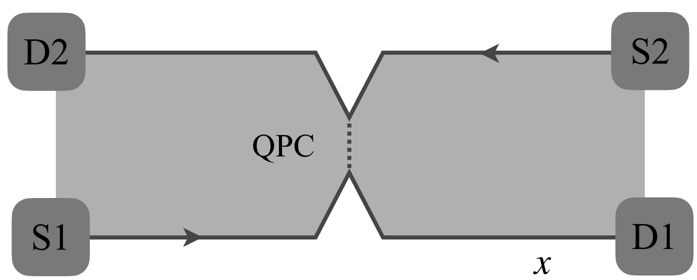

Figure 2.2: A single quantum point contact (QPC) is shown, where the two counter-propagating edges of the spin liquid come close and the tunneling between the edge modes takes place as indicated with a dashed line.

To discuss the tunneling behavior in the presence of point contacts between two different edges, we consider the model depicted in Fig. 2.2. The two edges host counter-propagating edge modes, and could either be edges of the same spin liquid, or different spin liquids. The lower and upper edges have two different temperatures, T_1 and T_2. This is achieved by bringing either of them in thermal equilibrium with its source S1 or S2, maintained at the temperature T_1 or T_2.

The Hamiltonian of this single-point-contact tunneling model is of the form

$$H = H_1 + H_2 + H_T, \tag{2.4}$$

where $H_{1,2}$ are the free Hamiltonians for the two chiral edges, and H_T is the tunneling Hamiltonian describing the tunneling of quasiparticles through the quantum point contact.

In general, the tunneling Hamiltonian can be written in the following form,

$$H_T = \Gamma\hat{T} + \Gamma^*\hat{T}^\dagger, \tag{2.5}$$

where $\hat{T}$ is a tunneling operator responsible for transporting one quasiparticle from the lower edge to the upper edge. When the tunneling quasiparticle is its own antiparticle, $\hat{T}$ and $\hat{T}^\dagger$ are equivalent, hence,

$$H_T = \Gamma\hat{T}, \tag{2.6}$$

where Γ is a real tunneling amplitude that ensures Hermiticity of the tunneling Hamiltonian H_T. The Hamiltonians (2.5,2.6) include only one most relevant tunneling process. This is justified at low energies for many topological orders.

In the presence of a tunneling point contact, the heat current flowing along the edges can tunnel across the contact, thus introducing a tunneling heat current I_T. Here we treat the contact Hamiltonian H_T as a perturbation and assume a small Γ. We can find the operator $\hat{I}_T$ for the heat current using the Heisenberg equation of motion,

$$\hat{I}_T = \frac{\partial H_1}{\partial t} = -i[H_1, H_1 + H_2 + H_T] = -i[H_1, H_T]. \tag{2.7}$$

Strictly speaking, the above expression gives the energy current. It is the same as the heat current provided that the electric current is zero. Otherwise, a correction, proportional to the square of the electric current, is conventionally subtracted [1]. We will ignore this complication, that is, we will assume a zero electric current. In the most interesting case of spin liquids, the electric current is constrained to be zero. In quantum Hall systems with a non-zero electric current, the energy and heat currents can be related to each other via known results for the electric current.

To the lowest order in perturbation theory, the expectation value of the heat current is

$$\langle I_T(t)\rangle = -i\int_{-\infty}^{t} dt' \langle[\hat{I}_T(t), H_T(t')]\rangle. \tag{2.8}$$

The tunneling heat current should be proportional to $|\Gamma|^2$, $I_T = r(T_1, T_2)|\Gamma|^2$, where the factor $r(T_1, T_2)$ depends on the details of the edge theory and the nature of tunneling quasiparticles. Typically, the tunneling of one quasiparticle type dominates in the low-energy regime of interest for this chapter. The dominant tunneling operator is the most relevant tunneling operator in the renormalization group sense. We will assume below that only one quasiparticle type together with its anti-particle can tunnel.

[1] The heat current is usually defined as the difference between the energy current and the product of the chemical potential and the particle current. The heat and energy currents become the same if the product of the particle number and the chemical potential is subtracted from the Hamiltonian. In the case of the Ising topological order, the number of the Majorana fermions is not defined and the chemical potential is always zero

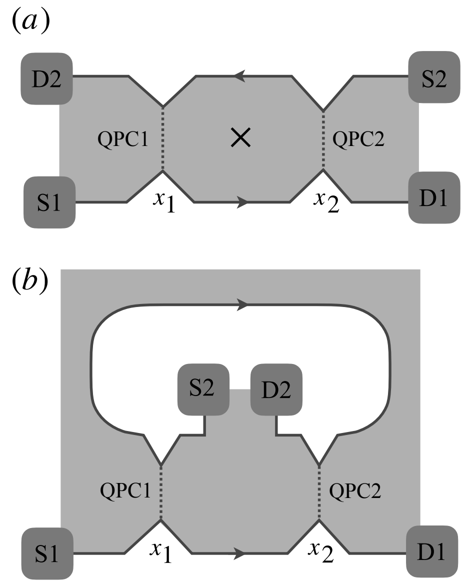

Figure 2.3: Schematics of (a) Fabry–Pérot and (b) Mach–Zehnder interferometers. Heat travels from sources S1 and S2 to drains D1 and D2 along chiral edges and tunnels between the edges at the two point contacts shown with dashed lines. A localized anyon is marked with a × symbol.

2.2.2 Fabry–Pérot interferometer

Following the discussion of the single-point-contact tunneling, we are in a position to consider thermal interferometers. Electronic Fabry–Pérot interferometers have been introduced to study the Aharonov–Bohm effect and fractional statistics in the quantum Hall regime [55]. This chapter considers a thermal Fabry–Pérot interferometer shown in Fig. 2.3(a). The device is similar to its electronic counterpart. It contains two point contacts, QPC1 and QPC2, located at coordinates x_1 and x_2. When a heat-carrying quasiparticle tunnels through the interferometer from the lower edge to the upper edge, it could take either of the two paths S1-QPC1-D2 or S1-QPC2-D2. This results in quantum interference, whose phase depends on the quasiparticle excitations in the central region between QPC1 and QPC2 as well as the device's size and the tunneling contacts' details. For electronic interferometers in QHE systems, the interference phase contains a sample-dependent contribution from QPCs, an Aharonov–Bohm phase, proportional to the magnetic flux through the interferometer, and a statistical phase due to quasiparticle excitations inside the interference loop. On the other hand, for a thermal interferometer probing charge-neutral excitations, the Aharonov–Bohm phase is absent.

The tunneling Hamiltonian in a Fabry–Pérot interferometer is

$$H_T = \Gamma_1 \hat{T}_1 + \Gamma_2 \hat{T}_2 + \text{H.c.}, \tag{2.9}$$

where $\Gamma_{1,2}$ are two generally complex tunneling amplitudes, $\hat{T}_1$ is the tunneling operator that corresponds to the transfer of a quasiparticle from the lower to upper edge through QPC1, and $\hat{T}_2$

corresponds to the transfer through QPC2. In the absence of localized quasiparticles in the interference loop, the tunneling thermal current takes the general form,

$$I_T = (|\Gamma_1|^2 + |\Gamma_2|^2) r(T_1, T_2) + 2\,\mathrm{Re}\{[\Gamma_1 \Gamma_2^* \tilde{r}(T_1, T_2, L_1 + L_2)]\}, \tag{2.10}$$

where Re stands for the real part, L_i denotes the distance between the two point contacts along edge $i = 1,\ 2$, and $\tilde{r}(T_1, T_2, L_1 + L_2)$ describes the interference term in the thermal current. In the presence of bulk quasiparticles, this term depends additionally on the statistical phase induced by these localized quasiparticles. The sum of the two distances enters the coefficient $\tilde{r}$, if only one edge mode exists and the edge velocities are identical on the two edges of the device. Otherwise, the length dependence of $\tilde{r}$ is more complicated. See Appendix I for the derivation of the length dependence and a detailed discussion of the relevant assumptions.

In an Abelian quantum Hall liquid with the filling factor $\nu = 1/(2m+1)$, the statistical phase accumulated by an anyon of charge νe around n localized anyons of the same charge is equal to $\phi = 2\pi\nu n$. However, for the tunneling of non-Abelian quasiparticles, we need to take the anyon fusion rule into consideration since it is possible for two non-Abelian anyons to fuse in more than one fusion channel. A detailed discussion can be found in Sec. 2.5.

2.2.3 Mach–Zehnder interferometer

A Mach–Zehnder interferometer [55, 57, 90] shown in Fig. 2.3(b) is superficially similar to a Fabry–Pérot interferometer. It also has two tunneling contacts and two interfering paths from S1 to D2. Yet, it has an important topological difference from the Fabry–Pérot setup: Drain D2 is inside the interference loop. Hence, in contrast to Fabry–Pérot interferometry, each tunneling event changes the localized topological charge in the central region. As a result, the statistical phase ϕ, accumulated by an anyon on the interference loop, changes after each quasiparticle tunneling event. Also, as seen from Fig. 2.3(b), the two edges in a Mach–Zehnder interferometer have the same propagation direction, thus, the thermal current depends on the difference of the distances between the point contacts on the two edges and not the sum, see Appendix I and Ref. [39].

The state of a Mach–Zehnder interferometer is characterized by the localized topological charge in the central region. Transitions between different states can be analyzed through a continuous-time Markov chain model.

The situation is particularly interesting if the tunneling anyon, whose topological charge is denoted as x, is its own antiparticle. The tunneling Hamiltonian for a single point contact is given in Eq. (2.6). The tunneling Hamiltonian in a Mach–Zehnder interferometer is

$$H_T = \Gamma_1 \hat{T}_1 + \Gamma_2 \hat{T}_2 e^{i\alpha}, \tag{2.11}$$

where $\Gamma_{1,2}$ are two real tunneling amplitudes at the two quantum point contacts, and the phase α ensures Hermiticity [86]. We compute the phase α in Appendix F. When the tunneling of x changes the localized topological charge from a to b, the tunneling rate can be expressed as [40]

$$p_{xa}^{b} = P_{xa}^{b} \tilde{p}(T_1, T_2, \Gamma_1, \Gamma_2, \phi_{xa}^{b}, |L_1 - L_2|), \tag{2.12}$$

where $P^b_{xa} = N^b_{xa} d_b/(d_x d_a)$ is the fusion probability for $x \times a \to b$, N^b_{xa} is the fusion multiplicity, d_α is the quantum dimension of anyon α, and $\tilde{p}$ incorporates the dependence on the temperatures $T_{1,2}$, the tunneling amplitudes $\Gamma_{1,2}$, the statistical phase ϕ^b_{xa}, and the interferometer size. When the path of topological charge x encloses localized charge a, according to the algebraic theory of anyons, the statistical phase is $\exp\left(i\phi^b_{xa}\right) = \theta_b/(\theta_a\theta_x)$, where θ_α are topological spins [28, 55].

In what follows we will assume that $|L_1 - L_2|$ is much shorter than the thermal length v/T, where v is the edge velocity. This will allow neglecting the interferometer size.

If we use f_a to denote the probability of the localized topological charge being a, we can write down the following kinetic equation [40],

$$\dot{f}_a = \sum_b f_b p^a_{xb} - \sum_c f_a p^c_{xa}. \tag{2.13}$$

This equation can also be written in a matrix form, $\dot{f}_a = M_{ab} f_b$, where the matrix entries M_{ab} are the tunneling rates,

$$M_{ab} = p^a_{xb} - \delta_{ab} \sum_c p^c_{xa}. \tag{2.14}$$

When the system is in dynamical equilibrium, $\dot{f}_a = 0$, one can solve for f_a. The average thermal current is given by

$$I^{\mathrm{MZ}} = \overline{\Delta E} \sum_{ab} f_a p^b_{xa}, \tag{2.15}$$

where $\overline{\Delta E}$ is the average heat transferred across the point contact by a tunneling event. Since we neglected the interferometer size, the statistical distribution of the transferred energy in one tunneling event is the same for all combinations of the topological charges a and b, and the same as for a single tunneling contact. Indeed, in our limit, the two constrictions can be fused into one.

As an example, a detailed calculation for interferometers built for probing the Ising topological order is shown in Sec. 2.4.

2.3 Tunneling between topological liquids

As a warming-up exercise, we consider tunneling between two Ising topological liquids through vacuum.

2.3.1 Single constriction

In the case of two adjacent spin liquids, some edge excitations may tunnel from one spin liquid to the other. Before we compute the thermal current in the two-constriction geometry, consider first the case of a single point contact. In this case, we will not obtain any interference effects. Nonetheless, we do obtain some non-trivial thermal transport.

The edge Hamiltonians have the standard form (2.1). Every contribution to the Hamiltonian must be topologically trivial. In particular, any allowed interaction between the two topological liquids is described by operators, which are products of two Bose fields acting on each of the liquids. Hence, the form of the tunneling Hamiltonian is such that only pairs of Majorana fermions tunnel,

$$H_T = -\Gamma\psi_1(x_0)\partial_x\psi_1(x_0)\psi_2(x_0)\partial_x\psi_2(x_0). \tag{2.16}$$

Here x_0 is the location of the constriction.

We can now define the thermal current as the time derivative of the free Hamiltonian of one of the edges and use the Heisenberg equations of motion as in Eq. (2.7). One obtains

$$\hat{I}_T = -v\Gamma\left(\partial_x\psi_1(x_0)\partial_x\psi_1(x_0) + \psi_1(x_0)\partial_x^2\psi_1(x_0)\right)\psi_2(x_0)\partial_x\psi_2(x_0). \tag{2.17}$$

Using perturbation theory (2.8), in Appendix C, we compute the thermal current between two spin liquids to the lowest order in the tunneling amplitude Γ as,

$$\langle I_T\rangle_\Gamma^{\text{non-int}} = \frac{4\pi^9\Gamma^2}{2835v^8}\Big[41(T_2^8 - T_1^8) + 62T_1^2T_2^2(T_2^4 - T_1^4)\Big]. \tag{2.18}$$

This is the contribution to the thermal current due to a single constriction between two spin liquids. Its non-trivial temperature dependence is a signature of the Ising topological order. It is instructive to compare the result with the heat current in a Luttinger liquid of topologically trivial bosons. The action density is $L_n \sim (\partial_t\theta_n)^2 + (\partial_x\theta_n)^2$ on edge $n = 1, 2$. The tunneling operator $\hat{T} \sim \partial_x\theta_1\partial_x\theta_2$. An easy calculation shows that the thermal current scales as the fourth power of the temperatures $\sim T_1^4, T_2^4$. For a 1D system of free electrons, the heat current scales as the square of the temperature. Thus, the $\sim T_1^8, T_2^8$ scaling in the above result is a signature of a non-trivial topological order. The same is true for the non-trivial coefficients 41 and 62.

In the two-constriction geometry, as considered in the next part of the section, the result we just obtained will exactly be the non-interference contribution from each of the constrictions. A detailed derivation of the above expression can be found as the non-interference part of the full calculation in Appendix C, where we consider a Fabry–Pérot interferometer. The calculations rely on some equations from Appendix B, where we consider a simpler model, in which single Majorana fermions are allowed to tunnel between the edges. This is only allowed when the edges surround the same spin liquid. In such a situation, fermion tunneling is not the most relevant tunneling process, as discussed in the next section. It can become the leading contribution to transport near a resonance.

2.3.2 Double constriction

We now turn our attention to the double constriction geometry. In this case, interference effects will come into play. The two-constriction geometry we consider here is the Fabry–Pérot interferometer made of two spin liquids.

Similar to a single constriction geometry, the tunneling Hamiltonian is just the sum of individual tunneling Hamiltonians at the two constrictions, x_1 and x_2,

$$H_T = -\sum_{i=1,2}\Gamma_i\psi_1(x_i)\partial_x\psi_1(x_i)\psi_2(x_i)\partial_x\psi_2(x_i). \tag{2.19}$$

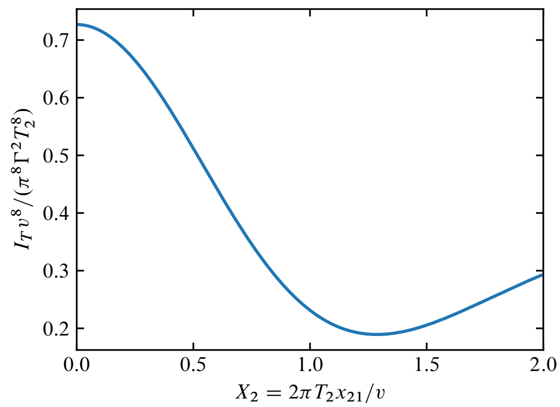

Figure 2.4: This curve shows how the total thermal current $I_T = 2\langle I_T\rangle_\Gamma^{\text{non-int}} + \langle I_T\rangle^{\text{int}}$ varies with x_{21} when the limit $T_1 \to 0$ is taken.

Using this tunneling Hamiltonian, we find the tunneling thermal current operator as defined in Eq. (2.7),

$$\hat{I}_T = -\sum_{i=1,2}\Big[\Gamma_i\left(\partial_x\psi_1(x_i)\partial_x\psi_1(x_i) + \psi_1(x_i)\partial_x^2\psi_1(x_i)\right)\psi_2(x_i)\partial_x\psi_2(x_i)\Big]. \tag{2.20}$$

Using perturbation theory in Eq. (2.8), one can now compute the thermal current between two spin liquids to the lowest order in the tunneling amplitude. In the $T_1 = 0$ limit and setting $\Gamma_1 = \Gamma_2 = \Gamma$, we find this expression to be,

$$\langle I_T\rangle = 2\langle I_T\rangle_\Gamma^{\text{non-int}} + \langle I_T\rangle^{\text{int}} \tag{2.21}$$

where,

$$\langle I_T\rangle^{\text{int}} = \frac{8\pi^9\Gamma^2 T_2^8}{3v^8}\Big[(7 - 80\coth^2 X_2 + 105\coth^4 X_2)\frac{1}{\sinh^4 X_2} - \frac{105}{X_2^8} + \frac{10}{X_2^6}\Big]. \tag{2.22}$$

Here we have defined $X_i = 2\pi T_i x_{21}/v$, where x_{21} is the separation between the two constrictions. We assume the separation to be the same on both edges. The non-interference term $\langle I_T\rangle_\Gamma^{\text{non-int}}$ is just the thermal current obtained in the single constriction geometry (2.18). The variation of the total thermal tunneling current with the separation between the two constrictions $X_2 = 2\pi T_2 x_{21}/v$ is shown in Fig. 2.4. The general expression for this tunneling thermal current in the case of $T_1 \neq 0$ and when the tunneling amplitudes at the two constrictions are not equal, i.e., $\Gamma_1 \neq \Gamma_2$, is given in Appendix C.

A curious feature of the above result is a non-monotonous dependence of the heat current on the distance between the tunneling contacts, Fig. 2.4. Similar behavior would be natural for charged systems in a magnetic field due to Aharonov–Bohm oscillations. Significantly, we deal with a neutral spin liquid. See Ref. [87] for related curious behavior.

The analysis of the Mach–Zehnder geometry is very similar and does not add much to the Fabry–Pérot case. This is a consequence of the trivial mutual statistics of tunneling bosons and confined anyons.

2.4 Ising anyon tunneling

We now address the tunneling of Ising anyons between the two edges of a topological liquid. As we will see, different tunneling currents correspond to different topological charges, trapped in an interferometer. It is not, however, obvious how to control the trapped charge. As an alternative approach to probing anyon statistics, one can compare heat currents through Fabry–Pérot and Mach–Zehnder interferometers.

2.4.1 Single constriction

We start with a single constriction. We discover that at a fixed ratio of the edge temperatures T_1/T_2, the tunneling heat current scales as $\sim T_1^{1/4}$. This is a signature of fractional statistics.

The most relevant tunneling operator transfers a single Ising anyon from one edge of the spin liquid to the other. These two edges, being the edges of the same spin liquid, can be thought of as parts of a single edge connected by an infinitely remote section [47, 91]. Correlation functions for the entire system decompose as products of correlation functions on the upper and lower edges along with a phase factor that depends on topological order [24]. The decomposition of correlation functions is discussed in Appendix D.

Within the conformal-field-theoretic treatment, the correlation functions of the primary operators are holomorphic functions of the complex coordinate $w = v\tau \pm ix = i(vt \pm x)$, where τ is the imaginary time. We may compute the thermal correlation functions of the primary fields using the conformal transformation between coordinates w on a cylinder [25, 50] and coordinates z on a plane, given as $z = e^{2\pi i w/v\beta}$, where $\beta = 1/T$ is the reciprocal of the edge temperature; then the two-point correlation functions satisfy the following relation,

$$\langle \sigma(w_1)\sigma(w_2)\rangle = \left(\frac{2\pi i z_1}{v\beta}\right)^h \left(\frac{2\pi i z_2}{v\beta}\right)^h \langle \sigma(z_1)\sigma(z_2)\rangle, \tag{2.23}$$

where $h = 1/16$ is the holomorphic conformal dimension of the Ising anyon field. With this we arrive at the thermal two-point correlation function of the Ising anyon field as,

$$\langle \sigma(w_1)\sigma(w_2)\rangle = \left(\frac{\pi T}{v}\right)^{\frac{1}{8}} \frac{1}{\sin^{\frac{1}{8}}[\pi T(w_1 - w_2)/v]} \tag{2.24}$$

The temperature T appearing in the two-point function corresponds to one of the edges. Introducing a regulator ϵ, the two-point function for the two edges can be written as,

$$\langle \sigma_1(x,t)\sigma_1(0,0)\rangle = \frac{(\pi T_1/v)^{1/8}}{\sin^{1/8}[\pi T_1(\epsilon + i(t - x/v))]} \tag{2.25}$$

$$\langle \sigma_2(x,t)\sigma_2(0,0)\rangle = \frac{(\pi T_2/v)^{1/8}}{\sin^{1/8}[\pi T_2(\epsilon + i(t + x/v))]} \tag{2.26}$$

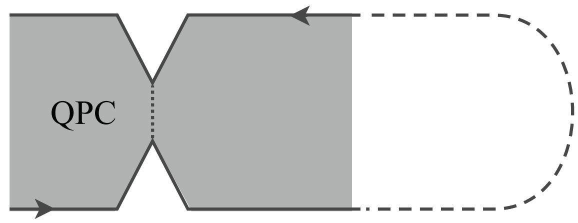

Figure 2.5: Geometry, in which the two edges of the spin liquid are treated as spatially separated parts of the same edge. The dashed line shows a long segment, of length L, connecting the two edges of the interferometer.

We may now treat the two opposite edges of the same spin liquid as different parts of a single edge connected by a long edge segment of length L (See Fig. 2.5). This allows us to use the above result and obtain the four-point correlation function in the limit of $L \to \infty$. This has been computed in Appendix D. Once we obtain the thermal four-point correlation functions, we are in a position to use the perturbation theory, as considered previously, to compute the thermal tunneling current due to Ising anyon tunneling. To separate the interference effects from the rest of the physics of the problem, we first consider the case of a single point contact and later generalize the calculation to interferometers.

The tunneling Hamiltonian creates anyons, which fuse to vacuum, on both sides of the constriction. Since the Ising anyon is its own antiparticle, the tunneling Hamiltonian creates anyons of the same type, and thus the form of the tunneling Hamiltonian can be written as,

$$H_T = e^{-i\pi/16}\Gamma\sigma_2(x_0,t)\sigma_1(x_0,t). \tag{2.27}$$

The subscripts on the Ising anyon field operators denote the side, on which the edge lies and are defined in the limit $L \to \infty$, as $\sigma_2(x) \equiv \sigma(L-x)$ and $\sigma_1(x) \equiv \sigma(x)$. The phase $e^{-i\pi/16}$ is fixed by the hermiticity condition for the tunneling Hamiltonian. Indeed, the average of H_T must be real. The form of the tunneling Hamiltonian suggests that the effect of a single point contact is to allow the tunneling of a single Ising anyon from one edge to the other. This is then treated perturbatively to the lowest order. The expectation value of the tunneling thermal current is given by Eq. (2.8). The full calculation can be found as the non-interference part of the calculation in Appendix E. We find the thermal current to be,

$$\langle I_T\rangle_\Gamma^{\text{non-int}} = \Gamma^2(\pi T_1)^{\frac{1}{8}}(\pi T_2)^{\frac{1}{8}}\frac{\cos(3\pi/8)}{4\sqrt{2}v^{1/4}}F_{\text{non-int}}(T_2/T_1), \tag{2.28}$$

where the $F_{\text{non-int}}(n)$ function in the integral representation is given as,

$$F_{\text{non-int}}(n) = \int_0^\infty d\tau\left(\frac{1}{\tau^{\frac{5}{4}}n^{\frac{1}{8}}} - \frac{\cosh(\tau)}{\sinh^{\frac{9}{8}}(\tau)}\frac{1}{\sinh^{\frac{1}{8}}(n\tau)}\right). \tag{2.29}$$

See Fig. 2.6(a) for the plot of $F_{\text{non-int}}$. Note that the calculation given in Appendix E corresponds to the Fabry–Pérot geometry, and the single-point-contact case corresponds to the non-interference part of the full calculation. A non-linear temperature dependence of the thermal current comes from the scaling dimension of the Ising anyon tunneling operator. Thus, it provides an experimental signature for fractional quasiparticle tunneling at a single point contact. In particular, at fixed T_2/T_1, the tunneling heat current scales as $T^{1/4}$.

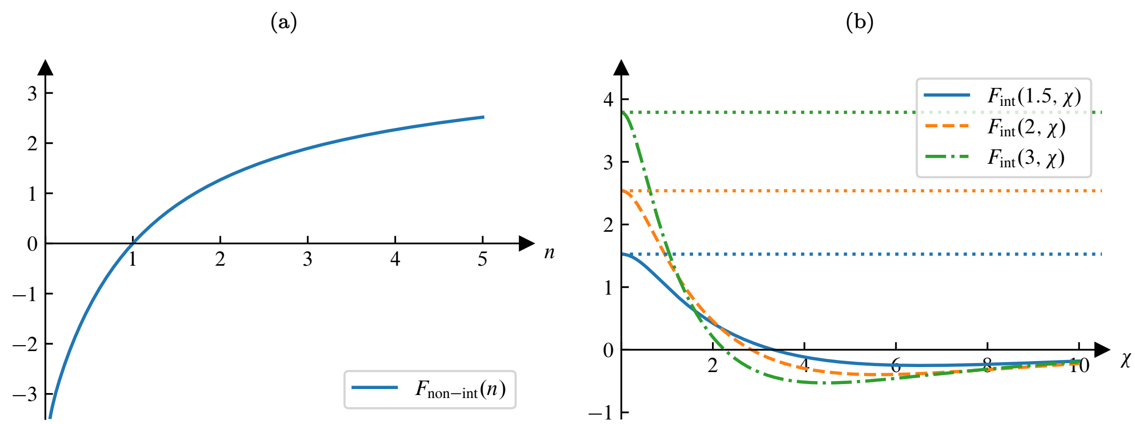

Figure 2.6: (a) The behavior of the function $F_{\text{non-int}}(n)$. (b) The behavior of the function $F_{\text{int}}(n, \chi)$ for $n = 1.5, 2, 3$. The dotted horizontal lines in (b) show the values of $2F_{\text{non-int}}(n)$ for $n = 1.5, 2, 3$, which become equal to $F_{\text{int}}(n, \chi)$ as $\chi \to 0$.

A universal scaling behavior has been predicted for tunneling electrical currents in fractional quantum Hall liquids, but theory rarely agrees with the data (for a review, see [55]). This has multiple reasons, at least one of which, specifically, long-range Coulomb forces [92, 93], is absent in a spin liquid. Thus, there may be a better chance to observe scaling in the tunneling heat current than for an electric current.

We now generalize our single-contact calculation to a Fabry–Pérot interferometer geometry, where the fractional quasi-particle interference effects and anyon braiding effects become relevant.

2.4.2 Fabry–Pérot geometry

The behavior of the tunneling thermal current obtained in the previous subsection captures the non-trivial topological charge of an anyon. Single-point-contact measurements therefore provide a probe of the topological charge of the quasiparticles involved in the tunneling process. A more direct evidence of statistics involves the braiding of two quasiparticles in the two-point-contact geometry. In this section, we generalize the previous calculation to a Fabry–Pérot interferometer geometry.

We use the two-point thermal correlation functions given in Eq. (2.25). These correlation functions are in turn used to compute the four-point correlation functions (Appendix D). The calculation relies on the factorization into products of correlations functions on two separate edges [23]. To find the thermal current operator, we use the Heisenberg equation along with the tunneling Hamiltonian, which in this geometry takes the form,

$$H_T = e^{-i\pi/16}\Gamma_1\sigma_2(x_1,t)\sigma_1(x_1,t) + e^{-i\pi/16}\Gamma_2\sigma_2(x_2,t)\sigma_1(x_2,t), \tag{2.30}$$

where x_i is the coordinate of the ith constriction, and correspondingly, Γ_i is its tunneling amplitude. We now apply perturbation theory to compute the lowest order expectation value using Eq. (2.8).

We start with the simplest case of a trivial topological charge trapped inside the device. We summarize the results here. Detailed calculations are contained in Appendix E.

In the simplest limit $\Gamma_1 = \Gamma_2 \equiv \Gamma$, we arrive at an expression that has the following form,

$$\langle I_T\rangle = 2\langle I_T\rangle_\Gamma^{\text{non-int}} + \langle I_T\rangle^{\text{int}}, \tag{2.31}$$

where $\langle I_T\rangle_\Gamma^{\text{non-int}}$ is the contribution of a single point contact given in Eq. (2.28), and $\langle I_T\rangle^{\text{int}}$ is the interference term that has the form (in the limit $\Gamma_1 = \Gamma_2 \equiv \Gamma$),

$$\langle I_T\rangle^{\text{int}} = \Gamma^2(\pi T_1)^{\frac{1}{8}}(\pi T_2)^{\frac{1}{8}}\frac{\cos(3\pi/8)}{4\sqrt{2}v^{1/4}}F_{\text{int}}(T_2/T_1, \pi T_1 x_{21}), \tag{2.32}$$

where the function $F_{\text{int}}(n,\chi)$ in the integral representation is given as,

$$F_{\text{int}}(n,\chi) = \int_0^\infty d\tau\left(\frac{1}{\tau^{\frac{9}{8}}\sinh^{\frac{1}{8}}(2n\chi)} - \frac{\cosh(\tau)}{\sinh^{\frac{9}{8}}(\tau)}\frac{1}{\sinh^{\frac{1}{8}}(n\tau+2n\chi)} - \frac{\cosh(\tau+2\chi)}{\sinh^{\frac{9}{8}}(\tau+2\chi)}\frac{1}{\sinh^{\frac{1}{8}}(n\tau)}\right). \tag{2.33}$$

The function F_{int} is plotted in Fig. 2.6(b). It can be checked that this function has the property that $\lim_{\chi\to 0} F_{\text{int}}(n,\chi) = 2F_{\text{non-int}}(n)$, where $F_{\text{non-int}}(n)$ is defined in Eq. (2.29). Therefore in the $x_{21} \equiv x_2 - x_1 \to 0$ limit, the two-point-contact case reduces to that of a single point contact. Note that the thermal current in the general case of $\Gamma_1 \neq \Gamma_2$ is computed in Appendix E. The only difference from the above result is the substitution of Γ^2 in the non-interference contribution with $(\Gamma_1^2+\Gamma_2^2)/2$ and with $\Gamma_1\Gamma_2$ in the interference contribution.

So far we assumed a trivial trapped topological charge in the device. The above result is easily extended to the other possible trapped topological charges ψ and σ. Since σ accumulates the phase π on a circle around ψ, the interference contribution changes its sign in comparison with the above equation. For the trapped charge σ, the even-odd effect is present [36, 37]. The tunneling anyon has two equally likely fusion channels with the trapped anyons: $\mathbf{1}$ and ψ. The corresponding interference phases $\phi_{\sigma\sigma}^{\mathbf{1}} = -i\log\big(\theta_{\mathbf{1}}/\theta_\sigma^2\big)$ and $\phi_{\sigma\sigma}^{\psi} = -i\log\big(\theta_\psi/\theta_\sigma^2\big)$ differ by π. Hence, only the non-interference contribution to the heat current survives.

If one can control the trapped topological charge, the existence of three different heat currents at the three possible trapped topological charges gives a signature of the Ising statistics. Presently, it is not clear how to control the trapped charge. As long as a device with the trapped charge σ or ψ can be fabricated, it will be possible to also obtain another trapped topological charge by doubling the size of the device: for example, connecting two identical devices, each of which confines σ, yields the total confined charge $\sigma\times\sigma$, which can be either $\mathbf{1}$ or ψ. It might happen, however, that the trapped charge is always $\mathbf{1}$. In that case, the Fabry–Pérot device would not be able to tell Ising anyons from bosons or fermions. To overcome this issue we consider a Mach–Zehnder interferometer.

2.4.3 Mach–Zehnder geometry

As we already observed, Fabry–Pérot interferometry, in the case of spin liquids, although sensitive to the enclosed topological charge, may not be very informative since it requires control over the topological charge enclosed between the two constrictions. In the case of electronic Fabry–Pérot interferometry, this issue did not arise since anyonic excitations in the sample carry charge. The number of the trapped excitations depends on the magnetic flux. Hence, the magnetic field becomes an external control parameter. Anyonic excitations in a Kitaev spin liquid, however, do not carry charge. Therefore magnetic field fails to provide such a control. It, instead, becomes useful to compare thermal transport in the Fabry–Pérot and Mach–Zehnder interferometers [86].

We thus turn to the double constriction case in the Mach–Zehnder geometry. In this geometry, one of the drains is topologically inside the loop, over which the interference phase is accumulated. Hence, with each tunneling event, the confined topological charge changes. The effective two-point tunneling Hamiltonian is given as,

$$H_T = \Gamma_1 \hat{T}_1 + \Gamma_2 \hat{T}_2 e^{i\alpha}. \tag{2.34}$$

where Γ_i, $i = 1, 2$ are real tunneling amplitudes, $\hat{T}_i$ are two tunneling operators that transfer Ising anyons from the outer edge to the inner edge, Fig. 2.3. The phase α ensures the Hermiticity of the tunneling Hamiltonian H_T. This phase is computed in Appendix F. For Ising anyons, $\alpha = \pi/8$ as a consequence of the general rule that $\exp(i\alpha)$ equals the topological spin of the tunneling anyon (Appendix F).

As highlighted in Sec. 2.2.3, since in the Mach–Zehnder interferometer the tunneling probability changes with each tunneling event, the thermal current is defined in terms of the tunneling rates $p^c_{\sigma b}$ given by Eq. (2.12). For the case of Ising anyons, we find the following tunneling rates,

$$p^\sigma_{\sigma\psi} = \left[\Gamma_1^2 + \Gamma_2^2 - 2\Gamma_1\Gamma_2 \cos(\pi/8)\right] p(T_1, T_2), \tag{2.35}$$

$$p^\sigma_{\sigma\mathbf{1}} = \left[\Gamma_1^2 + \Gamma_2^2 + 2\Gamma_1\Gamma_2 \cos(\pi/8)\right] p(T_1, T_2), \tag{2.36}$$

where $p(T_1, T_2)$ is computed in the single-point-contact geometry as,

$$p(T_1, T_2) = 2\pi \sum_{m,n} \left| \langle m| e^{-i\pi/8} \sigma_2(x_0)\sigma_1(x_0)|n\rangle \right|^2 \delta(E_m - E_n) P_n(T_1, T_2). \tag{2.37}$$

According to Eq. (2.28),

$$p(T_1, T_2) = (\pi T_1)^{\frac{1}{8}} (\pi T_2)^{\frac{1}{8}} \frac{\cos(3\pi/8)}{4\sqrt{2} v^{1/4}} F_{\text{non-int}}(T_2/T_1). \tag{2.38}$$

We remind the reader that, to simplify equations, we assume the temperature low enough for the thermal length v/T to exceed the interferometer size.

Since the Ising anyon σ is its own anti-particle, i.e., one of the fusion channels gives vacuum on fusing two σ anyons, we obtain the following relation from the algebraic theory of anyons [see Eq. (F.15)], in terms of the quantum dimensions, $p^b_{\sigma a} = p^a_{\sigma b}(d_b^2/d_a^2)$. This allows us to compute the remaining non-zero tunneling rates. Plugging this relation into Eq. (2.13), we solve for the probability f_a in dynamical equilibrium,

$$f_\sigma = \frac{1}{2}; \qquad f_{\mathbf{1}} = f_\psi = \frac{1}{4}. \tag{2.39}$$

Finally, the average heat $\overline{\Delta E}$ transferred in each tunneling event can be computed from a setup with a single point contact as a ratio between $r(T_1, T_2)$, calculated in Sec. 2.4.1, and $p(T_1, T_2)$. Given the tunneling rates $p^c_{\sigma b}$, the probabilities f_a, and the average transferred heat $\overline{\Delta E}$, we can find the thermal current from Eq. (2.15),

$$I_T = (\Gamma_1^2 + \Gamma_2^2)(\pi T_1)^{\frac{1}{8}}(\pi T_2)^{\frac{1}{8}} \frac{\cos(3\pi/8)}{4\sqrt{2}v^{1/4}} F_{\text{non-int}}(T_2/T_1), \tag{2.40}$$

where the function $F_{\text{non-int}}$ is defined in Eq. (2.29). We notice that the thermal current in the Mach–Zehnder geometry for Ising anyon tunneling is just the sum of the thermal current contributions from each of the single constrictions as found in Sec. 2.4.1, and the interference term is absent. This is a general feature of non-trivial topological orders as we will see in the next section where we treat an arbitrary anyon statistics.

The above behavior is quite different from the Fabry–Pérot geometry with a trivial trapped topological charge. It is also quite different from the behavior expected from bosons and fermions in the Mach–Zehnder geometry. Indeed, bosons and fermions show the same interference pattern in both geometries. Thus, a comparison of the two interferometer geometries provides a signature of the Ising statistics even if the trapped topological charge is bound to be trivial in the Fabry–Pérot setup. Note that a comparison of theory and experiment requires the knowledge of $\Gamma_{1,2}$. It can be obtained from a single-point-contact geometry.

2.5 Arbitrary anyon statistics

In addition to the Ising topological order in a Kitaev spin liquid, we would like to extend our theory of thermal interferometers to the case where anyons tunnel between two edges of an arbitrary topological phase of matter. We will use the algebraic theory of anyons in Ref. [28], and adopt the assumption that the distances $L_{1,2}$ along the two edges between the two point contacts in the interferometer are much less than the thermal length $l = v/T$. This assumption allows us to use an effective one-point tunneling amplitude for the interferometer and simplify the expressions for the tunneling thermal current.

As in previous sections, we start with a single point contact, then consider the interferometry of Abelian anyons and the interferometry of non-Abelian anyons. Before addressing technical details, we list the key results in the next subsection.

2.5.1 Summary of interferometry

For a topologically trivial system, the same behavior is expected in the Fabry–Pérot and Mach–Zehnder geometries. The interference phase does not depend on what particles are trapped in the device. Thus, one easily checks that in an interferometer with two tunneling amplitudes $\Gamma_{1,2}$ at the constrictions, the heat current scales as $|\Gamma_1 + \Gamma_2|^2$. Indeed, this is obvious from applying the results of the subsection on Abelian statistics to the case of the trivial topological order.

On the other hand, for non-trivial statistics, the thermal current through a Fabry–Pérot device depends on the trapped topological charge. The number of the possible values of the current reflects the number of possible anyon types. The current through the interferometer depends on the mutual statistical phases of the tunneling and trapped anyons. As is clear from Secs. 2.5.4 and 2.5.5, in the case of non-Abelian statistics, the current also depends on the fusion rules for the topological order.

Thus, a Fabry–Pérot device allows the identification of the topological order provided that one can control the trapped topological charge. If the trapped topological charge is always trivial, the Fabry–Pérot approach cannot distinguish non-trivial orders from the trivial order. We have to rely instead on the Mach–Zehnder geometry. Its behavior is strikingly simple and general: For any nontrivial topological order, the heat current scales as $|\Gamma_1|^2 + |\Gamma_2|^2$.

2.5.2 Single contact

We rely on Eq. (2.7) for finding the thermal current operator and Eq. (2.8) for the average heat current. For the purposes of this section, the exact forms of the operators and currents are unimportant. It will suffice to know their scaling dimensions. The current operator scales as the time derivative of the tunneling Hamiltonian. The average current scales as the time integral of the product of that time derivative and the tunneling Hamiltonian. Thus, the average current scales as a power of the temperature T^{2g}, where g is the scaling dimension of the tunneling operator. The exponent depends on statistics. For Ising anyons, $g = 1/8$ in agreement with the previous results. In the $\nu = 1/3$ Laughlin state [3] with the edge action $\frac{3}{4\pi}\int dxdt[\pm\partial_t\phi\partial_x\phi - v(\partial_x\phi)^2]$ and the charge density $e\partial_x\phi/(2\pi)$, the anyon tunneling operator is $\Gamma\exp(i\phi_1 + i\phi_2) + \text{H.c.}$, where the indices 1 and 2 refer to the two edges. Then $g = 1/3$.

2.5.3 Interferometry of Abelian anyons

In an Abelian topological order, the fusion channel of any pairs of anyons is unique, therefore there exists the smallest integer m, such that the fusion result of m anyons of type x is in the vacuum sector. In the following subsections, we will discuss the two cases $m = 2$ and $m > 2$ separately.

Tunneling anyon is its own antiparticle.

We first consider the case when $m = 2$; i.e. $x \times x = \mathbf{1}$, where $\mathbf{1}$ denotes vacuum. Obviously, x is its own antiparticle. One example is the semion topological order [27, 94]: it contains only one type of non-trivial topological charge s, and the only non-trivial fusion rule is $s \times s = \mathbf{1}$; the topological spin of s is $\theta_s = i$.

Given the one-point contact Hamiltonian $H_T = \Gamma\hat{T}$, where Γ is a real amplitude, the thermal current can be written as $I_T = r(T_1, T_2)\Gamma^2$ as demonstrated in Sec. 2.2. The tunneling rate is

$p(T_1,T_2)\Gamma^2$, where $p(T_1,T_2)$ can be found with Fermi's golden rule:

$$p(T_1,T_2) = 2\pi \sum_{mn} |\langle m|\hat{T}|n\rangle|^2 \delta(E_m - E_n) P_n(T_1,T_2), \tag{2.41}$$

$|n\rangle$, $|m\rangle$ are eigenstates of the unperturbed edge Hamiltonian, $E_{n,m}$ are the total energies of the two edges for the corresponding state, and P_n is the Gibbs distribution. The average heat transferred in each tunneling event is $\overline{\Delta E} = r(T_1,T_2)/p(T_1,T_2)$.

For a Fabry–Pérot interferometer, the tunneling Hamiltonian is given as

$$H_T = \Gamma_1 \hat{T}_1 + \Gamma_2 \hat{T}_2, \tag{2.42}$$

where $\Gamma_{1,2}$ are real amplitudes. The localized topological charge has at least two possible values: $\mathbf{1}$ or x. Below we focus on these two possibilities only. Depending on the sector, the tunneling current has two different values,

$$I_{\mathbf{1}}^{\mathrm{FP}} = (\Gamma_1 + \Gamma_2)^2 r(T_1,T_2), \tag{2.43}$$

$$I_{x}^{\mathrm{FP}} = |\Gamma_1 + \Gamma_2 e^{i\phi_{xx}^{\mathbf{1}}}|^2 r(T_1,T_2), \tag{2.44}$$

where $\exp\{(i\phi_{xx}^{\mathbf{1}})\} = \theta_{\mathbf{1}}/(\theta_x\theta_x)$ is the braiding phase. For semions, this phase factor is -1. This result actually applies to any Abelian statistics, as long as x is its own antiparticle and not a fermion or boson. Indeed, the topological spin of vacuum should satisfy $\theta_{\mathbf{1}} = \theta_x^4 = 1$, hence $\theta_x = \pm i$ or ± 1. The second option describes bosons and fermions and so we are left with $\theta_x = \pm i$ and $\exp(i\phi_{xx}^{\mathbf{1}}) = -1$.

In a Mach–Zehnder interferometer, the tunneling Hamiltonian in Eq. (2.11) contains an additional phase $e^{i\alpha} = \theta_x$ in front of Γ_2, as discussed in Appendix F. In the two sectors $\mathbf{1}$ and x, the effective one-point amplitudes are $\Gamma_1 + \Gamma_2\theta_x$ and $\Gamma_1 + \Gamma_2 \exp\{(i\phi_{xx}^{\mathbf{1}})\}\theta_x$ respectively. We further see that the tunneling rates are

$$p_{\mathbf{1}} = |\Gamma_1 + \Gamma_2\theta_x|^2\, p(T_1,T_2), \tag{2.45}$$

$$p_x = |\Gamma_1 - \Gamma_2\theta_x|^2\, p(T_1,T_2). \tag{2.46}$$

Since $\theta_x = \pm i$, the two rates are equal, but we will stick to the same notations as for other statistics. The kinetic equation is now

$$\dot{f}_x = f_{\mathbf{1}} p_{\mathbf{1}} - f_x p_x = 0. \tag{2.47}$$

Applying the requirement that the total probability is unity, we obtain the following solution:

$$f_k = \frac{1}{p_k}\left(\frac{1}{p_{\mathbf{1}}} + \frac{1}{p_x}\right)^{-1}, \quad k = \mathbf{1}, x. \tag{2.48}$$

The thermal current reads

$$\begin{aligned} I^{\mathrm{MZ}} &= \overline{\Delta E} \sum_{k=\mathbf{1},x} f_k p_k = 2\frac{r(T_1,T_2)}{p(T_1,T_2)}\left(\frac{1}{p_{\mathbf{1}}} + \frac{1}{p_a}\right)^{-1} \\ &= (\Gamma_1^2 + \Gamma_2^2) r(T_1,T_2), \end{aligned} \tag{2.49}$$

where the final equality only applies for $\theta_x = \pm i$. The comparison with the experiment requires the knowledge of $\Gamma_{1,2}$ and r. They can be found from a single-contact setup.

Tunneling anyon is not its own antiparticle

Now we consider the case when $m > 2$, which implies that x is not the same as its antiparticle $\bar{x}$. To analyze the tunneling at a single point contact, we write down the tunneling Hamiltonian,

$$H_T = \Gamma \hat{T} + \text{H.c.}, \tag{2.50}$$

where $\hat{T}$ is the tunneling operator which creates a particle-antiparticle pair at the constriction. Similar to Eq. (2.41), the thermal current can be expressed as

$$I_T = 2\pi|\Gamma|^2 \sum_{mn} \Delta E \Big[|\langle m|\hat{T}|n\rangle|^2 + |\langle m|\hat{T}^\dagger|n\rangle|^2 \Big] \delta(E_m - E_n) P_n(T_1, T_2), \tag{2.51}$$

where ΔE is the energy change on the upper edge in the process $|n\rangle \to |m\rangle$. This equation contains two summations for $\hat{T}$ and $\hat{T}^\dagger$ respectively. The two sums are equal in the low-temperature limit. Indeed, we expect that a conformal-field-theoretic description exists for the edge theory in that limit. The tunneling operator $\hat{T}$ for an Abelian topological order can be represented as an exponent $\exp(i\phi)$ of a Bose field ϕ. The conjugate operator $\hat{T}^\dagger = \exp(-i\phi)$. The edge theory is quadratic in Bose fields and hence invariant with respect to the transformation $\phi \to -\phi$. This transformation exchanges $\hat{T}$ and $\hat{T}^\dagger$. Hence, the two contributions to I_T are equal. The above argument may fail at a non-zero voltage in a conducting system if a carriers electric charge. The reason is that changing the sign of the Bose field will then also require changing the sign of the voltage. We assume zero voltage and find that

$$I_T = |\Gamma|^2 r(T_1, T_2), \tag{2.52}$$

where the factor $r(T_1, T_2)$ can be expressed as

$$r(T_1, T_2) = 4\pi \sum_{mn} \Delta E |\langle m|\hat{T}|n\rangle|^2 \delta(E_m - E_n) P_n(T_1, T_2). \tag{2.53}$$

A similar argument shows that the tunneling rates of x and $\bar{x}$ in the same direction are the same. The tunneling rates are $|\Gamma|^2 p^\pm(T_1, T_2)$ for the tunneling of x $(+)$ and $\bar{x}$ $(-)$, where, by an alternative form of Fermi's golden rule [95],

$$p^+(T_1, T_2) = \int_{-\infty}^{\infty} dt\, \langle \hat{T}^\dagger(t)\hat{T}(0)\rangle, \tag{2.54}$$

$$p^-(T_1, T_2) = \int_{-\infty}^{\infty} dt\, \langle \hat{T}(t)\hat{T}^\dagger(0)\rangle. \tag{2.55}$$

The above expressions change into each other when the sign of ϕ is changed. Hence $p^+(T_1, T_2) = p^-(T_1, T_2)$. We will also use the notation $p(T_1, T_2) = p^+(T_1, T_2) + p^-(T_1, T_2)$.

The above discussion shows that the tunneling of $\bar{x}$ transfers the same amount of average heat as the tunneling of x. The tunneling thermal current can be rewritten as

$$I_T = \overline{\Delta E}\, |\Gamma|^2 p(T_1, T_2), \tag{2.56}$$

where $\overline{\Delta E} = r(T_1, T_2)/p(T_1, T_2)$ is the average heat transferred.

It is easy to generalize from the single-constriction case to the Fabry–Pérot geometry with two tunneling contacts with the tunneling amplitudes $\Gamma_{1,2}$. One just needs to substitute $\Gamma \to \Gamma_1 + \Gamma_2 \exp(i\theta)$ in Eq. (2.52), where θ is the statistical phase accumulated by a on a circle around the topological charge, trapped in the interferometer.

Now we come back to the Mach–Zehnder interferometer. We assume that the initial localized topological charge is $\mathbf{1}$ (vacuum) and denote the localized topological charge inside the device after k tunneling events of x as b_k, hence $b_0 = \mathbf{1}$ and $b_k = kx$. Clearly, b_k is periodic in k, $b_{k+m} = b_k$. As we will see below, the same result for the average heat current obtains for any initial trapped charge of the form nx. If the initial trapped charge is not nx, our calculations require only a minor modification, and the final result for the heat current does not change.

For a Mach–Zehnder interferometer, its tunneling Hamiltonian is

$$H_T = \Gamma_1 \hat{T}_1 + \Gamma_2 \hat{T}_2 + \text{H.c.} \tag{2.57}$$

When the localized topological charge is b_k, the effective one-point tunneling amplitude is $\Gamma_1 + \Gamma_2 \exp\{(i\phi_k^{k+1})\}$ for the tunneling of x, and $\Gamma_1^* + \Gamma_2^* \exp\{(i\phi_k^{k-1})\}\theta_x^2$ for the tunneling of $\bar{x}$, where $\exp\{(i\phi_k^{k+1})\} = \theta_{b_{k+1}}/(\theta_x \theta_{b_k})$ and $\exp\{(i\phi_k^{k-1})\} = \theta_{b_{k-1}}/(\theta_{\bar{x}} \theta_{b_k})$. The origin of the factor θ_x^2 in the tunneling amplitude for $\bar{x}$ can be understood in the spirit of Eqs. (F.12-F.14) as well as from physical considerations: $T_2^\dagger$ describes tunneling of x from the inner edge of the interferometer to the outer edge. As a result, $\bar{x}$ is created and left behind on the inner edge. It affects the statistical phase in the tunneling amplitude.

The two tunneling rates for x and $\bar{x}$ can be written down separately,

$$p_k^+ = \frac{1}{2}\left|\Gamma_1 + \Gamma_2 e^{i\phi_k^{k+1}}\right|^2 p(T_1, T_2), \tag{2.58}$$

$$p_k^- = \frac{1}{2}\left|\Gamma_1^* + \Gamma_2^* e^{i\phi_k^{k-1}}\theta_x^2\right|^2 p(T_1, T_2). \tag{2.59}$$

It is worth noting that the following equations hold in the algebraic theory of anyons [28, 34],

$$|\theta_x| = 1, \quad \theta_x = \theta_{\bar{x}}, \quad \theta_{b_k} = (\theta_x)^{k^2}. \tag{2.60}$$

Using these relations, we can find the phases in the tunneling rates to be complex conjugate to each other,

$$e^{i\phi_k^{k+1}} = \frac{\theta_{b_{k+1}}}{\theta_x \theta_{b_k}} = (\theta_x)^{2k}, \tag{2.61}$$

$$e^{i\phi_{k+1}^{k}} = \frac{\theta_{b_k}\theta_x^2}{\theta_{\bar{x}}\theta_{b_{k+1}}} = (\theta_x)^{-2k} = (\theta_x^*)^{2k}. \tag{2.62}$$

Hence $p_k^+ = p_{k+1}^-$, which shows that the tunneling rates for x and $\bar{x}$ are the same, regardless of the topological charge of the localized anyon. The kinetic equation now reads

$$\dot{f}_k = f_{k-1}p_{k-1}^+ + f_{k+1}p_{k+1}^- - f_k(p_k^+ + p_k^-), \tag{2.63}$$

with $k = 0, 1, \ldots, m-1$. After setting $\dot{f}_k = 0$, the equation becomes

$$f_{k+1}p_k^+ - f_k p_k^+ = f_k p_{k-1}^+ - f_{k-1}p_{k-1}^+, \tag{2.64}$$

which means that $f_k = 1/m$ is independent of k. Hence, the heat current is proportional to the average tunneling amplitude

$$I_T = r(T_1, T_2)\frac{1}{m}\sum_{k=0}^{m-1} |\Gamma_1 + \Gamma_2\theta_x^{2k}|^2 = (|\Gamma_1^2| + |\Gamma_2|^2)r(T_1, T_2). \tag{2.65}$$

For comparison, the thermal current in a Fabry–Pérot interferometer has m distinct values

$$I_k^{\mathrm{FP}} = \left|\Gamma_1 + \Gamma_2 e^{i\phi_k^{k+1}}\right|^2 r(T_1, T_2). \tag{2.66}$$

2.5.4 Tunneling of non-Abelian anyons, which are their own antiparticles

Now we study the non-Abelian situation. As in the Abelian situation, we start with the case where the tunneling anyon is its own antiparticle. Examples of such anyons include Ising and Fibonacci anyons. The fusion rule can be written as

$$x \times x = \mathbf{1} + \ldots, \tag{2.67}$$

where $\ldots$ represents other possible fusion channels. The one-point tunneling Hamiltonian should be

$$H_T = \Gamma\hat{T} = \Gamma e^{-i\pi h_x}\hat{x}_2(x_1)\hat{x}_1(x_1), \tag{2.68}$$

where Γ is a real tunneling amplitude, $\hat{x}_2\hat{x}_1$ is the operator that creates a pair of anyons on the opposite edges of the interferometer, and h_x is the scaling dimension of the anyon field with topological charge x. Note that the topological spin θ_x and the scaling dimension h_x are related [28] as $\theta_x = e^{i2\pi h_x}$ for a holomorphic field x. Similar to the Abelian case, we can find the thermal current in a one-point contact geometry using Eq. (2.8), $I_T = r(T_1, T_2)\Gamma^2$. The average heat transferred in each tunneling event is the ratio between $r(T_1, T_2)$ and $p(T_1, T_2)$, where $p(T_1, T_2)$ is given by Eq. (2.41).

In a Mach–Zehnder interferometer, the effective two-point tunneling Hamiltonian is given in Eq. (2.11), where the additional phase $e^{i\alpha}$ is equal to θ_x. In a process where the tunneling anyon changes the trapped topological charge from a to b, the corresponding tunneling rate is

$$p_{xa}^b = P_{xa}^b p(T_1, T_2)|\Gamma_1 + e^{i\phi_{xa}^b + i\alpha}\Gamma_2|^2, \tag{2.69}$$

where $P_{xa}^b = N_{xa}^b d_b/(d_x d_a)$ and $\exp\left(i\phi_{xa}^b\right) = \theta_b/(\theta_a\theta_x)$, as in Eq. (2.12).

We can further write down and compare the tunneling rates for two different, yet related fusion routes for the localized anyon, $x \times a \to b$, and $x \times b \to a$,

$$p_{xa}^b = N_{xa}^b \frac{d_b}{d_x d_a}\left|\Gamma_1 + \Gamma_2 \cdot \frac{\theta_b}{\theta_x\theta_a}\cdot\theta_x\right|^2 p(T_1, T_2), \tag{2.70}$$

$$p_{xb}^a = N_{xb}^a \frac{d_a}{d_x d_b}\left|\Gamma_1 + \Gamma_2 \cdot \frac{\theta_a}{\theta_x\theta_b}\cdot\theta_x\right|^2 p(T_1, T_2). \tag{2.71}$$

In the algebraic theory of anyons [28], $N_{xa}^b = N_{\bar{x}b}^a = N_{xb}^a$ and $|\theta_a| = |\theta_b| = 1$. Since $\Gamma_{1,2}$ are real amplitudes, by comparing the two equations we find that $p_{xa}^b = (d_b/d_a)^2 p_{xb}^a$. Thus the kinetic equation (2.13) can be reduced to

$$\dot{f}_a = \sum_b p_{xb}^a \left[f_b - \left(\frac{d_b}{d_a}\right)^2 f_a \right] = 0. \tag{2.72}$$

It is easy to read out the solution, $f_a = d_a^2/D^2$, where $D = \sqrt{\sum_a d_a^2}$ is known as the global dimension. The tunneling heat current through a Mach–Zehnder interferometer is

$$I^{\mathrm{MZ}} = I_0 + I_1 + I_1^*, \tag{2.73}$$

where

$$\begin{aligned} I_0 &= (\Gamma_1^2 + \Gamma_2^2) r(T_1, T_2) \sum_{ab} N_{xa}^b \frac{d_a d_b}{d_x} \frac{1}{D^2} \\ &= (\Gamma_1^2 + \Gamma_2^2) r(T_1, T_2), \end{aligned} \tag{2.74}$$

and

$$\begin{aligned} I_1 &= \Gamma_1 \Gamma_2 r(T_1, T_2) \sum_{ab} N_{xa}^b \frac{d_a d_b}{d_x} \frac{1}{D^2} \frac{\theta_b}{\theta_a} \\ &= \Gamma_1 \Gamma_2 r(T_1, T_2) \frac{\theta_x}{d_x} \sum_a s_{a\bar{x}} s_{1a} = 0. \end{aligned} \tag{2.75}$$

Here, we have used the identity $d_a d_b = \sum_c N_{ab}^c d_c$. We also use the notion of the topological S-matrix $s_{ab} = \frac{1}{D} \sum_c N_{a\bar{b}}^c d_c \frac{\theta_c}{\theta_a \theta_b}$ and the orthogonality between s_{xa}/s_{x1} and s_{1a}/s_{11} [28, 40]. Therefore, $I^{\mathrm{MZ}} = (\Gamma_1^2 + \Gamma_2^2) r(T_1, T_2)$, and the heat current shows no interference in a Mach–Zehnder interferometer.

For comparison, the Fabry–Pérot current for a localized anyon of type a is

$$I_a^{\mathrm{FP}} = \sum_b N_{xa}^b \frac{d_b}{d_x d_a} \left| \Gamma_1 + \Gamma_2 \cdot \frac{\theta_b}{\theta_x \theta_a} \right|^2 r(T_1, T_2). \tag{2.76}$$

Now we test our results for the Fibonacci topological order. The Fibonacci topological order has only one non-trivial fusion rule: $\tau \times \tau = \mathbf{1} + \tau$. The quantum dimension of a Fibonacci anyon τ is $d_\tau = (1 + \sqrt{5})/2 \equiv \varphi$, and its topological spin is $\theta_\tau = e^{4\pi i/5}$ [20, 34]. According to Eq. (2.69), the tunneling rates in a Mach–Zehnder device are

$$p_{\tau\tau}^{\tau} = \frac{1}{\varphi} |\Gamma_1 + \Gamma_2|^2 \, p(T_1, T_2), \tag{2.77}$$

$$p_{\tau\tau}^{\mathbf{1}} = \frac{1}{\varphi^2} \left| \Gamma_1 + \Gamma_2 e^{-4\pi i/5} \right|^2 p(T_1, T_2), \tag{2.78}$$

$$p_{\tau\mathbf{1}}^{\tau} = \left| \Gamma_1 + \Gamma_2 e^{4\pi i/5} \right|^2 p(T_1, T_2). \tag{2.79}$$

The kinetic equations are

$$\dot{f}_\tau = f_{\mathbf{1}} p_{\tau\mathbf{1}}^{\tau} + f_\tau p_{\tau\tau}^{\tau} - f_\tau (p_{\tau\tau}^{\tau} + p_{\tau\tau}^{\mathbf{1}}), \tag{2.80}$$

$$\dot{f}_{\mathbf{1}} = f_\tau p_{\tau\tau}^{\mathbf{1}} - f_{\mathbf{1}} p_{\tau\mathbf{1}}^{\tau}. \tag{2.81}$$

The solution is

$$f_\tau = \frac{p^\tau_{\tau\mathbf{1}}}{p^{\mathbf{1}}_{\tau\tau} + p^\tau_{\tau\mathbf{1}}} = \frac{\varphi^2}{1+\varphi^2}, \tag{2.82}$$

$$f_{\mathbf{1}} = \frac{p^{\mathbf{1}}_{\tau\tau}}{p^{\mathbf{1}}_{\tau\tau} + p^\tau_{\tau\mathbf{1}}} = \frac{1}{1+\varphi^2}. \tag{2.83}$$

After a substitution back into the equation for the thermal current, one gets

$$I^{\mathrm{MZ}} = (\Gamma_1^2 + \Gamma_2^2)\,\overline{\Delta E}\,p(T_1, T_2) = (\Gamma_1^2 + \Gamma_2^2) r(T_1, T_2). \tag{2.84}$$

This confirms that Eqs. (2.73-2.75) is a general solution for all kinds of anyons in this category.

In summary, anyons that are their own antiparticles show no interference in the Mach–Zehnder geometry.

2.5.5 Tunneling of non-Abelian anyons, which are not their own antiparticles

Now let us consider the situation where the tunneling anyon x is different from its antiparticle $\bar{x}$. More specifically, we consider a topological order in which the fusion results of $x \times x$ and $a \times \bar{a} = \mathbf{1} + \ldots$ share no common topological charges for all possible a. This condition is satisfied by many interesting topological orders, including the $\mathbb{Z}_3$-parafermions and the $k=3, M=1$ Read–Rezayi state [89]. This property is automatically satisfied for charged anyons x since $x \times x$ carriers electric charge and $a \times \bar{a}$ is neutral.

We will rely on the following statement for such systems: if x could fuse with a into b, then $N^a_{xb} = 0$; that is, the available topological charges from the fusion between x and b do not include a. The proof of the statement is the following. Assume that $x \times a = b + \ldots$ and $x \times b = a + \ldots$, then $x \times x \times a = x \times b + \cdots = a + \ldots$. Hence, $x \times x \times a \times \bar{a} = a \times \bar{a} + \cdots = \mathbf{1} + \ldots$ Hence, $x \times x$ contains the antiparticle for at least one fusion channel in $a \times \bar{a}$. Since $a \times \bar{a}$ contains each possible fusion outcome together with its antiparticle, we obtain the desired result.

This result means that the Hermitian conjugate tunneling operators $\hat{T}$ and $\hat{T}^\dagger$ that transfer x between the two edges contribute independently to the tunneling process. This significantly simplifies our discussion below. For completeness, we give an example of an topological order that does not satisfy our condition in Appendix G.

The contributions to the thermal current from $\hat{T}$ and $\hat{T}^\dagger$ are denoted as $|\Gamma|^2 r^\pm(T_1, T_2)$ respectively. Using the perturbation theory and conformal field theory (CFT), one can show that $r^+(T_1, T_2) = r^-(T_1, T_2)$. First, we write the two quantities as integrals in the perturbation theory,

$$r^+(T_1, T_2) = -i \int_{-\infty}^{t} dt' \langle [\hat{T'}^\dagger(t), \hat{T}(t')] \rangle, \tag{2.85}$$

$$r^-(T_1, T_2) = -i \int_{-\infty}^{t} dt' \langle [\hat{T}'(t), \hat{T}^\dagger(t')] \rangle, \tag{2.86}$$

where $\hat{T} = \hat{x}_2(x,t)\hat{\bar{x}}_1(x,t)$ is the tunneling operator, and $\hat{T}' = -\hat{x}_2(x_1,t)\partial_t \hat{\bar{x}}_1(x_1,t)$. In 2D CFT, four-point correlation functions with two fields on each edge can be decomposed into products of two-point correlation functions (Appendix D); furthermore, the correlation function of two fields is fully determined by their conformal weights, or equivalently their scaling dimensions [25]. Using these two properties, one can find that $\langle[\hat{T'}^{\dagger}(t), \hat{T}(t')]\rangle = \langle[\hat{T}'(t), \hat{T}^{\dagger}(t')]\rangle$, hence $r^{+}(T_1, T_2)$ and $r^{-}(T_1, T_2)$ are equal. By the same argument, the tunneling rates given by $p^{\pm}(T_1, T_2)|\Gamma|^2$, where $p^{+}(T_1, T_2) = \int dt\langle\hat{T}^{\dagger}(0)\hat{T}(t)\rangle$ and $p^{-}(T_1, T_2) = \int dt\langle\hat{T}(0)\hat{T}^{\dagger}(t)\rangle$, are also equal to each other. The average heat transferred in a tunneling event is

$$\overline{\Delta E} = \frac{r^{+}(T_1, T_2)}{p^{+}(T_1, T_2)} = \frac{r^{-}(T_1, T_2)}{p^{-}(T_1, T_2)}. \tag{2.87}$$

In Mach–Zehnder interferometers, we consider again the two-point tunneling Hamiltonian given in Eq. (2.57). We assume that the temperature is so low that the distance between the two contacts along the edges is much shorter than the thermal length. Then it is legitimate to "fuse" the two contacts into one. The effective tunneling amplitude depends on the statistical phase accumulated by an anyon around the interferometer. When considering the process, in which the localized topological charge changes from a to b, we need to find out whether it's x or $\bar{x}$ tunneling that results in this fusion. Moreover, if x and a can fuse to b, then $\bar{x}$ and b can fuse to a since $N_{xa}^{b} = N_{\bar{x}b}^{a}$. Now we could write the tunneling rates as

$$p_{xa}^{b} = N_{xa}^{b}\frac{d_b}{d_x d_a}\left|\Gamma_1 + \Gamma_2 e^{i\phi^{+}}\right|^2 p^{+}(T_1, T_2), \tag{2.88}$$

$$p_{\bar{x}b}^{a} = N_{\bar{x}b}^{a}\frac{d_a}{d_{\bar{x}} d_b}\left|\Gamma_1^{*} + \Gamma_2^{*} e^{i\phi^{-}}\theta_x^2\right|^2 p^{-}(T_1, T_2), \tag{2.89}$$

where $e^{i\phi^{+}} = \theta_b/(\theta_x\theta_a)$, $e^{i\phi^{-}} = \theta_a/(\theta_{\bar{x}}\theta_b)$, and the origin of the θ_x^2 factor is the same as in the previous section. We observe that

$$p_{xa}^{b} = \frac{d_b^2}{d_a^2} p_{\bar{x}b}^{a}. \tag{2.90}$$

The matrix M in the kinetic equation (2.13) is of the following form,

$$M_{ab} = p_{xb}^{a} + p_{\bar{x}b}^{a} - \delta_{ab}\sum_{c}(p_{xb}^{c} + p_{\bar{x}b}^{c}), \tag{2.91}$$

but note that p_{xb}^{a} and $p_{\bar{x}b}^{a}$ cannot be nonzero at the same time. The same applies to p_{xb}^{c} and $p_{\bar{x}b}^{c}$. Using Eq. (2.90) we solve the kinetic equation: $f_a = d_a^2/D$. We now repeat the calculations from Eqs. (2.74) and (2.75) with almost no changes. The final result is

$$I^{MZ} \sim |\Gamma_1|^2 + |\Gamma_2|^2. \tag{2.92}$$

The Fabry–Pérot current for a localized anyon a in the fusion channel $x \times a \to b$ is

$$I_{xa}^{b} = \left|\Gamma_1 + \Gamma_2 \cdot \frac{\theta_b}{\theta_x\theta_a}\right|^2 r^{+}(T_1, T_2). \tag{2.93}$$

The total thermal current in the Fabry–Pérot setup is obtained by averaging over all possible fusion outcomes of x ($\bar{x}$) and the trapped anyon a:

$$I_a^{\mathrm{FP}} = \sum_b\left(N_{xa}^{b}\frac{d_b}{d_x d_a} I_{xa}^{b} + N_{\bar{x}a}^{b}\frac{d_b}{d_{\bar{x}} d_a} I_{\bar{x}a}^{b}\right). \tag{2.94}$$

We again emphasize that for a fixed b, it is impossible that both N_{xa}^{b} and $N_{\bar{x}a}^{b}$ are nonzero.

2.6 Noise in Fabry–Pérot interferometers

We now focus on the Ising statistics again. As we discussed, a Fabry–Pérot interferometer provides a clear signature of the Ising statistics as long as the trapped topological charge is under control. If that is not the case, we should compare the Fabry–Pérot and Mach–Zehnder geometries. Fabricating a Mach–Zehnder device is more challenging than making a Fabry–Pérot interferometer. In this section we propose an alternative approach to probing statistics on the basis of telegraph noise in a Fabry–Pérot device with a hole.

We consider the case where an inner closed edge is present in a Fabry–Pérot interferometer, and weak tunneling between the bottom edge and the inner edge is possible, as depicted in Fig. 2.7. The average time between tunneling events at position x_3 is τ. Each tunneling event at x_3 changes the topological charge trapped between QPC1 and QPC2. Because of that, the thermal current from S1 to D2 is subject to change over time. We assume that τ is much longer than the average time between tunneling events at QPC1 and QPC2 (Fig. 2.7). As in the previous section, we assume that the interferometer is shorter than the thermal length. As before, the tunneling amplitudes at QPC1 and QPC2 are Γ_1 and Γ_2. τ is determined by the tunneling amplitude at QPC3.

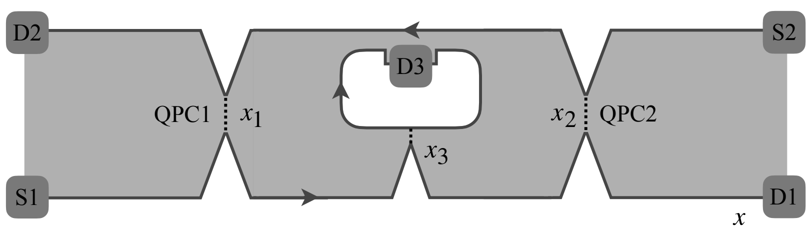

Figure 2.7: Fabry–Pérot interferometer with an inner closed edge inside the device. Telegraph noise due to weak tunneling between the bottom edge and the inner edge at x_3 gives an alternative way to probe statistics. As in a Mach–Zehnder device, each tunneling event changes the enclosed topological charge.

We consider the zero-frequency thermal shot noise given by the following equation [96],

$$S(\omega \to 0) = \lim_{\omega \to 0} \int_{-\infty}^{\infty} dt\, S(t) e^{i\omega t}, \tag{2.95}$$

where

$$S(t) = \langle \{I_T(t), I_T(0)\} \rangle - 2\langle I_T(t)\rangle \langle I_T(0)\rangle, \tag{2.96}$$

the angular brackets denote averaging, the curly brackets stand for an anticommutator, and I_T is the total thermal current between the upper and lower edges through QPC1 and QPC2.

We will treat the tunneling process at QPC3 as a Poisson process. We use the following notations: $t_0 < 0$ is the start time, t_k is the time when the k-th tunneling event happens, and the time interval between successive events follows an exponential distribution, whose rate parameter $\lambda = 1/\tau$. A tunneling event results in a change of the topological charge of the inner edge. The charge changes from σ to $\mathbf{1}$ or ψ with equal probability, but the next tunneling event must change it back to σ.

In this picture, we assume that the initial topological charge of the inner edge is σ, and the heat current at any time t is

$$I_T(t) = I_0 + \Delta I \sum_{k=1}^{\infty} s_k \theta(t - t_k), \tag{2.97}$$

where $I_0 = I_\sigma = r(T_1, T_2)(\Gamma_1^2 + \Gamma_2^2)$ is the current at time t_0, $\Delta I = 2r(T_1, T_2)\Gamma_1\Gamma_2$, and the random variables $s_k = \pm 1$ [97]. We treat s_{2k-1} as independent random variables with the probabilities $P(s_{2k-1} = -1) = P(s_{2k-1} = 1) = 1/2$, while the value of s_{2k} completely depends on s_{2k-1} via the constraint $s_{2k-1}s_{2k} = -1$. Note that the heat currents between the upper and lower edges for the inner-edge topological charges $\mathbf{1}$ and ψ are $I_{\mathbf{1}} = I_\sigma + \Delta I$ and $I_\psi = I_\sigma - \Delta I$. Thus, our definition of the current satisfies all the requirements we set above. The intervals $\tau_k = t_k - t_{k-1}$ are independent and identically distributed exponential random variables,

$$P(\tau_k > t) = e^{-\lambda t}, \quad t \geq 0. \tag{2.98}$$

Let us define $N(t)$ as the total number of the tunneling events at QPC3 during the time interval $(t_0, t]$,

$$N(t) = \max\{k \geq 0 : t_k \leq t\}. \tag{2.99}$$

This is known as a Poisson process, and $N(t)$ satisfies the Poisson distribution

$$P(N(t) = n) = e^{-\lambda(t-t_0)} \frac{(\lambda(t - t_0))^n}{n!}. \tag{2.100}$$

After taking the average with respect to the random variables s_{2k-1} and τ_k, we find (see Appendix H)

$$\lim_{\omega \to 0} \int_{-\infty}^{\infty} dt\, e^{i\omega t} S(t) = 2(\Delta I)^2 \tau (1 - e^{\lambda t_0}). \tag{2.101}$$

In the limit $t_0 \to -\infty$, the equation above reduces to $2(\Delta I)^2\tau$, and we can conclude that

$$S(\omega \to 0) = 8\tau [r(T_1, T_2)]^2 \Gamma_1^2 \Gamma_2^2. \tag{2.102}$$

If τ is large, a high noise can be observed.

2.7 Conclusions

We have learned that interferometry can be done with neutral anyons as long as we focus on thermal current. The basic idea of a thermal interferometer probe is rather similar to electronic interferometry. However, details of the setup differ. Controlling and measuring an electric current is relatively straightforward even for low currents used in experiments with the fractional quantum Hall effect. Dealing with tiny thermal currents is harder.

A breakthrough idea [98] allowed probing thermal currents in the quantum Hall effect. It turns out that thermal measurements can be reduced to purely electric measurements on the basis of Joule's law. This, of course, relies on a finite electrical conductance in QHE systems. Additional ideas are needed to deal with neutral systems such as Kitaev magnets. A crucial challenge is a very

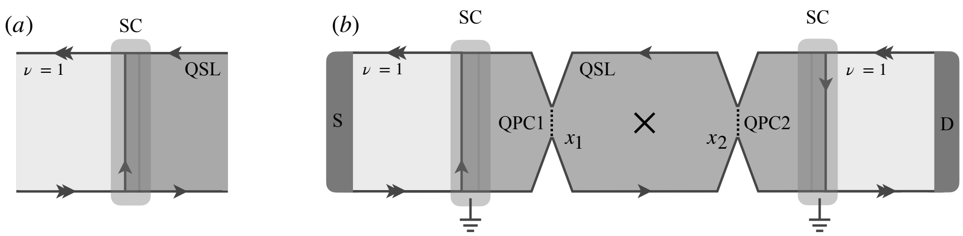

Figure 2.8: (a) The junction between a quantum spin liquid (QSL) and an integer quantum Hall liquid mediated by a superconductor (SC). The $\nu = 1$ edge state (double arrow), under the influence of a superconductor, gets separated into two co-propagating Majorana fermions. Due to strong interactions with the QSL, one of the Majorana modes and the spin liquid's edge Majorana mode form a gapped fermion condensate (faded line under the superconductor without any arrow) which partially 'sews' the two subsystems together. An emergent Majorana mode then continues on the edge of the QSL before recombining again with another Majorana mode on the other edge. Details of this process can be found in Ref. [31]. (b) Using the process described in (a), one can now consider a QSL interferometer between two superconducting junctions with two quantum Hall liquids. The whole system is then attached to an electrical source and drain and allows one to electrically probe the chiral Majorana edge states of the QSL.

low temperature at which the experiment has to be conducted. Indeed, the constriction size cannot be smaller than the unit cell size. This means the scale of the order of at least $a \sim 1$ nm in α-RuCl$_3$. The interferometer size should be at least an order of magnitude bigger, yet it should be shorter than the thermal length $\hbar v/T$, where the edge velocity $v \sim a\Delta/\hbar$, with Δ being the energy gap, is estimated at $\sim 10^5$ cm/s. Besides, the temperature should be much lower than the energy gap Δ estimated at a few Kelvin [29]. Thus, we have to deal with sub-Kelvin temperatures. Thermal currents $\sim T^2/h$ scale as the square of the temperature and are hard to probe in that temperature range.

One approach was advocated in Ref. [87] . The idea builds on using edge-phonon interactions for a sufficiently long edge. Such interactions are highly irrelevant in the renormalization group sense, and we will not address that approach here. See Ref. [87] for details. Two other approaches are possible. Both reduce a thermal measurement to an electric noise measurement.

One approach requires a junction of a spin liquid and a quantum Hall systems. It was proposed that such a junction between a Kitaev magnet and an integer QHE liquid can be mediated by a superconductor [31]. The edge structure is illustrated in Fig. 2.8(a). We can see that the QHE edge splits into a neutral channel running under a superconductor and a neutral edge of the Kitaev liquid. The modes recombine on the other side of the superconducting junction. We now consider a setup with an interferometer between two superconducting junctions [Fig. 2.8(b)]. If the QHE bars on the two sides are maintained at the same temperature, the noise in the drain equals the Nyquist noise at the common temperature. In a non-equilibrium situation, relevant for this chapter, the noise is no longer given by the Nyquist formula and depends on the tunneling heat current.

In another approach, heat is transferred between the interferometer edge and a quantum wire. The standard technique [82, 83, 98] can then be used to measure the heat current in the wire by

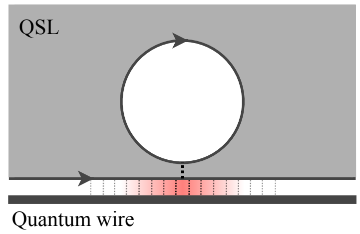

Figure 2.9: Interaction between the quantum wire and the spin liquid is more relevant in the renormalization group sense near the hole.

connecting it with a QHE system. The leading interaction of the wire and the Kitaev edge in contact, $\psi\partial_x\psi\partial_x\phi$, is proportional to the charge density $\sim \partial_x\phi$ in the wire and the energy density on the Kitaev edge. It is highly irrelevant in the renormalization group sense at low energies. Thus, a long region of contact may be needed. Two observations mitigate this challenge. First, the relevancy of the interaction can be increased by using the geometry from Fig. 2.9. Here a hole is made near the Kitaev edge. The interaction of the wire with the Kitaev liquid near the point, where the hole approaches the edge, is $\sigma_1\sigma_2\partial_x\phi$ with $\sigma_{1,2}$ denoting anyon operators on the edge of the hole and the outer edge of the Kitaev liquid. This interaction is significantly more relevant than the interaction without the hole, provided that the system is tuned close to resonance so that the $\sigma_1\sigma_2$ interaction is suppressed.

It is also important that the interferometry experiment does not require probing the precise energy current on the edge. It is enough to compare corrections to the edge thermal current due to the tunneling contacts at different trapped topological charges. This can be accomplished even if only a small portion of the heat current is transferred from the edge of the spin liquid to the wire. Indeed, the difference of the transferred heat currents with and without tunneling contacts in the Kitaev liquid is proportional to the tunneling heat current through the interferometer.

A Mach–Zehnder device cannot be confined in a single plane due to its complicated topology (Fig. 2.3). This is a fabrication challenge. We would like to emphasize that this challenge has been overcome for quantum Hall liquids [57, 90]. On the other hand, quantum coherence persists in Mach–Zehnder interferometers at a longer size than in Fabry–Pérot devices. Indeed, the current through a Fabry–Pérot interferometer depends on the sum of the distances between the tunneling contacts along the two edges. In the Mach–Zehnder case, only the length difference matters. In particular, the heat current depends on the combination of the thermal length and that difference (Appendix I). Thus, interference can be observed at shorter thermal lengths and higher temperatures than in a Fabry–Pérot interferometer of a similar size.

Interferometry is the most direct probe of statistics. A less direct but simpler probe involves heat current through a single contact. It scales as a universal power of the temperature at a fixed ratio of the temperatures on the two edges across the contact.

In conclusion, Fabry–Pérot interferometry shows distinct values of the heat current through the interferometer for each possible topological charge confined in the device. It may be challenging to control the trapped topological charge, in which case the heat current through the interferometer might be the same for anyons as for bosons and fermions. One can then distinguish anyons from fermions and bosons by using a Mach–Zehnder setup. A striking feature is the absence of interference signal in a Mach–Zehnder device for any non-trivial topological order. Besides, anyonic statistic induces a high telegraph noise of the heat current in a Fabry–Pérot device with a hole.

Chapter 3

Quantum Hall interferometry with multiple edge channels

3.1 Introduction

Interferometric methods have proven to be a powerful experimental tool for the investigation of quantum Hall systems [18, 35–39, 49–51, 55–58, 61, 63–66, 69–73, 75, 76]. Most dramatically, for fractional quantized Hall states, interferometry has provided direct measurements of the fractional statistics as well as the fractional charges of quasiparticle excitations. More generally, for both integer and fractional quantum Hall states, interferometry has provided information about the nature of the modes that propagate along the edges of the interferometer, including their interactions with localized charges in the bulk. At a higher level, interferometer experiments provide some sensitive tests of our understanding of quantum Hall states in real materials.

In this chapter, we restrict ourselves to quantum Hall interferometers of the Fabry–Pérot type [35]. In this geometry, two constrictions allow charged quasiparticles or electrons to tunnel between the chiral edge modes on the two sides of a quantum Hall region (Fig. 3.1). When a voltage difference is applied between the two edges of the device, any particles that tunnel across the constrictions will reduce the current transmitted along the edges, and this will lead to a decrease in the measured electrical conductance. If quasiparticles can propagate coherently along the edges between the two constrictions, the tunneling amplitudes will add coherently with a phase difference that depends on the magnetic flux passing through the interferometer region, with possible additional contributions due to quantum statistics when fractionally-charged quasiparticles are involved. As the enclosed flux is sensitive to relatively small changes in the applied magnetic field or to changes in the area of the device caused by changes in the voltage applied to nearby gates, changes in these parameters can lead to interference oscillations in the electrical resistance of the device. It should be noted that changes in the interferometer area can result from Coulomb interactions between the edge modes and charges in the bulk, as well as from direct interactions with the gates [49].

Experiments are most frequently carried out in the limit of small source-drain voltages, where the transmitted current is a linear function of the applied voltage. Further information can be obtained, however, from measurements at larger voltages. Voltage-dependencies in the case where the quantized Hall state has a single propagating mode along each edge, such as at filling factors $\nu = 1$ or $\nu = 1/3$, were discussed in Ref. [35] in 1997. The analysis predicted an oscillatory dependence of the interference amplitude on the applied voltage, with a voltage scale determined by the edge-mode velocity and the length of the interference path. The precise form of the voltage-dependence was found to depend on the filling factor ν.

In this chapter, we extend the theory to the case where there are two co-propagating modes on each edge. Specifically, we consider a fractional case with bulk filling factor $\nu = 2/5$ and the integer case $\nu = 2$. We take into account the Coulomb coupling between charge fluctuations along the two modes on a given edge, but we assume that over longer distances interactions are well screened, due to the presence of a nearby conducting gate. We also assume weak scattering of charges between the two edge modes. This assumption is justified in the case of $\nu = 2$, because the associated particles have different spins in the two modes. In the case of $\nu = 2/5$, scattering between the modes should be strongly suppressed due to their relatively large spatial separation [75, 99]. At the same time, inter-mode scattering cannot be ignored on the laboratory time scale. We will see that such rare scattering events dramatically suppress the observed time-averaged interference current in the non-linear regime.

When the interferometer edge contains two co-propagating modes, different interference phenomena can occur depending on the nature of the constrictions. If the constrictions are only weakly pinched off, tunneling will occur only between the inner modes of the two edges, while the outer modes pass freely through the constrictions [see Fig. 3.1(a)]. We shall see that in this case, the presence of the outer mode has relatively little effect on the interference signal, and the voltage-dependence of the interference amplitude is similar to what one would predict for the inner mode alone, using the formulas of Ref. [35]. The situation is more interesting in the regime where the constrictions are pinched to the extent that the inner mode is completely reflected, while the outer mode passes through the constrictions with only weak backscattering [see Fig. 1(b)]. This physical situation was previously addressed for $\nu = 2$ and $T = 0$ under the assumption of an infinite edge velocity [51]. We go well beyond that limiting case.

In another difference from the earlier work, we consider asymmetric voltage bias. It is usually assumed that the voltage bias is applied symmetrically, that is, the potentials V_d and V_u of the lower and upper edges equal $\pm V/2$, where V is the bias. In actual experiments [76] the bias is often asymmetric. We thus introduce the bias voltage $V = V_d - V_u$ and the average voltage $\tilde{V} = (V_u + V_d)/2$, which can often be treated as independent parameters. The degree of asymmetry is measured by the parameter $\eta = \tilde{V}/V$, which ranges from 0 to 1/2. Note that for a linear relation $\tilde{V} = \eta V$ between the bias and average voltages, the conductance depends on the derivatives of the current with respect to both V and $\tilde{V}$.

Experiments in the case of $\nu = 2/5$ appear to be in a regime where the Coulomb coupling between the two edge modes is relatively weak [75]. On the other hand, in the integer case, experiments can fall in a regime where the two modes are strongly coupled. Such strong coupling has been proposed [53] to explain the "pairing" phenomenon [67, 68] in GaAs systems, where the oscillation period in a range of filling factors above $\nu = 2$ coincides with what one might expect for particles of charge $2e$, and it has been observed directly in a graphene interferometer [76]. Consequently, in our analysis, we will focus on the strong-coupling regime for $\nu = 2$ but the weak coupling regime for $\nu = 2/5$.

The current through the interferometer naturally depends on the number of quasiparticles inside the interference loop. Besides their statistical effect in the fractional quantum Hall case, quasiparticles interact electrostatically with edge channels. For bulk quasiparticles, the latter effect may be neglected if the bulk-edge interaction is well screened, as we assume in this chapter. The effect cannot be neglected for anyons on the inner edge, which forms a closed loop. Thus, we have to account for possible fluctuations of the number of such anyons. In the linear transport regime, all fluctuations are thermal and become unimportant in the low-temperature regime we consider in this chapter. In the nonlinear transport regime, it is possible for charge to tunnel between the inner loop and the outer edge channels so that a small leakage current flows through the device. The tunneling time scale is much longer that the travel time of a charge through the interferometer along its edges. The main consequence of the fluctuations of the charge on the inner loop consists in a rapid suppression of the interference current at large voltages, since the fluctuations in the interferometry phase grow with the voltage bias. There is also a transport resonance when the bias voltage times a quasiparticle charge matches an energy level difference on the inner channel.

In the bulk of this chapter, we assume that Coulomb interactions between charges in the two-dimensional electron system are sufficiently screened by a nearby gate or gates that we can treat the interactions as instantaneous and local in space. However, in some of the most important experiments, screening is provided by a nearby two-dimensional electron gas, whose conductivity is itself strongly affected by the applied magnetic field [75, 100]. Even if the electron density in the screening layer is such that it is not in a quantized Hall state, the layer should have a longitudinal conductivity that will be much smaller than its Hall conductivity. In this case, the screening currents will be chiral and largely confined to the boundary of the layer [101]. Therefore, it may be appropriate to model the screening layer as an added chiral edge state, with its own capacitance and edge velocity, Coulomb coupled to the charges in the measured quantum Hall layer. We consider a model of this type in Section 3.5.

The organization of this chapter is as follows. In Section 3.2, we introduce the models used in this chapter. In Section 3.3, we consider in detail the integer quantum Hall effect at $\nu = 2$, while in Section 3.4, we consider $\nu = 2/5$. Effects of a screening layer are addressed in Section 3.5. In all cases we start a section with a discussion of the regime of the fixed charge on the inner island, formed by the closed edge channel. In that regime, tunneling between co-propagating edge channels can be neglected. We then address the regime of the fluctuating island charge. This amounts to averaging the results for the fixed charge over the statistical distribution of the charge on the inner edge channel. The fixed charge approximation applies in two cases: when the time-scale of the experiment is shorter than the time over which the island charge changes, and if the island charge does not fluctuate at all, as may be the case in the linear transport regime. We separately consider asymmetric and symmetric voltage bias at $\nu = 2$. Since experiments [75] at $\nu = 2/5$ were performed at an approximately symmetric voltage bias, we assume that the bias is symmetric in the discussion of $\nu = 2/5$.

In Section 3.6 we consider effects beyond lowest order in the backscattering at the contacts in the simplest case of an interferometer in the $\nu = 1$ quantum Hall state, with a single edge mode. For non-interacting electrons, the problem is exactly solvable [35]. However, the solution predicts a dependence on the source-drain voltage that does not agree with the data in, *e.g.*, Ref. [76], which were taken in a situation where electrons are 50 percent reflected at each contact. This forces us to consider the possible effects of Coulomb interactions.

Our findings are summarized in Section 3.7. Some technical details are addressed in Appendices J, N, O, and P. Appendix K contains a careful calculation of the Aharonov–Bohm phase. Experimental data are usually presented as a Fourier transform of the interference contribution to the current. We address subtleties of such a Fourier transform in Appendices L and M.

3.2 Model

3.2.1 Edge modes

We start with the model of a quantum Hall (QH) liquid with two co-propagating chiral edge modes. The outer mode separates the filling factor ν_1 from 0, and the inner mode separates the filling factor ν_1 from the filling factor $\nu = \nu_2 + \nu_1$. One example from the integer QH effect (IQHE) is the $\nu = 2$ liquid, where $\nu_1 = \nu_2 = 1$; another example from the fractional QH effect (FQHE) is the $\nu = 2/5$ liquid, where $\nu_1 = 1/3$ and $\nu_2 = 1/15$. The Lagrangian of a single chiral left-moving QH edge in the absence of the intermode interaction is

$$L = \frac{\hbar\partial_x\phi_\mathrm{o}(\partial_t - v_\mathrm{o}\partial_x)\phi_\mathrm{o}}{4\pi} + \frac{\hbar\partial_x\phi_\mathrm{i}(\partial_t - v_\mathrm{i}\partial_x)\phi_\mathrm{i}}{4\pi}, \tag{3.1}$$

where v_o and v_i are the velocities of the outer and inner modes. To describe the opposite propagation direction, one needs to change the sign in front of the time derivatives. The Bose fields ϕ describe the linear charge densities on the edge channels, $-\frac{e\sqrt{\nu_i}\partial_x\phi}{2\pi}$, for a left-moving channel with filling factor discontinuity ν_i. The charge density of a right-moving channel is defined with the opposite sign: $\frac{e\sqrt{\nu_i}\partial_x\phi}{2\pi}$.

In contrast to the case of a single edge mode, a Fabry–Pérot interferometer can now be operated in two ways: inner mode tunneling in Fig. 3.1(a) and outer mode tunneling in Fig. 3.1(b). In both cases, we assume that the distances between two quantum point-contacts (QPC1 and QPC2) are the same along the two edges, and the coordinates of QPC1 and QPC2 are x_1 and x_2. The distance is denoted as $a = x_2 - x_1$. An adjustment for an asymmetric device with the different distances is straightforward. Fig. 3.1(a) shows the situation of inner mode tunneling, where tunneling occurs between the counter-propagating modes on the upper (u) and lower (d) edges at the two QPCs.

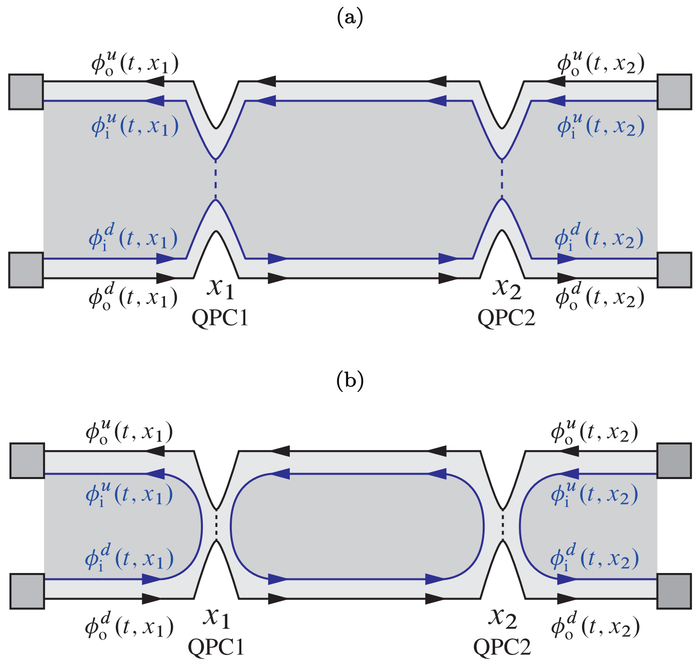

Figure 3.1: Schematics of an electronic Fabry–Pérot interferometer with filling factor $\nu = 2/5$, showing inner mode (a) and outer mode (b) tunneling. Tunneling is shown with dashed lines. On each edge of the interferometer, there are two co-propagating edge modes.

Fig. 3.1(b) shows the situation of outer mode tunneling, where the inner bulk region is completely pinched off by the side gates, and the inner mode forms a closed loop within the interference loop, leading to the direct tunneling through the outer bulk. Inner mode tunneling has been extensively studied in the past (see, in particular, Ref. [50]), and we address that case only briefly. The main focus of this chapter is a technically harder and physically richer case of outer mode tunneling.

The Lagrangian (3.1) is written in a gauge such that the vector potential of the magnetic field is along the edge away from the tunneling contacts. The vector potential is orthogonal to the x-direction in the contacts. Thus, the effect of the magnetic field on the open edge channels is fully captured by an Aharonov–Bohm phase in the tunneling operators. This phase depends continuously on the magnetic field. The coupling of the vector potential with the current along the closed inner loop is responsible for phase jumps.

Obviously, the noninteracting model (3.1) is oversimplified. In fact, it fails to explain the results observed in the experiment for $\nu = 2/5$ FQHE [75]. A more realistic model adds a short-range Coulomb interaction to the Lagrangian [51],

$$L_e = -\frac{\hbar w}{2\pi}(\partial_x \phi_o)(\partial_x \phi_i), \tag{3.2}$$

where the Coulomb repulsion strength $w > 0$. The total Lagrangian $L + L_e$ can be diagonalized by introducing the following transformation,

$$\begin{pmatrix} \phi_{\rm o} \\ \phi_{\rm i} \end{pmatrix} = \begin{pmatrix} \cos\theta & -\sin\theta \\ \sin\theta & \cos\theta \end{pmatrix} \begin{pmatrix} \phi_1 \\ \phi_2 \end{pmatrix} \tag{3.3}$$

where $\phi_{1,2}$ are the edge eigenmodes. Having in mind $\nu = 2/5$, we expect that the bare velocity $v_{\rm o}$ of the outer $1/3$ mode is faster than the velocity $v_{\rm i}$ of the inner $1/15$ mode. If we choose $0 < \theta < \pi/4$ satisfying $\tan(2\theta) = 2w/(v_{\rm o} - v_{\rm i})$, then the diagonalized Lagrangian is

$$L + L_e = \frac{\hbar\partial_x\phi_1(\partial_t - v_1\partial_x)\phi_1}{4\pi} + \frac{\hbar\partial_x\phi_2(\partial_t - v_2\partial_x)\phi_2}{4\pi}, \tag{3.4}$$

with the velocities of the eigenmodes being

$$v_1 = \frac{1}{2}\left[v_{\rm o} + v_{\rm i} + \sqrt{(v_{\rm o} - v_{\rm i})^2 + 4w^2}\right], \tag{3.5}$$

$$v_2 = \frac{1}{2}\left[v_{\rm o} + v_{\rm i} - \sqrt{(v_{\rm o} - v_{\rm i})^2 + 4w^2}\right]. \tag{3.6}$$

In the following sections, we shall deal with the inner and outer mode tunneling in the presence of short-range interaction. We discuss tunneling contacts in subsection 3.2.2. Subsection 3.2.3 deals with the case of the open inner channel. Subsections 3.2.4 and 3.2.5 address a much harder problem of the closed inner channel. We make the assumption that the interaction strength w is less than $\sqrt{v_{\rm i}v_{\rm o}}$ and hence $v_2 > 0$ as thermodynamic stability demands. We also assume weak tunneling between the modes on a single edge. At $\nu = 2/5$, this is justified by a relatively large separation of the two edge channels and a small interferometer size. At $\nu = 2$, one should also remember that the tunneling between the outer and inner modes involves spin flip. Nevertheless, rare tunneling events are important at a high bias. We thus approach the problem in two steps. First, we neglect inter-mode tunneling in subsection 3.2.4. This amounts to computing the tunneling current through the interferometer on a short time scale. Next, we introduce inter-mode tunneling between co-propagating channels in subsection 3.2.5. We only consider inter-mode tunneling events in the closed-loop geometry 1(b) since only in that case there is long-term memory of rare tunneling events due to the charge conservation on the closed loop. The memory effect means that the interference current, computed at a fixed charge of the inner island, should be averaged over all possible chargers on the inner loop. In principle, tunneling between the edges and localized states in the bulk of the interferometer can affect the current even in geometry 1(a), where both channels are open. We will not consider this part of physics in this chapter. Such tunneling was addressed in the linear transport regime at finite temperatures in Ref. [49].

Most of our analysis assumes symmetric voltage bias, $\tilde{V} = 0$. Yet, the experiment [76] at $\nu = 2$ was performed at asymmetric bias. We extend the theory to the asymmetric case in subsection 3.2.6.

3.2.2 Quantum point contacts

In general, for a two-point Fabry–Pérot interferometer where quasiparticles with charge e^* tunnel and a voltage bias V is applied, the total Hamiltonian is $\hat{H} + \hat{H}_T$, where $\hat{H}$ describes the edges and

$\hat{H}_T$ describes the interedge tunneling. The edge Hamiltonian $\hat{H}$ is the sum of the Hamiltonians of the upper and lower edges,

$$\hat{H} = \frac{\hbar v_1}{4\pi}[(\partial_x \phi_1^u)^2 + (\partial_x \phi_1^d)^2] + \frac{\hbar v_2}{4\pi}[(\partial_x \phi_2^u)^2 + (\partial_x \phi_2^d)^2], \tag{3.7}$$

where the indexes u and d refer to the top and bottom edges. As shown in Fig. 3.1, we choose the lower edge to be right-moving and the upper edge to be left-moving; therefore, their Bose fields satisfy the following commutation relation [21],

$$[\phi_j^{d/u}(t,x), \phi_k^{d/u}(t,y)] = \pm i\pi \,\mathrm{sgn}(x-y)\delta_{jk}, \tag{3.8}$$

where the plus sign corresponds to the lower edge (d) and the minus sign corresponds to the upper edge (u). The tunneling Hamiltonian $\hat{H}_T$ is expressed as

$$\hat{H}_T = \Gamma_1 \hat{T}(t,x_1) + \Gamma_2 \hat{T}(t,x_2) + \text{h.c.}, \tag{3.9}$$

where $\hat{T}(t,x)$ are the tunneling operators, $x_{1,2}$ are the locations of the QPCs, and $\Gamma_{1,2}$ are the tunneling amplitudes. Voltage bias enters as a difference of the chemical potentials of the edges. It can be eliminated in a usual way [39] in the interaction representation so that the tunneling Hamiltonian becomes

$$\hat{H}_T = \Gamma_1 e^{i\omega_J t}\hat{T}(t,x_1) + \Gamma_2 e^{i\omega_J t}\hat{T}(t,x_2) + \text{h.c.}, \tag{3.10}$$

where $\omega_J = e^* V/\hbar$ is the effective Josephson frequency, e^* is the charge of the tunneling particle, and $V \equiv V_d - V_u$ is the bias voltage, *i.e.*, the difference between voltages applied to the upper and lower edges. The bias voltage affects the average charge density on the edges. For a asymmetrically applied voltage bias, where $V_u + V_d \neq 0$, this may alter the net charge on the edge and induce a voltage-dependent shift in the interference phase [39]. We shall address this effect further below.

The tunneling current operator is the time derivative of the charge of one edge and can be represented as

$$\hat{I}_T = \frac{ie^*}{\hbar}[\Gamma_1 e^{i\omega_J t}\hat{T}(t,x_1) + \Gamma_2 e^{i\omega_J t}\hat{T}(t,x_2) - \text{h.c.}]. \tag{3.11}$$

Throughout this chapter, except for Section 3.6, we will work in the weak backscattering regime, *i.e.*, we assume a small tunneling amplitude for each quantum point contact and treat the tunneling Hamiltonian $\hat{H}_T$ as a perturbation. In the lowest-order perturbation theory, the expectation value for the current is found using the following standard formula,

$$I_T = -\frac{i}{\hbar}\int_{-\infty}^{0} dt \langle [\hat{I}_T(0), \hat{H}_T(t)]\rangle. \tag{3.12}$$

By defining

$$P(t,x) = \langle \hat{T}(t,x)\hat{T}^\dagger(0,0)\rangle = \langle \hat{T}^\dagger(t,x)\hat{T}(0,0)\rangle, \tag{3.13}$$

which satisfies the relation $P^*(t,x) = P(-t,-x)$, one can write down the non-interference part of the tunneling current $I_T = I_{\text{non-int}} + I_{\text{int}}$ as

$$I_{\text{non-int}} = \frac{e^*}{\hbar^2}\int_{-\infty}^{0} dt (|\Gamma_1|^2 + |\Gamma_2|^2)(e^{-i\omega_J t} - e^{i\omega_J t})[P(-t,0) - P(t,0)], \tag{3.14}$$

and the interference part as

$$I_{\text{int}} = \frac{e^*}{\hbar^2}\int_{-\infty}^{0} dt(\Gamma_1\Gamma_2^* e^{-i\omega_J t} - \text{c.c})[P(-t,-a) - P(t,a)] + (\Gamma_1^*\Gamma_2 e^{-i\omega_J t} - \text{c.c})[P(-t,a) - P(t,-a)], \tag{3.15}$$

where $a = |x_1 - x_2|$ is the distance between the two QPCs.

In the next two subsections we address the structure of the correlation functions for inner and outer mode tunneling. Another component of the model is the phase difference φ between the two tunneling amplitudes. Its behavior is rather subtle for outer mode tunneling. We discuss it in subsection 3.2.5.

3.2.3 Inner mode tunneling

In this section, we discuss the inner mode tunneling case shown in Fig. 3.1(a), with quasiparticle charge $e^* = \pm\nu e$, and voltage bias V. The quasiparticle charge can also be written as $e^* = n\nu_2 e$, where n is an integer, since ν/ν_2 is an integer. We touch inner mode tunneling only briefly. A detailed investigation of inner mode tunneling can be found in Ref. [50].

According to the bosonization technique, the tunneling operator $\hat{T}(t,x) = \delta^{-n^2\nu_2} e^{in\sqrt{\nu_2}\phi_{\text{i}}^u(t,x)} e^{-in\sqrt{\nu_2}\phi_{\text{i}}^d(t,x)}$, where δ is a short-time cutoff. We will denote the correlation function (3.13) as P_{i} since we deal with the inner modes.

Using standard formulas for correlation functions of Bose fields, it is easy to find that at zero temperature,

$$P_{\text{i}}(t,x) = G_d(t,x)G_u(t,x), \tag{3.16}$$

where

$$G_{d,u}(t,x) = [\delta + i(t \mp x/v_1)]^{-n^2\nu_2\sin^2\theta}[\delta + i(t \mp x/v_2)]^{-n^2\nu_2\cos^2\theta}. \tag{3.17}$$

We hence obtain an analytical result for the non-interference current as follows:

$$I_{\text{i,non-int}} = \frac{2\pi e^*(|\Gamma_1|^2 + |\Gamma_2|^2)}{\Gamma(2n^2\nu_2)\hbar^2}|\omega_J|^{2n^2\nu_2 - 1}\,\text{sgn}(\omega_J). \tag{3.18}$$

For the interference current, we first introduce $\exp(i\varphi)$ as the phase difference between Γ_1 and Γ_2, i.e., $\Gamma_1/\Gamma_2 = |\Gamma_1/\Gamma_2|\exp(i\varphi)$. The phase difference includes an Aharonov–Bohm phase, the statistical phase due to any localized anyons, a non-universal phase due to microscopic details of the tunneling contacts, and a possible correction due to asymmetry of the voltage bias (see Section 3.3). Since interference experiments are conducted in a regime where the interferometer contains a large number of flux quanta, a relatively small change in magnetic field or gate voltage can alter the Aharonov–Bohm phase by a large amount, while phase shifts due to changes in the contacts remain negligible. In our discussions, below, we also assume that there are no changes in the number of localized anyons produced by changes in the applied voltages or magnetic fields.

Noticing that $P_{\text{i}}(t,x) = P_{\text{i}}(t,-x)$, we can write the expression for $I_{\text{i,int}}$ as,

$$\frac{2e^*}{\hbar^2}|\Gamma_1\Gamma_2|\cos\varphi\int_{-\infty}^{0} dt\left[e^{-i\omega_J t}P(-t,a) - e^{i\omega_J t}P(-t,a) + \text{c.c.}\right]. \tag{3.19}$$

At a finite temperature T, we need to replace the zero-temperature correlation functions with the finite-temperature ones. This can be done by a conformal transformation [102], and the result is

$$G_{d,u}(t,x) = (\pi T/\hbar)^{n^2\nu_2}[\sin \pi T(\delta + i(t \mp x/v_1))/\hbar]^{-n^2\nu_2 \sin^2\theta} \times [\sin \pi T(\delta + i(t \mp x/v_2))/\hbar]^{-n^2\nu_2 \cos^2\theta}, \tag{3.20}$$

where we have taken $k_B = 1$.

3.2.4 Outer mode tunneling: fixed island charge

In this section, we discuss the geometry in Fig. 3.1(b) for the outer mode tunneling, where the tunneling charge e^* is $m\nu_1 e$, the tunneling operator $\hat{T}(t,x)$ is $\delta^{-m^2\nu_1} e^{im\sqrt{\nu_1}\phi_{\rm o}^u(t,x)} e^{-im\sqrt{\nu_1}\phi_{\rm o}^d(t,x)}$, and δ is the ultra-violet cutoff. However, in contrast to the inner mode tunneling, due to the presence of the inner closed loop, the correlation function (3.13), $P_{\rm o}(t,x)$, does not have a simple form as $P_{\rm i}(t,x)$ in Eq. (3.16). Indeed, even without tunneling, the interaction between the closed inner channel and the outer ν_1 channel scatters the two incoming ν_1 edge modes, $\phi_{\rm o}^d(\omega, x_1)$ and $\phi_{\rm o}^u(\omega, x_2)$, into the outgoing modes, $\phi_{\rm o}^u(\omega, x_1)$ and $\phi_{\rm o}^d(\omega, x_2)$. That scattering process in the main focus of subsection 3.2.4. In this subsection, we neglect inter-mode tunneling between the inner and outer channels. See subsection 3.2.5 for its discussion.

Scattering problem

We start by solving the problem without tunneling not only between co-propagating modes but also at the QPCs. Naively, the scattering problem involves four incoming and four outgoing channels: there are two incoming and two outgoing outer edge channels and two incoming and two outgoing inner edge channels. Fortunately, the chirality of the transport allows ignoring a half of those channels as we demonstrate below. This gives a major simplification in comparison with those QH states that have non-chiral edges such as the $\nu = 2/3$ state.

Before we can proceed, we need to specify what sections of the inner and outer edge channels interact with each other in Fig. 1(a). We assume that the nearby inner and outer modes interact on the top and bottom sides of the device for all x except in a narrow vicinity of points x_1 and x_2. No other other pairs of modes interact. In our model, the interaction strength is always the same whenever it is nonzero.

We next observe that nothing that happens downstream has any effect upstream (downstream and upstream mean down and up with respect to the propagation direction of chiral modes). Thus, we can ignore the interaction of all outgoing channels on the left and on the right of the interferometer. More interestingly, we can ignore the interaction of the incoming modes. The reason is that the solution of the scattering problem below only requires the knowledge of the time-dependent correlation functions of the outer incoming modes in point x_1 on the lower edge and point x_2 on the upper edge. These correlation functions are the same as on an infinite edge that does not contain any inter-mode interactions downstream from the point x_1 for the bottom edge and x_2 for the top edge. Such a non-interacting edge is in thermal equilibrium. In any point x far downstream from x_1

and x_2, the time-dependent correlation functions are the same as if no intermode interaction existed at any point of the edge. Yet, the correlation functions far downstream from the point contacts are exactly the same as in the point contacts since all elementary excitations travel ballistically with the same speed.

Thus, we can ignore the inner edge modes to the left of x_1 and to the right of x_2.

To understand the scattering process quantitatively, we will use the frequency-space representation of the Bose fields [21]. For a left- or right-moving field with velocity v,

$$\phi(t,x) = -\int_0^\infty \frac{d\omega}{\sqrt{\omega}}[e^{-i\omega t}\phi(\omega,x) + \text{H.c.}]e^{-\omega\delta/2}, \tag{3.21}$$

where

$$\phi(\omega,x) = e^{\mp i\omega x/v}\phi(\omega,0). \tag{3.22}$$

$\phi(\omega,x)$ satisfies the following commutation relation,

$$[\phi(\omega,x),\phi^\dagger(\omega',x)] = \delta(\omega-\omega'). \tag{3.23}$$

Such a relation applies in the limit of an infinitely long edge, which is relevant for the outer edge channels. The Bose fields that describe the closed inner channel in the interferometer drop out after the equations of motion are solved. The equations of motion are the first order differential equations for the charge densities $\sim \partial_x\phi$, which are derivatives themselves. We ignore that subtlety below and proceed as if one could remove one partial derivative with respect to the coordinates from all terms in the equations. This simplifies notations and does not affect our final results.

The outgoing fields depend on the incoming fields as follows,

$$\begin{pmatrix}\phi_\text{o}^u(\omega,x_1)\\ \phi_\text{o}^d(\omega,x_2)\end{pmatrix} = S\begin{pmatrix}\phi_\text{o}^d(\omega,x_1)\\ \phi_\text{o}^u(\omega,x_2)\end{pmatrix}, \tag{3.24}$$

with S being an unitary 2×2 matrix. Next, we try to find the matrix S by solving the propagation equations and boundary conditions. A similar problem was solved in Ref. [51], and we follow its approach here. In the region between the two QPCs, due to the interaction, the free-propagating fields are the eigenmodes in Eq. (3.3), hence, they satisfy the following equations,

$$\phi_j^d(\omega,x_2) = e^{i\omega a/v_j}\phi_j^d(\omega,x_1), \tag{3.25}$$

$$\phi_j^u(\omega,x_2) = e^{-i\omega a/v_j}\phi_j^u(\omega,x_1), \tag{3.26}$$

with $j=1,2$. In addition, the closed loop should satisfy the continuity conditions at the positions of the QPCs, where the interaction is minimal,

$$\phi_\text{i}^d(\omega,x_1) = \phi_\text{i}^u(\omega,x_1), \tag{3.27}$$

$$\phi_\text{i}^d(\omega,x_2) = \phi_\text{i}^u(\omega,x_2). \tag{3.28}$$

Solving for $\phi_o^u(\omega, x_1)$ and $\phi_o^d(\omega, x_2)$, we can find

$$S_{11} = -\frac{\sin^2\theta\cos^2\theta\left(e^{\frac{ia\omega}{v_1}} - e^{\frac{ia\omega}{v_2}}\right)^2}{-1 + \left(\sin^2\theta e^{\frac{ia\omega}{v_1}} + \cos^2\theta e^{\frac{ia\omega}{v_2}}\right)^2}, \tag{3.29}$$

$$S_{12} = \frac{2ie^{\frac{ia\omega(v_1+v_2)}{v_1 v_2}}\left[\sin^2\theta\sin\left(\frac{a\omega}{v_1}\right) + \cos^2\theta\sin\left(\frac{a\omega}{v_2}\right)\right]}{-1 + \left(\sin^2\theta e^{\frac{ia\omega}{v_1}} + \cos^2\theta e^{\frac{ia\omega}{v_2}}\right)^2}. \tag{3.30}$$

From the symmetry of the equations, $S_{11} = S_{22}$ and $S_{12} = S_{21}$.

Correlation functions

We can now compute $P_o(t, x)$ at zero temperature using the formula for free Bose fields A, B, C and D,

$$\langle e^{iA}e^{-iB}e^{iC}e^{-iD}\rangle = \exp\Big[-\frac{1}{2}(\langle A^2\rangle + \langle B^2\rangle + \langle C^2\rangle + \langle D^2\rangle) \\ +\langle AB\rangle - \langle AC\rangle + \langle AD\rangle + \langle BC\rangle - \langle BD\rangle + \langle CD\rangle\Big], \tag{3.31}$$

and the zero-temperature correlation functions between free chiral fields ϕ and $\phi^\dagger$,

$$\langle \phi(\omega, x)\phi^\dagger(\omega', x)\rangle = \delta(\omega - \omega')\Theta(\omega), \tag{3.32}$$

$$\langle \phi^\dagger(\omega, x)\phi(\omega', x)\rangle = 0 \tag{3.33}$$

(remember that ω is necessarily positive). All correlation functions can be expressed in terms of the correlation functions of the incoming outer edge modes at x_1 and x_2. The incoming fields in those two points are uncorrelated with each other due to chirality. Their self-correlation functions assume equilibrium values unaffected by the inner mode.

Computing $\langle \hat{T}(t, x_1)\hat{T}^\dagger(0, x_1)\rangle$ gives

$$P_o(t, 0) = \delta^{-2m^2\nu_1}\exp\Big\{-m^2\nu_1\int_0^\infty \frac{d\omega}{\omega}[2 - (S_{11} + S_{11}^*)](1 - e^{-i\omega t})e^{-\omega\delta}\Big\}, \tag{3.34}$$

and computing $\langle \hat{T}(t, x_2)\hat{T}^\dagger(0, x_1)\rangle$ gives

$$P_o(t, a) = \delta^{-2m^2\nu_1}P_1(a)\exp\Big\{-m^2\nu_1\int_0^\infty \frac{d\omega}{\omega}[2 - (S_{12} + S_{12}^*)e^{-i\omega t}]e^{-\omega\delta}\Big\}, \tag{3.35}$$

where

$$P_1(a) = \exp\left(2m^2\nu_1\int_0^\infty \frac{d\omega}{\omega}S_{11}^* e^{-\omega\delta}\right) \tag{3.36}$$

is a real number. We note that $P_o(t, a)$ satisfies the relation $P_o(t, a) = P_o(t, -a)$ as well.

We simplify the equations for the tunneling current as

$$I_{\text{o,non-int}} = \frac{2e^*}{\hbar^2}(|\Gamma_1|^2 + |\Gamma_2|^2)\int_{-\infty}^\infty dt\,\sin(\omega_J t)\,\mathrm{Im}\,P_o(-t, 0), \tag{3.37}$$

$$I_{\text{o,int}} = \frac{4e^*}{\hbar^2}|\Gamma_1\Gamma_2|\cos\varphi\int_{-\infty}^\infty dt\,\sin(\omega_J t)\,\mathrm{Im}\,P_o(-t, a), \tag{3.38}$$

where $\exp(i\varphi)$ is the phase difference between Γ_1 and Γ_2.

At a finite temperature T, we substitute the Bose–Einstein distribution into the correlation functions of the Bose fields, i.e.,

$$\langle \phi(\omega, x)\phi^\dagger(\omega', x)\rangle = \frac{\delta(\omega-\omega')}{1-e^{-\hbar\omega/T}}, \tag{3.39}$$

$$\langle \phi^\dagger(\omega, x)\phi(\omega', x)\rangle = \frac{\delta(\omega-\omega')}{e^{\hbar\omega/T}-1}. \tag{3.40}$$

Therefore we can find $P_\mathrm{o}(t,x)$ at a finite temperature as

$$P_\mathrm{o}(t,0) = \delta^{-2m^2\nu_1}\exp\left\{-m^2\nu_1\int_0^\infty \frac{d\omega}{\omega}[2-(S_{11}+S_{11}^*)]\left(\frac{1-e^{-i\omega t}}{1-e^{-\hbar\omega/T}}+\frac{1-e^{i\omega t}}{e^{\hbar\omega/T}-1}\right)e^{-\omega\delta}\right\}, \tag{3.41}$$

$$P_\mathrm{o}(t,a) = \delta^{-2m^2\nu_1}P_1(a)\exp\left\{-m^2\nu_1\int_0^\infty \frac{d\omega}{\omega}\left[\frac{2-(S_{12}+S_{12}^*)e^{-i\omega t}}{1-e^{-\hbar\omega/T}}+\frac{2-(S_{12}+S_{12}^*)e^{i\omega t}}{e^{\hbar\omega/T}-1}\right]e^{-\omega\delta}\right\}, \tag{3.42}$$

where

$$P_1(a) = \exp\left[2m^2\nu_1\int_0^\infty \frac{d\omega}{\omega}\left(\frac{S_{11}^*}{1-e^{-\hbar\omega/T}}+\frac{S_{11}}{e^{\hbar\omega/T}-1}\right)e^{-\omega\delta}\right]. \tag{3.43}$$

To numerically compute the current in Eq. (3.37) and (3.38), one needs to compute the integral in the expression for $P_\mathrm{o}(t,x)$ first. Unfortunately, there is no known analytical result for $P_\mathrm{o}(t,x)$. However, following a technique similar to that used in Ref. [51], one can write the integral in $P_\mathrm{o}(t,x)$ as a series. The details of this series expansion are explained in Appendix J.

3.2.5 Aharonov–Bohm phase and the average current on the laboratory time scale

We compute the interference contribution to the current and represent it as

$$I_{\mathrm{i,int}} = \tilde{I}\cos\varphi, \tag{3.44}$$

where φ is an effective Aharonov–Bohm phase, accumulated by the interfering charges. Our focus above was on $\tilde{I}$. The rich physics of the phase φ in the linear transport regime has been discussed in previous work on Coulomb-dominated interferometry [49, 55], and much of the same discussion applies to a well-screened case. It is not a goal of this manuscript to address the behavior of the phase in detail in the linear regime at finite temperatures. Some subtleties of its behavior are addressed in Appendices K and L. In the main text, we limit ourselves with a few comments and focus instead on the limit of low temperatures with the emphasis on non-linear transport. This regime is greatly affected by intermode tunneling between the inner and outer channels in the closed loop geometry of Fig. 1(b). Tunneling to localized states in the bulk of the interferometer may also be important, but will not be considered in this chapter.

The general structure of the phase factor is

$$\exp(i\varphi) = \exp\bigl[iC + i(\alpha_0 \tilde{V} + \alpha_1 \lambda_1) + i\gamma N\bigr], \tag{3.45}$$

where C is a constant, depending on microscopic details, such as the structure of the tunneling contacts; the $\alpha_0 \tilde{V}$ term represents the dependence of the phase on the average voltage $\tilde{V} = (V_d + V_u)/2$ due to the dependence of the area of the open channel on the chemical potential; γ represents the phase due to N electrons confined on the inner channel at $\nu = 2$ or due to N confined quasiparticles at $\nu = 2/5$. In both cases, Coulomb interaction of the N particles with the outer edge channel changes its area. At $\nu = 2/5$, γ also includes a statistical phase of anyons. The value of γ can always be chosen between $-\pi$ and π without affecting the phase (3.45) by adding a multiple of 2π, and we will assume such a choice. Finally, λ_1 represents an additional control parameter, such as the magnetic flux, and α_1 is a constant. One can think of $\alpha_1 \lambda_1$ as the Aharonov–Bohm phase due to the magnetic field through a fixed nominal area within the outer channel.

The total charge of the inner channels is easy to compute when it is open. It equals

$$Q = e^*[\text{linear function of the voltages } + \beta_1 \lambda_1], \tag{3.46}$$

where β_1 is a constant and e^* the quasiparticle charge. As discussed below, the charge of the closed inner edge is quantized. Still, Eq. (3.46) is an important reference point in that case too. In particular, in the linear response regime, $N = Q/e^*$ is the nearest integer to the prediction of the above equaiton.

Linear regime

If tunneling happens between the inner edges of the device, a simple model of a fixed-area interferometer may apply. The phase φ then combines a statistical phase due to localized anyons in the bulk of the device (at $\nu = 2/5$ only) and the standard Aharonov–Bohm phase proportional to the fixed area of the device, the magnetic field, and the charge of a tunneling quasiparticle. The situation is more complex when the inner channel is closed.

Indeed, in that case the fixed-area model does not work since the charge confined by the inner edge cannot change continuously in response to changing magnetic field or chemical potential. It is quantized as an integer number of electron charges at $\nu = 2$ and an integer number of $e/3$ charges at $\nu = 2/5$. The area within the channel jumps every time a new quasiparticle is added. Between such glitches, the area within the inner edge changes continuously to make sure that it confines a fixed magnetic flux. This may have an effect on the area confined by the outer edge, which in turn determines φ. Indeed, as the inner island compresses, more of its charge moves away from the outer edge. In the presence of a top gate, this decreases the electrostatic potential created by the charge of the inner island near the outer edge. The outer edge then adjusts its position to minimize its energy. In the strong-coupling regime, the total charge near the outer edge is independent of the magnetic flux and is set by the gate and bias voltages. Hence, at $\nu = 2$, a decrease of the area of the inner loop must be compensated by an equal increase of the area within the outer channel. As a result, the change of the Aharonov–Bohm phase in response to a small change of the magnetic field is the same as in a $\nu = 1$ device of the double area. This was indeed observed experimentally [76].

From time to time, the charge within the inner channel jumps. This jump is screened by an opposite-sign jump of the charge within the outer channel. In the strong coupling regime, the screening charge is exactly equal to one quasiparticle charge. Hence, at $\nu = 2$, such jumps are invisible in interferometry.

Appendix K computes the dependence of φ on the potentials V_d and V_u of the lower and upper edges in the intermediate coupling case. The dependence is linear between jumps of the charge of the inner channel. Such jumps result in discontinuities of φ. Appendix L analyses the Fourier transform of the current with respect to various control parameters in the presence of such glitches.

Glitches are only discontinuous at zero temperature. They are still sharp as long as the temperature is lower than the charging energy. In such a regime, one can extract φ from the experimental data by fitting the size of the jumps and the continuous change of the current between the jumps using an amplitude $\tilde{I}$, which does not depend on the magnetic field. At higher temperatures, the charge confined by the inner loop strongly fluctuates. The physics is similar to the fluctuations of the bulk charge in a poorly screened device. We do not address this effect here and refer the reader to earlier work [49].

Nonlinear regime

We now address slow fluctuations of the charge confined by the closed inner edge due to the tunneling between co-propagating edge modes on each side of the interferometer in the closed-loop geometry. The tunneling rate between the co-propagating channels is negligible in comparison with the tunneling rate through the QPCs. Nevertheless, it qualitatively modifies the physics.

We start with $\nu = 2$.

$\nu = 2$ case. We will only address charge fluctuations in the low-temperature limit. This differs from our results in the short-time regime, which apply at any temperature. The fluctuations are driven by the potential difference between the upper and lower edges of the interferometer. Their origin can be visualized in the model of non-interacting electrons on the QHE edges at $\nu = 2$, Fig. 3.2. The inner edge possesses a discrete set of electron energy levels. Electrons from the lower edge with a higher chemical potential can tunnel into available states of the inner edge below the chemical potential. This is a slow process, involving spin flips. Between such rare tunneling events, the inner edge equilibrates with the environment. The energy of the inner edge does not conserve due to its Coulomb interaction with the outside world. Thus, we expect the inner edge to relax into the lowest-energy state consistent with its charge. This happens on a much faster time scale than the tunneling events into the inner loop. At the same time, the chemical potential of the upper open edge is below the chemical potential of the inner loop. This leads to tunneling from the inner loop to the upper edge channel. Again, the inner loop rapidly sets into a ground state after any such tunneling event.

The above picture only applies in the non-linear transport regime. If the chemical potentials of the upper and lower edges are close to each other, the inner edge is unlikely to have an energy level between the two chemical potentials. This prevents the tunneling into the inner island.

In general, the tunneling rates between the inner loop and the outer edges depend on microscopic details. We will adopt a simple model in which the tunneling matrix elements are the same for all states of the inner edge. In other words, we simply assume that the tunneling rate between the lower and inner edges is proportional to the number of the empty energy levels on the inner edge below the chemical potential of the lower edge. The tunneling rate between the upper and inner edges is similarly proportional to the number of the occupied states on the inner edge above the chemical potential of the upper edge. This describes Ohmic transport since the currents between the inner loop and outer edges are proportional to the chemical potential differences between the inner island and the outer edges. The quantization of the charge of the inner edge means that its zero-temperature chemical potential assumes a discrete set of values. The number of possible values for a given voltage bias depends on the magnetic flux and other parameters and changes by ± 1 as they vary. In other words, at a fixed bias, two different level numbers k and $k+1$ are possible, depending on the magnetic flux or other parameters. This leads to periodic singularities in the Fourier transform of the current with respect to the magnetic field or other control parameters every time the voltage bias reaches a value consistent with a different set of the numbers $(k, k+1)$ of the electron levels in the transport energy window on the inner loop.

The range of possible electron numbers N on the inner edge as a function of V_d and V_u is computed in Appendix K. We denote the minimal and maximal allowed values for given V_d and V_u as $N_u < N_d$. We now introduce a kinetic equation for N.

The distribution function of the number of electrons N is f_N, and we consider its rate of change. When there are $N-1$ electrons on the inner edge, the electrons on the lower edge have enough energy to tunnel into any one of the unfilled $N_d-(N-1)$ levels, and we assume that the tunneling rates are all equal to $\Gamma_{\rm io}$. The rate of the $N-1 \to N$ transition is $\Gamma_{\rm io} f_{N-1}[N_d-(N-1)]$. Similarly, the rate of the $N+1 \to N$ transitions is $\Gamma_{\rm io} f_{N+1}(N+1-N_u)$. Finally, the combined rate of the $N \to N-1$ and $N \to N+1$ processes is $\Gamma_{\rm io} f_N[(N-N_u)+(N_d-N)]$. Therefore we have the following kinetic equation,

$$\dot{f}_N = -\Gamma_{\rm io} f_N (N_d - N_u) + \Gamma_{\rm io} f_{N-1}[N_d - (N-1)] + \Gamma_{\rm io} f_{N+1}(N+1-N_u). \tag{3.47}$$

The stationary distribution function for N can be found to be

$$f_N = \frac{C_{N_d-N_u}^{N-N_u}}{2^{N_d-N_u}}. \tag{3.48}$$

We will now average the interference current over f_N. This requires us to average the phase factor (3.45) in Eq. (3.44), where we use $\alpha_0 = -2ea/\hbar v_{\rm o}$, Eq. (K.6), and $\gamma = 2\pi w/v_{\rm o}$ (mod 2π), $-\pi < \gamma \leq \pi$, Eq. (K.7).

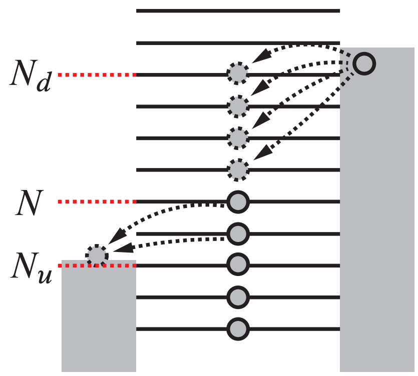

Figure 3.2: Schematics of the kinetics of quasiparticles on the inner loop in the low-temperature limit. The dashed arrows on the right represent the tunneling of quasiparticles from the lower edge into $N_d - N$ unfilled states. The dashed arrows on the left represent the tunneling of quasiparticles from $N - N_u$ filled states into the upper edge.

We observe that from the binomial formula,

$$\frac{1}{2^{N_{\max}}} \sum_{N=0}^{N_{\max}} C_{N_{\max}}^{N} e^{i\theta N} = \frac{1}{2^{N_{\max}}} (1 + e^{i\theta})^{N_{\max}} = (e^{i\theta/2})^{N_{\max}} \cos^{N_{\max}}(\theta/2). \tag{3.49}$$

Hence, the expected value of the phase factor is

$$\begin{aligned} &\sum_{N=N_u}^{N_d} f_N \exp\left[iC + i(\alpha_0 \tilde{V} + \alpha_1 \lambda_1) + i\gamma N\right] \\ &= \exp\left\{ iC + i(\alpha_0 \tilde{V} + \alpha_1 \lambda_1) + i\frac{\gamma}{2}(g_u + g_d) + (2\beta_0 \frac{v_o}{w}) \log\left(\cos\frac{\gamma}{2}\right) V \right. \\ &\quad \left. + F(g_d)\left[-i\frac{\gamma}{2} - \log\left(\cos\frac{\gamma}{2}\right)\right] + F(g_u)\left[-i\frac{\gamma}{2} + \log\left(\cos\frac{\gamma}{2}\right)\right] \right\}, \end{aligned} \tag{3.50}$$

where $V = V_d - V_u$ and we use the function $F(g) = g - [g]$, where $[x]$ is the nearest integer to x, and g_u and g_d are computed in Appendix K.2 as

$$g_u = \beta_0(\frac{2v_o}{w} V_u - V_u - V_d) + \beta_1 \lambda_1; \tag{3.51}$$

$$g_d = \beta_0(\frac{2v_o}{w} V_d - V_u - V_d) + \beta_1 \lambda_1. \tag{3.52}$$

As discussed in above, Eq. (3.46), and Appendix L, λ_1 is a control parameter, such as a gate voltage or the magnetic flux through the inner loop, and β_1 is a constant that depends on microscopic details.

A striking feature of the above expression is the $(V_d - V_u)(\log\cos\frac{\gamma}{2})$ term, responsible for the exponential suppression of the current at a large voltage bias $V_d - V_u$. Note also that if $\gamma = \pi$, there is no interference current as long as $N_u \neq N_d$.

$\nu = 2/5$ **case.** We will use an Ohmic model similar to the $\nu = 2$ problem. This may seem unjustified since the tunneling of fractionally charged quasiparticles is typically non-Ohmic in FQHE. That is, however, not the case for tunneling between co-propagating edge channels. Indeed, the edge theory with co-propagating modes can be interpreted as a chiral conformal field theory. Tunneling terms in the Hamiltonian must be Bose fields as is the case for any contribution to the Hamiltonian. Hence, their scaling dimension is integer. That integer is usually 1. In particular, this is the case for the inter-channel tunneling of $e/3$ anyons at $\nu = 2/5$. Since the scaling dimension is the same as at $\nu = 2$, the use of a similar model is justified.

We again find a binomial distribution f_N for the quasiparticle number. The statistical phase is computed in Appendix K and equals $\gamma = 2\pi\nu_1(\frac{\sqrt{\nu_1}w}{\sqrt{\nu_2}v_o} + 1)$. We can always assume that $-\pi < \gamma \leq \pi$ by adding an irrelevant multiple of 2π. We also compute the coefficient $\alpha_0 = -2\nu_1 ea/\hbar v_o$ in Appendix K. Finally, we average the phase factor over f_N and find

$$\begin{aligned}
&\sum_{N=N_u}^{N_d} f_N \exp\left[iC + i(\alpha_0\tilde{V} + \alpha_1\lambda_1) + i\gamma N\right] \\
&= \exp\left[iC + i(\alpha_0\tilde{V} + \alpha_1\lambda_1) + i\frac{\gamma}{2}(N_d + N_u) + (N_d - N_u)\log\left(\cos\frac{\gamma}{2}\right)\right] \\
&= \exp\left\{iC + i(\alpha_0\tilde{V} + \alpha_1\lambda_1) + i\frac{\gamma}{2}(g_u + g_d) + (2\beta_0\frac{v_o}{w})\frac{\nu_2}{\nu_1}\log\left(\cos\frac{\gamma}{2}\right)V \right. \\
&\quad \left. + F(g_d)\left[-i\frac{\gamma}{2} - \log\left(\cos\frac{\gamma}{2}\right)\right] + F(g_u)\left[-i\frac{\gamma}{2} + \log\left(\cos\frac{\gamma}{2}\right)\right]\right\},
\end{aligned} \tag{3.53}$$

where the definitions of g_u and g_d have been modified according to the discussion of $\nu = 2/5$ in Appendix K:

$$g_u = \frac{\sqrt{\nu_2}}{\nu_1}\beta_0(\frac{2v_o}{w}\sqrt{\nu_2}V_u - \sqrt{\nu_1}V_u - \sqrt{\nu_1}V_d) + \beta_1\lambda_1 \tag{3.54}$$

$$g_d = \frac{\sqrt{\nu_2}}{\nu_1}\beta_0(\frac{2v_o}{w}\sqrt{\nu_2}V_d - \sqrt{\nu_1}V_u - \sqrt{\nu_1}V_d) + \beta_1\lambda_1. \tag{3.55}$$

As at $\nu = 2$, the above expression reveals exponential suppression of the current at a high bias $V = V_u - V_d$. As before, $\gamma = \pi$ implies no interference current for $N_u \neq N_d$.

3.2.6 Asymmetric bias

In the previous subsections, we have discussed the response under the assumption that the bias voltage V is applied symmetrically to the two edges, i.e., that the voltages V_d and V_u applied to the lower and upper edges are equal to $V/2$ and $-V/2$ respectively. However in many experiments, the bias is applied asymmetrically, in many cases only to one of the edges. This is the case, for example, in the experiments of Ref. [76]. In the general case we may write

$$V_{d/u} = \tilde{V} \pm V/2 \tag{3.56}$$

where $\tilde{V}$ is the average of the applied voltages and V is their difference. A non-zero value of $\tilde{V}$ can introduce an additional phase factor into the tunneling amplitudes [39]. This reflects the charge, accumulated in the interferometer due to the applied voltage. Indeed, the phase accumulated by a particle on a path around an interferometer is proportional to the charge localized in the device [56].

In this subsection we address the effect of non-zero $\tilde{V}$. We limit our discussion to $\nu = 2$ since the relevant experiments [75] at $\nu = 2/5$ involve symmetric bias. We also assume a fixed charge of the inner island, since the the fluctuations of the island charge do not differ qualitatively between the cases of symmetric and asymmetric bias.

If $\tilde{V} \neq 0$ but $V = 0$, the system will remain in a state of thermal equilibrium, with some alteration of the total charge, which will generally lead to a shift in the interference phase φ. At a low temperature, the charge of the inner channel assumes a fixed value that minimizes the energy shifted by the total charge times the chemical potential. In what follows in this subsection, we will assume such a fixed charge of the inner loop even at a nonzero V. In addition to the bias, the fixed charge may depend on the magnetic flux and various gate voltages (parameter λ_1 in Eq. (3.45)). This may matter even in the symmetric case. At low temperatures, the fixed charge assumption always holds in the linear transport limit of the low voltage bias $V = V_d - V_u$.

Application of a symmetric bias V to the device will then lead to an interference current with an altered phase but with an amplitude computed in precisely the same way as in the case of a symmetric bias. Thus we may write

$$I_{\text{int}} = \tilde{I} \cos \varphi, \tag{3.57}$$

where φ depends on $\tilde{V}$ but is independent of V, while $\tilde{I}$ depends on V but not on $\tilde{V}$.

An important experimental quantity is differential conductivity, dI/dV. If the voltage is applied asymmetrically, with $\tilde{V} = \eta V$, we have

$$\frac{dI_{\text{int}}}{dV} = \frac{d\tilde{I}}{dV} \cos(\varphi) - \eta \tilde{I} \sin(\varphi) \frac{d\varphi}{d\tilde{V}}. \tag{3.58}$$

Typically, values of dI/dV are obtained over a range of control parameters, such as the magnetic field and/or one or more gate voltages, and one takes a Fourier transform of the data with respect to these parameters. The transform will have peaks at frequencies corresponding to the interference oscillations, and we wish to compute the amplitudes of these peaks. Asymmetry in the applied voltage can have an important effect on these amplitudes.

In the case of a Fabry–Pérot interferometer at $\nu = 1$, the factor $d\varphi/d\tilde{V}$ is a constant, equal to $2ea/\hbar v$. [See Ref. [39] and Section 3.6 below.] However, the case of $\nu = 2$ is more complicated. In particular, for interference of the outer mode, when the inner mode is completely reflected at the point contacts, the charge on the inner edge is restricted to integer values. At low temperatures, the accumulated charge on the inner edge minimizes the energy of the system. Since only an integer number of electrons can tunnel into the inner edge, the accumulated charge changes discontinuously as one more electron is added or removed in response to the changing bias. This may result in a discontinuous jump in φ due to the Coulomb interaction of the inner and outer edge modes. As a result, the interference phase will not depend linearly on $\tilde{V}$ or on parameters such as B or the gate voltages, so that the interference current is no longer a simple sinusoidal function of these parameters. As discussed in Appendix L this situation leads to an array of Fourier peaks, whose amplitudes may be analyzed separately. In the remainder of this subsection, we shall ignore this complication and assume that φ is a linear function of $\tilde{V}$ and the other parameters, so that $d\varphi/d\tilde{V}$ is a constant. However, we show in Appendix L, the essential results for the amplitude of the dominant finite-frequency Fourier peaks are unchanged after the phase jumps are properly taken into account, except for renormalization by a voltage-independent constant.

This linearity assumption is actually valid in the limit of very strong mode coupling, where an integer jump in the charge of the inner mode will be compensated by an opposite integer jump in the charge of the outer mode. The interference phase will consequently jump by a multiple of 2π, which will have no effect on the interference signal. In this limit, therefore, it is appropriate to ignore the jumps, so that φ is a linear function of $\tilde{V}$. This near-invisibility of phase jumps in the strong-coupling regime is also responsible for the appearance of a flux period normally associated with particles of charge $2e$ (cf. Appendix L). In this case, we find

$$\frac{d\varphi}{d\tilde{V}} = -\frac{2ea}{\hbar v_{\rm o}}, \tag{3.59}$$

as shown in Appendix K.

In the discussions above we ignored any effects on the edge modes due to changes in the occupation of localized states in the bulk of the interferometer. This accords with our assumption that the quantum Hall system is well screened by nearby gates. If this is not the case, the slope $|d\varphi/d\tilde{V}|$ may be reduced below the value $2ea/(\hbar v_{\rm o})$.

From the analysis of the previous section, we obtain for the outer mode

$$\tilde{I} = \frac{4e}{\hbar^2}|\Gamma_1||\Gamma_2| \int_{-\infty}^{\infty} dt \sin(\omega_J t)\, \mathrm{Im}\, P_{\rm o}(-t, a). \tag{3.60}$$

Now, if we perform the Fourier transform of (3.58) with respect to φ, the amplitude $\mathcal{A}$ is

$$\mathcal{A} = \left[\left(\frac{d\tilde{I}}{dV}\right)^2 + \left(\eta \frac{d\varphi}{d\tilde{V}}\tilde{I}\right)^2\right]^{\frac{1}{2}}. \tag{3.61}$$

3.3 Results for $\nu = 2$ QH liquids

In this section, we discuss our numerical results for $\nu = 2$ QH liquids, where $\nu_1 = \nu_2 = 1$, and concentrate on the outer mode tunneling as shown in Fig. 3.1(b). We start with the case when the charge, confined by the inner loop, is time-independent. We first consider an easier problem of symmetrically applied bias. We next address asymmetric bias. We discuss non-linear transport in the regime of fluctuating charge on the inner island in subsection 3.3.3. Note that the results of subsections 3.3.2 apply in the linear transport regime, even if the tunneling amplitude between co-propagating modes is not negligible, since at low temperatures, in the linear regime, the charge of the inner loop does not fluctuate.

3.3.1 Inner mode tunneling

We first briefly discuss the inner mode tunneling case for $\nu = 2$ interferometers. In this case, the bulk would not form a closed island, and the linearity of φ over $\tilde{V}$ always holds, so that

$$\frac{d\varphi}{d\tilde{V}} = -\frac{2ea(v_{\rm o} - w)}{\hbar(v_{\rm i}v_{\rm o} - w^2)} = -\frac{2ea}{\hbar v_1}. \tag{3.62}$$

To derive this equation one needs to remember that the same bias is applied to all open channels. The Fourier amplitude of the interference contribution to the conductance is thus given by Eq. (3.61). If we plot the Fourier amplitude curves for different choices of asymmetry factor η in Fig. 3.3, we can see that asymmetrically applied voltage bias lifts the curve.

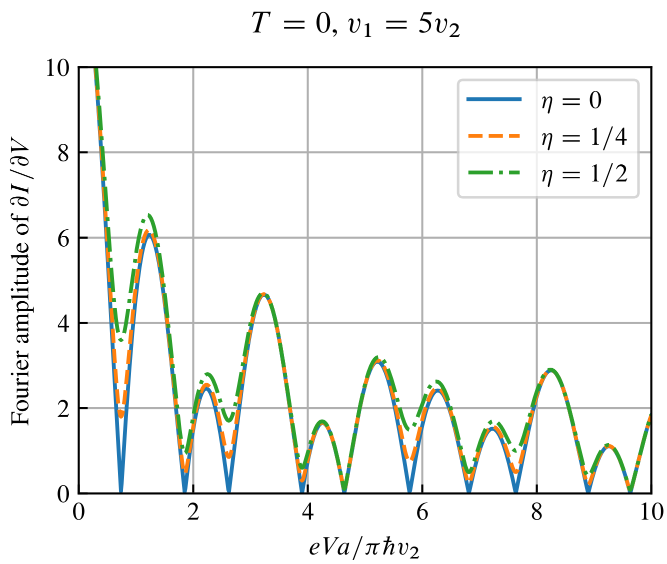

Figure 3.3: Inner mode tunneling at $\nu = 2$. Fourier amplitudes $\mathcal{A}$ of the differential conductance $\partial I/\partial V$ with different choices of η are plotted. The ratio between the faster and slower velocities of the normal modes is fixed at $v_1 = 5v_2$, and the temperature $T = 0$.

3.3.2 Outer mode tunneling: fixed island charge

Here we ignore tunneling between the inner and outer edge channels and hence assume a fixed charge of the inner closed loop. We start with the simplest limit of the symmetric voltage bias. In that case $\tilde{V} = 0$ in Eq. (3.45). The Fourier transform of the current with respect to the control parameter λ_1, Eq. (3.45), is trivial and essentially reduces to computing $\tilde{I}$.

Since $v_{\rm o} \approx v_{\rm i}$ due to the approximate symmetry of the spin-up and -down channels, the edge is in the strong interaction regime, i.e., $\theta = \pi/4$. The interaction strength w is reflected in the normal-mode velocities $v_{1,2}$, where v_1 is the velocity of the charged mode and v_2 is the much slower velocity of the neutral mode. A related problem was considered in Ref. [51] in the limit of an infinite velocity of the charged mode. This limit is problematic from the point of view of locality

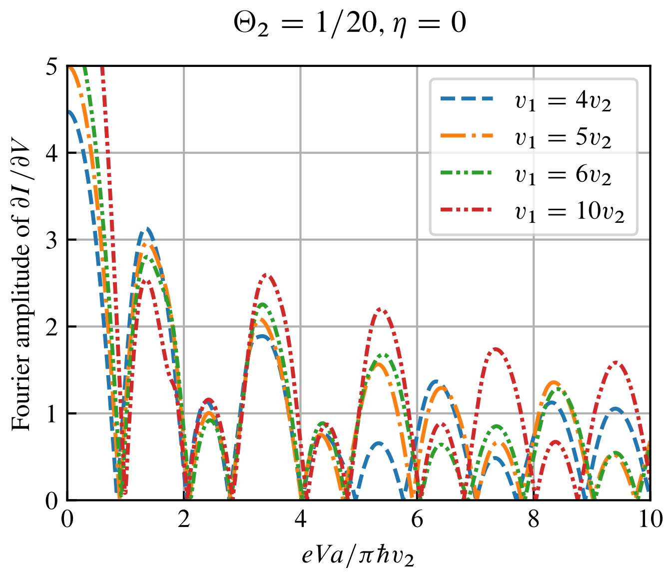

Figure 3.4: Outer mode tunneling at $\nu = 2$ at a fixed island charge. The plots show the dependence of the Fourier amplitude of the conductance on the voltage bias at different velocity ratios when the bias voltage is applied symmetrically. The temperature is represented with a dimensionless quantity $\Theta_2 = Ta/\hbar v_2$, and is fixed at $\Theta_2 = 1/20$.

since all events are causally related in a system with an infinite velocity of excitations. Ref. [51] focuses on zero temperature only and contains no plots of the voltage dependence of the interference current. Such plots are the main focus of this section, where we also address finite temperatures. In subsection 3.3.1 we also address the asymmetry of the voltage bias.

One of the experimentally measured quantities is the Fourier amplitude with respect to the Aharonov–Bohm (AB) phase φ_{AB} of the differential conductance dI/dV. We shall concentrate on that quantity, since it was the focus of recent experimental work [75, 76] at $\nu = 2$ and $\nu = 2/5$. This AB phase is introduced into the current through the phases of the tunneling amplitudes, hence, only the interference current shows the AB oscillations. The results of calculations along the lines of Section 3.2.4 and Appendix J are illustrated in Fig. 3.4. Note a series of nodes with the distance of roughly π in units of $eVa/\hbar v_2$. This corresponds to $eV = 2\pi\hbar v_2/2a$, where $2a$ is the perimeter of the interferometer, that is, to the lowest excitation energy on the loop of length $2a$ (v_2 is considerably slower than v_1).

Experiments in graphene were performed at a highly asymmetric voltage bias. This modifies the I–V curves as discussed in Section 3.2.6 and below.

Asymmetric bias

As above, linear dependence of the interference phase on the control parameters is assumed. Several plots of the Fourier amplitude at a finite temperature are shown in Fig. 3.5. In contrast to the $\nu = 1$

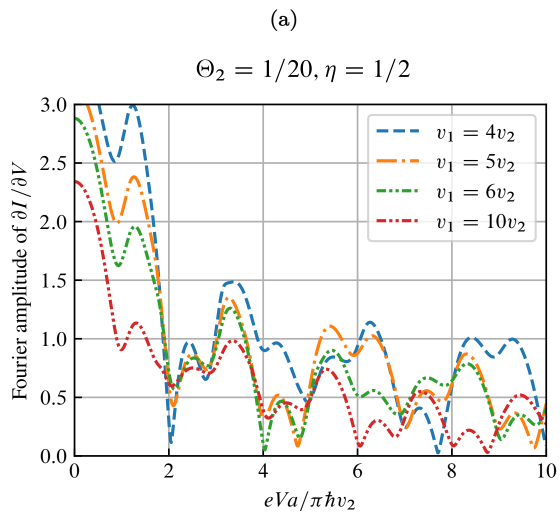

Figure 3.5: Outer mode tunneling at $\nu = 2$ at a fixed island charge. The plots show the dependence of the Fourier amplitude $\mathcal{A}$, Eq. (3.61), on the voltage bias at a finite temperature when the bias voltage is applied asymmetrically. The temperature is represented with a dimensionless quantity $\Theta_2 = Ta/\hbar v_2$, and is fixed at $\Theta_2 = 1/20$. (a) Fourier amplitude curves at different velocity ratios. (b) The ratio between the faster and slower velocities of the normal modes is fixed at $v_1 = 5v_2$, and Fourier amplitude curves with different choices of η are plotted.

interferometer (see Ref. [35]), where

$$\tilde{I} = \frac{e}{\hbar^3}(\Gamma_1\Gamma_2^* + \Gamma_1^*\Gamma_2)\frac{4\pi^2 T}{\sinh(2\pi Ta/\hbar v)}\sin(\omega_J a/v), \tag{3.63}$$

these curves are no longer periodic in the voltage. When the asymmetry η and bias voltage V are both small, the Fourier amplitude is close to $d\tilde{I}/dV$, which represents the differential conductance at $\varphi_{\text{AB}} = 0$. When η is greater, the values of the Fourier amplitude at the nodes increase and are non-zero, but the positions of the first few minima are relatively unchanged.

Even though no periodicity is seen, the plots exhibit a series of nodes whose distance is roughly π in units of $eVa/\hbar v_2$ just like in the symmetric case. This corresponds to $eV = 2\pi\hbar v_2/2a$, where $2a$ is the perimeter of the interferometer. This is the lowest excitation energy on the loop of length $2a$ as we already saw in subsection 3.3.2. The plots show the absolute value of the Fourier amplitude. It is thus natural to associate the effective period with twice the distance between successive nodes. We then discover approximately the same period as in Eq. (3.63) at $v = v_2$.

The above results apply in the weak backscattering regime. A perturbative calculation is insufficient for stronger tunneling. Note that for Fabry–Pérot interferometers, an exact solution is known at $\nu = 1$ [35]. This solution only works in the absence of inter-channel interaction near QPCs. We review the solution in Section 3.6 and also discuss the heating effect due to interactions across QPCs.

3.3.3 Outer mode tunneling: fluctuating island charge

We present here results for the current, averaged over phase fluctuations. Since we only solved the kinetic problem at zero temperature, the results apply only at low temperatures. At the same time, we consider an arbitrary voltage bias. We expect that the interference contribution to the current is suppressed by both high temperatures and high voltages, and the voltage and temperature effects should be comparable at $T \sim eV$.

The current follows equation (3.44) with the averaged phase factor (3.50). Motivated by the usual way to present experimental data, we focus on the Fourier transform of the conductance with respect to a control parameter λ_1 such as the magnetic field. Technical details of the Fourier transform can be found in Appendix M.

We now show results for several choices of the parameters in Fig. 3.6. We plot the voltage dependence of one prominent Fourier harmonic with respect to λ_1. In all cases we choose the harmonic of frequency α_1, Eq. (3.50). This is a natural choice since $\alpha_1\lambda_1$ should be understood as the a naive Aharonov–Bohm phase $2\pi\Phi/\Phi_0$, where Φ is the magnetic flux through the nominal area of the device and Φ_0 is a flux quantum. This choice also corresponds to $m = 0$ in Appendix M. As discussed in that appendix, dominant harmonics correspond to small m. They are also likely less sensitive to temperature effects. The value of β_1 (3.51,3.52) does not matter since it just rescales the plots. In all cases we set $T = 0$. The rest of the parameters are listed in the figures. The key difference from the case of the fixed island charge consists in a rapid decay of the signal at large V.

Another interesting feature is present at a discrete set of voltages. See, in particular, rectangular boxes and the inset in Fig. 3.6(c). One observes discontinuities in the Fourier amplitude of the conductance. Their origin is due to the tunneling between the outer modes and the inner island. As shown in Appendix K, the maximal and minimal electron numbers N_d and N_u on the inner loop equal $N_{d,u} = [g_{d,u}]$, where $g_{d,u}$ are given by Eqs. (K.10,K.11) and the square brackets denote the nearest integer. If $g_d - g_u = \beta_0 \frac{2v_o}{w}(V_d - V_u)$ is an integer, then the number $N_d - N_u + 1$ of the energy levels, available for transport between the outer edges through the inner loop, is exactly $g_d - g_u + 1$ irrespective of the flux λ_1 (see Appendix K). For non-integer $g_d - g_u$, the number of the available levels depends on the flux and varies between the largest integer less than $g_d - g_u + 1$ and the lowest integer greater than $g_d - g_u + 1$. In other words, the structure of the set of the available levels as a function of the flux changes at the integer values of $g_d - g_u$. This results in singularities in the Fourier transform with respect to λ_1 at

$$V = \frac{mw}{2\beta_0 v_o} \tag{3.64}$$

at each integer m. This feature can be used to extract the parameters of the edge theory from the data.

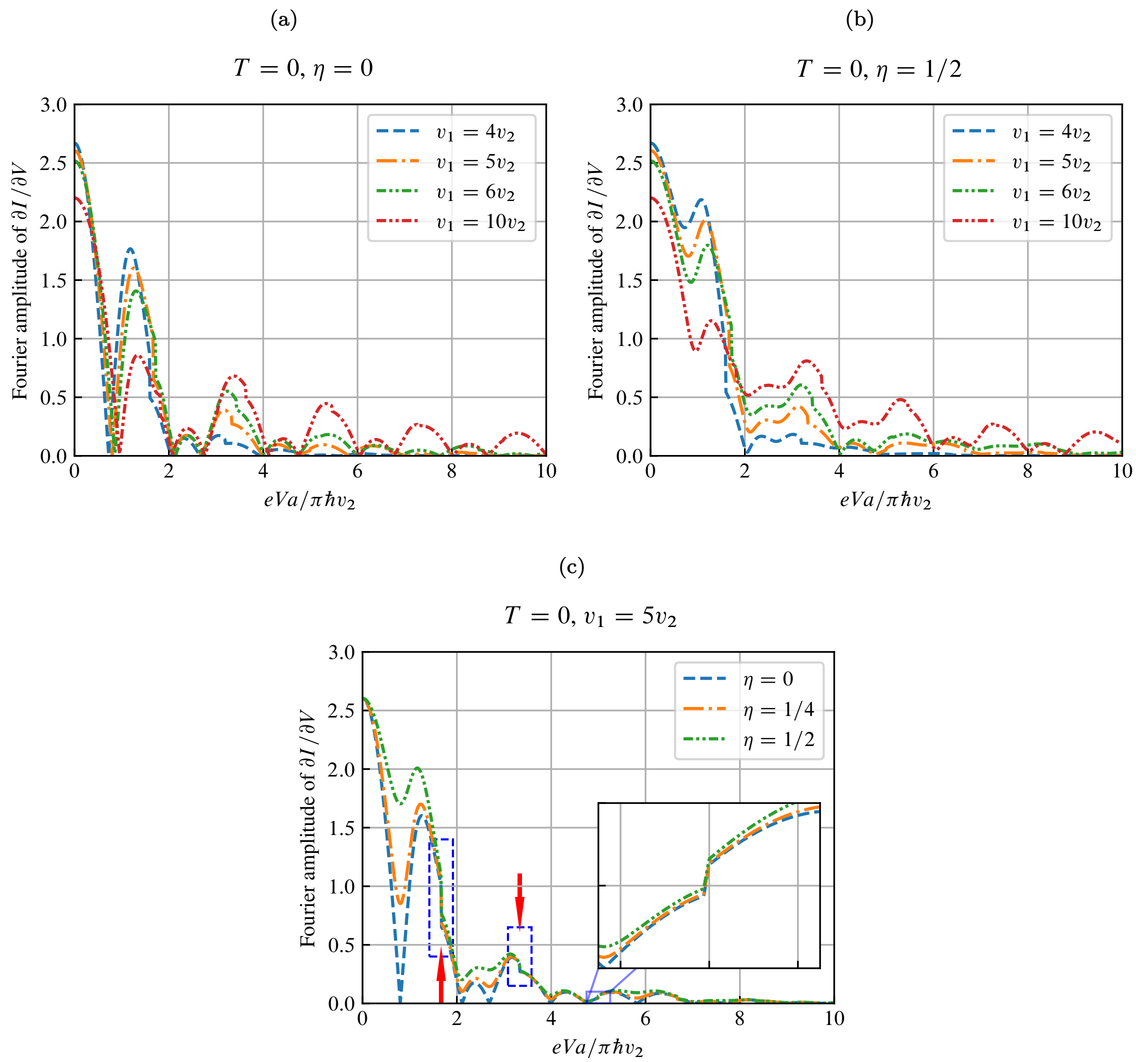

Figure 3.6: Outer mode tunneling in $\nu = 2$ interferometers for fluctuating island charge. (a) The dependence of the dominant Fourier amplitude on the voltage bias at zero temperature with a symmetric bias. (b) Fourier amplitude curves at different velocity ratios with a totally asymmetric bias. (c) The ratio between the faster and slower velocities of the normal modes is fixed at $v_1 = 5v_2$, and Fourier amplitude curves with different choices of η are plotted. Rectangular boxes and the inset show resonance features due to tunneling between co-propagating modes.

3.4 Results for $\nu = 2/5$ FQH liquids

In this section, we consider the interferometer in Fig. 3.1 for $\nu = 2/5$ QH liquids, where $\nu_1 = 1/3$ and $\nu_2 = 1/15$. We only study the case of symmetric voltage bias since the bias was applied symmetrically in the relevant experiment [75].

3.4.1 Inner mode tunneling

For the inner mode tunneling, we numerically computed the differential conductance of the interference current, and the results are shown in Figs. 3.7 and 3.8. In Fig. 3.7, we plot the voltage dependence of the Fourier amplitude of the interference contribution to the conductance with respect to the magnetic flux at a weak coupling $\theta = \pi/16$. One can observe that the location of the first node depends on the temperature, while the locations of the subsequent nodes show little temperature dependence.

It is instructive to compare the low-voltage, low-temperature limit with the same limit at $\nu = 1/3$. In the latter case the tunneling current follows $I \sim V^{2\times 1/3-1} = V^{-1/3}$ so that the current grows at low voltages. This is no longer the case at $\nu = 2/5$, where the low-voltage current follows the relation $I \sim V^{2\times 3/5-1} = V^{1/5}$. Of course, the perturbation theory only applies as long as the conductance $G \sim V^{-4/5}$ remains small.

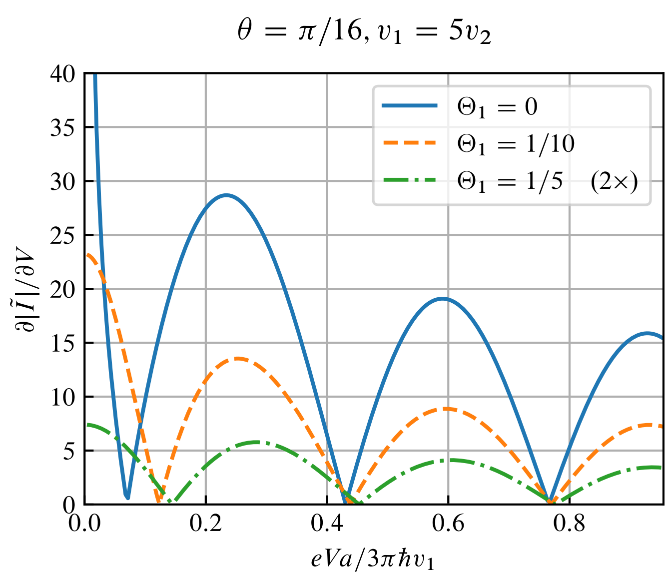

Figure 3.7: Inner mode tunneling at $\nu = 2/5$. The dependence of the Fourier amplitude of the differential conductance of the interference current on the voltage bias is shown at different temperatures, with $\theta = \pi/16$ and $v_1 = 5v_2$. Θ_1 is the dimensionless temperature $Ta/\hbar v_1$.

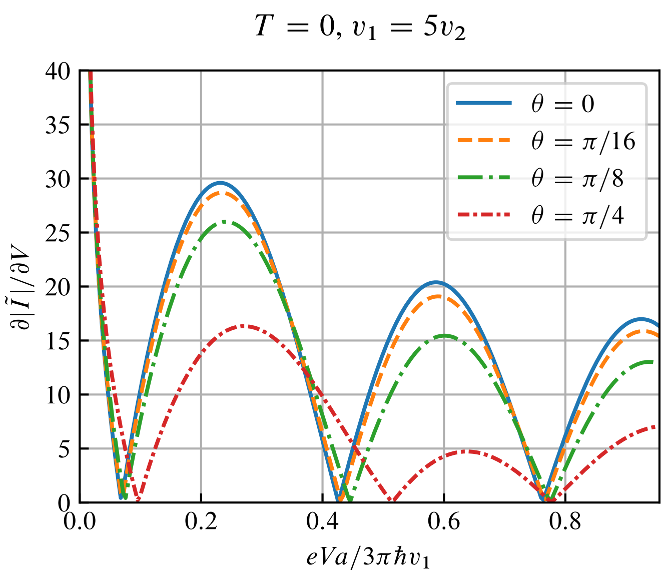

Figure 3.8: Inner mode tunneling at $\nu = 2/5$. The dependence of the Fourier amplitude of the conductance on the voltage bias is shown at different interaction strengths (represented with θ), with $v_1 = 5v_2$ and $T = 0$.

3.4.2 Outer mode tunneling

Fixed island charge

In this limit the charge of the inner closed loop is assumed to be independent of the voltage bias and the magnetic flux. We also assume a symmetric application of the voltage bias. It is then straightforward to plot the Fourier transform of the interference contribution ot the conductance with respect to the magnetic flux.

Figs. 3.9 and 3.10 show numerical results for the differential conductance of the interference current, with $\theta = \pi/16$ and $v_1 = 5v_2$. Immediately, one can notice a striking feature of resonance in these curves when the temperature is low enough.

The first resonance occurs when $eVa/3\hbar v_1 \approx \pi/5$, therefore $\hbar\omega_J \equiv \frac{e}{3}V \approx \pi\hbar v_1/(5a) = \pi\hbar v_2/a$. This reminds us of the energy levels of a closed edge mode $E_n = 2\pi\hbar n v/L$, where n is an integer, v is the edge velocity, and L is the circumference of the edge. Therefore, the resonance occurs when the Josephson energy $\hbar\omega_J$ of the tunneling quasiparticle matches the energy levels of plasmons on the inner mode, which are $n\hbar\pi v_2/a$. As can be seen from Fig. 3.9, there is a second resonance when $eVa/3\hbar v_1 \approx 2\pi/5$, in agreement with this picture. One can also check what happens when we change the ratio between v_1 and v_2, and the plots are shown in Fig. 3.10. When the ratio v_1/v_2 gets larger, the resonance occurs at a smaller value of $eVa/3\hbar v_1$. All these findings are consistent with our interpretation.

There is one issue in our argument: one can treat the closed inner $1/15$ mode as an eigenmode only in the weak interaction limit. To find out what happens in the strong interaction limit, we show

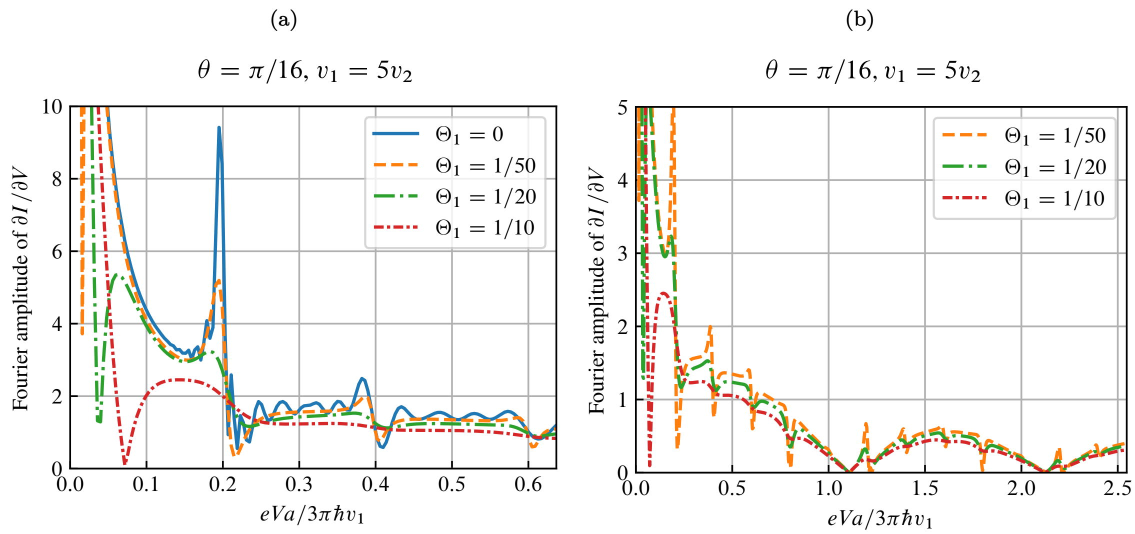

Figure 3.9: Outer mode tunneling at $\nu = 2/5$ at a fixed island charge. The Fourier amplitude of the interference contribution to the conductance is shown at different temperatures, with $\theta = \pi/16$, $v_1 = 5v_2$, and $\Theta_1 = Ta/\hbar v_1$. (a) A zoom-in view of the conductance curve for a better visualization of the first few resonances. (b) The conductance curve over a wider range, showing the modulation due to the outer mode.

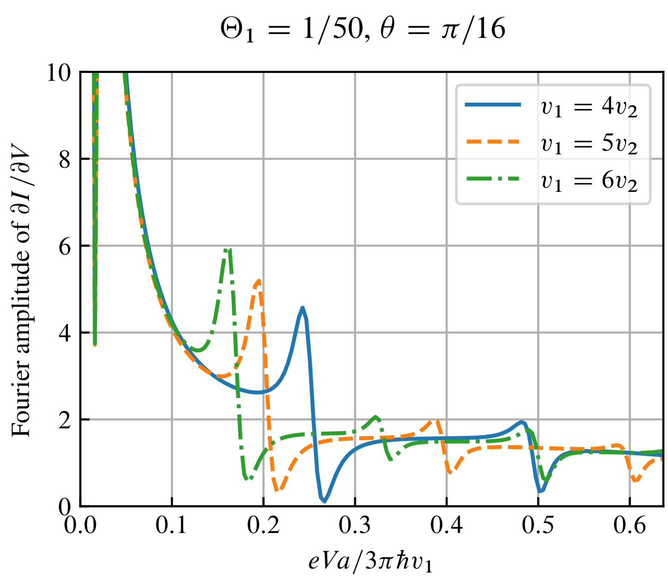

Figure 3.10: Outer mode tunneling at $\nu = 2/5$ at a fixed island charge. Comparison of Fourier amplitudes of the differential conductance $\partial I/\partial V$ for different velocity ratios v_1/v_2, with $\theta = \pi/16$ and $\Theta_1 = Ta/\hbar v_1 = 1/50$.

conductance curves at different θ in Fig. 3.11. Clearly, resonance is suppressed at strong interactions.

We give a theory of the resonance feature in the above plots in Appendix N. We find that at a

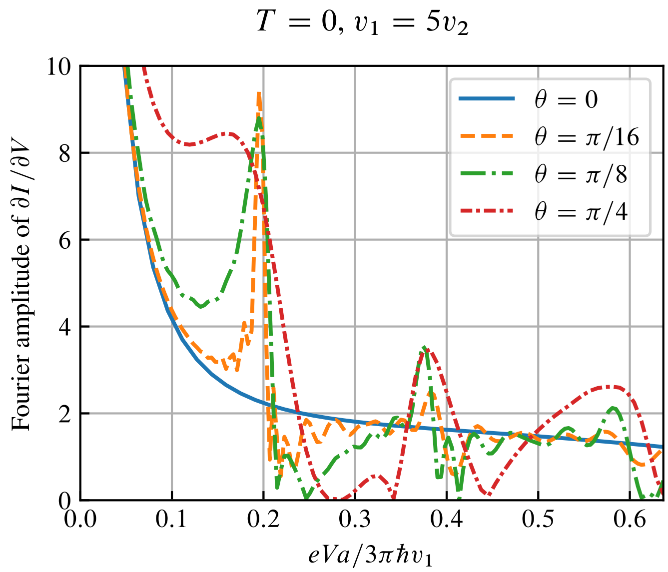

Figure 3.11: Outer mode tunneling at $\nu = 2/5$ at a fixed island charge. The Fourier amplitude of the differential conductance $\partial I/\partial V$ of the interference current is shown for different θ, with $v_1 = 5v_2$ and $T = 0$.

weak interaction θ and zero temperature, the width of the resonance scales as θ^2 and it height as $\theta^{-2/3}$.

Fluctuating island charge

Just like at $\nu = 2$, our analysis builds on the case of a fixed island charge and involves averaging the Aharonov–Bohm phase factor over the distribution of the charge of the inner loop. We use the results of Section II and the Fourier expansion from Appendix M. As at $\nu = 2$, our results apply only at low temperatures, and they are illustrated in Fig. 3.12 and 3.13. We plot one prominent Fourier harmonic with respect to the magnetic field λ_1. As at $\nu = 2$ we focus on zero temperature and chose the harmonic of frequency α_1. This corresponds to the $m = 0$ harmonic from Appendix M and is a natural choice since $\alpha_1\lambda_1$ can be understood as the naive Aharonov–Bohm phase $2\pi\Phi/3\Phi_0$, where Φ is the magnetic flux through the nominal area of the device and Φ_0 is the flux quantum. The value of β_1 does not matter since it only sets the scale of the vertical axis.

In contrast to $\nu = 2$, we see two types of resonance features in the conductance: the resonance from plasmon scattering, addressed in subsection 3.4.2, and the resonance from inter-mode tunneling, similar to the one discussed in Section 3.3 at $\nu = 2$. The plasmon resonance manifests itself as a sharp maximum with a nearby minimum on the curve. The inter-mode tunneling resonance is seen as a sharp drop on the curve at $eVa/3\pi\hbar v_1 \approx 0.4$. There are also discontinuities of the Fourier amplitude of the conductance at other voltages. Their locations can be deduced in the same way as Eq. (3.64) using the modified definitions of $g_{d,u}$ from the $\nu = 2/5$ subsection of Appendix K. One finds

$$V = m\frac{\nu_1 w}{2\nu_2\beta_0 v_o}, \tag{3.65}$$

where m is an integer, $\nu_1 = 1/3$, and $\nu_2 = 1/15$. As at $\nu = 2$, resonances allow extracting the parameters of the edge theory from the data.

Another important feature is a rapid decay of the current at a high voltage. As at $\nu = 2$, this is a manifestation of the long-time fluctuations of the Aharonov–Bohm phase due to the fluctuations of the charge on the inner loop. Note a similarity of the red curve in Fig. 3.13 with the red curve for a fixed island charge in Fig. 3.11. It reveals little suppression of interference by the fluctuations of the island charge. The reason is that γ in Eq. (3.53) is relatively close to 0 at $\theta = \pi/4$ and $v_1 = 5v_2$.

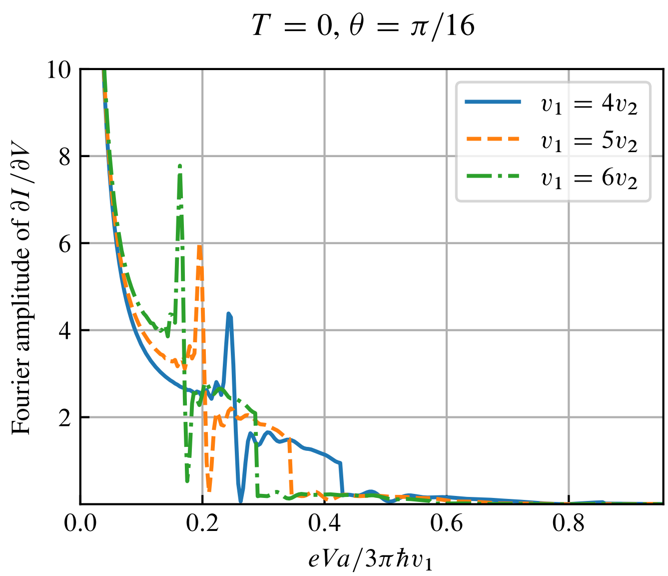

Figure 3.12: Outer mode tunneling at $\nu = 2/5$ for fluctuating island charge. The dominant Fourier amplitude of the differential conductance $\partial I/\partial V$ of the interference current is shown for different velocity ratios v_1/v_2, with $\theta = \pi/16$ and $T = 0$.

3.5 Effects of a screening layer on $\nu = 2/5$ FQH liquid

The key to the breakthrough interferometry experiment [70] were screening layers greatly suppressing bulk-edge interaction. A screening layer has a finite σ_{xx} and hence can be modeled as a metal plane in the low-frequency regime. This seems to justify the model of short range interaction on the edges of the 2D electron gas. However, one should remember that the low frequency description is only valid for slow processes such as the change of the charge localized in the bulk of the sample. A high-frequency language is necessary when addressing the intermode interaction on the edges since the relevant time is the time spent by edge charges in the interferometer. This time is controlled

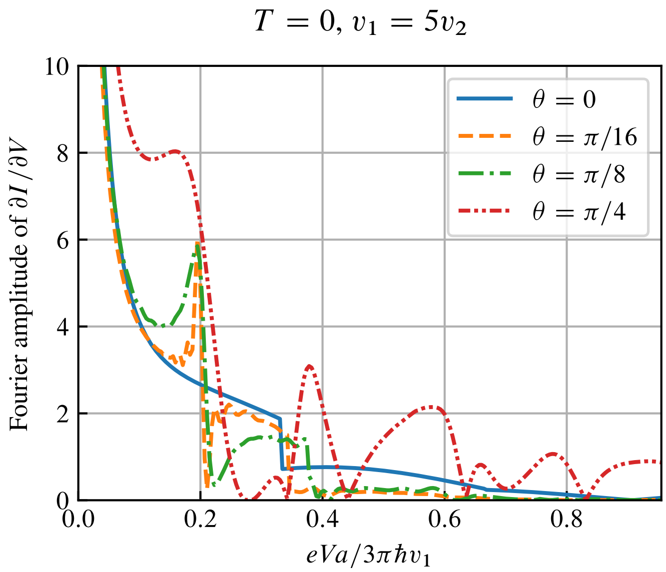

Figure 3.13: Outer mode tunneling at $\nu = 2/5$ for fluctuating island charge. The dominant Fourier amplitude of the differential conductance $\partial I/\partial V$ of the interference current is shown for different θ, with $v_1 = 5v_2$ and $T = 0$.

by the edge velocity and the mesoscopic interferometer size. Since σ_{xx} is orders of magnitude lower than σ_{xy} in the screening layers [100], it is legitimate to neglect σ_{xx} in the high-frequency regime.

This means that the screening layers should be modeled in the same way as quantum Hall edges, that is, by a chiral Luttinger liquid model. For simplicity, we only consider a model with a single screening layer and a single chiral channel in it. Strictly speaking, such model must include long-range interactions between the two edge modes of the 2D electron gas and the edge mode of the screening layer. This results in the renormalization of the velocity of the overall charged mode. The renormalization, however, depends on the edge length only logarithmically. For that reason, we will assume short range interactions and set the speed of the overall charged mode to be much greater than all other edge-mode velocities.

In this section we only focus on $\nu = 2/5$.

3.5.1 Edge structure

We start with the original Lagrangian $L_0 = L + L_e$ with two eigenmodes, ϕ_1 and ϕ_2,

$$L_0 = \frac{\hbar(\partial_x\phi_1)(\partial_t\phi_1 - v_1\partial_x\phi_1)}{4\pi} + \frac{\hbar(\partial_x\phi_2)(\partial_t\phi_2 - v_2\partial_x\phi_2)}{4\pi} \tag{3.66}$$

Since the Coulomb interaction couples to the total charge of the $2/5$ edge, it is better to use the charge and neutral modes. The definitions of the charge and neutral modes, ϕ_c and ϕ_n, are

$$\begin{pmatrix}\phi_c\\ \phi_n\end{pmatrix} = \begin{pmatrix}\sqrt{\frac{5}{6}} & \frac{1}{\sqrt{6}}\\ \frac{1}{\sqrt{6}} & -\sqrt{\frac{5}{6}}\end{pmatrix}\begin{pmatrix}\phi_{\mathrm{o}}\\ \phi_{\mathrm{i}}\end{pmatrix}. \tag{3.67}$$

Under this transformation,

$$L_0 = \frac{\hbar}{4\pi}\begin{pmatrix}\partial_x\phi_c\partial_x\phi_n\end{pmatrix}\begin{pmatrix}\partial_t\phi_c\\ \partial_t\phi_n\end{pmatrix} - \frac{\hbar}{4\pi}\begin{pmatrix}\partial_x\phi_c & \partial_x\phi_n\end{pmatrix}\begin{pmatrix}v_c & U_{cn}\\ U_{cn} & v_n\end{pmatrix}\begin{pmatrix}\partial_x\phi_c\\ \partial_x\phi_n\end{pmatrix}, \tag{3.68}$$

where

$$v_c = \frac{1}{6}\big[\sqrt{5}\sin(2\theta)(v_1 - v_2) + 2\cos(2\theta)(v_1 - v_2) + 3(v_1 + v_2)\big], \tag{3.69}$$

$$U_{cn} = \frac{1}{6}(v_1 - v_2)\big[-2\sin(2\theta) + \sqrt{5}\cos(2\theta)\big], \tag{3.70}$$

$$v_n = \frac{1}{6}\big[-\sqrt{5}\sin(2\theta)(v_1 - v_2) - 2\cos(2\theta)(v_1 - v_2) + 3(v_1 + v_2)\big]. \tag{3.71}$$

We model the additional screening layer as a $\nu = 1$ QH liquid, and its edge mode ϕ_s interacts with the charge mode ϕ_c of the $\nu = 2/5$ FQH liquid via Coulomb interaction, hence bringing an extra term to the Lagrangian,

$$L_1 = \frac{\hbar}{4\pi}[(\partial_x\phi_s)(\partial_t - v_s\partial_x)\phi_s - 2U(\partial_x\phi_c)(\partial_x\phi_s)], \tag{3.72}$$

where v_s is the velocity of the edge mode of the screening layer, and $U > 0$ describes the strength of the Coulomb interaction.

Now we rewrite the total Lagrangian $L_0 + L_1$ as $L_{cs} + L_n$, where L_{cs} describes the contribution that depends on ϕ_c and ϕ_s only,

$$L_{cs} = \frac{\hbar}{4\pi}[(\partial_x\phi_c)(\partial_t\phi_c) + (\partial_x\phi_s)(\partial_t\phi_s)] - \frac{\hbar}{4\pi}\begin{pmatrix}\partial_x\phi_c & \partial_x\phi_s\end{pmatrix}\begin{pmatrix}v_c & U\\ U & v_s\end{pmatrix}\begin{pmatrix}\partial_x\phi_c\\ \partial_x\phi_s\end{pmatrix}, \tag{3.73}$$

and L_n contains the interaction energy associated with ϕ_n,

$$L_n = \frac{\hbar}{4\pi}[(\partial_x\phi_n)(\partial_t - v_n\partial_x)\phi_n - 2U_{cn}(\partial_x\phi_c)(\partial_x\phi_n)]. \tag{3.74}$$

Next, we define the overall charge mode ϕ_ρ and a neutral mode ϕ_σ by transforming the modes ϕ_c and ϕ_s,

$$\begin{pmatrix}\phi_\rho\\ \phi_\sigma\end{pmatrix} = \begin{pmatrix}\sqrt{\frac{2}{7}} & \sqrt{\frac{5}{7}}\\ \sqrt{\frac{5}{7}} & -\sqrt{\frac{2}{7}}\end{pmatrix}\begin{pmatrix}\phi_c\\ \phi_s\end{pmatrix}. \tag{3.75}$$

After the transformation, L_{cs} is expressed using ϕ_ρ and ϕ_σ,

$$L_{cs} = \frac{\hbar}{4\pi}\begin{pmatrix}\partial_x\phi_\rho & \partial_x\phi_\sigma\end{pmatrix}\begin{pmatrix}\partial_t\phi_\rho\\ \partial_t\phi_\sigma\end{pmatrix} - \frac{\hbar}{4\pi}\begin{pmatrix}\partial_x\phi_\rho & \partial_x\phi_\sigma\end{pmatrix}\begin{pmatrix}v_\rho & U_{\rho\sigma}\\ U_{\rho\sigma} & v_\sigma\end{pmatrix}\begin{pmatrix}\partial_x\phi_\rho\\ \partial_x\phi_\sigma\end{pmatrix}, \tag{3.76}$$

where

$$v_\rho = \frac{1}{7}(2\sqrt{10}U + 5v_s + 2v_c), \tag{3.77}$$

$$U_{\rho\sigma} = \frac{1}{7}(3U - \sqrt{10}v_s + \sqrt{10}v_c), \tag{3.78}$$

$$v_\sigma = \frac{1}{7}(-2\sqrt{10}U + 2v_s + 5v_c). \tag{3.79}$$

L_n becomes

$$L_n = \frac{\hbar}{4\pi}\Big[(\partial_x\phi_n)(\partial_t - v_n\partial_x)\phi_n - 2\sqrt{\frac{2}{7}}U_{cn}(\partial_x\phi_\rho)(\partial_x\phi_n) - 2\sqrt{\frac{5}{7}}U_{cn}(\partial_x\phi_\sigma)(\partial_x\phi_n)\Big]. \tag{3.80}$$

We expect that the velocity of the overall charge mode ϕ_ρ is much greater than the velocities of the two neutral modes. Therefore, we can make an approximation when finding the eigenmodes: to the lowest order, we treat ϕ_ρ as one of the eigenmodes and ignore the interaction between ϕ_ρ and ϕ_n, as well as the interaction between ϕ_ρ and ϕ_σ. Hence, the total Lagrangian can be rewritten as

$$\begin{aligned} L_{cs} + L_n = \frac{\hbar}{4\pi}\Big[&(\partial_x\phi_\rho)(\partial_t - v_\rho\partial_x)\phi_\rho + (\partial_x\phi_\sigma)(\partial_t - v_\sigma\partial_x)\phi_\sigma \\ &+ (\partial_x\phi_n)(\partial_t - v_n\partial_x)\phi_n - 2U_{\sigma n}(\partial_x\phi_\sigma)(\partial_x\phi_n)\Big], \end{aligned} \tag{3.81}$$

where $U_{\sigma n} = \sqrt{5/7}U_{cn}$.

We need another parameter ψ to diagonalize the interaction matrix between ϕ_σ and ϕ_n. The transformation is given by

$$\begin{pmatrix}\phi_\sigma \\ \phi_n\end{pmatrix} = \begin{pmatrix}\cos\psi & -\sin\psi \\ \sin\psi & \cos\psi\end{pmatrix}\begin{pmatrix}\phi_a \\ \phi_b\end{pmatrix}. \tag{3.82}$$

If we assume $v_n < v_\sigma$ and $0 < 2\psi < \pi/2$, then

$$\tan(2\psi) = \frac{2U_{\sigma n}}{v_\sigma - v_n}, \tag{3.83}$$

and the eigenmode velocities are

$$v_a = \frac{1}{2}(v_\sigma + v_n + \sqrt{(v_\sigma - v_n)^2 + 4U_{\sigma n}^2}), \tag{3.84}$$

$$v_b = \frac{1}{2}(v_\sigma + v_n - \sqrt{(v_\sigma - v_n)^2 + 4U_{\sigma n}^2}). \tag{3.85}$$

Finally, a relation between the eigenmodes (ϕ_ρ, ϕ_a and ϕ_b) and the original modes ($\phi_{\rm o}$, $\phi_{\rm i}$, and ϕ_s) can be represented as

$$\begin{pmatrix}\phi_{\rm o} \\ \phi_{\rm i} \\ \phi_s\end{pmatrix} = M\begin{pmatrix}\phi_\rho \\ \phi_a \\ \phi_b\end{pmatrix}, \tag{3.86}$$

where the matrix M is

$$\begin{pmatrix} \sqrt{\frac{5}{21}} & \frac{\sin\psi}{\sqrt{6}} + \frac{5\cos\psi}{\sqrt{42}} & \frac{\cos\psi}{\sqrt{6}} - \frac{5\sin\psi}{\sqrt{42}} \\ \frac{1}{\sqrt{21}} & \sqrt{\frac{5}{42}}\cos\psi - \sqrt{\frac{5}{6}}\sin\psi & -\sqrt{\frac{5}{6}}\cos\psi - \sqrt{\frac{5}{42}}\sin\psi \\ \sqrt{\frac{5}{7}} & -\sqrt{\frac{2}{7}}\cos\psi & \sqrt{\frac{2}{7}}\sin\psi \end{pmatrix}. \tag{3.87}$$

3.5.2 Inner mode tunneling

For $\nu = 2/5$, quasiparticles with charge $e^* = e/5$ tunnel between the inner edge channels, and the tunneling operator $\hat{T}$ should be written as

$$\hat{T}(t,x) = \delta^{-3/5}e^{3i\phi_{\rm i}^u(t,x)/\sqrt{15}}e^{-3i\phi_{\rm i}^d(t,x)/\sqrt{15}}. \tag{3.88}$$

Using standard formulas for correlation functions of Bose fields, it is easy to find that at zero temperature,

$$P_{\mathrm{i}}(t,x) = G_d(t,x)G_u(t,x), \tag{3.89}$$

where

$$G_{d,u}(t,x) = [\delta + i(t \mp x/v_\rho)]^{-g_\rho}[\delta + i(t \mp x/v_\sigma)]^{-g_a}[\delta + i(t \mp x/v_c)]^{-g_b}, \tag{3.90}$$

and the three exponents are

$$g_\rho = \frac{3M_{21}^2}{5} = \frac{1}{35}, \tag{3.91}$$

$$g_a = \frac{3M_{22}^2}{5} = \left(-\frac{\sin\psi}{\sqrt{2}} + \frac{\cos\psi}{\sqrt{14}}\right)^2, \tag{3.92}$$

$$g_b = \frac{3M_{23}^2}{5} = \left(\frac{\sin\psi}{\sqrt{14}} + \frac{\cos\psi}{\sqrt{2}}\right)^2. \tag{3.93}$$

A conformal transformation yields the correlation function at a finite temperature (cf. Eq. (3.20)).

Fig. 3.14 shows the interference contribution to the nonlinear conductance as a function of the voltage. The figure reveals remarkably regular oscillations for the chosen parameters. This reflects a general rule that outer mode tunneling behaves in a simpler way than inner mode tunneling.

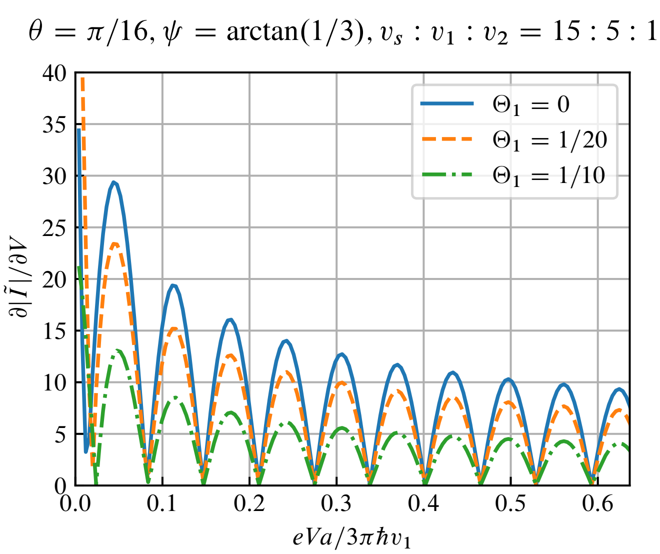

Figure 3.14: Inner mode tunneling at $\nu = 2/5$ with a screening layer. The Fourier amplitude of the differential conductance of the interference current is shown for different temperatures. Parameters are chosen as $\theta = \pi/16$, $\psi = \arctan(1/3)$, and $v_s = 3v_1 = 15v_2$. The dimensionless temperature $\Theta_1 = Ta/\hbar v_1$.

3.5.3 Outer mode tunneling

In this section, we discuss outer mode tunneling for $\nu = 2/5$, where $e^* = e/3$ and $\hat{T}(t,x) = \delta^{-1/3} e^{i\phi_{\mathrm{o}}^u(t,x)/\sqrt{3}} e^{-i\phi_{\mathrm{o}}^d(t,x)/\sqrt{3}}$ are used.

Fixed island charge

We first neglect tunneling between co-propagating modes and solve a scattering problem for bosons, similar to Section 3.2.4. We use this to compute the current on the short time scale, on which the fluctuations of the Aharonov–Bohm phase can be ignored. We assume a symmetrically applied bias.

We have six incoming edge modes and six outgoing ones. As before, the incoming and outgoing modes, separating the $\nu = 1/3$ and $\nu = 2/5$ liquids, drop out. Hence, scattering is described by a 4×4 matrix $\tilde{S}$, instead of a 2×2 matrix in Sec. 3.4.2,

$$\begin{pmatrix} \phi_{\mathrm{o}}^u(\omega, x_1) \\ \phi_s^u(\omega, x_1) \\ \phi_{\mathrm{o}}^d(\omega, x_2) \\ \phi_s^d(\omega, x_2) \end{pmatrix} = \tilde{S} \begin{pmatrix} \phi_{\mathrm{o}}^d(\omega, x_1) \\ \phi_s^d(\omega, x_1) \\ \phi_{\mathrm{o}}^u(\omega, x_2) \\ \phi_s^u(\omega, x_2) \end{pmatrix} \tag{3.94}$$

Again, we try to find the matrix $\tilde{S}$ by solving the propagation equations with boundary conditions. In the region between the two QPCs, due to interaction, the free-propagating fields are the eigenmodes ϕ_ρ, ϕ_a, and ϕ_b. They satisfy the following equations,

$$\phi_j^d(\omega, x_2) = e^{i\omega a/v_j} \phi_j^d(\omega, x_1), \tag{3.95}$$

$$\phi_j^u(\omega, x_2) = e^{-i\omega a/v_j} \phi_j^u(\omega, x_1), \tag{3.96}$$

with $j = \rho, a, b$. In addition, the closed loop should satisfy the continuity conditions at the positions of the QPCs, where the interaction is minimal,

$$\phi_{\mathrm{i}}^d(\omega, x_1) = \phi_{\mathrm{i}}^u(\omega, x_1), \tag{3.97}$$

$$\phi_{\mathrm{i}}^d(\omega, x_2) = \phi_{\mathrm{i}}^u(\omega, x_2). \tag{3.98}$$

Due to the complexity of the edge structure, the coefficients in the equations above are complicated, hence the expressions for the matrix elements of $\tilde{S}$ are not as simple as Eq. (3.29) and (3.30). Nevertheless, $\tilde{S}$ is also a unitary and symmetric matrix. It has some additional symmetries: $\tilde{S}_{11} = \tilde{S}_{33}$, $\tilde{S}_{22} = \tilde{S}_{33}$, $\tilde{S}_{12} = \tilde{S}_{34}$, and $\tilde{S}_{14} = \tilde{S}_{23}$. Some of these symmetries are consequences of the inversion symmetry of the device. In Appendix O, we show the expressions for $\tilde{S}_{11}$ and $\tilde{S}_{13}$, which are too complicated to be displayed here. These are the only matrix elements needed below.

Computing $\langle \hat{T}(t, x_1) \hat{T}^\dagger(0, x_1) \rangle$ gives

$$P_{\mathrm{o}}(t, 0) = \delta^{-2/3} \exp\Big\{ -\frac{1}{3} \int_0^\infty \frac{d\omega}{\omega} [2 - (\tilde{S}_{11} + \tilde{S}_{11}^*)](1 - e^{-i\omega t}) e^{-\omega\delta} \Big\}, \tag{3.99}$$

and computing $\langle \hat{T}(t, x_2) \hat{T}^\dagger(0, x_1) \rangle$ gives

$$P_{\mathrm{o}}(t, a) = \delta^{-2/3} \exp\Big\{ -\frac{1}{3} \int_0^\infty \frac{d\omega}{\omega} (2 - 2\tilde{S}_{11}^* - (\tilde{S}_{13} + \tilde{S}_{13}^*) e^{-i\omega t}) e^{-\omega\delta} \Big\}. \tag{3.100}$$

Now it is clear that of the six independent entries of $\tilde{S}$, only two, $\tilde{S}_{11}$ and $\tilde{S}_{13}$, are needed for computing the tunneling current. An example of such calculation is shown in Fig. 3.15. The zero temperature curve shows a remarkably complex behavior that greatly simplifies as the temperature is raised.

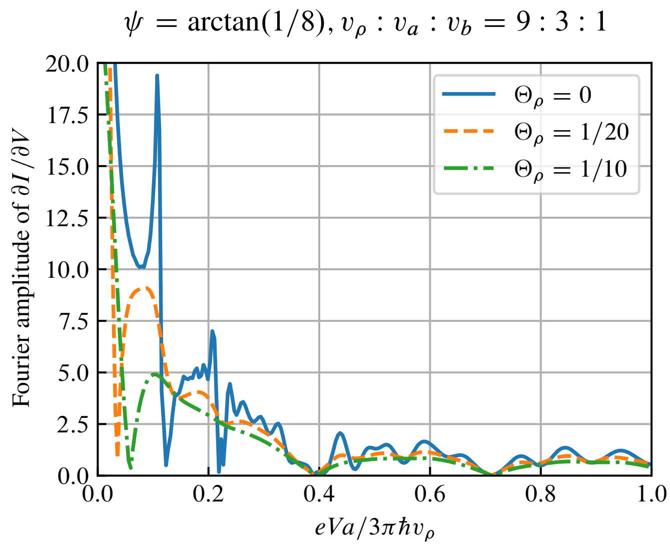

Figure 3.15: Outer mode tunneling at $\nu = 2/5$ with a screening layer at a fixed island charge. The Fourier amplitude of the differential conductance of the interference current is shown for different temperatures. Parameters are chosen as $\psi = \arctan(1/8)$, $v_\rho = 3v_a = 9v_b$. The dimensionless temperature $\Theta_\rho = Ta/\hbar v_\rho$.

Fluctuating island charge

The analysis closely follows the analysis of the long-time limit in the model of an ideal metallic screening layer without an additional chiral channel (Section 3.4). We use Green's functions from the previous subsection and the results of Appendix P, which addresses the minimum and maximum charges of the inner loop as functions of the bias. Fig. 3.16 shows an example of nonlinear transport behavior in this model at zero temperature. As in the previous sections, we do not care about the coefficient β_1 when we plot the Fourier transform with respect to the flux. We also only show the Fourier harmonics of frequency α_1, as in all previous plots for fluctuating island charge. One can see a complicated voltage dependence of the interference current. The dominant feature is the rapid decay at large voltages.

3.6 Fabry–Pérot interferometers at $\nu = 1$

The bulk of this chapter focuses on two-channel edge states. The one-channel case is much better understood theoretically. The simplest one-channel situation is the integer QH effect at $\nu = 1$.

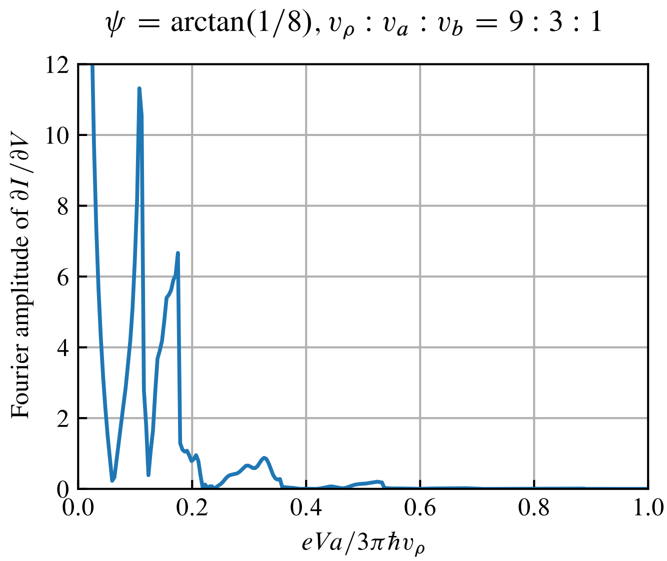

Figure 3.16: Outer mode tunneling at $\nu = 2/5$ with a screening layer for fluctuating island charge. The dominant Fourier amplitude of the differential conductance of the interference current is shown. Parameters are chosen as $\psi = \arctan(1/8)$, $v_\rho = 3v_a = 9v_b$, and $T = 0$.

At $\nu = 1$, the simplest model of an interferometer is just the model of free electrons. It can be easily solved exactly [35]. Recent experimental results for the non-linear I–V curve do not agree with the exact solution, however [76]. Instead, a rapid decrease of the current at high voltages is seen. This is similar to our predictions in the long-time limit in the two-channel problem, but the same physics cannot explain the experiment at $\nu = 1$ since there is no closed inner loop that could accommodate fluctuating charge. In fact, the charge in the localized states in the bulk of the interferometer fluctuates at a high voltage bias. However, localized quasiparticles generate no statistical phase since all quasiparticles are electrons. Their Coulomb field is efficiently screened by the top gate.

Instead, the explanation is likely due to Coulomb interactions between the counter-propagating edges across the point contacts. These are the regions, where the edges approach each other closely, and screening may be unable to suppress electrostatic forces. In this Section, we propose a model to account for that effect. Another crucial part of the explanation involves energy dissipation at the contacts. Such dissipation is irrelevant in the previous Sections since we assumed a low tunneling current. The experiments at $\nu = 1$, however, were performed in the regime of strong tunneling.

We start with a review of the exact solution in the absence of interactions. We consider right- and left-moving channels with the same velocity v. Consider first a single scatterer that allows electron tunneling between the channels. The scatterer is characterized by its reflection and transmission coefficients. The coefficients establish a relation between the incoming right- and left-moving waves ψ_{R-} and ψ_{L+} and the outgoing waves ψ_{R+} and ψ_{L-}. Similar to our approach to the two-channel problem, we consider waves of each frequency separately. A general relation between the incoming

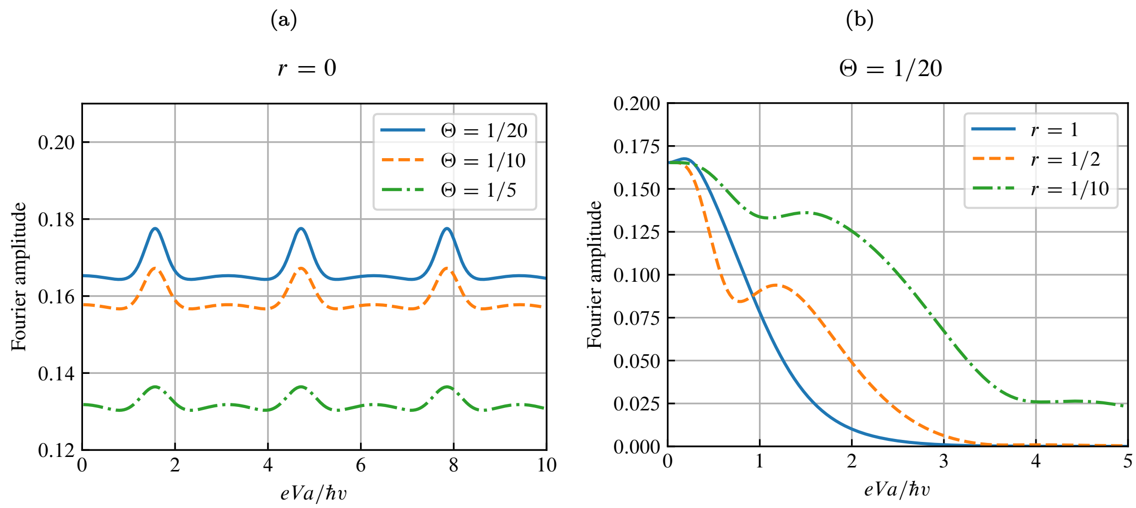

Figure 3.17: Plots of the Fourier amplitude of the interference contribution to the differential conductance at $\nu = 1$. (a) without heating; (b) with heating. The temperature is represented with a dimensionless quantity $\Theta = Ta/\hbar v$.

and outgoing waves is

$$\begin{pmatrix} \psi_{R+}(\omega) \\ \psi_{L-}(\omega) \end{pmatrix} = \begin{pmatrix} \mathfrak{t} & \mathfrak{r} \\ -\mathfrak{r}^* & \mathfrak{t} \end{pmatrix} \begin{pmatrix} \psi_{R-}(\omega) \\ \psi_{L+}(\omega) \end{pmatrix}, \tag{3.101}$$

where $\mathfrak{t}$ and $\mathfrak{r}$ are complex amplitudes and ω is the energy. $\mathcal{T} = |\mathfrak{t}|^2$ and $\mathcal{R} = |\mathfrak{r}|^2$ are the transmission and reflection coefficients for a single contact. For a geometry with two point-contacts, the transmission coefficient is

$$\mathcal{T}(\omega) = \frac{|\mathfrak{t}_1|^2|\mathfrak{t}_2|^2}{1 + |\mathfrak{r}_1|^2|\mathfrak{r}_2|^2 + (\mathfrak{r}_1\mathfrak{r}_2^* e^{2i\omega a/v} + \mathfrak{r}_1^*\mathfrak{r}_2 e^{-2i\omega a/v})}, \tag{3.102}$$

where a is the distance between the two point-contacts, and indexes 1 and 2 refer to the two contacts.

When a source-drain bias voltage $V = V_d - V_u$ is applied on the two edges, we again use the dimensionless quantity η to describe the asymmetry of the bias, so that the voltage V_d applied to the right-moving channel is $(2\eta + 1)V/2$ and the voltage V_u applied to the left-moving channel is $(2\eta - 1)V/2$. At a finite temperature T, the total current is

$$I = e\int_{-\infty}^{\infty} \frac{d\omega}{2\pi} \mathcal{T}(\omega + (2\eta - 1)\omega_J/2) \left[\frac{1}{e^{\beta(\omega-\omega_J)} + 1} - \frac{1}{e^{\beta\omega} + 1}\right]. \tag{3.103}$$

where $\beta = \hbar/T$ and $\omega_J = eV$. The tunneling current is $I_T = (e^2/h)V - I$.

Below, we focus on the special case motivated by the experimental setup in [76]. We consider the completely asymmetric case, where $\eta = 1/2$, i.e., $V_d = V$ and $V_u = 0$. The total differential conductance takes a simple form,

$$G = \frac{e}{\hbar}\frac{\partial I}{\partial \omega_J} = \frac{e^2}{\hbar}\int_{-\infty}^{\infty} \frac{d\omega}{2\pi} \mathcal{T}(\omega)\beta f(1 - f), \tag{3.104}$$

where $f = 1/(e^{\beta(\omega-\omega_J)}+1)$. We also focus on the situation of half transmission, hence the transmission and reflection coefficients for a single contact satisfy the following relations: $|\mathfrak{t}_1|^2 = |\mathfrak{t}_2|^2 = |\mathfrak{r}_1|^2 = |\mathfrak{r}_2|^2 = \frac{1}{2}$, and

$$\mathfrak{r}_1\mathfrak{r}_2^* = \frac{1}{2}e^{-i(\varphi_0+\varphi_{\mathrm{AB}})}, \tag{3.105}$$

where φ_0 is the relative phase of Γ_1 and Γ_2, and φ_{AB} is the AB phase. The transmission coefficient is reduced to

$$\mathcal{T}(\omega) = \frac{1}{5+4\cos(-\varphi_0-\varphi_{\mathrm{AB}}+2\omega a/v)}. \tag{3.106}$$

Using these equations, it is easy to find that the current is periodic in ω_J with a period of $2\pi v/a(2\eta+1)$. The plots of the Fourier amplitude (with respect to φ_{AB}) of the differential conductance are given in Fig. 3.17(a). It is clear that the amplitude of the interference current oscillates with respect to ω_J with a period of $\pi v/a$.

This exact result was obtained by ignoring the Coulomb interaction across the point contacts. The interacting problem is no longer exactly solvable. An important consequence of interactions is that they lead to dissipation effects, which come into play if one works beyond the lowest order in the backscattering at the constrictions. In particular, the tunneling of one particle across a constriction can lead to particle-hole excitations in the adjacent edge channels, which may reduced the interference signal in a manner similar to an increase in temperature. Here, we provide a rough estimate of these effects with a simple model. We use a non-interacting model at a higher temperature to describe the interacting case, with an effective temperature chosen self-consistently.

The heat power W due to the tunneling current is $I_T V$. We assume that a portion r of the heat power is absorbed inside the interferometer. This heat power rI_TV leaves the device along the edges. The heat current along the edges is quantized at $\pi^2k_B^2T_1^2/6h$ per channel [55], where T_1 is the effective temperature. The thermal energy, brought into the interferometer by the incoming edge channels is set by the ambient temperature T. We thus arrive to the following energy balance equation,

$$\frac{\pi^2k_B^2}{6h}(T_1^2-T^2) = r\frac{I_TV}{2}, \tag{3.107}$$

where a 2 in the denominator comes from the fact that the energy is equally absorbed by the upper and lower edges. Combing Eqs. (3.103) and (3.107) and recognizing β in Eq. (3.103) as $\hbar/T_1$, one can self-consistently solve for the tunneling current I_T for any given set of T, V, and φ_{AB}, therefore finding the conductance and its Fourier amplitude. The plots are shown in Fig. 3.17(b). They resemble the curves obtained from a recent experiment with graphene [76].

We see that the Fourier amplitude in Fig. 3.17(b) decays with increasing source-drain voltage, unlike for the non-interacting case. We note that a similar decay of the interference signal would be expected for interacting systems with multiple edge modes, if one goes beyond the limit of weak backscattering considered in earlier sections of this chapter. This effect would be present in addition to the effect of the fluctuating charge on the inner loop.

3.7 Summary

In the main part of this chapter, we have used bosonization methods to study nonlinear behavior of a quantum Hall Fabry–Pérot interferometer at finite source-drain voltage, in cases where the quantum Hall state contains two modes propagating in the same direction. Important examples are when the bulk filling factor is $\nu = 2/5$ or $\nu = 2$. We focus on the situations where the constrictions defining the interferometer region are either slightly pinched off, so that the inner mode is weakly backscattered while the outer mode is completely transmitted, or where the constriction is pinched off to an extent that the inner mode is completely reflected while the outer mode is weakly backscattered. These analyses were confined to situations where the interfering channel is only weakly backscattered, because situations with stronger backscattering are difficult to treat using the bosonization approach. In Section 3.6, however, we examined effects of intermediate backscattering in an exactly solvable model [35], with non-interacting electrons and only one edge mode, at $\nu = 1$.

The most interesting and challenging cases involve tunneling between the outer edge modes in devices where the inner mode forms a closed loop. In contrast to the tunneling between inner edge modes, these cases involve a nontrivial scattering process for bosonic edge plasmons between the opposite edges of the device. After the scattering problem is solved, however, the residual tunneling of quasiparticles can be treated perturbatively in the weak-backscattering limit. If the edge modes are not too strongly coupled, we find resonance features in the I–V curves at low temperatures, which emerge due to resonance states of plasmons on the closed inner channel. The resonances contain information about the velocity of the inner edge mode. A quantitative analytic theory of the resonances is possible in the limit of weak intermode interaction.

Previous investigations [51] have considered the theory for interferometers at $\nu = 2$, with strongly coupled edge modes, in the limit where the fast mode velocity is taken to infinity. Here we have extended the theory to the physically realistic case of finite edge velocities. We have also addressed effects of asymmetrically-applied voltage bias, since this is relevant for recent experiments in graphene [76]. Another novel effect addressed in this work is weak tunneling between co-propagating edge channel. While the leakage current through the inner closed loop is negligible in comparison with the total current through the interferometer, the long-term memory of tunneling events has a dramatic effect on the tunneling current at high voltages. Most importantly, the interference contribution to the current rapidly decays as a function of voltage in agreement with experiments. We have only addressed the memory effect at zero temperature, and an extension of the theory to finite temperatures would be important. Indeed, we find that many features of the I–V curve are highly sensitive to the temperature in the model without tunneling between co-propagating channels.

Given the role of efficient screening in the seminal experiments [70, 75] at $\nu = 2/5$, we have studied a model where the quantum Hall layer is Coulomb-coupled to a parallel electron layer with high conductivity. Due to effects of the applied magnetic field, we argue that the screening layer should be well represented by an extra chiral edge channel, coupled to the two edge channels of the quantum Hall liquid. The predicted I–V curve exhibits a rich set of features at low temperatures, though most features are suppressed as the temperature increases.

Because the calculations described above were done in the limit where the interfering mode is weakly backscattered, there are no effects analogous to heating as the applied voltage becomes large. For the non-interacting model with finite backscattering studied in Section 3.6, there is also no heating because of the absence of interaction effects. Indeed, one finds for the non-interacting model that the interference amplitude does not decay at large source-drain voltage but behaves as a periodic function of the applied voltage. In Section 3.6, we make a qualitative estimate of the effects of heating that should occur when interactions as well as strong backscattering are taken into account, which also should be applicable to cases where several propagating modes are present.

Interesting experimental data have arrived for nonlinear transport in multi-channel quantum Hall interferometers, and new experiments are being performed. We expect that new data, especially at low temperatures, will provide an opportunity for fruitful comparison with the theory. We predict resonance features in the weak coupling regime at $\nu = 2/5$, but the temperature was not sufficiently low to observe them in the recent experiment [75]. At the same time, our prediction of rapid suppression of interference at a high voltage bias even for weak tunneling at $\nu = 2/5$ agrees with the data [75]. The focus of our theory at $\nu = 2$ is on weak tunneling that can be treated perturbatively. At the same time, the experiment [76] focuses on the 50% transmission regime, and lower transmission is required for comparison with our work. Fortunately, the experimental regimes needed for comparison with this chapter are within reach.

Chapter 4

Conclusions

Electronic interferometers are powerful tools to probe fractional statistics. Recently years have seen major experimental breakthroughs in the observation of fractional statistics in FQH states using interferometers. These include the following experiments: Fabry–Pérot interferometers that directly measure the braiding phase at filling factor $\nu = 1/3$ [70] and $\nu = 2/5$ [75]; a Mach–Zehnder interferometer that shows the interference and braiding of anyons with a $\nu = 1/3$ edge mode in the $\nu = 2/5$ bulk [74]; Fabry–Pérot interferometers that demonstrate the fractional statistics at filling factor $\nu = 1/3$ through telegraph noise [77, 78].

We have achieved huge success in this direction, but some challenges also emerge. First, most experiments were performed with a single $\nu = 1/3$ edge mode and obtained nice results. This is not surprising since the quantum Hall interferometry is known to be robust when there is only one chiral edge mode, and the phase measured is related to the total charge inside, which is also fractionalized for Laughlin states [56]. However, compared with the case of a single-channel interferometer, the data collected for a two-channel interferometer are vague and hard to interpret. In Chapter 3, we address some subtleties in the electronic Fabry–Pérot interferometers with multiple edge channels. When quasiparticles on the outer mode tunnel, the closed loop formed by the totally reflected inner channel and the quasiparticle number fluctuations on the inner channel are important factors that affect the behavior of the measured current at a finite bias voltage. Still, there are other subtleties that remain open to us.

Second, there is no direct way to probe charge neutral excitations in quantum spin liquids using electronic interferometers. The thermal interferometers proposed in Chapter 2 of this thesis can overcome this challenge. By combining the results from thermal Fabry–Pérot interferometers and thermal Mach–Zehnder interferometers, we can see unique signatures of fractional statistics in an arbitrary system with non-trivial topological order, no matter whether the system is charged or not.

Last but not least, an exact solution cannot be obtained when the electronic quantum Hall Fabry–Pérot interferometer is operated under its optimal regime at fractional filings. In one of our works that is not included in this thesis, a new interferometer geometry is proposed and it admits a simple yet exact analytical solution under any regime [103]. This new geometry combines features from both the Fabry–Pérot geometry and Mach–Zehnder geometry, and allows probing the fractional statistics of FQH states in the Jain sequence with $\nu = p/(2p+1)$.

To conclude, the study of interferometers in topological liquids is entering a golden age right now. Interferometer experiments that explore more kinds of topological systems are expected to unveil the fractional statistics in these systems for us. We hope the work presented in this thesis will serve as building blocks for future theoretical and experimental investigations of fractional statistics and topological orders in topological quantum liquids.

Appendix A

Measurement of the heat current

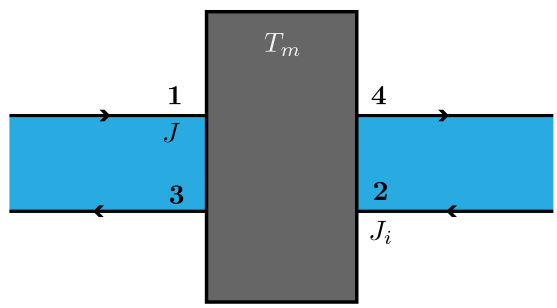

Figure A.1: Chiral quantum Hall edges 1 and 2 enter a piece of metal, and channels 3 and 4 exit it.

We assume that the heat current J is carried from the contact point of Kitaev and quantum Hall (QH) edges by the QH edge that exchanges heat with the magnetic material. We label that QH edge as edge 1. The heat current J can be measured with a high precision with the method from Refs. [82, 98]. Edge 1 is absorbed by a small piece of metal (Fig. A.1) which also absorbs edge 2 in equilibrium at the ambient temperature T_0. Edge 2 carries the heat current $J_i = KT_0^2/2$ into the piece of metal, where K is the quantized thermal conductance of a QH edge. Two chiral edges (3 and 4) emanate from the piece of metal. Their temperatures equal the temperature T_m of the piece of metal. Hence, they carry the total heat current $J_o = 2KT_m^2/2$. From the energy conservation, $J = J_o - J_i$. Hence, J can be found from the known temperature T_0 and the temperature T_m. The latter temperature can be determined from the low-frequency electric-current noise on edge 3. The noise is defined as

$$S_3 = \lim_{\omega \to 0} \int_{-\infty}^{\infty} dt \langle I_3(t) I_3(0) + I_3(0) I_3(t) \rangle \exp(i\omega t), \tag{A.1}$$

where I_3 is the electric current. The noises on the other edges have similar definitions. According to the fluctuation-dissipation theorem, the noise $S_2 = 2GT_0$, where G is the quantized electrical conductance of a QH edge.

The incoming currents I_1 and I_2 are uncorrelated. This does not hold for the currents I_3 and I_4. The currents $I_{3,4}$ can be represented as

$$I_n = I_n^T + G\delta V, \tag{A.2}$$

where I_n^T is the "Nyquist" contribution which alone would produce the noise $2GT_m$. It describes thermal fluctuations and results from the Gibbs distribution for the outgoing electrons. The second contribution is due to the voltage fluctuations δV in the piece of metal. The voltage fluctuations can be found from charge conservation:

$$2G\delta V + I_3^T + I_4^T = I_1 + I_2. \tag{A.3}$$

Since the currents I_1, I_2, I_3^T, and I_4^T are uncorrelated, computing S_3 is straightforward. An amplifier, measuring that noise, is always connected with another chiral channel at the ambient temperature T_0. Thus, the observed noise

$$S = GT_m + \frac{S_1}{4} + \frac{5}{2}GT_0, \tag{A.4}$$

where S_1 can be measured separately.

Equation (A.4) allows computing the heat current J. In general, this heat current differs from the heat current J_M flowing from the interferometer along the edge of a Kitaev magnet. Fortunately, the absolute value of J_M is of little interest. In the presence of anyons in the interferometer, the heat currents J_M and J acquire corrections, proportional to $\Gamma_{1,2}^2$. Information about fractional statistics can be extracted from the comparison of the corrections in different configurations.

Appendix B

ψ tunneling

Here we compute, in the leading order, the tunneling thermal current in a two-constriction Fabry–Pérot interferometer with single-Majorana-fermion tunneling from one edge of the spin-liquid to the other edge of the same spin-liquid, see also Ref. [87]. Several equations from this appendix are used in the calculations presented in Appendix C. The full Hamiltonian for the system is given as,

$$H = \frac{v}{4\pi}\int_{-L/2}^{L/2} dx \Big[-i : \psi_1 \partial_x \psi_1 : + i : \psi_2 \partial_x \psi_2 : \Big] + H_T. \tag{B.1}$$

where H_T is the single-Majorana fermion tunneling Hamiltonian at the quantum point contacts. The geometry of the Fabry–Pérot interferometer is shown in Fig. 2.3(a). The subscripts 1 and 2 on the Majorana fermion field ψ denote the two edges of the spin liquid. We work in the $L \to \infty$ limit and impose the periodic boundary conditions $\psi_a(x) \equiv \psi_a(x+L)$. The edges have different temperatures $T_{1,2}$. The free field Hamiltonian can be diagonalized by working in the Fourier space, defining,

$$\psi_1(x) = \sqrt{\frac{2\pi}{L}} \sum_k e^{ikx} \psi_{1,k}, \tag{B.2}$$

$$\psi_2(x) = \sqrt{\frac{2\pi}{L}} \sum_k e^{-ikx} \psi_{2,k}. \tag{B.3}$$

We first compute the Majorana-fermion two-point thermal correlation function,

$$\langle \psi_1(x,t)\psi_1(0,0)\rangle = \frac{2\pi}{L}\sum_{k,q} e^{ik(x-vt)} e^{-k\epsilon} \langle \psi_k \psi_q \rangle = \frac{2\pi}{L}\sum_{k,q} e^{ik(x-vt)} e^{-k\epsilon} \frac{\delta_{k+q}}{e^{-\beta v k}+1} \tag{B.4}$$

$$\xrightarrow{L\to\infty} \int dk \, \frac{e^{ik(x-vt+i\epsilon)}}{e^{-\beta v k}+1} = -\frac{\pi T_1}{v \sin[i\pi T_1(x/v - t + i\epsilon)]}. \tag{B.5}$$

The expression for ψ_2 is similar with a different temperature. The tunneling Hamiltonian is given as,

$$H_T = -i\Gamma_1 \psi_2(x_1,t)\psi_1(x_1,t) - i\Gamma_2 \psi_2(x_2,t)\psi_1(x_2,t), \tag{B.6}$$

where x_i is the location of the ith constriction (see Fig. 2.3(a)), and Γ_i is its real tunneling amplitude. Using the equation of motion, we can identify the tunneling current operator as,

$$\hat{I}_T(t) = i\Gamma_1\psi_2(x_1,t)\partial_t\psi_1(x_1,t) + i\Gamma_2\psi_2(x_2,t)\partial_t\psi_1(x_2,t), \tag{B.7}$$

where the time derivatives are computed from the edge theory without tunneling. An easy derivation consists in computing the commutator of the tunneling Hamiltonian with one of the edge Hamiltonians. We now use perturbation theory to compute the average thermal current to the first non-zero order in the tunneling amplitudes,

$$\begin{aligned}\langle I_T\rangle = -i\int_{-\infty}^{t} dt' \Big[&\Gamma_1^2\langle[\psi_2(x_1,t)\partial_t\psi_1(x_1,t), \psi_2(x_1,t')\psi_1(x_1,t')]\rangle \\ &+ \Gamma_2^2\langle[\psi_2(x_2,t)\partial_t\psi_1(x_2,t), \psi_2(x_2,t')\psi_1(x_2,t')]\rangle \\ &+ \Gamma_1\Gamma_2\big(\langle[\psi_2(x_1,t)\partial_t\psi_1(x_1,t), \psi_2(x_2,t')\psi_1(x_2,t')]\rangle \\ &+ \langle[\psi_2(x_2,t)\partial_t\psi_1(x_2,t), \psi_2(x_1,t')\psi_1(x_1,t')]\rangle\big)\Big],\end{aligned} \tag{B.8}$$

where the first two terms correspond to the independent single constriction contributions, and the last two terms are the interference terms between the two constrictions. Therefore, we can write the total thermal current as comprised of the non-interference and interference terms,

$$\langle I_T\rangle \equiv \sum_{j=1,2}\langle I_T\rangle^{\text{non-int}}_{\Gamma_j} + \langle I_T\rangle^{\text{int}}. \tag{B.9}$$

In the following two subsections, we individually focus on the non-interference and interference contributions. Note that the non-interference contribution $\langle I_T\rangle^{\text{non-int}}_{\Gamma_j}$ corresponds to the j^{th} constriction, $j = 1,2$ and is exactly what we obtain when we consider a single constriction geometry as shown in Fig. 2.2. Therefore, the thermal current in the single constriction case can be found as the non-interference part, corresponding to one of the tunneling amplitudes Γ_j, of the full calculation that is presented in this appendix.

Our calculations assume that the two edges of the interferometer remain in equilibrium at the temperatures of the sources. This assumption is legitimate for weak tunneling despite the nonequilibrium nature of tunneling transport, if the average time between two consecutive tunneling events is much longer then the travel time along the edges between the two constrictions [39]. See a detailed discussion of the validity conditions for the perturbation theory in Ref. [39]. Note that the physical situation is different from Ref. [104], where a strongly nonequilibrium edge state emerges due to the coexistence of counter-propagating channels of different temperatures on the same edge. In our case, the temperatures of the drain and source connected to the same edge are approximately equal.

Some topological orders allow counter-propagating edge modes on the same edge. Then equilibration processes on the edge change slightly the edge temperatures at small Γ_i. This effect is irrelevant in the lowest-order perturbation theory.

B.1 Non-interference term

We first compute the non-interference terms. We use the above derived thermal correlation functions, in which we set $v = 1$,

$$\langle \psi_1(x_1, t_1)\psi_1(x_2, t_2)\rangle = \frac{\pi T_1}{\sin[\pi T_1(\epsilon + i(t_1 - t_2 + x_2 - x_1))]}, \tag{B.10}$$

$$\langle \psi_2(x_1, t_1)\psi_2(x_2, t_2)\rangle = \frac{\pi T_2}{\sin[\pi T_2(\epsilon + i(t_1 - t_2 + x_1 - x_2))]}. \tag{B.11}$$

Plugging these into the non-interference contribution $\langle I_T\rangle^{\text{non-int}}_{\Gamma_j}$ to the thermal current due to the j^{th} constriction, we obtain the expression,

$$\langle I_T\rangle^{\text{non-int}}_{\Gamma_j} = \Gamma_j^2 \int_{-\infty}^{t} dt' \left[\frac{(\pi T_2)(\pi T_1)^2\ \cos[\pi T_1(\epsilon + i(t - t'))]}{\sin^2[\pi T_1(\epsilon + i(t - t'))]\sin[\pi T_2(\epsilon + i(t - t'))]} + (t \leftrightarrow t')\right], \qquad (j = 1, 2). \tag{B.12}$$

Defining $\tau \equiv \pi T_1(t - t')$ and $n = T_2/T_1$, we write the above integral as,

$$\langle I_T\rangle^{\text{non-int}}_{\Gamma_j} = \pi^2\Gamma_j^2 T_1 T_2 \int_{-\infty}^{\infty} d\tau\ \frac{\cos(-i\tau + \epsilon)}{\sin^2(-i\tau + \epsilon)\sin[n(-i\tau + \epsilon)]}. \tag{B.13}$$

Since the $\epsilon \to 0$ limit is to be taken after evaluating the integral, to evaluate the integral, we deform the integration contour as shown in Fig. B.1(a),

$$\begin{aligned}\langle I_T\rangle^{\text{non-int}}_{\Gamma_j} = \pi^2\Gamma_j^2 T_1 T_2 \Bigg[&\int_{-\infty}^{-\epsilon} d\tau\ \frac{\cos(-i\tau)}{\sin^2(-i\tau)\sin(-in\tau)} + \int_C d\tau\ \frac{\cos(-i\tau)}{\sin^2(-i\tau)\sin(-in\tau)} \\ &+ \int_{\epsilon}^{\infty} d\tau\ \frac{\cos(-i\tau)}{\sin^2(-i\tau)\sin(-in\tau)}\Bigg].\end{aligned} \tag{B.14}$$

Here C is a half-circle near the origin. Pictorially, the integration contour is deformed as shown in Fig. B.1(a). Close to the origin, the integration variable can be defined as $\tau = \epsilon e^{i\theta}$.

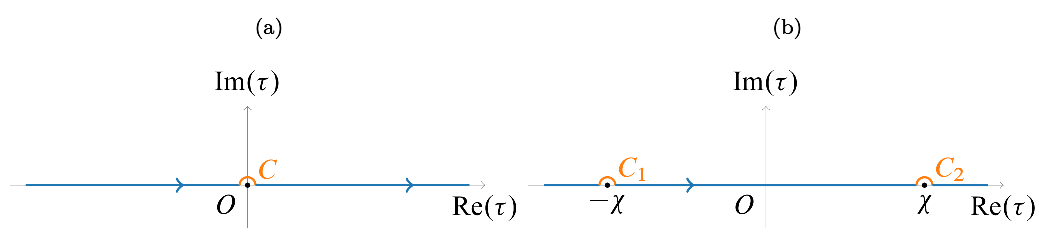

Figure B.1: Contours used to compute the integrals in Appendices B, C and E. Contour (a) is used for the non-interference terms, and contour (b) is used for the interference terms. χ is proportional to the distance x_{21} between the constrictions.

On inspection, it's easy to see that the first and the last integrals cancel out, hence only the integral along the contour C gives a non-zero contribution,

$$\int_C d\tau \frac{\cos(-i\tau)}{\sin^2(-i\tau)\sin(-in\tau)} = \int_{\pi}^{0} d\theta \frac{\tau\cosh\tau}{\sinh^2\tau\sinh(n\tau)}. \tag{B.15}$$

Since ϵ is small, we may use the expansion,

$$\frac{\cosh\tau}{\sinh^2\tau\sinh(n\tau)} = \frac{1}{n\tau^3} + \frac{1-n^2}{6n\tau} + \mathcal{O}(\tau). \tag{B.16}$$

Using this, we evaluate the integral in the $\epsilon \to 0$ limit,

$$\int_\pi^0 d\theta \frac{\tau\cosh\tau}{\sinh^2\tau\sinh(n\tau)} = \frac{\pi(n^2-1)}{6n} = \frac{\pi(T_2^2-T_1^2)}{6T_1T_2}. \tag{B.17}$$

Putting the result of the integral back into the expression for the non-interference terms in the thermal current we obtain,

$$\sum_{j=1,2}\langle I_T\rangle_{\Gamma_j}^{\text{non-int}} = \frac{\pi^3(\Gamma_1^2+\Gamma_2^2)}{6}(T_2^2-T_1^2). \tag{B.18}$$

This is the contribution to the thermal current from two independent constrictions. Calculation of the thermal current in the single constriction geometry would involve only the non-interference contribution $\langle I_T\rangle_{\Gamma_j}^{\text{non-int}}$ due to one of the constrictions.

B.2 Interference term

In the double constriction Fabry–Pérot geometry, there is an interference contribution as well, which we compute now,

$$\begin{aligned}\langle I_T\rangle^{\text{int}} = \Gamma_1\Gamma_2\int_{-\infty}^{t}dt'\Bigg[&\frac{(\pi T_2)(\pi T_1)^2\quad\cos[\pi T_1(\epsilon+i(t-t'+x_{21}))]}{\sin^2[\pi T_1(\epsilon+i(t-t'+x_{21}))]\sin[\pi T_2(\epsilon+i(t-t'-x_{21}))]}\\ &+\frac{(\pi T_2)(\pi T_1)^2\quad\cos[\pi T_1(\epsilon+i(t'-t-x_{21}))]}{\sin^2[\pi T_1(\epsilon+i(t'-t-x_{21}))]\sin[\pi T_2(\epsilon+i(t'-t+x_{21}))]}+(x_{21}\to -x_{21})\Bigg].\end{aligned} \tag{B.19}$$

Like before, for convenience, we define $\tau \equiv \pi T_1(t-t')$, $\chi \equiv \pi T_1 x_{21}$, and $n = T_2/T_1$,

$$\begin{aligned}\langle I_T\rangle^{\text{int}} &= \pi^2\Gamma_1\Gamma_2T_1T_2\int_0^\infty d\tau\left[\frac{\cos[i(\tau+\chi)+\epsilon]}{\sin^2[i(\tau+\chi)+\epsilon]\sin[n(i(\tau-\chi)+\epsilon)]}+\frac{\cos[-i(\tau+\chi)+\epsilon]}{\sin^2[-i(\tau+\chi)+\epsilon]\sin[n(-i(\tau-\chi)+\epsilon)]}\right]\\ &\quad+(\chi\to-\chi) \qquad\qquad (B.20)\\ &= \pi^2\Gamma_1\Gamma_2T_1T_2\int_{-\infty}^\infty d\tau\left[\frac{\cos[-i(\tau+\chi)+\epsilon]}{\sin^2[-i(\tau+\chi)+\epsilon]\sin[n(-i(\tau-\chi)+\epsilon)]}+(\chi\to-\chi)\right]. \qquad (B.21)\end{aligned}$$

The integral is evaluated using the contour defined in Fig. B.1(b). After deforming the contour around $\tau = \pm\chi$ as shown in Fig. B.1(b), we observe that the only surviving terms are

$$\langle I_T\rangle^{\text{int}} = -i\pi^2\Gamma_1\Gamma_2T_1T_2\int_{C_1+C_2}d\tau\left[\frac{\cosh(\tau+\chi)}{\sinh^2(\tau+\chi)\sinh[n(\tau-\chi)]}+\frac{\cosh(\tau-\chi)}{\sinh^2(\tau-\chi)\sinh[n(\tau+\chi)]}\right], \tag{B.22}$$

The integration variable near $-\chi$ is given by $\eta = \epsilon e^{i\theta} - \chi$, and the integration variable near χ is given by $\eta = \epsilon e^{i\theta} + \chi$. Again, since ϵ is small, we use the series expansions to perform the integrals and then take the $\epsilon \to 0$ limit,

$$\frac{\cosh\tau}{\sinh^2\tau} = \frac{1}{\tau^2} + \frac{1}{6} + \mathcal{O}(\tau^2), \tag{B.23}$$

$$\frac{1}{\sinh\tau} = \frac{1}{\tau} - \frac{\tau}{3} + \mathcal{O}(\tau^3). \tag{B.24}$$

Using these expansions, we arrive at the expression,

$$\langle I_T\rangle^{\text{int}} = 2\pi^3\Gamma_1\Gamma_2\left[T_2^2\frac{\cosh(2\pi T_2 x_{21})}{\sinh^2(2\pi T_2 x_{21})} - T_1^2\frac{\cosh(2\pi T_1 x_{21})}{\sinh^2(2\pi T_1 x_{21})}\right]. \tag{B.25}$$

Combining the interference and non-interference terms together, we arrive at the expression for the thermal current,

$$\langle I_T\rangle = \frac{\pi^3(\Gamma_1^2+\Gamma_2^2)}{6}(T_2^2 - T_1^2) + 2\pi^3\Gamma_1\Gamma_2\left[T_2^2\frac{\cosh(2\pi T_2 x_{21})}{\sinh^2(2\pi T_2 x_{21})} - T_1^2\frac{\cosh(2\pi T_1 x_{21})}{\sinh^2(2\pi T_1 x_{21})}\right]. \tag{B.26}$$

Appendix C

$\psi\partial_x\psi$ tunneling

In this appendix, we compute the tunneling thermal current between adjacent spin liquids as discussed in the main text in Sec. 2.3. Note that the calculation for the single constriction geometry, as discussed in Sec. 2.3.1, corresponds to the non-interference part $\langle I_T\rangle_\Gamma^{\text{non-int}}$ (here $\Gamma_i = \Gamma$) of the full calculation in the double constriction Fabry–Pérot geometry which we present in this appendix. We set the edge velocity $v = 1$. Therefore, the final answers should be divided by v^8. We rely on Green's functions, computed in Appendix B.

From perturbation theory and the expression of the tunneling thermal current operator, Eq. (2.17), the leading contribution to the tunneling thermal current is

$$\begin{aligned}\langle I_T(t)\rangle = &-4(\Gamma_1^2+\Gamma_2^2)\pi^9T_1^5T_2^4\int_{-\infty}^{\infty}d\tau\frac{\cos[i\pi T_1(\tau+i\epsilon)]}{\sin^5[i\pi T_1(\tau+i\epsilon)]}\frac{1}{\sin^4[i\pi T_2(\tau+i\epsilon)]}\\&-4\Gamma_1\Gamma_2\pi^9T_1^5T_2^4\left[\int_{-\infty}^{\infty}d\tau\frac{\cos[i\pi T_1(\tau+\chi+i\epsilon)]}{\sin^5[i\pi T_1(\tau+\chi+i\epsilon)]}\frac{1}{\sin^4[i\pi T_2(\tau-\chi+i\epsilon)]}+(\chi\to-\chi)\right]\end{aligned}\tag{C.1}$$

$$\begin{aligned}= &\,4i(\Gamma_1^2+\Gamma_2^2)\pi^9T_1^5T_2^4\int_{-\infty}^{\infty}d\tau\frac{\cosh[\pi T_1(\tau+i\epsilon)]}{\sinh^5[\pi T_1(\tau+i\epsilon)]}\frac{1}{\sinh^4[\pi T_2(\tau+i\epsilon)]}\\&+4i\Gamma_1\Gamma_2\pi^9T_1^5T_2^4\left[\int_{-\infty}^{\infty}d\tau\frac{\cosh[\pi T_1(\tau+\chi+i\epsilon)]}{\sinh^5[\pi T_1(\tau+\chi+i\epsilon)]}\frac{1}{\sinh^4[\pi T_2(\tau-\chi+i\epsilon)]}+(\chi\to-\chi)\right],\end{aligned}\tag{C.2}$$

where χ is the distance between the two tunneling contacts divided by v. We assume $\chi > 0$. We redefine the variables for convenience, $\eta = \pi T_1\tau$, $\lambda = T_2/T_1$, and $\chi \to \pi T_1\chi$. This gives,

$$\begin{aligned}\langle I_T(t)\rangle = &\,4i(\Gamma_1^2+\Gamma_2^2)\pi^8T_1^4T_2^4\int_{-\infty}^{\infty}d\eta\frac{\cosh\eta}{\sinh^5(\eta+i\epsilon)}\frac{1}{\sinh^4(\lambda\eta+i\epsilon)}\\&+4i\Gamma_1\Gamma_2\pi^8T_1^4T_2^4\left[\int_{-\infty}^{\infty}d\tau\frac{\cosh(\eta+\chi)}{\sinh^5(\eta+\chi+i\epsilon)}\frac{1}{\sinh^4(\lambda\eta-\lambda\chi+i\epsilon)}+(\chi\to-\chi)\right].\end{aligned}\tag{C.3}$$

This expression consists of the non-interference contributions due to each of the constrictions independently, and the interference contribution. Therefore, the total tunneling thermal current can be written as $\langle I_T\rangle = \sum_{j=1,2}\langle I_T\rangle^{\text{non-int}}_{\Gamma_j} + \langle I_T\rangle^{\text{int}}$, where the non-interference and interference contributions are given as,

$$\langle I_T\rangle^{\text{non-int}}_{\Gamma_j} = 4i\Gamma_j^2\pi^8T_1^4T_2^4\int_{-\infty}^{\infty} d\eta\frac{\cosh\eta}{\sinh^5(\eta+i\epsilon)}\frac{1}{\sinh^4(\lambda\eta+i\epsilon)}, \qquad j=1,2, \tag{C.4}$$

$$\langle I_T\rangle^{\text{int}} = 4i\Gamma_1\Gamma_2\pi^8T_1^4T_2^4\left[\int_{-\infty}^{\infty} d\tau\frac{\cosh(\eta+\chi)}{\sinh^5(\eta+\chi+i\epsilon)}\frac{1}{\sinh^4(\lambda\eta-\lambda\chi+i\epsilon)} + (\chi\to-\chi)\right]. \tag{C.5}$$

In the following two subsections, we focus on the non-interference and interference contributions separately. Note that the non-interference contribution $\langle I_T\rangle^{\text{non-int}}_{\Gamma_j}$ corresponding to each Γ_j, $j=1,2$, is exactly what we obtain when we consider single constriction geometry between two different spin liquids. Therefore, the thermal current in the single constriction case, as discussed in Sec. 2.3.1, can be found as the non-interference part, corresponding to one of the tunneling amplitudes Γ_i, of the full calculation presented in this appendix.

C.1 Non-interference term

First we consider the non-interference contribution (Eq. (C.4)) to the tunneling thermal current. It can be rewritten as,

$$\langle I_T\rangle^{\text{non-int}}_{\Gamma_j} = 4i\Gamma_j^2\pi^8T_1^4T_2^4\int_{-\infty}^{\infty} d\eta\frac{\cosh\eta}{\sinh^5(\eta+i\epsilon)\sinh^4(\lambda\eta+i\epsilon)} \tag{C.6}$$

$$= 4i\Gamma_j^2\pi^8T_1^4T_2^4\left[\int_{-\infty}^{-\epsilon} d\eta\frac{\cosh\eta}{\sinh^5(\eta)\sinh^4(\lambda\eta)} + \int_{\epsilon}^{\infty} d\eta\frac{\cosh\eta}{\sinh^5(\eta)\sinh^4(\lambda\eta)} + \int_C d\eta\frac{\cosh\eta}{\sinh^5(\eta)\sinh^4(\lambda\eta)}\right] \tag{C.7}$$

$$= 4i\Gamma_j^2\pi^8T_1^4T_2^4\int_C d\eta\frac{\cosh\eta}{\sinh^5(\eta)\sinh^4(\lambda\eta)}, \tag{C.8}$$

where $j=1,2$. Here, the integration contour is deformed as shown in Fig. B.1(a). Close to the origin, the integration variable can be written as $\eta=\epsilon e^{i\theta}$. Since $\epsilon\ll 1$, we expand the integrand,

$$\frac{\cosh\eta}{\sinh^5(\eta)\sinh^4(\lambda\eta)} = \cdots + \frac{1}{\eta}\left[\frac{41(\lambda^8-1)}{2835\ \lambda^4} + \frac{62(\lambda^4-1)}{2835\ \lambda^2}\right] + \mathcal{O}(\eta^0). \tag{C.9}$$

All the terms in $\ldots$ contain negative odd powers of η, and since $d\eta = i\epsilon e^{i\theta}d\theta$, on integration from π to 0, these terms give zero. The only non-zero contribution comes from the $1/\eta$ term. This allows us to perform the integral and take the $\epsilon\to 0$ limit, and we thus obtain,

$$\sum_{j=1,2}\langle I_T\rangle^{\text{non-int}}_{\Gamma_j} = 4\pi^9(\Gamma_1^2+\Gamma_2^2)\frac{1}{2835}[41(T_2^8-T_1^8) + 62T_1^2T_2^2(T_2^4-T_1^4)]. \tag{C.10}$$

This is the non-interference contribution to the thermal current due to two independent constrictions. The results discussed in the main text in Sec. 2.3.1 correspond to $\langle I_T\rangle^{\text{non-int}}_{\Gamma_j}$ where Γ_j is set to Γ.

C.2 Interference term

We now look at the interference contribution to the tunneling thermal current, Eq. (C.5); this is given as,

$$\langle I_T\rangle^{\rm int} = 4i\Gamma_1\Gamma_2\pi^8 T_1^4 T_2^4 \left[\int_{-\infty}^{\infty} d\eta \frac{\cosh(\eta+\chi)}{\sinh^5(\eta+\chi+i\epsilon)} \frac{1}{\sinh^4(\lambda\eta-\lambda\chi+i\epsilon)} + (\chi\to-\chi)\right]. \tag{C.11}$$

The contour can be deformed according to Fig. B.1(b) and the integral rewritten as,

$$\begin{aligned}\langle I_T\rangle^{\rm int} = 4i\Gamma_1\Gamma_2\pi^8 T_1^4 T_2^4 \Bigg[&\int_{-\infty}^{-\chi-\epsilon} d\eta \frac{\cosh(\eta+\chi)}{\sinh^5(\eta+\chi)} \frac{1}{\sinh^4(\lambda\eta-\lambda\chi)} + \int_{C_1} d\eta \frac{\cosh(\eta+\chi)}{\sinh^5(\eta+\chi)} \frac{1}{\sinh^4(\lambda\eta-\lambda\chi)} \\ &+ \int_{-\chi+\epsilon}^{\chi-\epsilon} d\eta \frac{\cosh(\eta+\chi)}{\sinh^5(\eta+\chi)} \frac{1}{\sinh^4(\lambda\eta-\lambda\chi)} + \int_{C_2} d\eta \frac{\cosh(\eta+\chi)}{\sinh^5(\eta+\chi)} \frac{1}{\sinh^4(\lambda\eta-\lambda\chi)} \\ &+ \int_{\chi+\epsilon}^{\infty} d\eta \frac{\cosh(\eta+\chi)}{\sinh^5(\eta+\chi)} \frac{1}{\sinh^4(\lambda\eta-\lambda\chi)} + (\chi\to-\chi)\Bigg],\end{aligned} \tag{C.12}$$

where the contours C_1 and C_2 represent respectively the integration variable going over the upper half-plane near $-\chi$ with $\eta = \epsilon e^{i\theta} - \chi$, and similarly the integration variable going over the upper half-plane near χ with $\eta = \epsilon e^{i\theta} + \chi$. The integrals are evaluated using the contour shown in Fig. B.1(b). Rearranging these integrals allows the cancellation of a few terms, and we are left with,

$$\begin{aligned}\langle I_T\rangle^{\rm int} = 4i\Gamma_1\Gamma_2\pi^8 T_1^4 T_2^4 \Bigg[&\int_{C_1} d\eta \frac{\cosh(\eta+\chi)}{\sinh^5(\eta+\chi)} \frac{1}{\sinh^4(\lambda\eta-\lambda\chi)} \\ &+ \int_{C_2} d\eta \frac{\cosh(\eta+\chi)}{\sinh^5(\eta+\chi)} \frac{1}{\sinh^4(\lambda\eta-\lambda\chi)} + (\chi\to-\chi)\Bigg].\end{aligned} \tag{C.13}$$

We now use the following expansions to compute the above integrals,

$$\begin{aligned}\frac{1}{\sinh^4(\epsilon e^{i\theta}+2\chi)} = &\frac{1}{\sinh^4(2\chi)} - \frac{4\epsilon e^{i\theta}\cosh(2\chi)}{\sinh^5(2\chi)} + \frac{\epsilon^2 e^{2i\theta}}{\sinh^4(2\chi)}\left[\frac{10\cosh^2(2\chi)}{\sinh^2(2\chi)} - 2\right] \\ &- \frac{4\epsilon^3 e^{3i\theta}}{3\sinh^4(2\chi)}\left[\frac{15\cosh^3(2\chi)}{\sinh^3(2\chi)} - \frac{7\cosh(2\chi)}{\sinh(2\chi)}\right] \\ &+ \frac{\epsilon^4 e^{4i\theta}}{3\sinh^4(2\chi)}\left[\frac{105\cosh^4(2\chi)}{\sinh^4(2\chi)} - \frac{80\cosh^2(2\chi)}{\sinh^2(2\chi)} + 7\right] + \mathcal{O}(\epsilon^5).\end{aligned} \tag{C.14}$$

Similarly, we have,

$$\begin{aligned}\frac{\cosh\left(\epsilon e^{i\theta}+2\chi\right)}{\sinh^5(\epsilon e^{i\theta}+2\chi)} = &\frac{\cosh(2\chi)}{\sinh(2\chi)} + \epsilon e^{i\theta}\left[\frac{1}{\sinh^4(2\chi)} - \frac{5\cosh^2(2\chi)}{\sinh^6(2\chi)}\right] - \epsilon^2 e^{2i\theta}\left[\frac{7\cosh(2\chi)}{\sinh^5(2\chi)} - \frac{15\cosh^3(2\chi)}{\sinh^7(2\chi)}\right] \\ &+ \frac{\epsilon^3 e^{3i\theta}}{3}\left[\frac{80\cosh^2(2\chi)}{\sinh^6(2\chi)} - \frac{105\cosh^4(2\chi)}{\sinh^8(2\chi)} - \frac{7}{\sinh^4(2\chi)}\right] + \mathcal{O}(\epsilon^4).\end{aligned} \tag{C.15}$$

Using these, we find the interference contribution to the thermal current,

$$\begin{aligned}\langle I_T\rangle^{\text{int}} = 4i\Gamma_1\Gamma_2\pi^8 T_1^4 T_2^4 \Bigg[&\int_\pi^0 d\theta i\epsilon e^{i\theta}\left[\frac{1}{\epsilon^5 e^{5i\theta}} - \frac{1}{3\epsilon^3 e^{3i\theta}} + \mathcal{O}(\epsilon)\right]\frac{1}{\sinh^4(\lambda\epsilon e^{i\theta} - 2\lambda\chi)} \\ &+ \int_\pi^0 d\theta i\epsilon e^{i\theta}\frac{\cosh\left(\epsilon e^{i\theta}+2\chi\right)}{\sinh^5(\epsilon e^{i\theta}+2\chi)}\left[\frac{1}{\epsilon^4\lambda^4 e^{4i\theta}} - \frac{2}{3\epsilon^2\lambda^2 e^{2i\theta}} + \mathcal{O}(\epsilon^0)\right] \\ &+ \int_\pi^0 d\theta i\epsilon e^{i\theta}\frac{\cosh\left(\epsilon e^{i\theta}-2\chi\right)}{\sinh^5(\epsilon e^{i\theta}-2\chi)}\left[\frac{1}{\epsilon^4\lambda^4 e^{4i\theta}} - \frac{2}{3\epsilon^2\lambda^2 e^{2i\theta}} + \mathcal{O}(\epsilon^0)\right] \\ &+ \int_\pi^0 d\theta i\epsilon e^{i\theta}\left[\frac{1}{\epsilon^5 e^{5i\theta}} - \frac{1}{3\epsilon^3 e^{3i\theta}} + \mathcal{O}(\epsilon)\right]\frac{1}{\sinh^4(\lambda\epsilon e^{i\theta} + 2\lambda\chi)}\Bigg]. \end{aligned} \tag{C.16}$$

Now we observe that all the terms with negative odd powers of ϵ give non-zero contributions, since we integrate from π to 0 (even powers of ϵ come with $e^{2in\theta}$ that gives zero on integration unless $n = 0$). The term of order ϵ^0 will also give a non-zero contribution. All positive powers of ϵ vanish since we take the $\epsilon \to 0$ limit at the end of the calculation. We need to make sure that the remaining ϵ-dependent terms with odd negative powers cancel out so that in the $\epsilon \to 0$ limit, the integral remains well behaved. Indeed that happens since in Eq. (C.16), we note that in the first and fourth integrals (and similarly the second and third integrals), the negative odd powers of ϵ terms come with opposite signs, which is how they cancel. Out of all these, the only remaining terms that give a non-zero contribution are ϵ^0-order terms,

$$\begin{aligned}\langle I_T\rangle^{\text{int}} = \Lambda\Bigg[&\int_\pi^0 d\theta i\frac{2\lambda^4}{3\sinh^4(2\lambda\chi)}\left[\frac{105\cosh^4(2\lambda\chi)}{\sinh^4(2\lambda\chi)} - \frac{80\cosh^2(2\lambda\chi)}{\sinh^2(2\lambda\chi)} + 7\right] \\ &- \int_\pi^0 d\theta i\frac{2}{3}\frac{\lambda^2}{\sinh^4(2\lambda\chi)}\left[\frac{10\cosh^2(2\lambda\chi)}{\sinh^2(2\lambda\chi)} - 2\right] \\ &+ \int_\pi^0 d\theta i\frac{1}{3}\left[\frac{80\cosh^2(2\chi)}{\sinh^6(2\chi)} - \frac{105\cosh^4(2\chi)}{\sinh^8(2\chi)} - \frac{7}{\sinh^4(2\chi)}\right]\frac{2}{\lambda^4} \\ &- \int_\pi^0 d\theta i\left[\frac{1}{\sinh^4(2\chi)} - \frac{5\cosh^2(2\chi)}{\sinh^6(2\chi)}\right]\frac{4}{3\lambda^2}\Bigg], \end{aligned} \tag{C.17}$$

where we defined $\Lambda = 4i\Gamma_1\Gamma_2\pi^8 T_1^4 T_2^4$ for convenience. This integral can now be computed to give,

$$\begin{aligned}\langle I_T\rangle^{\text{int}} = 4\Gamma_1\Gamma_2\pi^9 T_1^4 T_2^4\Bigg[&\frac{2\lambda^4}{3\sinh^4(2\lambda\chi)}\left[\frac{105\cosh^4(2\lambda\chi)}{\sinh^4(2\lambda\chi)} - \frac{80\cosh^2(2\lambda\chi)}{\sinh^2(2\lambda\chi)} + 7\right] \\ &+ \frac{2\lambda^2}{3\sinh^4(2\lambda\chi)}\left[2 - \frac{10\cosh^2(2\lambda\chi)}{\sinh^2(2\lambda\chi)}\right] \\ &- \frac{2}{3\lambda^4\sinh^4(2\chi)}\left[\frac{105\cosh^4(2\chi)}{\sinh^4(2\chi)} - \frac{80\cosh^2(2\chi)}{\sinh^2(2\chi)} + 7\right] \\ &- \frac{2}{3\lambda^2\sinh^4(2\chi)}\left[2 - \frac{10\cosh^2(2\chi)}{\sinh^2(2\chi)}\right]\Bigg]. \end{aligned} \tag{C.18}$$

Plugging back the values of χ and λ gives,

$$\begin{aligned}\langle I_T\rangle^{\text{int}} = \frac{8}{3}\Gamma_1\Gamma_2\pi^9\Bigg\{ & \frac{T_2^8}{\sinh^4(2\pi T_2 x_{21})}\left[\frac{105\cosh^4(2\pi T_2 x_{21})}{\sinh^4(2\pi T_2 x_{21})} - \frac{80\cosh^2(2\pi T_2 x_{21})}{\sinh^2(2\pi T_2 x_{21})} + 7\right] \\ & + \frac{T_1^2 T_2^6}{\sinh^4(2\pi T_2 x_{21})}\left[2 - \frac{10\cosh^2(2\pi T_2 x_{21})}{\sinh^2(2\pi T_2 x_{21})}\right] \\ & - \frac{T_1^8}{\sinh^4(2\pi T_1 x_{21})}\left[\frac{105\cosh^4(2\pi T_1 x_{21})}{\sinh^4(2\pi T_1 x_{21})} - \frac{80\cosh^2(2\pi T_1 x_{21})}{\sinh^2(2\pi T_1 x_{21})} + 7\right] \\ & - \frac{T_1^6 T_2^2}{\sinh^4(2\pi T_1 x_{21})}\left[2 - \frac{10\cosh^2(2\pi T_1 x_{21})}{\sinh^2(2\pi T_1 x_{21})}\right]\Bigg\}. \end{aligned} \tag{C.19}$$

Finally, combining the interference and non-interference contributions to the thermal current gives the total tunneling thermal current,

$$\begin{aligned}\langle I_T\rangle = {} & \pi^9(\Gamma_1^2+\Gamma_2^2)\frac{4}{2835}[41(T_2^8 - T_1^8) + 62T_1^2T_2^2(T_2^4 - T_1^4)] + \frac{8}{3}\Gamma_1\Gamma_2\pi^9\Bigg[\\ & + T_1^2T_2^6\,\text{csch}^4(2\pi T_2 x_{21})\left[2 - 10\coth^2(2\pi T_2 x_{21})\right] \\ & - T_1^6T_2^2\,\text{csch}^4(2\pi T_1 x_{21})\left[2 - 10\coth^2(2\pi T_1 x_{21})\right] \\ & + T_2^8\,\text{csch}^4(2\pi T_2 x_{21})\left[105\coth^4(2\pi T_2 x_{21}) - 80\coth^2(2\pi T_2 x_{21}) + 7\right] \\ & - T_1^8\,\text{csch}^4(2\pi T_1 x_{21})\left[105\coth^4(2\pi T_1 x_{21}) - 80\coth^2(2\pi T_1 x_{21}) + 7\right]\Bigg]. \end{aligned} \tag{C.20}$$

We now analyze this expression by varying $X_1 \equiv 2\pi T_1 x_{21}/v$ at a fixed ratio $n \equiv T_2/T_1$ (Fig. C.1(a)), and then by varying the ratio of the temperatures at a fixed $X_1 \equiv 2\pi T_1 x_{21}/v$ (Fig. C.1(b)). If the two edges of the spin liquids are maintained at constant temperatures, the parameter X_1 is controlled by the distance between the two constrictions x_{21}. We also see from Fig. C.1(a) that as $X_1 \to 0$, at $\Gamma_1 = \Gamma_2$, the tunneling thermal current equals twice the non-interference contribution $\langle I_T\rangle_\Gamma^{\text{non-int}}$ indicated by the broken line in Fig. C.1(a).

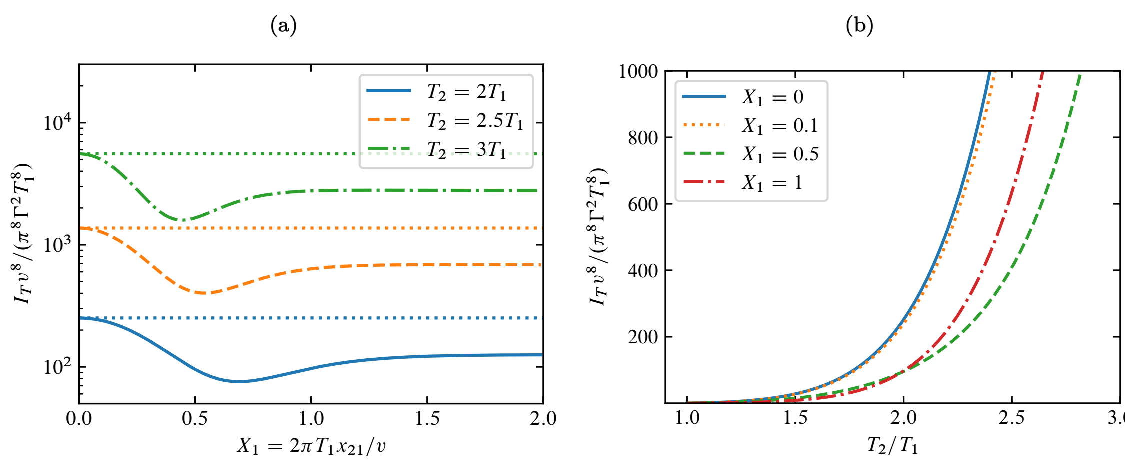

Figure C.1: Thermal current between two spin liquids when $\Gamma_1 = \Gamma_2 = \Gamma$. (a) Variation with X_1 at a fixed temperature ratio. The broken line shows the value of $2\langle I_T\rangle_\Gamma^{\text{non-int}}$. (b) Variation with $n = T_2/T_1$ shows the expected monotonic behavior.

Appendix D

Decomposition of correlation functions of Ising fields

In this appendix, we demonstrate how the correlation functions of the fields defined on two edges can be decomposed into the product of two correlation functions of the fields on the same edge. To achieve this, we assume that the two edges are connected by a long section of length L. We will take this length to be infinite to achieve the decomposition.

The tunneling operators create two excitations that fuse to vacuum on both sides of the constriction at x_0. Since Ising anyons are their own antiparticles, the form of the tunneling operator at the times t and t' is

$$T_{12} \equiv \sigma_2(x_0,t)\sigma_1(x_0,t) \tag{D.1a}$$

$$T_{34} \equiv \sigma_2(x_0,t')\sigma_1(x_0,t'), \tag{D.1b}$$

up to a constant factor $\sim \exp(-i\pi/16)$. The subscript on the Ising field corresponds to the edge on which it is defined, and since the two edges are assumed to be connected, the two fields can be written in terms of each other as $\sigma_2(x_0) = \sigma_1(L - x_0)$. Notice however, this is well defined only in the $L \to \infty$ limit. We use the following coordinates,

$$u_1 = t - x_0 \tag{D.2a}$$

$$u_2 = t - (-x_0 + L) \tag{D.2b}$$

$$u_3 = t' - x_0 \tag{D.2c}$$

$$u_4 = t' - (-x_0 + L) \tag{D.2d}$$

and assume that the edge velocity $v = 1$. In this convention, the four-point functions can then be computed using the relation [25]

$$\langle T_{12}T_{34}\rangle^2 = \frac{1}{2}\left[\left(\frac{z_{13}z_{24}}{z_{12}z_{23}z_{34}z_{14}}\right)^{1/4} + \left(\frac{z_{14}z_{23}}{z_{13}z_{24}z_{12}z_{34}}\right)^{1/4}\right], \tag{D.3}$$

where $z_{ij} = \sin[\pi T(\epsilon + iu_{ij})]/\pi T$, and $u_{ij} \equiv u_i - u_j$. Notice that when we take the $L \to \infty$ limit, the first term drops out and we arrive at the expression,

$$\langle T_{12}T_{34}\rangle \sim \frac{1}{\sqrt{2}}\frac{e^{i\pi/8}}{(z_{13}z_{24})^{1/8}}\left(\frac{\sinh(\pi T u_{14})\sinh(\pi T u_{32})}{\sinh(\pi T u_{12})\sinh(\pi T u_{34})}\right)^{1/8} \xrightarrow{L\to\infty} \frac{e^{i\pi/8}}{\sqrt{2}(z_{13}z_{24})^{1/8}} \tag{D.4}$$

We now notice that the final expression, after taking the limit, can be written as a product of two-point functions defined on one of the edges, Eq. (2.25). Therefore,

$$\langle\sigma_2(x_0,t)\sigma_1(x_0,t)\sigma_2(x_0,t')\sigma_1(x_0,t')\rangle = \frac{e^{i\pi/8}}{\sqrt{2}}\langle\sigma_2(x_0,t)\sigma_2(x_0,t')\rangle\langle\sigma_1(x_0,t)\sigma_1(x_0,t')\rangle. \tag{D.5}$$

The choice of the branch in the above formula is dictated by the hermiticity of the tunneling operators $\sim \exp(-i\pi/16)\sigma_2\sigma_1$. Indeed, the average of the square of a tunneling operator must be real and positive.

Appendix E

σ tunneling

In this appendix, we compute the thermal tunneling current due to Ising anyon tunneling at two point contacts at x_1 and x_2 in the Fabry–Pérot geometry (Fig. 2.3 (a)). The single constriction calculation is the non-interference part $\langle I_T \rangle_{\Gamma_j}^{\text{non-int}}$ of the full calculation presented in this appendix with contributions from only one of the tunneling amplitudes $\Gamma_j,\ j = 1, 2$. We assume identical distances between the tunneling contacts along the two edges and identical edge velocities on the two edges. Since the result depends only on the sum of the edge lengths (Appendix I), the first assumption can be easily removed.

In the calculation, we assume that the interferometer confines a trivial topological charge. We generalize to an arbitrary confined charge in the main text.

The full tunneling Hamiltonian is given by,

$$H_T = e^{-i\pi/16}\Gamma_1\sigma_2(x_1,t)\sigma_1(x_1,t) + e^{-i\pi/16}\Gamma_2\sigma_2(x_2,t)\sigma_1(x_2,t). \tag{E.1}$$

We define the current operator using the Heisenberg equation of motion,

$$I_T^{(1)} = \frac{\partial H_1}{\partial t} = -i[H_1, H] = -i[H_1, H_T], \tag{E.2}$$

where H_1 and H_2 correspond to the free field Hamiltonian (2.1) defined on the left- and right-moving edges respectively. From here, we identify the current operator as,

$$I_T^{(1)} = -e^{-i\pi/16}\Gamma_1\sigma_2(x_1,t)\partial_t\sigma_1(x_1,t) - e^{-i\pi/16}\Gamma_2\sigma_2(x_2,t)\partial_t\sigma_1(x_2,t), \tag{E.3}$$

where all Heisenberg operators are defined in terms of the edge Hamiltonian without tunneling. Using perturbation theory, we obtain the expectation value of the thermal current due to the tunneling, to the lowest non-zero order,

$$\langle I_T^{(1)}(t)\rangle = -i\int_{-\infty}^{t} dt' \langle [I_T^{(1)}(t), H_T(t')]\rangle. \tag{E.4}$$

Inserting the operators into the above expression gives,

$$\begin{aligned}\langle I_T^{(1)}(t)\rangle = ie^{-i\pi/8}\int_{-\infty}^{t} dt' \Big[&\Gamma_1^2\langle\big[\sigma_2(x_1,t)\partial_t\sigma_1(x_1,t),\sigma_2(x_1,t')\sigma_1(x_1,t')\big]\rangle\\ &+\Gamma_2^2\langle\big[\sigma_2(x_2,t)\partial_t\sigma_1(x_2,t),\sigma_2(x_2,t')\sigma_1(x_2,t')\big]\rangle\\ &+\Gamma_1\Gamma_2\langle\big[\sigma_2(x_1,t)\partial_t\sigma_1(x_1,t),\sigma_2(x_2,t')\sigma_1(x_2,t')\big]\rangle\\ &+\Gamma_1\Gamma_2\langle\big[\sigma_2(x_2,t)\partial_t\sigma_1(x_2,t),\sigma_2(x_1,t')\sigma_1(x_1,t')\big]\rangle\Big].\end{aligned} \tag{E.5}$$

From here we see that the thermal current is composed of non-interference and interference contributions, $\langle I_T\rangle = \sum_{j=1,2}\langle I_T\rangle_{\Gamma_j}^{\text{non-int}} + \langle I_T\rangle^{\text{int}}$. The thermal correlation functions are

$$\langle\sigma_1(x_1,t_1)\sigma_1(x_2,t_2)\rangle = \frac{(\pi T_1)^{1/8}}{\sin^{1/8}[\pi T_1(\epsilon + i(t_1-t_2+x_2-x_1))]} \tag{E.6}$$

$$\langle\sigma_2(x_1,t_1)\sigma_2(x_2,t_2)\rangle = \frac{(\pi T_2)^{1/8}}{\sin^{1/8}[\pi T_2(\epsilon + i(t_1-t_2+x_1-x_2))]} \tag{E.7}$$

and, of course, the cross-correlations go to zero in the $L\to\infty$ limit (Appendix D). To simplify notations, we set $v=1$. In the following two subsections, we separately focus on the non-interference and interference contributions.

E.1 Non-interference term

Using the above correlation functions and the results of Appendix D on the four-point correlation functions, we first compute the expression for the non-interference contribution ($j=1,2$).

$$\begin{aligned}\langle I\rangle_{\Gamma_j}^{\text{non-int}} = \frac{\Gamma_j^2}{8\sqrt{2}}\int_{-\infty}^{t} dt' \Bigg[&\frac{(\pi T_2)^{\frac{1}{8}}(\pi T_1)^{\frac{9}{8}}\cos[\pi T_1(\epsilon+i(t-t'))]}{\sin^{\frac{9}{8}}[\pi T_1(\epsilon+i(t-t'))]\sin^{\frac{1}{8}}[\pi T_2(\epsilon+i(t-t'))]}\\ &+\frac{(\pi T_2)^{\frac{1}{8}}(\pi T_1)^{\frac{9}{8}}\cos[\pi T_1(\epsilon+i(t'-t))]}{\sin^{\frac{9}{8}}[\pi T_1(\epsilon+i(t'-t))]\sin^{\frac{1}{8}}[\pi T_2(\epsilon+i(t'-t))]}\Bigg].\end{aligned} \tag{E.8}$$

Defining $\pi T_1(t-t')\equiv\tau$ and $n=T_2/T_1$, we can simplify the above integral,

$$\begin{aligned}\langle I_T\rangle_{\Gamma_j}^{\text{non-int}} &= -\frac{\Gamma_j^2}{8\sqrt{2}}(\pi T_1)^{\frac{1}{8}}(\pi T_2)^{\frac{1}{8}}\int_{\infty}^{0} d\tau\left[\frac{\cos(i\tau+\epsilon)}{\sin^{\frac{9}{8}}(i\tau+\epsilon)\sin^{\frac{1}{8}}[n(i\tau+\epsilon)]}+\frac{\cos(-i\tau+\epsilon)}{\sin^{\frac{9}{8}}(-i\tau+\epsilon)\sin^{\frac{1}{8}}[n(-i\tau+\epsilon)]}\right]\\ &= \frac{\Gamma_j^2}{8\sqrt{2}}(\pi T_1)^{\frac{1}{8}}(\pi T_2)^{\frac{1}{8}}\int_{-\infty}^{\infty} d\tau\ \frac{\cos(-i\tau+\epsilon)}{\sin^{\frac{9}{8}}(-i\tau+\epsilon)\sin^{\frac{1}{8}}[n(-i\tau+\epsilon)]}.\end{aligned} \tag{E.9}$$

To evaluate the integral, we deform the contour as shown in Fig. B.1(a),

$$\begin{aligned}\langle I_T\rangle_{\Gamma_j}^{\text{non-int}} = \frac{\Gamma_j^2}{8\sqrt{2}}(\pi T_1)^{\frac{1}{8}}(\pi T_2)^{\frac{1}{8}}\Bigg[&\int_{-\infty}^{-\epsilon}\frac{d\tau\ \cos(-i\tau)}{\sin^{\frac{9}{8}}(-i\tau)\sin^{\frac{1}{8}}(-in\tau)}+\int_C\frac{d\tau\ \cos(-i\tau)}{\sin^{\frac{9}{8}}(-i\tau)\sin^{\frac{1}{8}}(-in\tau)}\\ &+\int_{\epsilon}^{\infty}\frac{d\tau\ \cos(-i\tau)}{\sin^{\frac{9}{8}}(-i\tau)\sin^{\frac{1}{8}}(-in\tau)}\Bigg].\end{aligned} \tag{E.10}$$

Near the origin, the integration variable can be written as $\tau = \epsilon e^{i\theta}$. Carefully taking the $\epsilon \to 0$ limit and writing the integrands in terms of hyperbolic functions, we get a phase factor depending upon the location on the contour,

$$\langle I_T \rangle^{\text{non-int}}_{\Gamma_j} = \frac{\Gamma_j^2}{8\sqrt{2}} (\pi T_1)^{\frac{1}{8}} (\pi T_2)^{\frac{1}{8}} \left[\int_\epsilon^\infty \frac{d\tau\ e^{-i\frac{5\pi}{8}} \cosh \tau}{\sinh^{\frac{9}{8}} \tau \sinh^{\frac{1}{8}}(n\tau)} + \int_C \frac{d\tau\ \cos(-i\tau)}{\sin^{\frac{9}{8}}(-i\tau) \sin^{\frac{1}{8}}(-in\tau)} \right.$$
$$\left. + \int_\epsilon^\infty \frac{d\tau\ e^{i\frac{5\pi}{8}} \cosh \tau}{\sinh^{\frac{9}{8}} \tau \sinh^{\frac{1}{8}}(n\tau)} \right] \tag{E.11}$$

$$\langle I_T \rangle^{\text{non-int}}_{\Gamma_j} = \frac{\Gamma_j^2}{8\sqrt{2}} (\pi T_1)^{\frac{1}{8}} (\pi T_2)^{\frac{1}{8}} \left[\int_\epsilon^\infty \frac{d\tau\ 2\cos(5\pi/8) \cosh \tau}{\sinh^{\frac{9}{8}} \tau \sinh^{\frac{1}{8}}(n\tau)} + \int_C \frac{d\tau\ \cos(-i\tau)}{\sin^{\frac{9}{8}}(-i\tau) \sin^{\frac{1}{8}}(-in\tau)} \right]. \tag{E.12}$$

To evaluate the integral over the contour C, we note that $\tau \sim \epsilon$, so we expand the integrand as,

$$\left. \frac{\cos(-i\tau)}{\sin^{\frac{9}{8}}(-i\tau) \sin^{\frac{1}{8}}(-in\tau)} \right|_{\tau=0} = \frac{1}{n^{\frac{1}{8}} (-i\tau)^{\frac{5}{4}}} + \mathcal{O}(\tau^{\frac{3}{4}}). \tag{E.13}$$

Since $d\tau = i\tau d\theta$, in the $\epsilon \to 0$ limit, higher order terms vanish. The only remaining term is

$$\int_C \frac{d\tau\ \cos(-i\tau)}{\sin^{\frac{9}{8}}(-i\tau) \sin^{\frac{1}{8}}(-in\tau)} = \int_C d\tau \frac{1}{n^{\frac{1}{8}} (-i\tau)^{\frac{5}{4}}} = e^{i\frac{5\pi}{8}} \int_\pi^0 d\theta\ i\epsilon e^{i\theta} \frac{1}{n^{\frac{1}{8}} \epsilon^{\frac{5}{4}} e^{i\frac{5\theta}{4}}} = -\frac{4}{n^{\frac{1}{8}} \epsilon^{\frac{1}{4}}} 2\cos(5\pi/8). \tag{E.14}$$

We note that the divergence of this term cancels the divergence of the first integral in Eq. (E.12). We thus write it in a similar form,

$$\frac{4}{\epsilon^{\frac{1}{4}}} = \int_\epsilon^\infty d\tau \frac{1}{\tau^{\frac{5}{4}}}. \tag{E.15}$$

Therefore the expression for the non-interference term is

$$\sum_{j=1,2} \langle I_T \rangle^{\text{non-int}}_{\Gamma_j} = \frac{(\Gamma_1^2 + \Gamma_2^2)}{4\sqrt{2}} (\pi T_1)^{\frac{1}{8}} (\pi T_2)^{\frac{1}{8}} \cos(5\pi/8) \int_0^\infty d\tau \left[\frac{\cosh(\tau)}{\sinh^{\frac{9}{8}}(\tau) \sinh^{\frac{1}{8}}(n\tau)} - \frac{1}{n^{\frac{1}{8}} \tau^{\frac{5}{4}}} \right]$$
$$= \frac{(\Gamma_1^2 + \Gamma_2^2)}{4\sqrt{2}} (\pi T_1)^{\frac{1}{8}} (\pi T_2)^{\frac{1}{8}} \cos(3\pi/8)\ F_{\text{non-int}}(n), \tag{E.16}$$

where we defined $F_{\text{non-int}}(n)$ as in Eq. (2.29). Note that the non-interference contribution, individually for each of Γ_j, $j = 1, 2$, is exactly what we obtain when we consider single-constriction geometry. Results discussed in the main text in Sec. 2.4.1 corresponds to $\langle I_T \rangle^{\text{non-int}}_{\Gamma_j}$ where Γ_j is set to Γ of the single constriction.

E.2 Interference term

We now look at the interference contribution.

$$\langle I_T \rangle^{\text{int}} = \frac{\Gamma_1 \Gamma_2}{8\sqrt{2}} (\pi T_1)^{\frac{9}{8}} (\pi T_2)^{\frac{1}{8}} \int_{-\infty}^t dt' \left[\frac{\cos[\pi T_1(\epsilon + i(t - t' + x_{21}))]}{\sin^{\frac{9}{8}}[\pi T_1(\epsilon + i(t - t' + x_{21}))] \sin^{\frac{1}{8}}[\pi T_2(\epsilon + i(t - t' - x_{21}))]} \right.$$
$$\left. + \frac{\cos[\pi T_1(\epsilon - i(t - t' + x_{21}))]}{\sin^{\frac{9}{8}}[\pi T_1(\epsilon - i(t - t' + x_{21}))] \sin^{\frac{1}{8}}[\pi T_2(\epsilon - i(t - t' - x_{21}))]} + (x_{21} \leftrightarrow -x_{21}) \right] \tag{E.17}$$

Defining $\tau \equiv \pi T_1(t-t')$, $\chi \equiv \pi T_1 x_{21}$, and $n = T_2/T_1$, we may simplify the above integral,

$$\langle I_T\rangle^{\text{int}} = \frac{\Gamma_1\Gamma_2}{8\sqrt{2}}(\pi T_1)^{\frac{1}{8}}(\pi T_2)^{\frac{1}{8}}\int_{-\infty}^{\infty} d\tau\Bigg[\frac{\cos[\epsilon - i(\tau-\chi)]}{\sin^{\frac{9}{8}}[\epsilon - i(\tau-\chi)]\sin^{\frac{1}{8}}[n(\epsilon - i(\tau+\chi))]} + \frac{\cos[\epsilon - i(\tau+\chi)]}{\sin^{\frac{9}{8}}[\epsilon - i(\tau+\chi)]\sin^{\frac{1}{8}}[n(\epsilon - i(\tau-\chi))]}\Bigg] \tag{E.18}$$

Like before, we can now deform the contour as shown in Fig. B.1(b),

$$\langle I_T\rangle^{\text{int}} = \frac{\Gamma_1\Gamma_2}{8\sqrt{2}}(\pi T_1)^{\frac{1}{8}}(\pi T_2)^{\frac{1}{8}}\left[\int_{-\infty}^{-\chi-\epsilon} d\tau\ I + \int_{C_1} d\tau\ I + \int_{-\chi+\epsilon}^{\chi-\epsilon} d\tau\ I + \int_{C_2} d\tau\ I + \int_{\chi+\epsilon}^{\infty} d\tau\ I \quad + \quad (\chi \leftrightarrow -\chi)\right], \tag{E.19}$$

where the integrand I is given as

$$I = \frac{\cos[-i(\tau-\chi)]}{\sin^{\frac{9}{8}}[-i(\tau-\chi)]\sin^{\frac{1}{8}}[-in(\tau+\chi)]}. \tag{E.20}$$

The integration variable near $-\chi$ is given by $\eta = \epsilon e^{i\theta} - \chi$, the integration variable near χ is given by $\eta = \epsilon e^{i\theta} + \chi$. We now look at each contribution to (E.19) individually. In particular,

$$\int_{-\infty}^{-\chi-\epsilon} d\tau \frac{\cos[-i(\tau-\chi)]}{\sin^{\frac{9}{8}}[-i(\tau-\chi)]\sin^{\frac{1}{8}}[-in(\tau+\chi)]} = \int_{\chi+\epsilon}^{\infty} d\tau \frac{e^{-i\frac{5\pi}{8}}\cosh(\tau+\chi)}{\sinh^{\frac{9}{8}}(\tau+\chi)\sinh^{\frac{1}{8}}[n(\tau-\chi)]} \tag{E.21}$$

$$\int_{-\infty}^{-\chi-\epsilon} d\tau \frac{\cos[-i(\tau+\chi)]}{\sin^{\frac{9}{8}}[-i(\tau+\chi)]\sin^{\frac{1}{8}}[-in(\tau-\chi)]} = \int_{\chi+\epsilon}^{\infty} d\tau \frac{e^{-i\frac{5\pi}{8}}\cosh(\tau-\chi)}{\sinh^{\frac{9}{8}}(\tau-\chi)\sinh^{\frac{1}{8}}[n(\tau+\chi)]} \tag{E.22}$$

Similarly,

$$\int_{\chi+\epsilon}^{\infty} d\tau \frac{\cos[-i(\tau-\chi)]}{\sin^{\frac{9}{8}}[-i(\tau-\chi)]\sin^{\frac{1}{8}}[-in(\tau+\chi)]} = \int_{\chi+\epsilon}^{\infty} d\tau \frac{e^{i\frac{5\pi}{8}}\cosh(\tau-\chi)}{\sinh^{\frac{9}{8}}(\tau-\chi)\sinh^{\frac{1}{8}}[n(\tau+\chi)]} \tag{E.23}$$

$$\int_{\chi+\epsilon}^{\infty} d\tau \frac{\cos[-i(\tau+\chi)]}{\sin^{\frac{9}{8}}[-i(\tau+\chi)]\sin^{\frac{1}{8}}[-in(\tau-\chi)]} = \int_{\chi+\epsilon}^{\infty} d\tau \frac{e^{i\frac{5\pi}{8}}\cosh(\tau+\chi)}{\sinh^{\frac{9}{8}}(\tau+\chi)\sinh^{\frac{1}{8}}[n(\tau-\chi)]} \tag{E.24}$$

Combining Eqs. (E.21-E.24) together gives,

$$\begin{aligned}\mathbb{I}_1 &\equiv \int_{-\infty}^{-\chi-\epsilon} d\tau\,[I + (\chi\leftrightarrow-\chi)] + \int_{\chi+\epsilon}^{\infty} d\tau\,[I + (\chi\leftrightarrow-\chi)] \\ &= 2\cos(5\pi/8)\int_{\chi+\epsilon}^{\infty} d\tau\left[\frac{\cosh(\tau-\chi)}{\sinh^{\frac{9}{8}}(\tau-\chi)\sinh^{\frac{1}{8}}[n(\tau+\chi)]} + (\chi\leftrightarrow-\chi)\right]\end{aligned} \tag{E.25}$$

In the final expression, we make a variable shift $\tau \to \tau - \chi$, giving,

$$\mathbb{I}_1 = 2\cos(5\pi/8)\int_{\epsilon}^{\infty} d\tau\left[\frac{\cosh(\tau)}{\sinh^{\frac{9}{8}}(\tau)\sinh^{\frac{1}{8}}[n(\tau+2\chi)]} + \frac{\cosh(\tau+2\chi)}{\sinh^{\frac{9}{8}}(\tau+2\chi)\sinh^{\frac{1}{8}}(n\tau)}\right] \tag{E.26}$$

We now look at the integrals corresponding to path C_1 in Eq. (E.19),

$$\int_{C_1} d\tau \frac{\cos[-i(\tau-\chi)]}{\sin^{\frac{9}{8}}[-i(\tau-\chi)]\sin^{\frac{1}{8}}[-in(\tau+\chi)]} \sim \int_{\pi}^{0} d\theta i\epsilon e^{i\theta} \frac{e^{-i\frac{5\pi}{8}}\cosh(2\chi)}{\sinh^{\frac{9}{8}}(2\chi)(n\epsilon e^{i\theta})^{\frac{1}{8}}} \xrightarrow{\epsilon\to 0} 0 \tag{E.27}$$

$$\begin{aligned}
\int_{C_1} d\tau \frac{\cos[-i(\tau+\chi)]}{\sin^{\frac{9}{8}}[-i(\tau+\chi)]\sin^{\frac{1}{8}}[-in(\tau-\chi)]} &= \int_{\pi}^{0} d\theta\ i\epsilon e^{i\theta} \frac{\cos\left(-i\epsilon e^{i\theta}\right)}{\sin^{\frac{9}{8}}(-i\epsilon e^{i\theta})\sin^{\frac{1}{8}}[in(2\chi-\epsilon e^{i\theta})]} \\
&= \int_{\pi}^{0} d\theta\ i\epsilon e^{i\theta} \frac{1}{(-i\epsilon e^{i\theta})^{\frac{9}{8}}\sin^{\frac{1}{8}}(in2\chi)} \\
&= \frac{e^{i\frac{\pi}{2}}}{\sinh^{\frac{1}{8}}(2n\chi)} \int_{\pi}^{0} d\theta\ i\epsilon e^{i\theta} \frac{1}{\epsilon^{\frac{9}{8}} e^{i\frac{9\theta}{8}}} \\
&= \frac{-e^{i\frac{\pi}{2}}(1-e^{-i\frac{\pi}{8}})}{\sinh^{\frac{1}{8}}(2n\chi)} \int_{\epsilon}^{\infty} d\tau \frac{1}{\tau^{9/8}}
\end{aligned} \tag{E.28}$$

Similarly, the integrals corresponding to path C_2,

$$\begin{aligned}
\int_{C_2} d\tau \frac{\cos[-i(\tau-\chi)]}{\sin^{\frac{9}{8}}[-i(\tau-\chi)]\sin^{\frac{1}{8}}[-in(\tau+\chi)]} &= \int_{\pi}^{0} d\theta\ i\epsilon e^{i\theta} \frac{\cos\left(-i\epsilon e^{i\theta}\right)}{\sin^{\frac{9}{8}}(-i\epsilon e^{i\theta})\sin^{\frac{1}{8}}[-in(2\chi+\epsilon e^{i\theta})]} \\
&= \int_{\pi}^{0} d\theta\ i\epsilon e^{i\theta} \frac{1}{(-i\epsilon e^{i\theta})^{\frac{9}{8}}\sin^{\frac{1}{8}}(-in2\chi)} \\
&= \frac{e^{i\frac{5\pi}{8}}}{\sinh^{\frac{1}{8}}(2n\chi)} \int_{\pi}^{0} d\theta\ i\epsilon e^{i\theta} \frac{1}{\epsilon^{\frac{9}{8}} e^{i\frac{9\theta}{8}}} \\
&= \frac{-e^{i\frac{5\pi}{8}}(1-e^{-i\frac{\pi}{8}})}{\sinh^{\frac{1}{8}}(2n\chi)} \int_{\epsilon}^{\infty} d\tau \frac{1}{\tau^{9/8}}
\end{aligned} \tag{E.29}$$

$$\int_{C_2} d\tau \frac{\cos[-i(\tau+\chi)]}{\sin^{\frac{9}{8}}[-i(\tau+\chi)]\sin^{\frac{1}{8}}[-in(\tau-\chi)]} \sim \int_{0}^{\pi} d\theta i\epsilon e^{i\theta} \frac{e^{i\frac{5\pi}{8}}\cosh(2\chi)}{\sinh^{\frac{9}{8}}(2\chi)(n\epsilon e^{i\theta})^{\frac{1}{8}}} \xrightarrow{\epsilon\to 0} 0 \tag{E.30}$$

Combining the non-zero contributions from Eqs. (E.27-E.30),

$$\mathbb{I}_2 \equiv \int_{C_1+C_2} d\tau[I+(\chi\leftrightarrow-\chi)] = \frac{-(e^{i\frac{\pi}{2}}-e^{i\frac{3\pi}{8}}+e^{i\frac{5\pi}{8}}-e^{i\frac{\pi}{2}})}{\sinh^{\frac{1}{8}}(2n\chi)} \int_{\epsilon}^{\infty} d\tau \frac{1}{\tau^{9/8}} = \frac{-2\cos(5\pi/8)}{\sinh^{\frac{1}{8}}(2n\chi)} \int_{\epsilon}^{\infty} d\tau \frac{1}{\tau^{9/8}} \tag{E.31}$$

Finally, the integrals over the interval $[-\chi+\epsilon, \chi-\epsilon]$ in Eq. (E.19) are

$$\int_{-\chi+\epsilon}^{\chi-\epsilon} d\tau \frac{\cos[-i(\tau-\chi)]}{\sin^{\frac{9}{8}}[-i(\tau-\chi)]\sin^{\frac{1}{8}}[-in(\tau+\chi)]} = e^{-i\pi/2} \int_{-\chi+\epsilon}^{\chi-\epsilon} d\tau \frac{\cosh(\chi-\tau)}{\sinh^{\frac{9}{8}}(\chi-\tau)\sinh^{\frac{1}{8}}[n(\chi+\tau)]} \tag{E.32}$$

$$\int_{-\chi+\epsilon}^{\chi-\epsilon} d\tau \frac{\cos[-i(\tau+\chi)]}{\sin^{\frac{9}{8}}[-i(\tau+\chi)]\sin^{\frac{1}{8}}[-in(\tau-\chi)]} = e^{i\pi/2} \int_{-\chi+\epsilon}^{\chi-\epsilon} d\tau \frac{\cosh(\chi+\tau)}{\sinh^{\frac{9}{8}}(\chi+\tau)\sinh^{\frac{1}{8}}[n(\chi-\tau)]} \tag{E.33}$$

Clearly the sum of these two integrals vanishes. Now we combine all non-zero contributions, specifically Eqs. (E.26) and (E.31). Notice that the divergences are canceled out once these integrals are combined to give the interference contribution to the thermal current as,

$$\begin{aligned}
\langle I_T \rangle^{\text{int}} &= \frac{\Gamma_1 \Gamma_2}{4\sqrt{2}} (\pi T_1)^{\frac{1}{8}} (\pi T_2)^{\frac{1}{8}} \cos(5\pi/8) \int_0^{\infty} d\tau \left[\frac{\cosh(\tau + 2\chi)}{\sinh^{\frac{9}{8}}(\tau + 2\chi) \sinh^{\frac{1}{8}}(n\tau)} \right. \\
&\quad \left. + \frac{\cosh(\tau)}{\sinh^{\frac{9}{8}}(\tau) \sinh^{\frac{1}{8}}(n\tau + 2n\chi)} - \frac{1}{\tau^{\frac{9}{8}} \sinh^{\frac{1}{8}}(2n\chi)} \right] \\
&= \frac{\Gamma_1 \Gamma_2}{4\sqrt{2}} (\pi T_1)^{\frac{1}{8}} (\pi T_2)^{\frac{1}{8}} \cos(3\pi/8)\ F_{\text{int}}(n, \chi)
\end{aligned} \tag{E.34}$$

where we defined the function $F_{\text{non-int}}(n, \chi)$ as in Eq. (2.33). We thus arrive at the expression for the total thermal current due to anyon tunneling,

$$\langle I_T \rangle = \frac{(\pi T_1)^{\frac{1}{8}} (\pi T_2)^{\frac{1}{8}} \cos(3\pi/8)}{4\sqrt{2}} \left[(\Gamma_1^2 + \Gamma_2^2)\ F_{\text{non-int}}(n) + \Gamma_1 \Gamma_2\ F_{\text{int}}(n, \chi) \right] \tag{E.35}$$

The edge velocity was set to 1 above. Therefore the answer should be divided by $v^{1/4}$.

Appendix F

Tunneling in Mach–Zehnder geometry

The purpose of this appendix is to find the additional phase α in the Mach–Zehnder tunneling Hamiltonian, Eq. (2.34). We will do this with three different methods, all of which produce the same result. The first approach involves the calculation of a partition function in conformal field theory (CFT) and will only be used for the Ising statistics. The second and third approaches will be applied to a general case. The second method builds on the algebraic theory of anyons. The third method uses detailed balance.

In our first approach we also use the principle of detailed balance, assuming that the temperatures of the edges are equal. For a stationary distribution, the transition probabilities $p^b_{\sigma a}$ satisfy the detailed balance equations, which state that the probabilities associated to the process $\sigma \times a \to b$ and the reverse process $\sigma \times b \to a$ are related. The two probabilities are given as,

$$p^b_{\sigma a} = \frac{2\pi}{\hbar} \sum_{nm} |\langle m|H_T|n\rangle|^2 \delta(E_m - E_n) P^a_n(T,T) \tag{F.1a}$$

$$p^a_{\sigma b} = \frac{2\pi}{\hbar} \sum_{nm} |\langle n|H_T|m\rangle|^2 \delta(E_n - E_m) P^b_m(T,T). \tag{F.1b}$$

Notice that these two probabilities differ only by the partition functions in the Gibbs factors $P^a_n = \exp(-E_n/T)/Z_a(T)$, where the partition functions are calculated in the superselection sectors defined by the topological charge a. Now the ratio of the two probabilities in the above equations equals the ratio of the partition functions, which can be computed using conformal field theory.

We first solve for the energy spectrum of fermions on each of the two edges. This calls for the choice of the boundary conditions, periodic (Ramond), or anti-periodic (Neveu–Schwarz). The two are related by a twist field operator σ of conformal dimension $h_\sigma = 1/16$, which is precisely the Ising field we worked with in Sec. 2.4.1. This then leads to the following spectra in the two sectors [25]:

$$H_{\text{R.}} = \frac{2\pi}{L}\left[\sum_{k>0} k c_{-k} c_k + \frac{1}{24}\right] \qquad k \in \mathbb{Z} \quad \text{(Ramond)} \tag{F.2}$$

$$H_{\text{N.S.}} = \frac{2\pi}{L}\left[\sum_{k>0} k c_{-k} c_k - \frac{1}{48}\right] \qquad k \in (\mathbb{Z}+1/2) \quad \text{(Neveu–Schwarz)} \tag{F.3}$$

The energy spectra in the two sectors can now be used to compute the partition functions of the system in the fermionic, ψ, and anyonic, σ, topological sectors. Notice that the above equations correspond to only one of the edges. To compute the partition function of the full system we also take into account the other edge independently of the first. We now calculate the partition function of one of the edges for the ψ sector that corresponds to the Ramond boundary case,

$$\begin{aligned} Z_\psi = \operatorname{Tr}\left(e^{-\beta H_{\text{R.}}}\right) &= \operatorname{Tr}\left(\prod_{k\in\mathbb{Z}^+} \exp(-2\pi\beta k \hat{n}_k/L)\exp(-2\pi\beta/24L)\right) \\ &= \prod_{k\in\mathbb{Z}^+} \exp(-2\pi\beta/24L)\Big(1+\exp(-2\pi\beta k/L)\Big). \end{aligned} \tag{F.4}$$

For the σ sector that corresponds to the Neveu–Schwarz boundary case, we get a similar expression except that the sum runs over $(\mathbb{Z}+1/2)$,

$$\begin{aligned} Z_\sigma = \operatorname{Tr}\left(e^{-\beta H_{\text{N.S.}}}\right) &= \operatorname{Tr}\left(\prod_{k\in\mathbb{Z}^+\cup\{0\}} \exp\Big(-2\pi\beta(k+1/2)\hat{n}_{k+\frac{1}{2}}/L\Big)\exp(2\pi\beta/48L)\right) \\ &= \prod_{k\in\mathbb{Z}^+\cup\{0\}} \exp(2\pi\beta/48L)\Big(1+\exp(-2\pi\beta k/L)\exp(-\pi\beta/L)\Big) \end{aligned} \tag{F.5}$$

The overall exponential factor in both partition functions is irrelevant since in the thermodynamic limit $L\to\infty$, it gives 1. We now compute the ratio of the remaining product terms,

$$P \equiv \frac{\prod_{k\in\mathbb{Z}^+}(1+\exp(-2\pi\beta k/L))}{\prod_{k\in\mathbb{Z}^+\cup\{0\}}(1+\exp\{(-2\pi\beta k/L)\}\exp(-\pi\beta/L))} \tag{F.6}$$

$$\log P = -\log(2) + \sum_{k=0}^{\infty}\left[\log\left(1+\exp(-2\pi\beta k/L)\right) - \log(1+\exp(-2\pi\beta k/L)\exp(-\pi\beta/L))\right] \tag{F.7}$$

Since we are interested in the thermodynamic limit, we take the continuum limit. Substituting $2\pi\beta k/L = t$, we have $\sum_{k\in\mathbb{Z}\cup\{0\}} \to (L/2\pi\beta)\int_0^\infty dt$. Therefore we have,

$$\begin{aligned} \log(P) &= -\log(2) - \frac{L}{2\pi\beta}\int_0^\infty dt\, \log\left(\frac{1+e^{-t}e^{-\pi\beta/L}}{1+e^{-t}}\right) \\ &= -\log(2) + \frac{1}{2}\int_0^\infty dt\left(\frac{e^{-t}}{1+e^{-t}}\right) + \mathcal{O}\left(\frac{1}{L}\right) \qquad \text{(F.8)} \\ &= -\log(2) + \frac{1}{2}\log(2) + \mathcal{O}\left(\frac{1}{L}\right) \xrightarrow{L\to\infty} \log\left(\frac{1}{\sqrt{2}}\right) \qquad \text{(F.9)} \end{aligned}$$

As mentioned before, a free system is described by the sum of free Hamiltonians on each edge of the interferometer and therefore, the total partition function will be the product of the two partition functions obtained above. Thus,

$$\frac{Z_{\psi}^{\text{total}}}{Z_{\sigma}^{\text{total}}} = \frac{1}{2}. \tag{F.10}$$

This then gives the detailed balance condition $p^{\sigma}_{\sigma\psi} = 2p^{\psi}_{\sigma\sigma}$, and from the comparison with the tunneling probabilities from Sec. 2.4.3,

$$p^{\sigma}_{\sigma\psi} = p(T_1,T_2)|\Gamma_1 - \Gamma_2 e^{i\alpha}|^2, \qquad p^{\psi}_{\sigma\sigma} = \frac{p(T_1,T_2)}{2}|\Gamma_1 - \Gamma_2 e^{i\alpha - i\pi/4}|^2, \tag{F.11}$$

we obtain the phase $\alpha = \pi/8 + n\pi$. The choice of the integer n has no effect on physics. As a consistency check, it can be seen that this choice of α also makes the tunneling Hamiltonian (2.34) Hermitian. Indeed this phase can also be directly computed by demanding Hermiticity condition as we now demonstrate.

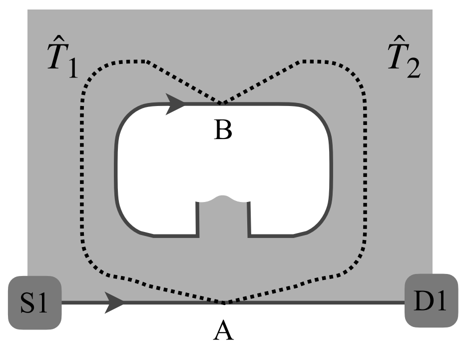

Figure F.1: In the low-energy effective model of a Mach–Zehnder interferometer, the two tunneling operators $\hat{T}_{1,2}$ describe anyon transfer along the two dashed lines between points A and B.

In this discussion we do not specialize to the case of the Ising statistics and only assume that the tunneling anyon x is its own antiparticle. We simply demand that the tunneling Hamiltonian $H_T = \Gamma_1\hat{T}_1 + \Gamma_2\hat{T}_2 e^{i\alpha}$ be Hermitian, and compare H_T and $H_T^{\dagger}$. Note that this Hamiltonian corresponds to the case when the tunneling anyon x is its own anti-particle. The case $x \neq \bar{x}$ is treated in Secs. 2.5.3 and 2.5.5.

We observe that the statistical phase $\exp\left(i\phi^{c}_{ab}\right)$ describes the phase accumulated by an anyon a on a full counterclockwise circle around an anyon b under the assumption that the two anyons fuse to c. Restricting ourselves to the low-energy effective model, we see that the two tunneling operators $\hat{T}_{1,2}$, transfer anyons between the same points, taking them from point A on the lower edge to point B on the upper edge, see Fig. F.1. This forms a closed loop, and therefore allows us to relate the two tunneling operators, restricted to a particular topological sector, via a statistical phase $\exp\left(i\phi^{c}_{ab}\right)$. However, since we deal with non-Abelian anyons, we also need to restrict ourselves to a particular fusion channel. Therefore we introduce the projectors $\Pi_a = \Pi_a^{\dagger}$ that project to the sector with the trapped topological charge a. Using this we can now relate the two tunneling operators as,

$$\Pi_c \hat{T}_2 \Pi_b = \Pi_c \hat{T}_1 \Pi_b \exp(i\phi^{c}_{xb}). \tag{F.12}$$

The Hermiticity of the tunneling Hamiltonian requires $\hat{T}_2 e^{i\alpha} = \hat{T}_2^\dagger e^{-i\alpha}$. We can now restrict this tunneling operator to a particular fusion channel,

$$\Pi_c \hat{T}_2 \Pi_b e^{i\alpha} = (\Pi_b \hat{T}_2 \Pi_c)^\dagger e^{-i\alpha}. \tag{F.13}$$

We observe that the operator on the left hand side transfers an anyon x from point A on the lower edge to point B on the upper edge when initially the trapped topological charge is b, and at the end, x and b fuse to c inside the Mach–Zehnder interferometer. The operator on the right hand side however describes the reverse process. We now make use of the relation in Eq. (F.12) and the relation $\hat{T}_1 = \hat{T}_1^\dagger$ to obtain,

$$e^{2i\alpha} \Pi_c \hat{T}_1 \Pi_b = \theta_x^2 \Pi_c \hat{T}_1 \Pi_b, \tag{F.14}$$

where we used the equation $\exp\left(i\phi_{xb}^c\right) = \theta_c/(\theta_x\theta_b)$. This fixes the phase $\exp(i\alpha) = \pm\theta_x$.

We now turn to another method to compute the phase α again using the principle of detailed balance. The heat current goes to zero in the case when the temperatures of the two edges are equal, however, the tunneling probabilities are non-zero. For a stationary distribution, the transition probabilities p_{xa}^b satisfy the detailed balance conditions between the processes $x \times a \to b$ and $x \times b \to a$. The probabilities are given by Eqs. (F.1a) and (F.1b) with x in place of σ. Notice that the probabilities of these processes differ only by their partition functions calculated in a particular superselection sector. We computed the ratio of the partition functions in different superselection sectors explicitly for the Ising anyon case and found it to be a constant that in turn gives the detailed balance condition. In fact we see that for a general case, the ratio of the partition functions, each computed in a particular superselection sector, is independent of the tunneling amplitudes $\Gamma_{1,2}$, and therefore the ratio of the probabilities p_{xa}^b/p_{xb}^a is independent of $\Gamma_{1,2}$. This restriction allows us to compare the probabilities of the mutually reverse processes and fix the phase α, provided the tunneling anyon, in this case anyon x, is other than a fermion or a boson. We may now compare the probabilities for the two processes $x \times a \to b$ and $x \times b \to a$,

$$p_{xa}^b = N_{xa}^b \frac{d_b}{d_x d_a} |\Gamma_1 + \Gamma_2 e^{i\alpha + i\phi_{xa}^b}|^2 p(T,T), \quad \text{and} \quad p_{xb}^a = N_{xb}^a \frac{d_a}{d_x d_b} |\Gamma_1 + \Gamma_2 e^{i\alpha + i\phi_{xb}^a}|^2 p(T,T). \tag{F.15}$$

As argued above, their ratio should be independent of $\Gamma_{1,2}$, which amounts to saying that the ratio $\lambda \equiv \frac{|\Gamma_1 + \Gamma_2 \exp(i\varphi_1)|^2}{|\Gamma_1 + \Gamma_2 \exp(i\varphi_2)|^2}$ is independent of $\Gamma_{1,2}$, where we defined $\varphi_1 = \alpha + \phi_{xa}^b$ and $\varphi_2 = \alpha + \phi_{xb}^a$. This gives a condition on the angles $\varphi_{1,2}$,

$$\cos(\varphi_1) - \lambda \cos(\varphi_2) = \frac{(\lambda - 1)(\Gamma_1^2 + \Gamma_2^2)}{2\Gamma_1\Gamma_2}. \tag{F.16}$$

We want this condition to be independent of $\Gamma_{1,2}$ for arbitrary $\Gamma_{1,2}$. This is only possible when $\lambda = 1$. This then gives, $\cos(\varphi_1) = \cos(\varphi_2)$, or $\varphi_1 = 2n\pi \pm \varphi_2$, where $n \in \mathbb{Z}$. The first case, $\varphi_1 = \varphi_2 \bmod 2\pi$, puts no restriction on α, when $\phi_{xa}^b = \phi_{xb}^a \bmod 2\pi$. This however implies that $\phi_{x\mathbf{1}}^x = \phi_{xx}^{\mathbf{1}}$. This is only possible for $\theta_x = \pm 1$, i.e., for tunneling particles, which are bosons or fermions. Assuming that is not the case, we use the other condition, $\varphi_1 = -\varphi_2 \bmod 2\pi$, to obtain a restriction on α,

$$e^{i\alpha} = \pm e^{-i\frac{(\phi_{xa}^b + \phi_{xb}^a)}{2}}. \tag{F.17}$$

Upon using $\exp\left(i\phi^{c}_{ab}\right) = \frac{\theta_c}{\theta_a\theta_b}$, we get $e^{i\alpha} = \pm\theta_x$ consistent with the Hermiticity condition, as well as the phase found for the special case of Ising anyons.

Appendix G

Topological order with unusual fusion rules

In Sec. 2.5.5, we consider anyon models having the following property: if $x \neq \bar{x}$, the fusion results of $x \times x$ and $a \times \bar{a}$ share no common topological charge for all possible a. It is not true that all anyon models satisfy this requirement. As a counterexample, an anyon model is constructed in this Appendix through the approach used in Ref. [105].

We briefly summarize the approach in this paragraph. Given a discrete group $\bar{H}$, one can extend it to a quasi-triangular Hopf algebra $D(\bar{H})$ with the basis $\{{}^{g}\lfloor_{x}\}_{g,x\in\bar{H}}$. Different representations of the Hopf algebra $D(\bar{H})$ are interpreted as anyons with different topological charges (called superselection sectors in [105]), and the representations are labeled in two steps: (1) find the Ath conjugacy class ${}^{A}C$ of H, of which ${}^{A}g_1$ is an element; (2) find the αth representation ${}^{\alpha}\Gamma$ of the centralizer ${}^{A}N$ of ${}^{A}g_1$ in $\bar{H}$. We use $|{}^{A}C, {}^{\alpha}\Gamma\rangle$ or Π^{A}_{α} to denote the topological charges or representations. An explicit construction of a representation of $D(\bar{H})$ is as follows: (1) Let ${}^{A}C = \{{}^{A}g_1, {}^{A}g_2, \ldots, {}^{A}g_k\}$; (2) choose representatives $\{{}^{A}x_1, {}^{A}x_2, \ldots, {}^{A}x_k\}$ of the equivalence classes in $\bar{H}/{}^{A}N$ under the requirement ${}^{A}g_i = {}^{A}x_i{}^{A}g_1{}^{A}x_i^{-1}$; (3) denote basis elements of the irreducible representation ${}^{\alpha}\Gamma$ as ${}^{\alpha}v_j$; (4) in the vector space V^{A}_{α} spanned by $|{}^{A}g_i, {}^{\alpha}v_j\rangle$, where $i = 1, 2, \ldots, \dim\alpha$ and $j = 1, 2, \ldots, k$, a representation of $D(\bar{H})$ is

$$\Pi^{A}_{\alpha}({}^{g}\lfloor_{x})|{}^{A}g_i, {}^{\alpha}v_j\rangle = \delta_{g, x\,{}^{A}g_i\,x^{-1}}|x\,{}^{A}g_i\,x^{-1}, {}^{\alpha}\Gamma\left({}^{A}x_l^{-1}\,x\,{}^{A}x_i\right){}^{\alpha}v_j\rangle, \tag{G.1}$$

where the index l is chosen by letting ${}^{A}g_l = x{}^{A}g_i x^{-1}$. To find the fusion rules, we consider the tensor product of two representations of the algebra $D(\bar{H})$, $\Pi^{A}_{\alpha} \otimes \Pi^{B}_{\beta}$. Using comultiplication $\Delta : D(\bar{H}) \to D(\bar{H}) \otimes D(\bar{H})$, one interprets the product as another representation of $D(\bar{H})$. The decomposition of the tensor product into irreducible representations,

$$\Pi^{A}_{\alpha} \otimes \Pi^{B}_{\beta} = N^{ABC}_{\alpha\beta\gamma}\Pi^{C}_{\gamma}, \tag{G.2}$$

is known as a fusion rule.

Here we only consider the sector whose conjugacy class is that of the identity element e of the group $\bar{H}$, also known as the magnetic vacuum sector. The conjugacy class is the set ${}^1C = \{e\}$. The centralizer ${}^1N$ is thus $\bar{H}$, and $\bar{H}/{}^1N$ contains only one equivalence class, namely $\bar{H}$, whose representative is chosen to be e. For a unitary irreducible representation ${}^\alpha\Gamma$ of ${}^1N = \bar{H}$, we can find the representation Π^1_α of $D(\bar{H})$ on the vector space spanned by the basis $|e, {}^1v_i\rangle$ as

$$\Pi^1_\alpha({}^{g}\llcorner_{x})|e, {}^\alpha v_i\rangle = \delta_{g,e}|e, {}^\alpha\Gamma(x){}^\alpha v_i\rangle. \tag{G.3}$$

The above representations of $D(\bar{H})$ are equivalent to those of $\bar{H}$. The tensor product of two representations of $\bar{H}$ can be decomposed into irreducible representations of $\bar{H}$. Hence, the fusion rule for Π^1_α, $\Pi^1_\alpha \otimes \Pi^1_\beta = N^{11\gamma}_{\alpha\beta 1}\Pi^1_\gamma$, is equivalent to ${}^\alpha\Gamma \otimes {}^\beta\Gamma = N^{11\gamma}_{\alpha\beta 1}{}^\gamma\Gamma$.

Table G.1: Character table of the group $C_2^3.F_8$, adapted from Ref. [106]. This group has 10 conjugacy classes, each of them corresponds to one column in the table. There are 10 irreducible representations, whose characters are shown in the rows. ζ_7 is used to denote $\exp(2\pi i/7)$ in this table.

class	1	2	4A	4B	7A	7B	7C	7D	7E	7F
size	1	7	28	28	64	64	64	64	64	64
ρ_1	1	1	1	1	1	1	1	1	1	1
ρ_2	1	1	1	1	ζ_7^4	ζ_7^6	ζ_7^2	ζ_7^5	ζ_7	ζ_7^3
ρ_3	1	1	1	1	ζ_7^2	ζ_7^3	ζ_7	ζ_7^6	ζ_7^4	ζ_7^5
ρ_4	1	1	1	1	ζ_7^5	ζ_7^4	ζ_7^6	ζ_7	ζ_7^3	ζ_7^2
ρ_5	1	1	1	1	ζ_7^3	ζ_7	ζ_7^5	ζ_7^2	ζ_7^6	ζ_7^4
ρ_6	1	1	1	1	ζ_7	ζ_7^5	ζ_7^4	ζ_7^3	ζ_7^2	ζ_7^6
ρ_7	1	1	1	1	ζ_7^6	ζ_7^2	ζ_7^3	ζ_7^4	ζ_7^5	ζ_7
ρ_8	7	7	-1	-1	0	0	0	0	0	0
ρ_9	14	-2	$-2i$	$2i$	0	0	0	0	0	0
ρ_{10}	14	-2	$2i$	$-2i$	0	0	0	0	0	0

Now we provide an example where $\bar{H} = C_2^3.F_8$ is a group of order 448. Table G.1 is its character table. Anyons corresponding to the representations in the table are denoted as $|e, \rho_i\rangle$. Note that this should not be confused with the basis $|e, {}^\alpha v_i\rangle$ used above.

Observe that ρ_9 and ρ_{10} are conjugate representations and their tensor product is $\rho_9 \times \rho_{10} = \rho_1 + \rho_2 + \cdots + \rho_7 + 3\rho_8 + 6\rho_9 + 6\rho_{10}$. The tensor product of ρ_9 with itself is $\rho_9 \times \rho_9 = 4\rho_8 + 6\rho_9 + 6\rho_{10}$. Identifying $|e, \rho_1\rangle$ as the vacuum, we find that $|e, \rho_9\rangle$ and $|e, \rho_{10}\rangle$ are mutual antiparticles, and further $|e, \rho_9\rangle \times |e, \rho_9\rangle \to |e, \rho_8\rangle$, $|e, \rho_{10}\rangle \times |e, \rho_9\rangle \to |e, \rho_8\rangle$. In the tunneling problem we considered, this means that both $|e, \rho_9\rangle$ and its antiparticle contribute to the process where the topological charge on edge 2 changes from $|e, \rho_9\rangle$ to $|e, \rho_8\rangle$. Hence, in general, one cannot separate the operators T and $T^\dagger$ as done in Eq. (2.51). However, as seen in this example, anyon models with such a property are complicated, so we omit the discussion of those models in the main text.

Appendix H

Calculation of the average noise

This appendix provides details of the noise calculation from Sec. 2.6. Specifically, we calculate the expectation value of some expressions containing the heat current with respect to the random variables s_{2k-1} and t_k. First, consider the expectation value of the heat current $I_T(t)$, Eq. (2.97),

$$\langle I_T(t)\rangle = I_0 + \Delta I \sum_{k=1}^{\infty} \langle s_k \rangle \theta(t-t_k). \tag{H.1}$$

After averaging over the Bernoulli random variables s_{2k-1}, the ΔI term vanishes, so we find that $\langle I_T(t)\rangle = I_0$. Then we consider the expression $I_T(0)I_T(t)$ in the definition of the noise (Eq. (2.95)),

$$I_T(0)I_T(t) = I_0^2 + I_0\Delta I\left(\sum_{k=1}^{\infty} s_k\theta(-t_k) + \sum_{k=1}^{\infty} s_k\theta(t-t_k)\right) + (\Delta I)^2\left(\sum_{k=1}^{\infty} s_k\theta(-t_k)\right)\left(\sum_{k=1}^{\infty} s_k\theta(t-t_k)\right). \tag{H.2}$$

To find the average, we choose to average over the Bernoulli random variables s_{2k-1} first, then we take the average over the Poisson process t_k. First, when averaging over all s_{2k-1}'s, only terms containing $s_{2k-1}s_{2k} = -1$ or $(s_k)^2 = 1$ are non-zero.

$$\langle I_T(0)I_T(t)\rangle_{\text{avg.}} = I_0^2 + (\Delta I)^2\left(\sum_{k=1}^{\infty} -\theta(-t_{2k-1})\theta(t-t_{2k}) - \theta(-t_{2k})\theta(t-t_{2k-1}) + \sum_{l=1}^{\infty}\theta(-t_l)\theta(t-t_l)\right). \tag{H.3}$$

Following the definition in Eq. (2.99), $N(0)$ is used to denote the total number of tunneling events up to the time $t=0$, and our subsequent analysis will depend on the parity of $N(0)$. When $N(0)$ is odd, we have $t_{2n-1} \leq 0 < t_{2n}$. The coefficient of $(\Delta I)^2$ is found to be

$$-\sum_{k=1}^{n}\theta(-t_{2k-1})\theta(t-t_{2k}) - \sum_{k=1}^{n-1}\theta(-t_{2k})\theta(t-t_{2k-1}) + \sum_{l=1}^{2n-1}\theta(-t_l)\theta(t-t_l) = \theta(t-t_{2n-1}) - \theta(t-t_{2n}). \tag{H.4}$$

The following integral appearing in the definition of the zero-frequency noise gives,

$$\lim_{\omega\to 0}\int dt\, e^{i\omega t}\left[\langle I_T(0)I_T(t)\rangle_{\text{avg.}} - \langle I_T(t)\rangle\langle I_T(0)\rangle\right] = (\Delta I)^2(t_{2n} - t_{2n-1}). \tag{H.5}$$

On the other hand, $N(0)$ being even is equivalent to the condition $t_{2n} \leq 0 < t_{2n+1}$. The coefficient of $(\Delta I)^2$ vanishes in such case:

$$-\sum_{k=1}^{n} \theta(-t_{2k-1})\theta(t - t_{2k}) - \sum_{k=1}^{n} \theta(-t_{2k})\theta(t - t_{2k-1}) + \sum_{l=1}^{2n} \theta(-t_l)\theta(t - t_l) = 0. \tag{H.6}$$

Thus, the corresponding integral in the definition of the noise also vanishes.

Finally we can find the average integral under the Poisson process given by the τ_k's. Since we know that only odd $N(0)$ contribute, the expectation value could be written as

$$(\Delta I)^2 \sum_{\substack{\text{odd } n, \\ n>0}} P(N(0) = n) \int_{t_0}^{0} dt_n \int_{0}^{\infty} dt_{n+1}\, f(t_{n+1}, t_n)\, (t_{n+1} - t_n), \tag{H.7}$$

where $f(t_{n+1}, t_n)$ is the joint conditional probability distribution function for t_n and t_{n+1} under the condition $N(0) = n$. Poisson process has the property that it is memoryless: given $N(0) = n$, t_{n+1} is exponentially distributed with the parameter λ and independent of the history up to time 0. Furthermore the distributions of t_{n+1} and t_n are independent, and we know that

$$E(t_{n+1}|N(0) = n) = \tau, \qquad E(t_n|N(0) = n) = \frac{t_0}{n+1}. \tag{H.8}$$

So the average coefficient of $(\Delta I)^2$ is

$$\sum_{\substack{\text{odd } n, \\ n>0}} e^{\lambda t_0} \frac{(-\lambda t_0)^n}{n!} \left(\tau - \frac{t_0}{n+1}\right) = e^{\lambda t_0} \tau \sinh(-\lambda t_0) + e^{\lambda t_0} \frac{1}{\lambda} \sum_{\text{odd } n} \frac{(-\lambda t_0)^{n+1}}{(n+1)!} \tag{H.9}$$

$$= e^{\lambda t_0} \tau \sinh(-\lambda t_0) + e^{\lambda t_0} \tau [\cosh(-\lambda t_0) - 1] \tag{H.10}$$

$$= \tau(1 - e^{\lambda t_0}). \tag{H.11}$$

It is now straightforward to obtain Eq. (2.101) in Sec. 2.6.

Appendix I

Dependence of the tunneling heat current on the size of the interferometer

In this appendix, we discuss the dependence of the tunneling heat current on the interferometer size. We consider topological orders allowing a single edge mode. One of such orders is the Ising order in Kitaev liquids. For simplicity, we assume that the edge velocity is coordinate-independent and identical on both edges. It is easy to generalize our results to coordinate-dependent velocities. We also assume that the tunneling operators at the two constrictions have precisely the same structure except for an overall amplitude multiplying the tunneling operator. The latter assumption is true for many topological orders as long as it is legitimate to focus on only the most relevant tunneling operator. As claimed in Sec. 2.2.2 and 2.2.3, the tunneling heat current in a Fabry–Pérot interferometer depends on the sum of the distances between the tunneling contacts along the two edges, $L_1 + L_2$. The heat current in a Mach–Zehnder interferometer depends on the difference of the distances $|L_1 - L_2|$.

We consider the tunneling of anyons of type x with an arbitrary statistics: $\hat{x}_{1,2}(y,t)$ is the operator that creates an anyon with topological charge x on edge 1 or 2 of the interferometer at position y and time t, and $\hat{\bar{x}}_{1,2}(y,t)$ creates its antiparticle. The two tunneling operators across one constriction are Hermitian conjugate to each other; we use $\hat{T} \sim \hat{x}_2(y,t)\hat{\bar{x}}_1(y,t)$ and $\hat{T}^\dagger \sim \hat{x}_1(y,t)\hat{\bar{x}}_2(y,t)$ to denote them. We adopt the following convention: when considering two separate edges, lower and upper, the coordinate axes on the two edges are always chosen to be in the same right-moving direction.

For a Fabry–Pérot geometry, on the lower edge (edge 1), the two constrictions are labeled by their coordinates y_1 and y_2, and the distance between them is $L_1 = y_2 - y_1$. We choose the coordinates on the upper edge (edge 2) to be y_1 and $y_2 + \ell$, then $L_2 = L_1 + \ell$. The tunneling Hamiltonian is given by

$$H_T = \Gamma_1 \hat{T}_1 + \Gamma_2 \hat{T}_2 + \text{H.c.} = \Gamma_1 \hat{x}_2(y_1,t)\hat{\bar{x}}_1(y_1,t) + \Gamma_2 \hat{x}_2(y_2+\ell,t)\hat{\bar{x}}_1(y_2,t) + \text{H.c.} \tag{I.1}$$

By the same argument as in Appendix E, the operator for the tunneling heat current is

$$I_T = \Gamma_1 \hat{T'}_1 + \Gamma_2 \hat{T'}_2 + \text{H.c.} = -\Gamma_1 \hat{x}_2(y_1,t)\partial_t \hat{\bar{x}}_1(y_1,t) - \Gamma_2 \hat{x}_2(y_2+\ell,t)\partial_t \hat{\bar{x}}_1(y_2,t) + \text{H.c.}, \tag{I.2}$$

where $\hat{T'}_{1,2} = -\hat{x}_2(y_1,t)\partial_t \hat{\bar{x}}_1(y_1,t)$ contains the time derivative on $\hat{\bar{x}}_1$. The derivative should be computed in the theory without tunneling. One can find the interference terms in the expectation value of the heat current as

$$-i\int_{-\infty}^{t} dt' \left\{ \Gamma_1\Gamma_2^* \langle [\hat{T'}_1(t), \hat{T}_2^\dagger(t')]\rangle + \Gamma_1\Gamma_2^* \langle [\hat{T'}_2^\dagger(t), \hat{T}_1(t')]\rangle - \text{H.c.} \right\}. \tag{I.3}$$

Due to the translational symmetry, the two-point correlation functions can be expressed as

$$\langle \hat{x}_1(y_1,t_1)\hat{\bar{x}}_1(y_2,t_2)\rangle = \langle \hat{\bar{x}}_1(y_1,t_1)\hat{x}_1(y_2,t_2)\rangle = G_1(t_1-t_2-y_1+y_2), \tag{I.4}$$

$$\langle \hat{x}_2(y_1,t_1)\hat{\bar{x}}_2(y_2,t_2)\rangle = \langle \hat{\bar{x}}_2(y_1,t_1)\hat{x}_2(y_2,t_2)\rangle = G_2(t_1-t_2+y_1-y_2). \tag{I.5}$$

Since the correlation functions of the form $\langle \hat{x}_2(y_1)\hat{\bar{x}}_1(y_2)\hat{x}_1(y_3)\hat{\bar{x}}_2(y_4)\rangle$ can be decomposed into conformal blocks $\langle \hat{x}_2(y_1)\hat{\bar{x}}_2(y_4)\rangle\langle \hat{\bar{x}}_1(y_2)\hat{x}_1(y_3)\rangle$, we find the following relations,

$$\langle \hat{T'}_1(t)\hat{T}_2^\dagger(t')\rangle - \langle \hat{T}_1(t')\hat{T'}_2^\dagger(t)\rangle \propto G_1'(t-t'+y_{21})G_2(t-t'-y_{21}-\ell) + (t \leftrightarrow t'), \tag{I.6}$$

where G' denotes the derivative of G, and

$$\langle \hat{T'}_2^\dagger(t)\hat{T}_1(t')\rangle - \langle \hat{T}_2^\dagger(t')\hat{T'}_1(t)\rangle \propto G_1'(t-t'-y_{21})G_2(t-t'+y_{21}+\ell) + (t \leftrightarrow t'). \tag{I.7}$$

Hence, the integral in Eq. (I.3) can be written as

$$\int_{-\infty}^{t} dt' \left\{ \langle [\hat{T'}_1(t), \hat{T}_2^\dagger(t')]\rangle + \langle [\hat{T'}_2^\dagger(t), \hat{T}_1(t')]\rangle \right\} \propto \int_{-\infty}^{\infty} d\tau \, [G_1'(\tau)G_2(\tau - 2y_{21} - \ell) + G_1'(\tau)G_2(\tau + 2y_{21} + \ell)]. \tag{I.8}$$

Combining this equation with Eq. (I.3), we find that the tunneling heat current in a Fabry–Pérot interferometer depends on $L_1 + L_2 = 2y_{21} + \ell$.

For the Mach–Zehnder geometry, we make the same choice for the coordinates of the two constrictions on the upper and lower edges. Naively, the tunneling Hamiltonian can be written as,

$$H_T = \Gamma_1 \hat{T}_1 + \Gamma_2 \hat{T}_2 + \text{H.c.} = \Gamma_1 \hat{x}_2(y_1,t)\hat{\bar{x}}_1(y_1,t) + \Gamma_2 \hat{x}_2(y_2+\ell,t)\hat{\bar{x}}_1(y_2,t) + \text{H.c.} \tag{I.9}$$

This naive Hamiltonian is actually incorrect though it will be useful to us below. The problem is that the above Hamiltonian violates locality: the two tunneling operators do not commute. The issue can be fixed in a systematic way with the help of Klein factors. Besides fixing the commutativity problem, the Klein factors keep track of the confined topological charge.

An alternative approach is based on Appendix F. The tunneling paths in the two constrictions run on the two sides of the hole in the interferometer. This leads to a number of technical challenges.

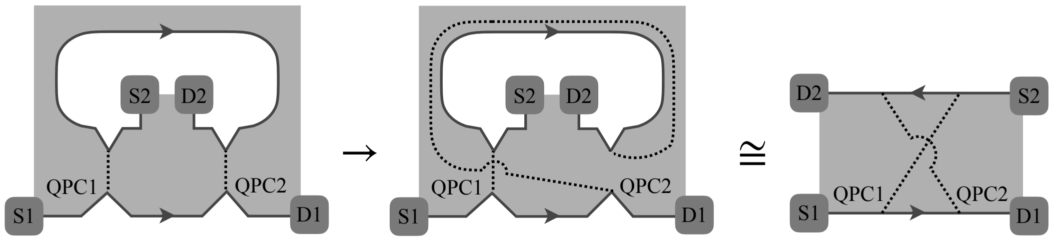

Figure I.1: Topology of a Mach–Zehnder interferometer. Dotted lines show tunneling contacts. The paths through QPC2 in the left panel can be deformed as in Appendix F. This results in the configuration from the right panel.

In particular, it becomes impossible to connect the upper and lower edges as in Appendix D. The problem can be solved by flipping one of the two tunneling paths to the other side of the hole (Fig. I.1) as in Appendix F. Klein factors are no longer needed after that since the topological charge between the tunneling paths no longer changes after each tunneling event. Also, the tunneling operators no longer have to commute since the two tunneling paths cross (Fig. I.1). Of course, this comes at the price of the model being useful for computing the tunneling probability only for a given value of the trapped topological charge in a given fusion channel with the tunneling anyon. This is enough, however, for the purposes of this appendix and justifies the use of the above non-local Hamiltonian.

In contrast to the Fabry–Pérot geometry, the two edges are co-propagating. The correlation function on edge 2 should be of the form,

$$\langle \hat{x}_2(y_1,t_1)\hat{\bar{x}}_2(y_2,t_2)\rangle = \langle \hat{\bar{x}}_2(y_1,t_1)\hat{x}_2(y_2,t_2)\rangle = G_2(t_1-t_2-y_1+y_2) \tag{I.10}$$

We focus on the interference contribution again,

$$\langle \hat{T'}_1(t)\hat{T}_2^\dagger(t')\rangle - \langle \hat{T}_1(t')\hat{T'}_2^\dagger(t)\rangle \propto G_1'(t-t'+y_{21})G_2(t-t'+y_{21}+\ell) + (t\leftrightarrow t'), \tag{I.11}$$

and

$$\langle \hat{T'}_2^\dagger(t)\hat{T}_1(t')\rangle - \langle \hat{T}_2^\dagger(t')\hat{T'}_1(t)\rangle \propto G_1'(t'-t-y_{21})G_2(t'-t-y_{21}-\ell) + (t\leftrightarrow t'). \tag{I.12}$$

Comparing with the expression for the interference contribution to the tunneling heat current in the Fabry–Pérot geometry, we can obtain the result for a Mach–Zehnder interferometer by replacing the parameter $2y_{21}+\ell$ with ℓ. We have consequently shown that the tunneling heat current in Mach–Zehnder interferometers depends on the difference of the distances between the two point contacts on the two edges, i.e. $|L_1 - L_2|$.

Appendix J

Series expansion of $P_{\rm o}(t,x)$

Ref. [51] provides a technique to represent $P_{\rm o}(t,x)$ as an exponential function of a series, for $\theta = \pi/4$ and $v_1 \to \infty$. We follow this technique in this appendix, and extend it to an arbitrary θ and a more general v_1, as well as to the finite-temperature regime.

J.1 Zero temperature

For the purpose of numerical integration, it is better to write $P_{\rm o}(t,a)$ as the product $P_1(a)P_2(t,a)P_3(t)$ of the following three expressions,

$$P_1(a) = \exp\Big(2m^2\nu_1 \int_0^\infty \frac{d\omega}{\omega} S_{11}^* e^{-\omega\delta}\Big), \tag{J.1}$$

$$P_2(t,a) = \exp\Big[m^2\nu_1 \int_0^\infty d\omega \frac{1}{\omega}(S_{12} + S_{12}^* - 2)e^{-i\omega t}e^{-\omega\delta}\Big], \tag{J.2}$$

$$\begin{aligned} P_3(t) &= \delta^{-2m^2\nu_1} \exp\Big[-2m^2\nu_1 \int_0^\infty \frac{d\omega}{\omega}(1-e^{-i\omega t})e^{-\omega\delta}\Big] \\ &= (\delta + it)^{-2m^2\nu_1}. \end{aligned} \tag{J.3}$$

We will set $v_1 = kv_2$, where k is an integer. All our plots correspond to such a choice of the velocities. It is straightforward to generalize to a rational k. The technique does not generalize to the case, where k is an irrational number, but this is irrelevant from the physical point of view. Now we take the coefficients S_{11} and S_{12} as functions of the dimensionless variable $\omega' = a\omega/v_1$. Expanding S_{11} and $S_{12}-1$ in series in $\xi = e^{i\omega'}$, we can find

$$S_{11} = \sum_{n=0}^{\infty} a_n(1-\xi)\xi^n, \tag{J.4}$$

$$S_{12} - 1 = \sum_{n=0}^{\infty} b_n(1-\xi)\xi^n, \tag{J.5}$$

where a_n and b_n are real numbers. Next, we will make use of the following formula,

$$f(\eta, A) = \int_0^\infty \frac{d\omega}{\omega}(1-e^{-i\omega\eta})e^{-\omega A} = \ln\Big(1 + i\frac{\eta}{A}\Big). \tag{J.6}$$

Therefore, P_1 and P_2 in Eqs. (J.1) and (J.2) can be expressed in the following form,

$$P_1(a) = \exp\Big\{2m^2\nu_1 \sum_{n=0}^{\infty} a_n f(1, in + \frac{v_1\delta}{a})\Big\}, \tag{J.7}$$

$$P_2(t,a) = \exp\Big\{m^2\nu_1 \sum_{n=0}^{\infty} b_n\big[f(-1, -in + i\frac{v_1 t}{a} + \frac{v_1\delta}{a})f(1, in + i\frac{v_1 t}{a} + \frac{v_1\delta}{a})\big]\Big\}. \tag{J.8}$$

For the purpose of numerical computations, we only keep a finite number of terms in these expansions, and the exact number of terms depends on the rate of convergence. One can show that the rate of convergence increases as we increase θ. For the curves shown in Fig. 3.11, we keep 400 terms for $\theta = \pi/32$; 300 terms for $\theta = \pi/16$; 100 terms for $\theta = \pi/8$; 80 terms for $\theta = \pi/4$.

J.2 Finite temperature

At a finite temperature T, $P_o(t,a)$ can be written as $P_1(a)P_2(t,a)P_3(t)$ as well. The finite-temperature expressions of the factors are

$$P_1(a) = \exp\left[2m^2\nu_1 \int_0^{\infty} \frac{d\omega}{\omega}\left(\frac{S_{11}^*}{1-e^{-\hbar\omega/T}} + \frac{S_{11}}{e^{\hbar\omega/T}-1}\right)e^{-\omega\delta}\right], \tag{J.9}$$

$$P_2(t,a) = \exp\left[m^2\nu_1 \int_0^{\infty} \frac{d\omega}{\omega}(S_{12}+S_{12}^*-2)\left(\frac{e^{-i\omega t}}{1-e^{-\hbar\omega/T}} + \frac{e^{i\omega t}}{e^{\hbar\omega/T}-1}\right)e^{-\omega\delta}\right], \tag{J.10}$$

$$P_3(t) = \delta^{-2m^2\nu_1}\exp\left[-2m^2\nu_1 \int_0^{\infty} \frac{d\omega}{\omega}\left(\frac{1-e^{-i\omega t}}{1-e^{-\hbar\omega/T}} + \frac{1-e^{i\omega t}}{e^{\hbar\omega/T}-1}\right)e^{-\omega\delta}\right] = \frac{(\pi T/\hbar)^{2m\nu_1^2}}{\sin^{2m\nu_1^2}[(\pi T/\hbar)(\delta+it)]}. \tag{J.11}$$

To derive an expansion at a finite temperature, a generalization of Eq. (J.6) is required. We use the following formula (for a derivation, see Ref. [21]),

$$\begin{aligned} g(\eta, A, \beta) &= \int_{2\pi/L}^{\infty} \frac{d\omega}{\omega}\left(\frac{e^{-i\omega\eta}}{1-e^{-\beta\omega}} + \frac{e^{i\omega\eta}}{e^{\beta\omega}-1}\right)e^{-\omega A} \\ &= -\ln\left\{\frac{2\beta}{L}\sin\left[\frac{\pi}{\beta}(A+i\eta)\right]\right\}, \end{aligned} \tag{J.12}$$

where the limit $L \to \infty$ is assumed. One can check the agreement with Eq. (J.6) by computing $g(\eta, A, \beta) - g(0, A, \beta)$ in the limit of $\beta \to \infty$.

We take the coefficients S_{11} and S_{12} as functions of the dimensionless variable $\omega' = a\omega/v_1$ again, but use a different expansion in $\xi = e^{i\omega'}$,

$$S_{11} = \sum_{n=0}^{\infty} c_n \xi^n, \tag{J.13}$$

$$S_{12} - 1 = \sum_{n=0}^{\infty} d_n \xi^n. \tag{J.14}$$

For a side note, one can derive the following relations between a_n, b_n and c_n, d_n,

$$c_n = a_n - a_{n-1}, \quad c_0 = a_0, \tag{J.15}$$

$$d_n = b_n - b_{n-1}, \quad d_0 = b_0. \tag{J.16}$$

In Eqs. (J.9) and (J.10), P_1 and P_2 can be represented as

$$P_1(a) = \exp\left[2m^2\nu_1 \sum_{n=0}^{\infty} c_n g(n, \frac{v_1\delta}{a}, \frac{\hbar v_1}{Ta})\right], \tag{J.17}$$

$$P_2(t,a) = \exp\left\{m^2\nu_1 \sum_{n=0}^{\infty} d_n [g(-n+\frac{v_1 t}{a}, \frac{v_1\delta}{a}, \frac{\hbar v_1}{Ta}) g(n+\frac{v_1 t}{a}, \frac{v_1\delta}{a}, \frac{\hbar v_1}{Ta})]\right\}. \tag{J.18}$$

J.3 Series representation of $P_{\mathrm{o}}(t,0)$

Finally, for the completeness of the discussion, we give an expansion for $P_{\mathrm{o}}(t,0)$ as well. At zero temperature, we write $P_{\mathrm{o}}(t,0)$ as $P_3(t)P_4(t)$, where $P_3(t)$ is given in Eq. (J.3) and $P_4(t)$ is

$$\exp\left\{m^2\nu_1 \int_0^{\infty} \frac{d\omega}{\omega}(S_{11}+S_{11}^*)(1-e^{-i\omega t})e^{-\omega\delta}\right\}. \tag{J.19}$$

We adopt the expansion of S_{11} in the form of Eq. (J.13). Therefore P_4 is represented as

$$\exp\left\{m^2\nu_1 \sum_{n=0}^{\infty} c_n \left[f(\frac{v_1 t}{a}, -in+\frac{v_1\delta}{a}) + f(\frac{v_1 t}{a}, in+\frac{v_1\delta}{a})\right]\right\}. \tag{J.20}$$

At a finite temperature, $P_3(t)$ is given in Eq. (J.11), and P_4 is

$$\exp\left\{m^2\nu_1 \int_0^{\infty} \frac{d\omega}{\omega}(S_{11}+S_{11}^*)\left(\frac{1-e^{-i\omega t}}{1-e^{-\hbar\omega/T}} + \frac{1-e^{i\omega t}}{e^{\hbar\omega/T}-1}\right)e^{-\omega\delta}\right\}, \tag{J.21}$$

which can be represented in the following series form,

$$\begin{aligned}\exp\Bigg\{m^2\nu_1 \sum_{n=0}^{\infty} c_n [&g(0, \frac{v_1\delta}{a}-in, \frac{\hbar v_1}{Ta}) - g(\frac{v_1 t}{a}, \frac{v_1\delta}{a}-in, \frac{\hbar v_1}{Ta}) \\ &+ g(0, \frac{v_1\delta}{a}+in, \frac{\hbar v_1}{Ta}) - g(\frac{v_1 t}{a}, \frac{v_1\delta}{a}+in, \frac{\hbar v_1}{Ta})]\Bigg\}.\end{aligned} \tag{J.22}$$

Appendix K

Effect of asymmetric bias and charge fluctuations on the Aharonov–Bohm phase

We need to consider the phase due to the accumulation of charge in the device, in addition to the usual Aharonov–Bohm phase. This additional phase depends on the bias voltages applied to the lower and upper edges. Also, as discussed in Appendix L, it exhibits discrete jumps when the charge on the closed inner channel changes between its allowed quantized values. In the first part of this Appendix, we explicitly calculate this additional phase for the $\nu = 2$ interferometer in terms of the bias voltages V_d, V_u, and the total charge of the inner mode Ne, where N is an integer. We also determine possible occupation numbers on the closed inner edge as functions of the bias at zero temperature. In the second subsection, we perform a similar calculation at $\nu = 2/5$.

K.1 $\nu = 2$

The charge density of the right- or left-moving $\nu = 1$ mode is $\pm\frac{e\partial_x\phi}{2\pi}$. We first write down the Hamiltonian in terms of the original outer and inner modes,

$$H = a\left[\frac{\hbar v_{\rm o}}{4\pi}(\partial_x\phi_{\rm o}^u)^2 + \frac{\hbar v_{\rm i}}{4\pi}(\partial_x\phi_{\rm i}^u)^2 + \frac{2\hbar w}{4\pi}(\partial_x\phi_{\rm o}^u)(\partial_x\phi_{\rm i}^u) + \frac{\hbar v_{\rm o}}{4\pi}(\partial_x\phi_{\rm o}^d)^2 + \frac{\hbar v_{\rm i}}{4\pi}(\partial_x\phi_{\rm i}^d)^2 + \frac{2\hbar w}{4\pi}(\partial_x\phi_{\rm o}^d)(\partial_x\phi_{\rm i}^d)\right]$$
$$-a\left[V_d\frac{e\partial_x\phi_{\rm o}^d}{2\pi} + V_u\left(-\frac{e\partial_x\phi_{\rm o}^u}{2\pi}\right)\right], \tag{K.1}$$

where $\pm e\partial_x\phi/2\pi$ stay for average time-independent charge densities, which do not depend on the coordinate on the lower and upper edges.

To find the phase factor, we must know the charge densities in the ground state. Therefore, we minimize the Hamiltonian with respect to the charge densities [39]. The total charge on the inner channel is Ne, therefore we have a constraint

$$\frac{e\partial_x\phi_{\rm i}^d}{2\pi} - \frac{e\partial_x\phi_{\rm i}^u}{2\pi} = \frac{Ne}{a}, \tag{K.2}$$

where a is the distance between the QPCs.

We first assume a constant $N = 0$. Differentiating the Hamiltonian with respect to the three variables $\partial_x\phi_{\rm i}^u$, $\partial_x\phi_{\rm o}^u$ and $\partial_x\phi_{\rm o}^d$, we find the condition for the extrema

$$\partial_x\phi_{\rm i}^u = q_{\rm i}^u = -\frac{e(V_d - V_u)w}{2\left(v_{\rm i}v_{\rm o} - w^2\right)}, \tag{K.3}$$

$$\partial_x\phi_{\rm o}^u = q_{\rm o}^u = -\frac{2eV_u v_{\rm i}v_{\rm o} - eV_u w^2 - eV_d w^2}{2v_{\rm o}\left(v_{\rm i}v_{\rm o} - w^2\right)}, \tag{K.4}$$

$$\partial_x\phi_{\rm o}^d = q_{\rm o}^i = \frac{2eV_d v_{\rm i}v_{\rm o} - eV_u w^2 - eV_d w^2}{2v_{\rm o}\left(v_{\rm i}v_{\rm o} - w^2\right)}. \tag{K.5}$$

To make the ground state expectation values $\langle\partial_x\phi_{\rm o/i}^{u/d}\rangle$ vanish, we shift the fields $\phi_{\rm o/i}^{u/d} \to \phi_{\rm o/i}^{u/d} - q_{\rm o/i}^{u/d}x$, and the additional phase factor for Γ_2 is then given by

$$\exp\left[i(q_{\rm o}^u - q_{\rm o}^d)a\right] = \exp\left[-\frac{ie(V_d + V_u)a}{\hbar v_{\rm o}}\right] \tag{K.6}$$

This phase depends only on the outer mode velocity $v_{\rm o}$.

Next, we consider the general case when the charge on the inner edge is $Ne \neq 0$ and induces an additional charge of $-Ne(w/v_{\rm o})$ on the outer edge. Then, the outer-edge phase factor is

$$\exp\left[\frac{-ie(V_d + V_u)a}{\hbar v_{\rm o}} + 2\pi i N\frac{w}{v_{\rm o}}\right]. \tag{K.7}$$

As an example, when $v_{\rm i} = v_{\rm o}$ and the ratio between the eigen-mode velocities is $v_1 = 5v_2$, from Eq. (3.5), we can find $v_{\rm o} = v_{\rm i} = 3v_2$ and $w = 2v_2$. Therefore, the phase jump due to each electron charge in the inner channel is $+4\pi/3$, which equals $-2\pi/3 \pmod{2\pi}$. At zero temperature, the phase jumps happen when the energy is the same for two subsequent values of N.

We now address the dynamics of N. To set up the kinetic equations, we need to count the number of the available states on the inner loop. To do this we introduce the chemical potential $eV_{\rm i}$ of the inner loop, that is, subtract $a\left[V_{\rm i}\frac{e}{2\pi}\partial_x\phi_{\rm i}^d - V_{\rm i}\frac{e}{2\pi}\partial_x\phi_{\rm i}^u\right]$ from the Hamiltonian. Our task is to count available values of the electron number n on the inner edge for $V_d > V_i > V_u$. The number of electrons that minimizes the Hamiltonian for a given choice of $V_{\rm i}$ is

$$N = [\beta_0\left(\frac{2v_o}{w}V_{\rm i} - V_u - V_d\right)], \tag{K.8}$$

where $[x]$ is the nearest integer to x and

$$\beta_0 = \frac{ea}{2\pi\hbar}\frac{w}{v_{\rm i}v_{\rm o} - w^2}. \tag{K.9}$$

Within the above model the maximal and minimal occupancy of the inner loop can be obtained by substituting $V_{\rm i} = V_d$ and $V_{\rm i} = V_u$. There is, however, two subtleties, which require a slight modification of our model. The inner loop may couple to various gates. In the simplest model, the electrostatic coupling shifts $V_{\rm i}$ by a constant. A similar shift is needed to accommodate the coupling of the current along the inner loop and the magnetic field [39]. With this in mind, we set $N = N_u \equiv [g_u]$ for $V_{\rm i} = V_u$ and $N = N_d \equiv [g_d]$ for $V_{\rm i} = V_d$, where the brackets mean the nearest integer,

$$g_u = \beta_0(\frac{2v_{\rm o}}{w}V_u - V_u - V_d) + \beta_1\lambda_1, \tag{K.10}$$

$$g_d = \beta_0(\frac{2v_{\rm o}}{w}V_d - V_u - V_d) + \beta_1\lambda_1, \tag{K.11}$$

and λ_1 is a control parameter, such as the magnetic flux. β_1 is a constant that depends on the details of the system. In general, multiple control parameters may be present. We ignore this point to make the notations simpler. We assume that $V_d > V_u$ and hence $N_d > N_u$. Then the range of possible number of electrons on the inner loop is between N_d and N_u.

K.2 $\nu = 2/5$

When $\nu = 2/5$, the Hamiltonian is given by

$$\begin{aligned} H = a\Big[&\frac{\hbar v_{\rm o}}{4\pi}(\partial_x\phi_{\rm o}^u)^2 + \frac{\hbar v_{\rm i}}{4\pi}(\partial_x\phi_{\rm i}^u)^2 + \frac{2\hbar w}{4\pi}(\partial_x\phi_{\rm o}^u)(\partial_x\phi_{\rm i}^u) \\ &+ \frac{\hbar v_{\rm o}}{4\pi}(\partial_x\phi_{\rm o}^d)^2 + \frac{\hbar v_{\rm i}}{4\pi}(\partial_x\phi_{\rm i}^d)^2 + \frac{2\hbar w}{4\pi}(\partial_x\phi_{\rm o}^d)(\partial_x\phi_{\rm i}^d) \\ &- V_d\sqrt{\nu_1}\frac{e\partial_x\phi_{\rm o}^d}{2\pi} - V_u\sqrt{\nu_1}\left(-\frac{e\partial_x\phi_{\rm o}^u}{2\pi}\right) - V_{\rm i}\sqrt{\nu_2}\frac{e}{2\pi}\partial_x\phi_{\rm i}^d + V_{\rm i}\sqrt{\nu_2}\frac{e}{2\pi}\partial_x\phi_{\rm i}^u\Big]. \end{aligned} \tag{K.12}$$

where $\nu_1 = 1/3$ and $\nu_2 = 1/15$. If we assume that quasiparticles with charge $\nu_1 e$ can tunnel into the inner edge from the outer edge channels, then a general restriction on the charge of the inner edge is

$$\sqrt{\nu_2}\frac{e\partial_x\phi_{\rm i}^d}{2\pi} - \sqrt{\nu_2}\frac{e\partial_x\phi_{\rm i}^u}{2\pi} = \frac{N\nu_1 e}{a}. \tag{K.13}$$

The Aharonov–Bohm phase introduced by the variation of the charge density in response to the voltage bias and the electric field of N quasiparticles on the inner edge is

$$\exp\left(i\varphi_{2/5}^{AB}\right) = \exp\left[i\sqrt{\nu_1}(\partial_x\phi_{\rm o}^u - \partial_x\phi_{\rm o}^d)a\right]. \tag{K.14}$$

It is computed the same way as at $\nu = 2$:

$$\exp\left(i\varphi_{2/5}^{AB}\right) = \exp\left\{i\left[-\frac{e\nu_1(V_d + V_u)a}{\hbar v_{\rm o}} + 2\pi N(\nu_1\sqrt{\nu_1}/\sqrt{\nu_2})\frac{w}{v_{\rm o}}\right]\right\} \tag{K.15}$$

There is also an additional statistical phase $2\pi N\nu_1$.

Just like at $\nu = 2$, we need to find the minimal and maximal numbers N_u and N_d of the quasiparticles, consistent with the chemical potentials V_u and V_d. The calculation follows the same route as at $\nu = 2$. We find $N_u = [g_u]$ and $N_d = [g_d]$, where the brackets mean the closest integer, with a slightly different definitions of $g_{u,d}$ than at $\nu = 2$,

$$g_u = \frac{\sqrt{\nu_2}}{\nu_1}\beta_0(\frac{2v_o}{w}\sqrt{\nu_2}V_u - \sqrt{\nu_1}V_u - \sqrt{\nu_1}V_d) + \beta_1\lambda_1; \tag{K.16}$$

$$g_d = \frac{\sqrt{\nu_2}}{\nu_1}\beta_0(\frac{2v_o}{w}\sqrt{\nu_2}V_d - \sqrt{\nu_1}V_u - \sqrt{\nu_1}V_d) + \beta_1\lambda_1. \tag{K.17}$$

Just like above, the $\beta_1\lambda_1$ term accounts the effect of the variations of the magnetic field and gate voltages on the closed inner loop.

Appendix L

Fourier Expansion with Phase Jumps

We discuss here effects of phase jumps arising from an integer constraint on the charge on a closed inner mode on the Fourier expansions of the interference current and the differential conductance. We limit our discussion to the short-time limit at $\nu = 2$. It also applies to linear transport.

Assume the effective Aharonov–Bohm phase φ can be written as

$$\varphi = C + \alpha_L + P(g) \tag{L.1}$$

where C is a constant,

$$\alpha_L = \sum_{j=0}^{N} \bar{\alpha}_j \lambda_j, \tag{L.2}$$

$$g = \sum_{j=0}^{N} \bar{\beta}_j \lambda_j, \tag{L.3}$$

and P is a periodic function of g, where λ_j, for $1 \leq j \leq N$ are parameters such as the magnetic field and various gate voltages, while $\lambda_0 = \tilde{V}$. The coefficients $\bar{\alpha}_j, \bar{\beta}_j$ are constants that depend on details of the system, and with no loss of generality, we can choose the period of P to be 1.

To describe sharp phase jumps, we choose P to be a sawtooth function,

$$P(g) = \bar{\gamma}(g - [g] + D), \tag{L.4}$$

where $[g]$ is the closest integer to g, and D is a constant. Such a choice is justified by the discussion in Section 3.2.5. Without loss of generality, we can set $D = 0$ by changing the value of C. Then

$$P(g) = \sum_{n} \gamma_n e^{2\pi i n g}, \tag{L.5}$$

where $\gamma_n = i\bar{\gamma}(-1)^n / 2\pi n$ and $\gamma_0 = 0$.

A similar expansion can be used in a situation where the inner mode is not perfectly reflected at the QPCs. In this case, the saw-tooth steps will be rounded, and the values of γ_n will fall off exponentially at large n.

In the same way, we can write

$$e^{iP(g)} = \sum_n c_n e^{2\pi i n g} = \sum_n c_n e^{2\pi i n(\bar{\beta}_0 \tilde{V} + \sum \bar{\beta}_j \lambda_j)}. \tag{L.6}$$

The coefficients c_n may be expanded in terms of products of the γ_n, if $\bar{\gamma}$ is small.

We wish to take the Fourier transform of $e^{i\varphi}$ with respect to one or more of the parameters λ_j for $j \geq 1$. In the simplest case, we just choose $j = 1$, and hold λ_j fixed for all other j. (Without loss of generality, we can set these parameters equal to zero by adjusting the constant C and shifting λ_1.)

Let us define

$$h(k) = \int_{-\infty}^{\infty} d\lambda_1 e^{-ik\lambda_1} e^{i\varphi} \tag{L.7}$$

We then find that

$$h(k) = 2\pi e^{iC} \sum_n c_n e^{i\tilde{V}(\bar{\alpha}_0 + 2\pi n \bar{\beta}_0)} \, \delta(k - \bar{\alpha}_1 - 2\pi n \bar{\beta}_1). \tag{L.8}$$

We see that a non-zero value of $\tilde{V}$ leads to linear shifts in phases but no change in the magnitudes of the various Fourier components.

If $\bar{\gamma} = 0$, we have

$$h(k) = 2\pi \delta(k - \bar{\alpha}_1) e^{i\bar{\alpha}_0 \tilde{V}} e^{iC} \tag{L.9}$$

More generally, if $\bar{\gamma} = 2\pi m$, where m is an integer, we have $c_n = 0$ for $n \neq m$, and

$$h(k) = 2\pi \delta(k - \bar{\alpha}_1 - 2\pi m \bar{\beta}_1) e^{i\tilde{V}(\bar{\alpha}_0 + 2\pi m \bar{\beta}_0)} e^{iC}. \tag{L.10}$$

If m is not an integer, h will contain multiple Fourier components, but the largest peak in $h(k)$ will correspond to the integer n that is closest to m.

As an example, we consider the case where the parameter $\lambda_1 = B\bar{A}$, where $\bar{A}$ is the nominal area enclosed by the outer edge mode, ignoring the small periodic area oscillations that occur as one varies parameters. Then $\bar{\alpha}_1 = e/\hbar$. We assume that the nominal area enclosed by inner mode is slightly smaller than $\bar{A}$, and we write it as $r\bar{A}$, where r is slightly smaller than 1. Then $2\pi\bar{\beta}_1 = re/\hbar$, The $n = 0$ peak of the Fourier transform then occurs at a frequency $k = e/\hbar$ while the $n = 1$ peak occurs at $k = (1+r)e/\hbar \approx 2e/\hbar$. In the limit of strong coupling, where $v_1/v_2 \to \infty$, we have $\bar{\gamma} \to 2\pi$, and only the $n = 1$ peak survives.

Using Eq. (3.44) from the main text, we have

$$I_{\text{int}} = \frac{\tilde{I}(V)}{2} \sum_n [e^{i\lambda_1(\bar{\alpha}_1 + 2\pi n \bar{\beta}_1)} e^{2\pi i n \bar{\beta}_0 \tilde{V}} c_n e^{iC} e^{i\bar{\alpha}_0 \tilde{V}} + \text{c.c.}]. \tag{L.11}$$

Then

$$\frac{dI_{\text{int}}}{dV} = \sum_n [(A_n + A'_n) e^{i\lambda_1(\bar{\alpha}_1 + 2\pi n \bar{\beta}_1)} e^{2\pi i n \bar{\beta}_0 \tilde{V}} + \text{c.c.}], \tag{L.12}$$

where

$$A_n = \frac{1}{2}\frac{d\tilde{I}}{dV}\, c_n e^{iC} e^{i\bar{\alpha}_0 \tilde{V}}, \tag{L.13}$$

$$A'_n = i\eta(\tilde{I}/2)\, c_n e^{iC} e^{i\bar{\alpha}_0 \tilde{V}} (2\pi n\bar{\beta}_0 + \bar{\alpha}_0), \tag{L.14}$$

and $\eta = d\tilde{V}/dV$. If we calculate $\int_{-\infty}^{\infty} d\lambda_1 e^{-ik\lambda_1}(dI_{\text{int}}/dV)$, the Fourier transform of (L.12), we will obtain a set of δ-function peaks at frequencies $k = k_n^{\pm} = \pm(\bar{\alpha}_1 + 2\pi n\bar{\beta}_1)$, with amplitudes given by $(A_n + A'_n)e^{2\pi i n\bar{\beta}_0 \tilde{V}}$ or its complex conjugate. If $\bar{\alpha}_1$ is not commensurate with $2\pi\bar{\beta}_1$, these peaks are distinct, and their amplitudes can be measured separately. The magnitudes will be independent of $\tilde{V}$ and will be given by

$$\mathcal{A}_n = (|A_n|^2 + |A'_n|^2)^{1/2}. \tag{L.15}$$

In our model, if one is in the strong coupling regime, where $\bar{\gamma}$ is close to 2π, the dominant coefficient c_n will come from $n = 1$, and the dominant term in (L.12) will come from $n = 1$.

If $\bar{\alpha}_1$ and $2\pi\bar{\beta}_1$ are commensurate, however, some of the peaks may coincide. Thus, if $r = 1$, we have $k_1^+ = k_{-3}^-$, resulting in a single peak with an amplitude $(A_1 + A'_1)e^{2\pi i\bar{\beta}_0 \tilde{V}} + (A_{-3}^* + A'^*_{-3})e^{6\pi i\bar{\beta}_0 \tilde{V}}$. Then, if c_{-3} is not negligible compared to c_1, the magnitude will depend on $\tilde{V}$ and on the phase offset e^{iC}. As remarked above, the coefficients other than c_1 all vanish in the limit of strong coupling between the modes.

The discussions above can be readily generalized to finite temperatures if one replaces $e^{iP(g)}$ in (L.6) by a thermal average $\langle e^{iP(g)}\rangle$ and takes into account the Gaussian phase distribution arising from thermal fluctuations of the charge on the outer edge. Thermal fluctuations will typically lead to an exponential decrease of the interference signal at high temperatures, with the weaker Fourier coefficients c_n decaying faster than the dominant one. The discussion can also be readily generalized to situations where one considers two or more parameters λ_j and takes a multidimensional Fourier transform with respect to them.

We finally comment on the slope $\frac{d\varphi}{d\tilde{V}}$. If $2a$ is taken to be the same for the two modes, we find

$$\bar{\alpha}_0 = 2\pi\bar{\beta}_0 = -2\frac{ea}{\hbar(v_\text{o} + w)}, \tag{L.16}$$

$$\bar{\gamma} = 2\pi w/v_\text{o}. \tag{L.17}$$

The slope $d\varphi/d\tilde{V}$ between phase jumps is then given by

$$\frac{d\varphi}{d\tilde{V}} = \bar{\alpha}_0 + \bar{\gamma}\bar{\beta}_0 = -2\frac{ea}{\hbar v_\text{o}}, \tag{L.18}$$

as found in Appendix K.

By contrast, the slope extracted in an interference experiment from the dominant $n = 1$ Fourier peak will be given by

$$\frac{\Delta\varphi}{\Delta\tilde{V}} = -4\frac{ea}{\hbar(v_\text{o} + w)}, \tag{L.19}$$

as implied by (L.11). This will be somewhat larger than the differential rate if $w < v_\text{o}$. This difference can also be understood from the results of Appendix K. When $\tilde{V}$ is increased by the amount necessary to change φ by 4π, the occupations of the inner and outer modes will have each increased by one, so that one phase jump will have occurred. If the negative charge jump on the outer mode has a magnitude less than one, this will reduce the change $\Delta\tilde{V}$ necessary to produce a net increase of one electron on the outer edge.

In Section 3.2.5, we average the phase factor over the distribution function f_N, where N is fluctuating between N_d and N_u. If we assume $V_d = V_u = \tilde{V}$, then $N_d = N_u$ and N would no longer fluctuate. The effective phases reduces to

$$\varphi = C + \alpha_0\lambda_1 + \alpha_1\lambda_1 + \gamma N, \tag{L.20}$$

where $N = [g]$ and $g = \kappa\beta_0\tilde{V} + \beta_1\lambda_1$. For the case of $\nu = 2$, $\kappa = 2(v_\mathrm{o} - w)/w$. Now φ has the same form as in Eq. (L.1), and one can hence make connections between the coefficients α_j, β_j and $\bar{\alpha}_j, \bar{\beta}_j$. We assume $\bar{\gamma} = \gamma + 2\pi l$, where l is an integer, and we have the following relations,

$$\bar{\alpha}_j + (2\pi l + \gamma)\bar{\beta}_j = \alpha_j, \tag{L.21}$$

$$-\bar{\beta}_0 = \kappa\beta_0, \tag{L.22}$$

$$-\bar{\beta}_1 = \beta_1. \tag{L.23}$$

Appendix M

Fourier expansion of a discontinuous function

We consider the Fourier expansion of the following function,

$$\exp[iC_1F(g+A)+iC_2F(g+B)] = \sum_m a_m e^{i2\pi mg}, \tag{M.1}$$

where A, B, C_1, C_2 are constants and $F(g) = g - [g]$. The form of the above function is motivated by Eq. (3.50). The Fourier coefficient a_m is given by the formula

$$a_m = \int_{-\frac{1}{2}}^{\frac{1}{2}} dg\, e^{-i2\pi mg} \exp[iC_1F(g+A)+iC_2F(g+B)]. \tag{M.2}$$

We find that $F(g+A)$ can be written as,

$$F(g+A) = F(g+A-\lfloor A\rfloor) = \begin{cases} g+A-\lfloor A\rfloor & -\frac{1}{2} < g < \frac{1}{2}-(A-\lfloor A\rfloor) \\ g+A-\lfloor A\rfloor - 1 & \frac{1}{2}-(A-\lfloor A\rfloor) < g < \frac{1}{2} \end{cases}. \tag{M.3}$$

In the following calculations, we will use the notation $a \equiv A - \lfloor A\rfloor$ and $b \equiv B - \lfloor B\rfloor$. We first assume that $a > b$. Then

$$C_1F(g+A)+C_2F(g+B) = \begin{cases} C_1(g+a)+C_2(g+b) & -\frac{1}{2} < g < \frac{1}{2}-a \\ C_1(g+a-1)+C_2(g+b) & \frac{1}{2}-a < g < \frac{1}{2}-b \\ C_1(g+a-1)+C_2(g+b-1) & \frac{1}{2}-b < g < \frac{1}{2} \end{cases}. \tag{M.4}$$

Next, a_m can be found as

$$\begin{aligned} a_m &= \frac{ie^{iC_1a+iC_2b}}{2\pi m - C_1 - C_2} e^{-i(2\pi m - C_1 - C_2)/2} \\ &\times [e^{-i(2\pi m-C_1-C_2)(-b)} e^{-iC_1}(-e^{-iC_2}+1) + e^{-i(2\pi m-C_1-C_2)(-a)}(-e^{-iC_1}+1)]. \end{aligned} \tag{M.5}$$

One can analyze the case of $a < b$ by the substitution $A \leftrightarrow B$ and $C_1 \leftrightarrow C_2$ so that

$$\begin{aligned} a_m &= \frac{ie^{iC_1 a + iC_2 b}}{2\pi m - C_1 - C_2} e^{-i(2\pi m - C_1 - C_2)/2} \\ &\times [e^{-i(2\pi m - C_1 - C_2)(-a)} e^{-iC_2}(-e^{-iC_1} + 1) + e^{-i(2\pi m - C_1 - C_2)(-b)}(-e^{-iC_2} + 1)]. \end{aligned} \tag{M.6}$$

Due to the definitions of a and b, there seems to be an apparent discontinuity in our coefficient a_m (M.5) and (M.6) when A or B is an integer. However, this discontinuity is actually absent. Indeed, in the limit $a \to 1^-$, b is less than a. We now use (M.5) and find that

$$\begin{aligned} a_m &= \frac{ie^{-i(2\pi m - C_1 - C_2)/2}}{2\pi m - C_1 - C_2} e^{iC_1 + iC_2 b} \\ &\times [e^{-i(2\pi m - C_1 - C_2)(-b)} e^{-iC_1}(-e^{-iC_2} + 1) + e^{i(-C_1 - C_2)}(-e^{-iC_1} + 1)]. \end{aligned} \tag{M.7}$$

In the limit $a \to 0^+$,

$$\begin{aligned} a_m &= \frac{ie^{-i(2\pi m - C_1 - C_2)/2}}{2\pi m - C_1 - C_2} e^{iC_2 b} \\ &\times [e^{-iC_2}(-e^{-iC_1} + 1) + e^{-i(2\pi m - C_1 - C_2)(-b)}(-e^{-iC_2} + 1)]. \end{aligned} \tag{M.8}$$

One can see that the two limits are equal, hence no discontinuity occurs.

Eq. (M.5) simplifies in terms of the parameter $\gamma = \frac{2\pi w}{v_o} \pmod{2\pi}$, $C_1 = -\frac{\gamma}{2} - i\log\left(\cos\frac{\gamma}{2}\right)$, and $C_2 = -\frac{\gamma}{2} + i\log\left(\cos\frac{\gamma}{2}\right)$ found in Eq. (3.50) as

$$\begin{aligned} a_m &= -\frac{2}{2\pi m + \gamma} e^{i\pi m(a+b-1)} \cos^{a-b}(\gamma/2) \left(\sin\left[\frac{(2\pi m + \gamma)(a-b) - \gamma}{2}\right] + \cos^{-1}(\gamma/2) \sin\left[\frac{(2\pi m + \gamma)(b-a)}{2}\right] \right) \\ &= \frac{2\tan(\gamma/2)}{2\pi m + \gamma} e^{i\pi m(a+b-1)} \cos^{a-b}(\gamma/2) \cos\left[\frac{(2\pi m + \gamma)(a-b) - \gamma}{2}\right]. \end{aligned} \tag{M.9}$$

The result for $a < b$ can be found by exchanging $a \leftrightarrow b$ and $C_1 \leftrightarrow C_2$,

$$\begin{aligned} a_m &= -\frac{2}{2\pi m + \gamma} e^{i\pi m(a+b-1)} \cos^{a-b}(\gamma/2) \left(\sin\left[\frac{(2\pi m + \gamma)(b-a) - \gamma}{2}\right] + \cos(\gamma/2) \sin\left[\frac{(2\pi m + \gamma)(a-b)}{2}\right] \right) \\ &= \frac{2\sin(\gamma/2)}{2\pi m + \gamma} e^{i\pi m(a+b-1)} \cos^{a-b}(\gamma/2) \cos\left[\frac{(2\pi m + \gamma)(a-b)}{2}\right]. \end{aligned} \tag{M.10}$$

We expect a large contribution from $m = 0$ in the strong coupling regime $\gamma = \frac{2\pi w}{v_o} \pmod{2\pi} \approx 0$.

Appendix N

Theory of the resonance

In this section, we provide a quantitative theory of the resonance seen in Fig. 3.9. We assume weak interaction between the inner and outer edge modes, i.e., θ is small. From Eq. (3.35), we can find the correction ΔP to $P_{\mathrm{o}}(t,a)$ due to this weak interaction. The correction from ΔS_{11} is merely a constant (independent of t) after integration and can be ignored. The correction due to ΔS_{12} equals

$$\Delta P = \frac{1}{3} P_{\mathrm{o}}^0(t,a) \int_0^\infty \frac{d\omega}{\omega} \Delta(S_{12} + S_{12}^*) e^{-i\omega t} e^{-\omega\delta}, \tag{N.1}$$

where $P_{\mathrm{o}}^0(t,a) = [\delta + i(t + a/v_1)]^{-1/3}[\delta + i(t - a/v_1)]^{-1/3}$ is the value of $P_{\mathrm{o}}(t,a)$ when $\theta = 0$. By looking at Eq. (3.30), we can find that

$$\Delta S_{12} = -\frac{2\theta^2 \left(e^{\frac{ia\omega(v_1+v_2)}{v_1 v_2}} \left(\cos\left(\frac{a\omega}{v_1}\right) - \cos\left(\frac{a\omega}{v_2}\right) \right) \right) + O\left(\theta^4\right)}{\left(-1 + e^{\frac{2ia\omega}{v_2}}\right) - 2\theta^2 \left(e^{\frac{2ia\omega}{v_2}} - e^{\frac{ia\omega(v_1+v_2)}{v_1 v_2}} \right) + O\left(\theta^4\right)}. \tag{N.2}$$

To the lowest order, the poles of ΔS_{12} can be found by calculating the zeroes of the denominator, and we can write the poles as $a\omega_n/v_2 = n\pi + \epsilon_n + i\Delta_n$, where

$$\epsilon_n + i\Delta_n = -i\theta^2[1 - (-1)^n e^{in\pi/k}] \tag{N.3}$$

with $k = v_1/v_2$. In this equation, we notice that $\Delta_n = -\theta^2[1 - (-1)^n \cos(n\pi/k)] \leq 0$. One needs to go to the next order in θ, if the above imaginary part is zero. Below we only focus on leading resonances with small n and assume that the imaginary part of Eq. (N.3) is nonzero.

To find ΔP, we first assume that $t > 0$ and consider the contour integral,

$$\int_{C_1+C_2+C_3} \frac{dz}{z} \Delta(S_{12} + S_{12}^*) e^{-izt} e^{-z\delta}, \tag{N.4}$$

where $C_1 : z = s, s \in (0,\infty)$ is the positive real axis, $C_2 : z = Re^{i\phi}, \phi \in (0, -\pi/2), R \to \infty$ is a quarter circle, and $C_3 : z = is, s \in (-\infty, 0)$ is the negative imaginary axis. We denote the residue of ΔS_{12} at the nth pole as M_n, and find the value of the integral as

$$D_1(t) = 2\pi i \sum_n \left(\frac{M_n e^{-i\omega_n t}}{\omega_n} \right). \tag{N.5}$$

The integral along C_2 is obviously zero. The integral along C_3 is a featureless function of t since the integrand has no poles close to the imaginary axis. We call that function $h(t)$. Notice that $h(t)$ is a real function. Therefore, we can write

$$\int_0^\infty \frac{d\omega}{\omega}\Delta(S_{12}+S_{12}^*)e^{-i\omega t}e^{-\omega\delta} = D_1(t) - h(t) \tag{N.6}$$

when $t > 0$. When $t < 0$, we close the contour in the counterclockwise direction and observe that the integral along C_1 is $D_2(t) - h(-t)$, where

$$D_2(t) = -2\pi i \sum_n \left(\frac{M_n e^{-i\omega_n t}}{\omega_n}\right)^* . \tag{N.7}$$

For all signs of t, we can conclude that the value of the integral is $D(t) - h(|t|)$, where

$$D(t) = 2\pi i \sum_n \left[\operatorname{sgn}(t)\,\mathrm{Re}\left(\frac{M_n e^{-i\omega_n t}}{\omega_n}\right) + i\,\mathrm{Im}\left(\frac{M_n e^{-i\omega_n t}}{\omega_n}\right)\right]. \tag{N.8}$$

Looking at the formula for the interference current,

$$\frac{2e^*}{\hbar^2}|\Gamma_1\Gamma_2|\cos\varphi \int_{-\infty}^0 dt\,\left[e^{-i\omega_J t}P(-t,a) - e^{i\omega_J t}P(-t,a) + \text{c.c.}\right], \tag{N.9}$$

we focus on the correction to the current due to $D(t)$, which can be expressed as

$$\Delta I = \frac{2e^*}{\hbar^2}|\Gamma_1\Gamma_2|\cos\varphi \sum_n \int_{-\infty}^0 dt$$
$$\left[\frac{2\pi i}{3}P_{\text{o}}^0(-t,a)\frac{M_n}{\omega_n}\left(e^{-i(\omega_J-\omega_n)t} - e^{i(\omega_J+\omega_n)t}\right) + \text{c.c.}\right]. \tag{N.10}$$

We thus expect a resonance when ω_J is close to $v_2(n\pi+\epsilon_n)/a \approx n\pi v_2/a$. The width of the resonance is set by $v_2\Delta_n/a \sim \theta^2$. The height of the conductance maximum can be estimated from the zero bias anomaly for quasiparticle tunneling at $\nu = 1/3$. To estimate the height we use the voltage on the order of the resonance width. Then the height is proportional to $M_n\Delta_n^{-1/3}/\omega_n \sim \theta^{4/3}$. The conductance peak scales as $M_n\Delta_n^{-4/3}\omega_n \sim \theta^{-2/3}$. All these predictions are in qualitative agreement with the features of the resonance observed in Fig. 3.11. A quantitative comparison is not possible at large θ.

Appendix O

Scattering matrix for the $\nu = 2/5$ FQH liquid with a chiral channel in the screening layer

The matrix entry $\tilde{S}_{11}$ can be written as the ratio of two expressions R_{11} and Q, $\tilde{S}_{11} = R_{11}/Q$. The numerator $R_{11}(e^{ia\omega/v_\rho}, e^{ia\omega/v_a}, e^{ia\omega/v_b}; \psi)$ is

$$\begin{aligned}
&-5\Big[-4\sqrt{7}\sin(3\psi)\left(e^{\frac{ia\omega}{v_a}} - e^{\frac{ia\omega}{v_b}}\right)\left(4e^{\frac{ia\omega}{v_\rho}} + 9e^{\frac{ia\omega}{v_a}} - 13e^{\frac{ia\omega}{v_b}}\right)\\
&+\sqrt{7}\sin(\psi)\left(-44e^{\frac{ia\omega(v_\rho+v_a)}{v_\rho v_a}} + 36e^{\frac{ia\omega(v_\rho+v_b)}{v_\rho v_b}} + 4e^{\frac{2ia\omega}{v_\rho}} - 62e^{\frac{ia\omega(v_a+v_b)}{v_a v_b}} + 53e^{\frac{2ia\omega}{v_a}} + 13e^{\frac{2ia\omega}{v_b}}\right)\\
&-28\cos(3\psi)\left(e^{\frac{ia\omega}{v_a}} - e^{\frac{ia\omega}{v_b}}\right)\left(-4e^{\frac{ia\omega}{v_\rho}} + 3e^{\frac{ia\omega}{v_a}} + e^{\frac{ia\omega}{v_b}}\right)\\
&+7\cos(\psi)\left(4e^{\frac{ia\omega(v_\rho+v_a)}{v_\rho v_a}} - 12e^{\frac{ia\omega(v_\rho+v_b)}{v_\rho v_b}} + 4e^{\frac{2ia\omega}{v_\rho}} - 62e^{\frac{ia\omega(v_a+v_b)}{v_a v_b}} + 29e^{\frac{2ia\omega}{v_a}} + 37e^{\frac{2ia\omega}{v_b}}\right)\\
&-40\sqrt{7}\sin(5\psi)\left(e^{\frac{ia\omega}{v_a}} - e^{\frac{ia\omega}{v_b}}\right)^2 + 56\cos(5\psi)\left(e^{\frac{ia\omega}{v_a}} - e^{\frac{ia\omega}{v_b}}\right)^2\Big]
\end{aligned} \tag{O.1}$$

The denominator $Q(e^{ia\omega/v_\rho}, e^{ia\omega/v_a}, e^{ia\omega/v_b}; \psi)$ is

$$\begin{aligned}
&\left(\sqrt{7}\sin(\psi) + 7\cos(\psi)\right)\Big\{5\left(e^{\frac{ia\omega}{v_a}} - e^{\frac{ia\omega}{v_b}}\right)\Big[\sqrt{7}\Big(15\sin(4\psi)\left(e^{\frac{ia\omega}{v_a}} - e^{\frac{ia\omega}{v_b}}\right) - 4\sin(2\psi)\left(e^{\frac{ia\omega}{v_\rho}} + 10e^{\frac{ia\omega}{v_a}} + 10e^{\frac{ia\omega}{v_b}}\right)\Big)\\
&-12\cos(2\psi)\left(e^{\frac{ia\omega}{v_\rho}} + 10e^{\frac{ia\omega}{v_a}} + 10e^{\frac{ia\omega}{v_b}}\right) + 5\cos(4\psi)\left(e^{\frac{ia\omega}{v_a}} - e^{\frac{ia\omega}{v_b}}\right)\Big]\\
&+4\left(20e^{\frac{ia\omega(v_\rho+v_a)}{v_\rho v_a}} + 20e^{\frac{ia\omega(v_\rho+v_b)}{v_\rho v_b}} + e^{\frac{2ia\omega}{v_\rho}} + 100e^{\frac{ia\omega(v_a+v_b)}{v_a v_b}} + 150e^{\frac{2ia\omega}{v_a}} + 150e^{\frac{2ia\omega}{v_b}} - 441\right)\Big\}
\end{aligned} \tag{O.2}$$

The matrix element $\tilde{S}_{13}$ is written as R_{13}/Q. The numerator $R_{13}(e^{ia\omega/v_\rho}, e^{ia\omega/v_a}, e^{ia\omega/v_b}; \psi)$ is

$$\begin{aligned}
&3\Big\{25\sqrt{7}\sin(5\psi)e^{\frac{ia\omega}{v_\rho}}\left(e^{\frac{ia\omega}{v_a}}-e^{\frac{ia\omega}{v_b}}\right)^2\\
&-2\sqrt{7}\sin(3\psi)\big[10e^{\frac{ia\omega(v_\rho(v_a+v_b)+v_av_b)}{v_\rho v_a v_b}}+30e^{\frac{ia\omega(2v_\rho+v_a)}{v_\rho v_a}}+e^{\frac{ia\omega(v_\rho+2v_a)}{v_\rho v_a}}-40e^{\frac{ia\omega(2v_\rho+v_b)}{v_\rho v_b}}\\
&-e^{\frac{ia\omega(v_\rho+2v_b)}{v_\rho v_b}}-125e^{\frac{ia\omega(2v_a+v_b)}{v_a v_b}}+125e^{\frac{ia\omega(v_a+2v_b)}{v_a v_b}}+154e^{\frac{ia\omega}{v_a}}-154e^{\frac{ia\omega}{v_b}}\big]\\
&+\sqrt{7}\sin(\psi)\big[70e^{\frac{ia\omega(v_\rho(v_a+v_b)+v_av_b)}{v_\rho v_a v_b}}+55e^{\frac{ia\omega(2v_\rho+v_a)}{v_\rho v_a}}+6e^{\frac{ia\omega(v_\rho+2v_a)}{v_\rho v_a}}+55e^{\frac{ia\omega(2v_\rho+v_b)}{v_\rho v_b}}\\
&+2e^{\frac{ia\omega(v_\rho+2v_b)}{v_\rho v_b}}-140e^{\frac{ia\omega}{v_\rho}}+300e^{\frac{ia\omega(2v_a+v_b)}{v_a v_b}}+100e^{\frac{ia\omega(v_a+2v_b)}{v_a v_b}}-406e^{\frac{ia\omega}{v_a}}-42e^{\frac{ia\omega}{v_b}}\big]\\
&+35\cos(5\psi)e^{\frac{ia\omega}{v_\rho}}\left(e^{\frac{ia\omega}{v_a}}-e^{\frac{ia\omega}{v_b}}\right)^2\\
&+7\cos(\psi)\big[70e^{\frac{ia\omega(v_\rho(v_a+v_b)+v_av_b)}{v_\rho v_a v_b}}+15e^{\frac{ia\omega(2v_\rho+v_a)}{v_\rho v_a}}+2e^{\frac{ia\omega(v_\rho+2v_a)}{v_\rho v_a}}+95e^{\frac{ia\omega(2v_\rho+v_b)}{v_\rho v_b}}+6e^{\frac{ia\omega(v_\rho+2v_b)}{v_\rho v_b}}\\
&-140e^{\frac{ia\omega}{v_\rho}}+300e^{\frac{ia\omega(2v_a+v_b)}{v_a v_b}}+100e^{\frac{ia\omega(v_a+2v_b)}{v_a v_b}}-322e^{\frac{ia\omega}{v_a}}-126e^{\frac{ia\omega}{v_b}}\big]\\
&-14\cos(3\psi)\big[10e^{\frac{ia\omega(v_\rho(v_a+v_b)+v_av_b)}{v_\rho v_a v_b}}+10e^{\frac{ia\omega(2v_\rho+v_a)}{v_\rho v_a}}+e^{\frac{ia\omega(v_\rho+2v_a)}{v_\rho v_a}}-20e^{\frac{ia\omega(2v_\rho+v_b)}{v_\rho v_b}}\\
&-e^{\frac{ia\omega(v_\rho+2v_b)}{v_\rho v_b}}-25e^{\frac{ia\omega(2v_a+v_b)}{v_a v_b}}+25e^{\frac{ia\omega(v_a+2v_b)}{v_a v_b}}+14e^{\frac{ia\omega}{v_a}}-14e^{\frac{ia\omega}{v_b}}\big]\Big\}
\end{aligned} \tag{O.3}$$

Appendix P

Effects of charge tunneling between co-propagating modes in the presence of a chiral channel in the screening layer

We need to understand possible values of the charge on the inner closed loop at zero temperature in the presence of a voltage bias. For this we need to minimize the effective Hamiltonian

$$H_{\text{eff}} = H - V_d\sqrt{\nu_1}\frac{e\partial_x\phi_{\text{o}}^d}{2\pi} - V_u\sqrt{\nu_1}\left(-\frac{e\partial_x\phi_{\text{o}}^u}{2\pi}\right) - V_{\text{i}}\sqrt{\nu_2}\frac{e}{2\pi}\partial_x\phi_{\text{i}}^d + V_{\text{i}}\sqrt{\nu_2}\frac{e}{2\pi}\partial_x\phi_{\text{i}}^u, \tag{P.1}$$

where H is the Hamiltonian from Section 3.5; $V_d > V_u$ set the chemical potentials of the lower and upper open channels in the 2D electron gas and V_{i} sets the chemical potential of the inner loop; the indexes d and u refer to the upper and lower parts of the outer and inner channels. The chemical potential of the screening layer is set to 0.

We use the following notation for the coefficients:

$$A = \frac{\hbar v_{\text{i}}}{2\pi}, \quad B = \frac{\hbar v_{\text{o}}}{2\pi}, \quad C = \frac{\hbar w}{2\pi}, \quad E = \frac{\hbar v_s}{2\pi}, \quad D_1 = \sqrt{\frac{5}{6}}\frac{\hbar U}{2\pi}, \quad D_2 = \sqrt{\frac{1}{6}}\frac{\hbar U}{2\pi},$$
$$\alpha = \sqrt{\nu_1}\frac{eV_u}{2\pi}, \quad \beta = \sqrt{\nu_1}\frac{eV_d}{2\pi}, \quad \delta = \sqrt{\nu_2}\frac{eV_{\text{i}}}{2\pi}, \quad \tilde{n} = \frac{\nu_1}{\sqrt{\nu_2}}\frac{2\pi N}{a}, \tag{P.2}$$

where N is the number of the quasiparticles on the inner closed loop.

The minimization of the Hamiltonian at a fixed N yields

$$H[\alpha, \beta; n] = a\left(\frac{P}{Q} - \delta\tilde{n}\right) \tag{P.3}$$

where

$$
\begin{aligned}
P =& 2(\alpha+\beta)(D_1D_2-CE) \\
&\times\left[A\left(D_1^2-BE\right)+BD_2^2+C^2E-2CD_1D_2\right]\tilde{n} \\
&+\left(A\left(D_1^2-BE\right)+BD_2^2+C^2E-2CD_1D_2\right)^2\tilde{n}^2 \\
&+E\left(2B\left(\alpha^2+\beta^2\right)\left(D_2^2-AE\right)+C^2E(\alpha+\beta)^2\right) \\
&+D_1^2\left(2AE\left(\alpha^2+\beta^2\right)-D_2^2(\alpha-\beta)^2\right)-2CD_1D_2E(\alpha+\beta)^2
\end{aligned} \tag{P.4}
$$

and

$$
Q = 4\left(D_1^2-BE\right)\left(A\left(D_1^2-BE\right)+BD_2^2+C^2E-2CD_1D_2\right) \tag{P.5}
$$

The number of quasiparticles that minimizes the energy equals

$$
N = [\frac{\sqrt{\nu_2}}{\nu_1}\beta_0\left(2\Lambda\sqrt{\nu_2}V_{\mathrm{i}}-\sqrt{\nu_1}V_u-\sqrt{\nu_1}V_d\right)], \tag{P.6}
$$

where the bracket means the closest integer, β_0 is defined as

$$
\beta_0 = \frac{ea}{2\pi\hbar}\frac{\frac{\sqrt{5}}{6}U^2-wv_s}{v_{\mathrm{i}}(\frac{5}{6}U^2-v_{\mathrm{o}}v_s)+v_{\mathrm{o}}\frac{1}{6}U^2+w^2v_s-2w\frac{\sqrt{5}}{6}U^2}, \tag{P.7}
$$

and we use another shorthand notation

$$
\Lambda = \frac{D_1^2-BE}{D_1D_2-CE} = \frac{v_{\mathrm{o}}v_s-\frac{5}{6}U^2}{wv_s-\frac{\sqrt{5}}{6}U^2}. \tag{P.8}
$$

Similar to the discussion at $\nu=2$, we need to find the maximal and minimal allowed $N=N_d,N_u$ by substituting $V_{\mathrm{i}}=V_d,V_u$. We find $N_u=[g_u]$ and $N_d=[g_d]$, where the bracket means the closest integer, and $g_{u,d}$ are defined as

$$
\begin{aligned}
g_u &= \frac{\sqrt{\nu_2}}{\nu_1}\beta_0\left(2\Lambda\sqrt{\nu_2}V_u-\sqrt{\nu_1}V_u-\sqrt{\nu_1}V_d\right)+\beta_1\lambda_1 && \text{(P.9)} \\
g_d &= \frac{\sqrt{\nu_2}}{\nu_1}\beta_0\left(2\Lambda\sqrt{\nu_2}V_d-\sqrt{\nu_1}V_u-\sqrt{\nu_1}V_d\right)+\beta_1\lambda_1. && \text{(P.10)}
\end{aligned}
$$

As before, $\beta_1\lambda_1$ reflects the energy dependence on the magnetic flux through the nominal area of the inner loop or a gate voltage. The N-dependent part of the Aharonov–Bohm phase equals $\exp\{(i\gamma N)\}$, where $\gamma=2\pi\nu_1(\frac{\sqrt{\nu_1}}{\sqrt{\nu_2}\Lambda}+1) \pmod{2\pi}$, $-\pi<\gamma\le\pi$.

As in Section 3.2, at zero temperature, the allowed population numbers N on the inner loop follow a binomial distribution f_N. The average Aharonov–Bohm phase factor

$$
\begin{aligned}
&\sum_{N=N_u}^{N_d} f_N\exp\left[iC+i(\alpha_0\tilde{V}+\alpha_1\lambda_1)+i\gamma N\right] \\
=&\sum_n a_n e^{iC}\exp[i(2\pi n\beta_1+\alpha_1+\gamma\beta_1)\lambda_1]\exp\left\{i\left[\alpha_0+2\gamma\frac{\sqrt{\nu_2}}{\nu_1}\beta_0(\Lambda\sqrt{\nu_2}-\sqrt{\nu_1})\right]\tilde{V}\right\} \\
&\times\exp\left[2\beta_0\Lambda\frac{\nu_2}{\nu_1}\log\left(\cos\frac{\gamma}{2}\right)V\right],
\end{aligned} \tag{P.11}
$$

where

$$\alpha_0 = -\frac{2\nu_1 ea}{\hbar}\frac{v_s}{v_\text{o} v_s - \frac{5}{6}U^2}, \tag{P.12}$$

and $\alpha_1\lambda_1$ contains information about the magnetic flux through the device.

Bibliography

[1] J. M. Kosterlitz and D. J. Thouless, "Ordering, metastability and phase transitions in two-dimensional systems", J. Phys. C: Solid State Phys. **6**, 1181 (1973).

[2] K. v. Klitzing, G. Dorda, and M. Pepper, "New method for high-accuracy determination of the fine-structure constant based on quantized Hall resistance", Phys. Rev. Lett. **45**, 494–497 (1980).

[3] X.-G. Wen, *Quantum field theory of many-body systems: from the origin of sound to an origin of light and electrons* (Oxford University Press, Oxford, 2004).

[4] D. Tong, "Lectures on the quantum Hall effect", arXiv:1606.06687 [hep-th].

[5] D. C. Tsui, H. L. Stormer, and A. C. Gossard, "Two-dimensional magnetotransport in the extreme quantum limit", Phys. Rev. Lett. **48**, 1559–1562 (1982).

[6] H. L. Stormer, D. C. Tsui, and A. C. Gossard, "The fractional quantum Hall effect", Rev. Mod. Phys. **71**, S298–S305 (1999).

[7] C. Wang, A. Gupta, S. K. Singh, Y. J. Chung, L. N. Pfeiffer, K. W. West, K. W. Baldwin, R. Winkler, and M. Shayegan, "Even-denominator fractional quantum Hall state at filling factor $\nu = 3/4$", Phys. Rev. Lett. **129**, 156801 (2022).

[8] R. B. Laughlin, "Quantized Hall conductivity in two dimensions", Phys. Rev. B **23**, 5632–5633 (1981).

[9] B. I. Halperin, "Quantized Hall conductance, current-carrying edge states, and the existence of extended states in a two-dimensional disordered potential", Phys. Rev. B **25**, 2185–2190 (1982).

[10] R. B. Laughlin, "Anomalous quantum Hall effect: an incompressible quantum fluid with fractionally charged excitations", Phys. Rev. Lett. **50**, 1395–1398 (1983).

[11] D. Arovas, J. R. Schrieffer, and F. Wilczek, "Fractional statistics and the quantum Hall effect", Phys. Rev. Lett. **53**, 722–723 (1984).

[12] B. I. Halperin, "Statistics of quasiparticles and the hierarchy of fractional quantized Hall states", Phys. Rev. Lett. **52**, 1583–1586 (1984).

[13] F. D. M. Haldane, "Fractional quantization of the Hall effect: a hierarchy of incompressible quantum fluid states", Phys. Rev. Lett. **51**, 605–608 (1983).

[14] J. K. Jain, "Composite-fermion approach for the fractional quantum Hall effect", Phys. Rev. Lett. **63**, 199–202 (1989).

[15] J. K. Jain, *Composite fermions* (Cambridge University Press, Cambridge, 2007).

[16] G. Moore and N. Read, "Nonabelions in the fractional quantum Hall effect", Nucl. Phys. B **360**, 362–396 (1991).

[17] C. Nayak and F. Wilczek, "$2n$-quasihole states realize 2^{n-1}-dimensional spinor braiding statistics in paired quantum Hall states", Nucl. Phys. B **479**, 529–553 (1996).

[18] S. Das Sarma, M. Freedman, and C. Nayak, "Topologically protected qubits from a possible non-Abelian fractional quantum Hall state", Phys. Rev. Lett. **94**, 166802 (2005).

[19] X. G. Wen and A. Zee, "Classification of Abelian quantum Hall states and matrix formulation of topological fluids", Phys. Rev. B **46**, 2290–2301 (1992).

[20] C. Nayak, S. H. Simon, A. Stern, M. Freedman, and S. Das Sarma, "Non-Abelian anyons and topological quantum computation", Rev. Mod. Phys. **80**, 1083–1159 (2008).

[21] J. von Delft and H. Schoeller, "Bosonization for beginners — refermionization for experts", Ann. Phys. (Leipzig) **7**, 225–305 (1998).

[22] R. Guyon, P. Devillard, T. Martin, and I. Safi, "Klein factors in multiple fractional quantum Hall edge tunneling", Phys. Rev. B **65**, 153304 (2002).

[23] P. Fendley, M. P. A. Fisher, and C. Nayak, "Dynamical disentanglement across a point contact in a non-Abelian quantum Hall state", Phys. Rev. Lett. **97**, 036801 (2006).

[24] P. Fendley, M. P. A. Fisher, and C. Nayak, "Edge states and tunneling of non-Abelian quasiparticles in the $\nu = 5/2$ quantum Hall state and $p + ip$ superconductors", Phys. Rev. B **75**, 045317 (2007).

[25] P. Di Francesco, P. Mathieu, and D. Sénéchal, *Conformal field theory* (Springer, New York, 1997).

[26] P. Anderson, "Resonating valence bonds: a new kind of insulator?", Mater. Res. Bull. **8**, 153–160 (1973).

[27] V. Kalmeyer and R. B. Laughlin, "Equivalence of the resonating-valence-bond and fractional quantum Hall states", Phys. Rev. Lett. **59**, 2095–2098 (1987).

[28] A. Kitaev, "Anyons in an exactly solved model and beyond", Ann. Phys. (N. Y.) **321**, 2–111 (2006).

[29] Y. Kasahara, T. Ohnishi, Y. Mizukami, O. Tanaka, S. Ma, K. Sugii, N. Kurita, H. Tanaka, J. Nasu, Y. Motome, T. Shibauchi, and Y. Matsuda, "Majorana quantization and half-integer thermal quantum Hall effect in a Kitaev spin liquid", Nature **559**, 227 (2017).

[30] P. A. Lee, *Quantized (or not quantized) thermal Hall effect and oscillations in the thermal conductivity in the Kitaev spin liquid candidate α–$RuCl_3$*, DOI: `10.36471/JCCM_November_2021_02`, 2021.

[31] D. Aasen, R. S. K. Mong, B. M. Hunt, D. Mandrus, and J. Alicea, "Electrical probes of the non-Abelian spin liquid in Kitaev materials", Phys. Rev. X **10**, 031014 (2020).

[32] J. M. Leinaas and J. Myrheim, "On the theory of identical particles", Nuovo Cim B **37**, 1–23 (1977).

[33] F. Wilczek, "Quantum mechanics of fractional-spin particles", Phys. Rev. Lett. **49**, 957–959 (1982).

[34] J. Preskill, *Lecture notes for physics 219: quantum computation*, `http://theory.caltech.edu/~preskill/ph219/topological.pdf`, June 2004.

[35] C. de C. Chamon, D. E. Freed, S. A. Kivelson, S. L. Sondhi, and X. G. Wen, "Two point-contact interferometer for quantum Hall systems", Phys. Rev. B **55**, 2331–2343 (1997).

[36] A. Stern and B. I. Halperin, "Proposed experiments to probe the non-Abelian $\nu = 5/2$ quantum Hall state", Phys. Rev. Lett. **96**, 016802 (2006).

[37] P. Bonderson, A. Kitaev, and K. Shtengel, "Detecting non-Abelian statistics in the $\nu = 5/2$ fractional quantum Hall state", Phys. Rev. Lett. **96**, 016803 (2006).

[38] D. E. Feldman and A. Kitaev, "Detecting non-Abelian statistics with an electronic Mach-Zehnder interferometer", Phys. Rev. Lett. **97**, 186803 (2006).

[39] K. T. Law, D. E. Feldman, and Y. Gefen, "Electronic Mach-Zehnder interferometer as a tool to probe fractional statistics", Phys. Rev. B **74**, 045319 (2006).

[40] D. E. Feldman, Y. Gefen, A. Kitaev, K. T. Law, and A. Stern, "Shot noise in an anyonic Mach-Zehnder interferometer", Phys. Rev. B **76**, 085333 (2007).

[41] B. Rosenow, B. I. Halperin, S. H. Simon, and A. Stern, "Bulk-edge coupling in the non-Abelian $\nu = 5/2$ quantum Hall interferometer", Phys. Rev. Lett. **100**, 226803 (2008).

[42] Z.-X. Hu, E. H. Rezayi, X. Wan, and K. Yang, "Edge-mode velocities and thermal coherence of quantum Hall interferometers", Phys. Rev. B **80**, 235330 (2009).

[43] V. V. Ponomarenko and D. V. Averin, "Mach-Zehnder interferometer in the fractional quantum Hall regime", Phys. Rev. Lett. **99**, 066803 (2007).

[44] V. V. Ponomarenko and D. V. Averin, "Splitting electrons into quasiparticles with a fractional edge-state Mach-Zehnder interferometer", Phys. Rev. B **79**, 045303 (2009).

[45] V. V. Ponomarenko and D. V. Averin, "Charge transfer statistics in symmetric fractional edge-state Mach-Zehnder interferometer", Phys. Rev. B **80**, 201313 (2009).

[46] V. V. Ponomarenko and D. V. Averin, "Braiding of anyonic quasiparticles in charge transfer statistics of a symmetric fractional edge-state Mach-Zehnder interferometer", Phys. Rev. B **82**, 205411 (2010).

[47] W. Bishara and C. Nayak, "Edge states and interferometers in the Pfaffian and anti-Pfaffian states of the $\nu = \frac{5}{2}$ quantum Hall system", Phys. Rev. B **77**, 165302 (2008).

[48] W. Bishara and C. Nayak, "Odd-even crossover in a non-Abelian $\nu = 5/2$ interferometer", Phys. Rev. B **80**, 155304 (2009).

[49] B. I. Halperin, A. Stern, I. Neder, and B. Rosenow, "Theory of the Fabry-Pérot quantum Hall interferometer", Phys. Rev. B **83**, 155440 (2011).

[50] O. Smits, J. K. Slingerland, and S. H. Simon, "Tunneling current through fractional quantum Hall interferometers", Phys. Rev. B **89**, 045308 (2014).

[51] D. Ferraro and E. Sukhorukov, "Interaction effects in a multi-channel Fabry-Pérot interferometer in the Aharonov-Bohm regime", SciPost Phys. **3**, 014 (2017).

[52] G. A. Frigeri, D. D. Scherer, and B. Rosenow, "Sub-periods and apparent pairing in integer quantum Hall interferometers", EPL **126**, 67007 (2019).

[53] G. A. Frigeri and B. Rosenow, "Electron pairing in the quantum Hall regime due to neutralon exchange", Phys. Rev. Res. **2**, 043396 (2020).

[54] B. Rosenow and A. Stern, "Flux superperiods and periodicity transitions in quantum Hall interferometers", Phys. Rev. Lett. **124**, 106805 (2020).

[55] D. E. Feldman and B. I. Halperin, "Fractional charge and fractional statistics in the quantum Hall effects", Rep. Prog. Phys. **84**, 076501 (2021).

[56] D. E. Feldman and B. I. Halperin, "Robustness of quantum Hall interferometry", Phys. Rev. B **105**, 165310 (2022).

[57] Y. Ji, Y. Chung, D. Sprinzak, M. Heiblum, D. Mahalu, and H. Shtrikman, "An electronic Mach–Zehnder interferometer", Nature **422**, 415 (2003).

[58] F. E. Camino, W. Zhou, and V. J. Goldman, "$e/3$ Laughlin quasiparticle primary-filling $\nu = 1/3$ interferometer", Phys. Rev. Lett. **98**, 076805 (2007).

[59] E. V. Deviatov and A. Lorke, "Experimental realization of a Fabry-Perot-type interferometer by copropagating edge states in the quantum Hall regime", Phys. Rev. B **77**, 161302 (2008).

[60] E. V. Deviatov, B. Marquardt, A. Lorke, G. Biasiol, and L. Sorba, "Interference effects in transport across a single incompressible strip at the edge of the fractional quantum Hall system", Phys. Rev. B **79**, 125312 (2009).

[61] R. L. Willett, L. N. Pfeiffer, and K. W. West, "Measurement of filling factor 5/2 quasiparticle interference with observation of charge $e/4$ and $e/2$ period oscillations", Proc. Natl. Acad. Sci. U.S.A. **106**, 8853–8858 (2009).

[62] R. L. Willett, L. N. Pfeiffer, and K. W. West, "Alternation and interchange of $e/4$ and $e/2$ period interference oscillations consistent with filling factor 5/2 non-Abelian quasiparticles", Phys. Rev. B **82**, 205301 (2010).

[63] Y. Zhang, D. T. McClure, E. M. Levenson-Falk, C. M. Marcus, L. N. Pfeiffer, and K. W. West, "Distinct signatures for Coulomb blockade and Aharonov-Bohm interference in electronic Fabry-Perot interferometers", Phys. Rev. B **79**, 241304 (2009).

[64] D. T. McClure, Y. Zhang, B. Rosenow, E. M. Levenson-Falk, C. M. Marcus, L. N. Pfeiffer, and K. W. West, "Edge-state velocity and coherence in a quantum Hall Fabry-Pérot interferometer", Phys. Rev. Lett. **103**, 206806 (2009).

[65] N. Ofek, A. Bid, M. Heiblum, A. Stern, V. Umansky, and D. Mahalu, "Role of interactions in an electronic Fabry–Perot interferometer operating in the quantum Hall effect regime", Proc. Natl. Acad. Sci. U.S.A. **107**, 5276–5281 (2010).

[66] D. T. McClure, W. Chang, C. M. Marcus, L. N. Pfeiffer, and K. W. West, "Fabry-Perot interferometry with fractional charges", Phys. Rev. Lett. **108**, 256804 (2012).

[67] H. K. Choi, I. Sivan, A. Rosenblatt, M. Heiblum, V. Umansky, and D. Mahalu, "Robust electron pairing in the integer quantum Hall effect regime", Nat. Commun. **6**, 7435 (2015).

[68] I. Sivan, R. Bhattacharyya, H. K. Choi, M. Heiblum, D. E. Feldman, D. Mahalu, and V. Umansky, "Interaction-induced interference in the integer quantum Hall effect", Phys. Rev. B **97**, 125405 (2018).

[69] J. Nakamura, S. Fallahi, H. Sahasrabudhe, R. Rahman, S. Liang, G. C. Gardner, and M. J. Manfra, "Aharonov–Bohm interference of fractional quantum Hall edge modes", Nat. Phys. **15**, 563 (2019).

[70] J. Nakamura, S. Liang, G. C. Gardner, and M. J. Manfra, "Direct observation of anyonic braiding statistics at the $\nu = 1/3$ fractional quantum Hall state", Nat. Phys. **16**, 931 (2020).

[71] C. Déprez, L. Veyrat, H. Vignaud, G. Nayak, K. Watanabe, T. Taniguchi, F. Gay, H. Sellier, and B. Sacépé, "A tunable Fabry–Pérot quantum Hall interferometer in graphene", Nat. Nanotechnol. **16**, 555–562 (2021).

[72] Y. Ronen, T. Werkmeister, D. Haie Najafabadi, A. T. Pierce, L. E. Anderson, Y. J. Shin, S. Y. Lee, Y. H. Lee, B. Johnson, K. Watanabe, T. Taniguchi, A. Yacoby, and P. Kim, "Aharonov–Bohm effect in graphene-based Fabry–Pérot quantum Hall interferometers", Nat. Nanotechnol. **16**, 563–569 (2021).

[73] L. Zhao, E. G. Arnault, T. F. Larson, Z. Iftikhar, A. Seredinski, T. Fleming, K. Watanabe, T. Taniguchi, F. Amet, and G. Finkelstein, "Graphene-based quantum Hall interferometer with self-aligned side gates", Nano Lett. **22**, 9645–9651 (2022).

[74] H. K. Kundu, S. Biswas, N. Ofek, V. Umansky, and M. Heiblum, "Anyonic interference and braiding phase in a Mach-Zehnder interferometer", Nature Physics **19**, 515–521 (2023).

[75] J. Nakamura, S. Liang, G. C. Gardner, and M. J. Manfra, "Fabry-Pérot interferometry at the $\nu = 2/5$ fractional quantum Hall state", Phys. Rev. X **13**, 041012 (2023).

[76] T. Werkmeister, J. R. Ehrets, Y. Ronen, M. E. Wesson, D. Najafabadi, K. Watanabe, T. Taniguchi, Z. Wei, D. E. Feldman, B. I. Halperin, A. Yacoby, and P. Kim, "Strongly coupled edge states in a graphene quantum Hall interferometer", arXiv:2312.03150 [cond-mat.mes-hall].

[77] N. L. Samuelson, L. A. Cohen, W. Wang, S. Blanch, T. Taniguchi, K. Watanabe, M. P. Zaletel, and A. F. Young, "Anyonic statistics and slow quasiparticle dynamics in a graphene fractional quantum Hall interferometer", arXiv:2403.19628 [cond-mat.mes-hall].

[78] T. Werkmeister, J. R. Ehrets, M. E. Wesson, D. H. Najafabadi, K. Watanabe, T. Taniguchi, B. I. Halperin, A. Yacoby, and P. Kim, "Anyon braiding and telegraph noise in a graphene interferometer", arXiv:2403.18983 [cond-mat.mes-hall].

[79] C. L. Kane and M. P. A. Fisher, "Quantized thermal transport in the fractional quantum Hall effect", Phys. Rev. B **55**, 15832–15837 (1997).

[80] N. Read and D. Green, "Paired states of fermions in two dimensions with breaking of parity and time-reversal symmetries and the fractional quantum Hall effect", Phys. Rev. B **61**, 10267–10297 (2000).

[81] A. Cappelli, M. Huerta, and G. R. Zemba, "Thermal transport in chiral conformal theories and hierarchical quantum Hall states", Nucl. Phys. B **636**, 568–582 (2002).

[82] M. Banerjee, M. Heiblum, A. Rosenblatt, Y. Oreg, D. E. Feldman, A. Stern, and V. Umansky, "Observed quantization of anyonic heat flow", Nature **545**, 75 (2017).

[83] M. Banerjee, M. Heiblum, V. Umansky, D. E. Feldman, Y. Oreg, and A. Stern, "Observation of half-integer thermal Hall conductance", Nature **559**, 205 (2018).

[84] S. K. Srivastav, M. R. Sahu, K. Watanabe, T. Taniguchi, S. Banerjee, and A. Das, "Universal quantized thermal conductance in graphene", Sci. Adv. **5**, eaaw5798 (2019).

[85] H. Bartolomei, M. Kumar, R. Bisognin, A. Marguerite, J.-M. Berroir, E. Bocquillon, B. Plaçais, A. Cavanna, Q. Dong, U. Gennser, Y. Jin, and G. Féve, "Fractional statistics in anyon collisions", Science **368**, 173–177 (2020).

[86] Z. Wei, V. F. Mitrovi ć, and D. E. Feldman, "Thermal interferometry of anyons in spin liquids", Phys. Rev. Lett. **127**, 167204 (2021).

[87] K. Klocke, J. E. Moore, J. Alicea, and G. B. Halász, "Thermal probes of phonon-coupled Kitaev spin liquids: from accurate extraction of quantized edge transport to anyon interferometry", Phys. Rev. X **12**, 011034 (2022).

[88] D. S. Shapiro, D. E. Feldman, A. D. Mirlin, and A. Shnirman, "Thermoelectric transport in junctions of Majorana and Dirac channels", Phys. Rev. B **95**, 195425 (2017).

[89] P. H. Bonderson, "Non-Abelian anyons and interferometry", PhD thesis (California Institute of Technology, 2007).

[90] M. Heiblum and D. E. Feldman, "Edge probes of topological order", Int. J. Mod. Phys. A **35**, 2030009 (2020).

[91] J. Nilsson and A. R. Akhmerov, "Theory of non-Abelian Fabry-Perot interferometry in topological insulators", Phys. Rev. B **81**, 205110 (2010).

[92] E. Papa and A. H. MacDonald, "Interactions suppress quasiparticle tunneling at Hall bar constrictions", Phys. Rev. Lett. **93**, 126801 (2004).

[93] G. Yang and D. E. Feldman, "Influence of device geometry on tunneling in $\nu = 5/2$ quantum Hall liquid", Phys. Rev. B **88**, 085317 (2013).

[94] F. D. M. Haldane, ""Fractional statistics" in arbitrary dimensions: A generalization of the Pauli principle", Phys. Rev. Lett. **67**, 937–940 (1991).

[95] G. E. Stedman, "Fermi's golden rule—an exercise in quantum field theory", Am. J. Phys. **39**, 205–214 (1971).

[96] T. Martin, "Noise in mesoscopic physics", in *Nanophysics: coherence and transport*, Vol. 81, edited by H. Bouchiat, Y. Gefen, S. Guéron, G. Montambaux, and J. Dalibard, Les Houches (Elsevier, Amsterdam, 2005), pp. 283–359.

[97] C. L. Kane, "Telegraph noise and fractional statistics in the quantum Hall effect", Phys. Rev. Lett. **90**, 226802 (2003).

[98] S. Jezouin, F. D. Parmentier, A. Anthore, U. Gennser, A. Cavanna, Y. Jin, and F. Pierre, "Quantum limit of heat flow across a single electronic channel", Science **342**, 601–604 (2013).

[99] D. B. Chklovskii, B. I. Shklovskii, and L. I. Glazman, "Electrostatics of edge channels", Phys. Rev. B **46**, 4026–4034 (1992).

[100] M. J. Manfra, private communication.

[101] L. S. Levitov, A. V. Shytov, and B. I. Halperin, "Effective action of a compressible quantum Hall state edge: application to tunneling", Phys. Rev. B **64**, 075322 (2001).

[102] C. de C. Chamon, D. E. Freed, and X. G. Wen, "Tunneling and quantum noise in one-dimensional Luttinger liquids", Phys. Rev. B **51**, 2363–2379 (1995).

[103] N. Batra, Z. Wei, S. Vishveshwara, and D. E. Feldman, "Anyonic Mach-Zehnder interferometer on a single edge of a two-dimensional electron gas", Phys. Rev. B **108**, L241302 (2023).

[104] R. A. Melcer, B. Dutta, C. Spånslätt, J. Park, A. D. Mirlin, and V. Umansky, "Absent thermal equilibration on fractional quantum Hall edges over macroscopic scale", Nat. Commun. **13**, 376 (2022).

[105] F. A. Bais, P. van Driel, and M. de Wild Propitius, "Quantum symmetries in discrete gauge theories", Phys. Lett. B **280**, 63 (1992).

[106] T. Dokchitser, *Character tables - GroupNames*, `https://people.maths.bris.ac.uk/~matyd/GroupNames/characters.html`.